The Reacting Atmosphere 2

Matthias Ehrhardt *Editor*

Mathematical Modelling and Numerical Simulation of Oil Pollution Problems

The Reacting Atmosphere 2

The series *The Reacting Atmosphere* will present the objectives and visions of a new research network combining different disciplines involved in climate research. The objective of the network is to understand the highly complex regulatory cycles in the atmosphere taking into account all important parameters, to identify important atmospheric processes, to examine policies with respect to their consequences and, based on this to derive recommendations on how in a changing world targeted suggestions for improvement can be realized. The participating academic institutions will exploit synergies through joint research activities and make an important contribution to international research efforts directed at understanding climate change. The reader will learn about the activities and probably find a point of contact for future collaborations.

More information about this series http://www.springer.com/series/13396

Matthias Ehrhardt
Editor

Mathematical Modelling and Numerical Simulation of Oil Pollution Problems


Springer

Editor
Matthias Ehrhardt
Chair of Applied Mathematics and
Numerical Analysis
Fachbereich C
Bergische Universität Wuppertal
Wuppertal
Germany

ISSN 2199-1138 ISSN 2199-1146 (electronic)
The Reacting Atmosphere
ISBN 978-3-319-16458-8 ISBN 978-3-319-16459-5 (eBook)
DOI 10.1007/978-3-319-16459-5

Library of Congress Control Number: 2015933619

Mathematics Subject Classification (2010): 65Mxx, 62P12, 62P30, 62P35, 91B76

Springer Cham Heidelberg New York Dordrecht London

Printed on acid-free paper

Springer International Publishing AG Switzerland is part of Springer Science+Business Media (www.springer.com)

Preface

This is the second volume of the series "The Reacting Atmosphere", which stems from the transdisciplinary Research Network coordinated at the University of Wuppertal, Germany. It combines the competences in atmospheric physics and chemistry, applied mathematics and socio-economic science.

This second volume is edited by the applied mathematics group organized at the Institute of Mathematical Modelling, Analysis and Computational Mathematics (IMACM). There is a strong interest at the IMACM in tackling mathematical problems arising in the environmental sciences like the modelling of oil spills, especially the analysis of mathematical models of these spills in seas, design of numerical algorithms for transport of oil spills, and creating methods for determining the location, time and total power of oil emissions (inverse problems), i.e. for the simulation and detection of oil spill emitters.

Let me emphasize that there are close links between oil pollution problems and air pollution models. First, on a modelling level the oil pollution on the sea surface is naturally coupled to pollution in the lower layers of the atmosphere. Secondly, from a purely mathematical point of view, the models, i.e. the partial differential equations exhibit a very similar structure. Finally, from a socio-economic viewpoint, a major part of the pollution in both areas is caused by humans and is often the result of economic decisions or behaviour.

The collected chapters in this book cover a wide range of subjects, from pure mathematics to real-world applications in the oil spill engineering business. The reader will quickly recognize the increasingly interdisciplinary nature of these works. It is indispensable that different disciplines of mathematics, like analysis and numerics, together with physics, biology, fluid dynamics, environmental engineering and marine science join forces to solve today's oil pollution problems.

(photo by Sebastian Jarych)

The principal audience of this book is graduate and Ph.D. students in the environmental sciences, mathematics and physics, lecturers in the environmental sciences, mathematics and physics, and researchers working in the oil spill pollution industry, offering them a professional reference resource.

Wuppertal, February 2015 Matthias Ehrhardt

Contents

Contributors

Andrea L. Bertozzi Department of Mathematics and Applied Mathematics Laboratory, University of California, Los Angeles, CA, USA

Merv Fingas Spill Science, Edmonton, AB, Canada

Gustavo J. Goni Atlantic Oceanographic and Meteorological Laboratory, National Oceanic and Atmospheric Administration, Miami, FL, USA

Weijun Guo College of Environmental Sciences and Engineering, Dalian Maritime University, Dalian, China

Ben R. Hodges Department of Civil, Architectural, and Environmental Engineering, University of Texas at Austin, Austin, USA

Xianlong Hou Department of Civil, Architectural, and Environmental Engineering, University of Texas at Austin, Austin, USA

Marc L. Imhoff Pacific Northwest National Laboratory Joint Global Change Research Institute, College Park, MD, USA

Sungyon Lee Department of Mechanical Engineering, Texas A&M, College Station, TX, USA

Amy MacFadyen Office of Response and Restoration, Emergency Response Division, National Oceanic and Atmospheric Administration, Seattle, WA, USA

Frank Muller-Karger College of Marine Science, University of South Florida, St. Petersburg, FL, USA

Frédéric Muttin EIGSI, La Rochelle and Casablanca Engineering School, La Rochelle, France

María Josefina Olascoaga Rosenstiel School of Marine and Atmospheric Science, Ocean Sciences Department, University of Miami, Miami, FL, USA

Alejandro Orfila Marine Technology and Operational Oceanography Department, Mediterranean Institute for Advanced Studies (CSIC-UIB), Mallorca, Spain

David Parra-Guevara Centro de Ciencias de la Atmósfera, Universidad Nacional Autónoma de México, Circuito Exterior, Ciudad Universitaria, Mexico, D.F., Mexico

Mitchell A. Roffer Roffers Ocean Fishing Forecasting Service, Inc., West Melbourne, FL, USA

Juan M. Sayol Marine Technology and Operational Oceanography Department, Mediterranean Institute for Advanced Studies (CSIC-UIB), Mallorca, Spain

Yuri N. Skiba Centro de Ciencias de la Atmósfera, Universidad Nacional Autónoma de México, Circuito Exterior, Ciudad Universitaria, Mexico, D.F., Mexico

Davida Streett National Environmental Satellite Data and Information Service, Office of Satellite and Product Operations, National Oceanic and Atmospheric Administration, Camp Springs, MD, USA

Joaquin A. Trinanes Atlantic Oceanographic and Meteorological Laboratory, National Oceanic and Atmospheric Administration, Miami, FL, USA; Rosenstiel School of Marine and Atmospheric Science, Cooperative Institute for Marine and Atmospheric Studies, University of Miami, Miami, FL, USA; Technological Research Institute, University of Santiago de Compostela Laboratory of Systems, Santiago, Spain; National Environmental Satellite Data and Information Service, CoastWatch, National Oceanic and Atmospheric Administration, Camp Springs, MD, USA

Jeffrey Wong Department of Mathematics and Applied Mathematics Laboratory, University of California, Los Angeles, CA, USA

Tiaojian Xu State Key Laboratory of Coastal and Offshore Engineering, Dalian University of Technology, Dalian, China

Chapter 1
Variability of the Deepwater Horizon Surface Oil Spill Extent and Its Relationship to Varying Ocean Currents and Extreme Weather Conditions

Gustavo J. Goni, Joaquin A. Trinanes, Amy MacFadyen, Davida Streett, María Josefina Olascoaga, Marc L. Imhoff, Frank Muller-Karger and Mitchell A. Roffer

Abstract Satellite observations and their derived products played a key role during the Deepwater Horizon oil spill monitoring efforts in the Gulf of Mexico in April–July 2010. These observations were sometimes the only source of synoptic information available to monitor and analyse several critical parameters on a daily basis. These products also complemented in situ observations and provided data to assimilate into or validate model. The ocean surface dynamics in the Gulf of Mexico are dominated by strong seasonal cycles in surface temperature and mixing due to convective and storm energy, and by major currents that include the Loop Current and its associated rings. Shelf processes are also strongly influenced by seasonal river discharge, winds, and storms. Satellite observations were used to determine that the Loop Current exhibited a very northern excursion (to approximately 28°N) during the month of May, placing the core of this current and of the ring that it later shed at approximately 150 km south of the oil spill site. Knowledge gained about the Gulf of Mexico since the 1980s using a wide range of satellite observations helped understand the timing and process of separation of an anticyclonic ring from the Loop Current during this time. The surface extent of the oil spill varied largely based upon several factors, such as the rate of oil flowing from the well, clean up and recovery efforts, and biological, chemical, and physical processes. Satellite observations from active and passive radars, as well as from visible and infrared sensors were used to determine the surface extent of the oil spill. Results indicate that the maximum and total cumulative areal extent were approximately 45×10^3 km^2 and 130×10^3 km^2, respectively. The

G.J. Goni (✉) · J.A. Trinanes
Atlantic Oceanographic and Meteorological Laboratory, National Oceanic and Atmospheric Administration, 4301 Rickenbacker Causeway, Miami, FL 33149, USA
e-mail: gustavo.goni@noaa.gov

J.A. Trinanes
Rosenstiel School of Marine and Atmospheric Science, Cooperative Institute for Marine and Atmospheric Studies, University of Miami, 4600 Rickenbacker Causeway, Miami, FL 33149, USA
e-mail: joaquin.trinanes@noaa.gov

M. Ehrhardt (ed.), *Mathematical Modelling and Numerical Simulation of Oil Pollution Problems*, The Reacting Atmosphere 2, DOI 10.1007/978-3-319-16459-5_1

largest increase of surface oil occurred between April 22 and May 22, at an average rate of 1.3×10^3 km^2 per day. The largest decrease in the extent of surface oil started on June 26, at an average rate of 4.4×10^3 km^2 per day. Surface oil areas larger than approximately 40×10^3 km^2 occurred during several periods between late May and the end of June. The southernmost surface oil extent reached approximately 85°W 27°N during the beginning of June. Results obtained indicate that surface currents may have partly controlled the southern and eastern extent of the surface oil during May and June, while intense southeast winds associated with Hurricane Alex caused a reduction of the surface oil extent at the end of June and beginning of July, as oil was driven onshore and mixed underwater. Given the suite of factors determining the variability of the oil spill extent at ocean surface, work presented here shows the importance of data analyses to compare against assessments made to evaluate numerical models.

J.A. Trinanes
Technological Research Institute, University of Santiago de Compostela Laboratory of Systems, Campus Vida 15782, Santiago, Spain

J.A. Trinanes
National Environmental Satellite Data and Information Service, CoastWatch, National Oceanic and Atmospheric Administration, 5200 Auth Road, Camp Springs, MD 20746, USA

A. MacFadyen
Office of Response and Restoration, Emergency Response Division, National Oceanic and Atmospheric Administration, 7600 Sandpoint Way, Seattle, WA 98115, USA
e-mail: amy.macfadyen@noaa.gov

D. Streett
National Environmental Satellite Data and Information Service, Office of Satellite and Product Operations, National Oceanic and Atmospheric Administration, Camp Springs, MD 20746, USA
e-mail: davida.streett@noaa.gov

M.J. Olascoaga
Rosenstiel School of Marine and Atmospheric Science, Ocean Sciences Department, University of Miami, 4600 Rickenbacker Causeway, Miami, FL 33149, USA
e-mail: jolascoaga@rsmas.miami.edu

M.L. Imhoff
Pacific Northwest National Laboratorys Joint Global Change Research Institute, 5825 University Research Court, College Park, MD 20740, USA
e-mail: Marc.Imhoff@pnnl.gov

F. Muller-Karger
College of Marine Science, University of South Florida, 140 7th Avenue South, St. Petersburg, FL, USA
e-mail: carib@usf.edu

M.A. Roffer
Roffers Ocean Fishing Forecasting Service, Inc., 60 Westover Drive, West Melbourne, FL 32904, USA
e-mail: roffers@bellsouth.net

1.1 Introduction

A major crude oil spill occurred following an explosion aboard the Deepwater Horizon (DWH) drilling platform in the northern Gulf of Mexico (GOM) on April 20, 2010. This spill differed from other significant oil spill events in that it was the largest accidental oil spill in US history [19]. It occurred in the open ocean at a depth of 1500 m, and both oil and dissolved oil had the potential to affect distant areas of the GOM at the ocean surface and subsurface. This spill occurred in a significant ecosystem that supports major fisheries, and numerous endemic and migrating populations of fish, reptiles, birds, marine mammals, plankton and various sensitive benthic communities. A very large effort was initiated and sustained by the scientific and operational communities of the nations bordering the GOM to assess the extent to which oil was spreading. The oil continuously entered the deep GOM between late April and the time of final capping on July 15, 2010, spreading by means ocean and wind forcing at the surface and subsurface [16].

A suite of satellite-derived products and analyses were developed and generated in real time to address the need to observe the synoptic scales of the spill which is critical to assess numerical model outputs. The satellite data and products were provided through joint government, academic, and private sector partnerships to help the operational community with its response efforts to task and direct oil-spill clean-up and recovery-related efforts. These satellite data and their derived products served as a critical complement to observations collected from field programs and, at times, provided the only available observations and products to perform rapid estimates of a number of environmental parameters over large geographic areas. For example, these observations proved to be critical for real-time analysis and assessment of the GOM conditions to: (a) Monitor the extent and variability of the oil spill at the ocean surface; (b) Assess the surface circulation that could create surface oil pathways and boundaries to the surface oil extent; (c) Monitor surface winds that could force the motions of oil and water; and (d) Initialize and validate numerical models. This chapter provides a review of the extent of the surface oil and of the upper ocean dynamic conditions (a through c) as observed using a suite of satellite observations, analyses, and products, during the 2010 DWH oil spill.

Satellite and in situ observations were used to monitor the variability of the extent of the surface oil. Aircraft overflights with observers and a wide collection of sensors, such as side-looking airborne radar and infrared and hyper-spectral sensors, were used to complement and validate the satellite observations and to provide additional details about oil location, oil thickness, and areal coverage. Some of these datasets will take years to process to fully exploit their information content. The large areal extent of the spill, however, precluded aircraft mapping of the entire surface oil area. Therefore, the integration of aircraft and satellite data provided an overview of the spill that neither observational platform could achieve alone. In addition, satellite monitoring was also used to assess whether and how upper ocean dynamics were conduits for the long distance transport of water and oil particles to areas far removed from the oil spill source. This was particularly important early in the spill. There were

concerns about oil becoming entrained in the Loop Current (LC) and in Loop Current Rings (LCR). Although existing methodologies [11] and numerical model efforts in general allow estimating the upper ocean thermal structure from satellite altimetry observations, research cruises still supply needed critical in situ information used to validate and assess satellite ocean current observations and to provide a suite of subsurface data that could not have been obtained otherwise [30, 31] to perform a correct water mass analysis.

Trajectory models, initialized and validated by satellite observations, also played a key role in contingency planning and determining the likelihood water and oil particles located at or in the vicinity of the oil spill site to reach remote regions, such as the west Florida shelf, Florida Keys, etc. [14, 17]. Northern GOM waters have been observed in these downstream regions, such as the Florida Straits via the LC [7, 23, 24]. In addition, historical surface drifter trajectories indicated that material particles travelling near the oil spill site had the potential to enter the North Atlantic [30]. However, oil did not reach the western-central or southwest coast of Florida, consistent with earlier expectations of [35], who examined satellite-tracked drifter trajectories in this region. The flow regime of this region minimizes the cross shelf transport in the West Florida Shelf [13, 28]. This region, however, shows seasonal variation [26] that can be related to the northward excursions of the LC, which extends from 24°N to 28°N. Specifically, the circulation in this region would allow surface materials in the GOM to be closer to the shoreline when the edge of the LC reaches a maximum northern excursion, and farther away when the LC is at its southernmost location [6, 26, 28].

When the DWH incident began on April 20, 2010, the LC was in its northern extension, reaching approximately 27.5°N, still south of the wellhead location (88.36°W, 28.73°N). Numerical models initialized with in situ and satellite observations reflecting these conditions were used to calculate the trajectories of synthetic Lagrangian water particles deployed in the oil spill site to examine potential transport pathways arising from ocean currents. A numerical methodology based on Finite Time Lyapunov Exponents, which is an averaged measure of the separation rate of initially nearby fluid particle trajectories, was used to identify regions that could act as barriers not allowing the intrusion of waters near the west Florida coast and to estimate potential oil pathways at the surface. Numerical model-derived particle trajectories exhibited a number of pathways with a potential to reach areas beyond the oil spill site, to be carried into the southern GOM, and to enter into the Florida Current and North Atlantic Ocean at the surface (Fig. 1.1) and subsurface. Depending on the decay rate assigned to these particles, some could reach remote regions, although with a very low density or probability [1].

Real-time evaluation of surface current fields mostly derived from satellite observations became a critical component of the monitoring effort. The complexity of these fields is enhanced by the mechanisms involved in the separation of rings from the LC [33], which usually occur at different times at surface and subsurface. The separation of the LCRs at the subsurface is only verifiable with in situ measurements as satellite observations are limited to surface parameters. The spatial resolution of the fields derived from multiple satellites became especially important for real-time

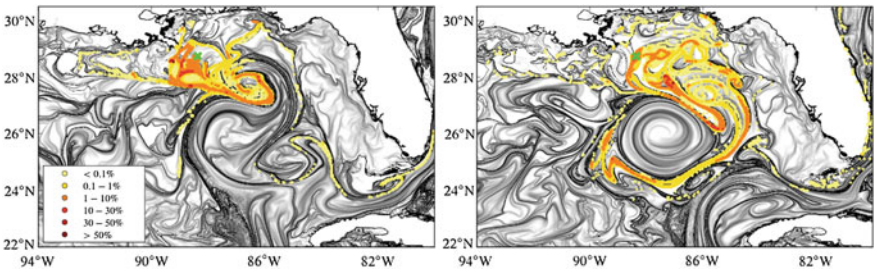

Fig. 1.1 Finite Time Lyapunov Exponents fields used to evaluate the path of particles at the surface for the ocean surface conditions on (*left*) May 20 and (*right*) June 2, 2010. Convoluted bands of most intense *black tones* indicate attracting Lagrangian Coherent Structures, which delineate the pathways of the particles. In a numerical experiment, 10,000 water particles were released daily near the location of the Deepwater Horizon oil well starting on April 20 and finishing on (*left*) May 20 and (*right*) June 2, 2010. The water particle density denoted by colours *yellow* (low values) to *orange* (higher values) is expressed as percentage of the daily discharge in 1/25 × 1/25 bins. No particles were found to enter the West Florida Shelf and only a minimal fraction entered into the Loop Current and Florida Current systems

mapping of mesoscale features present in the GOM, which are frequently observed along the periphery of the larger features, including the LC. The complex surface current field, which could not be measured by one satellite alone, necessitated continuous monitoring of the highly variable dynamic conditions of the upper ocean and was accomplished by using a combined analysis of satellite together with in situ observations and numerical modelling.

This work shows the importance of a combined analysis of observations and numerical modelling. The goal of this chapter is to present results obtained from this combined analysis on the link between the variability of the surface oil extent with synoptic surface ocean currents and winds during the DWH event. This chapter is organized as follows. The data and methods used to identify surface oil and surface currents are presented in Sect. 1.3. Results obtained from a suite of hydrographic and satellite observations and from numerical models outputs are shown in Sect. 1.4 detailing the evolution of the LC system during April–August 2010 from satellite fields that were used to identify the main ocean features and to explore potential links between ocean dynamics and the oil spill extent. Section 1.5 summarizes the main conclusions of this chapter.

1.2 Upper Ocean Dynamics in the Gulf of Mexico

The upper ocean circulation in the GOM is characterized by the excursions of the LC, which irregularly sheds anticyclonic rings that travel in a northwest direction into the GOM. The LC forms an intense anticyclonic flow, which expands north westward [9] and can extend northward into the GOM to 28°N, in the vicinity of the

shelf break of the northern portion of the West Florida Shelf (WFS) at about 250 km off the coast [21]. The northern intrusions of the LC may occur in any season with periods ranging from 6 to 17 months, but tend to be more frequent during the spring months [15, 20, 34]. Results derived from hydrographic and satellite observations show that large, warm-core anticyclonic rings, referred to as LCRs, are usually shed from the LC and propagate westward at mean translation speeds of approximately 4 km/day and have mean lifetimes of days to around a year [12, 23, 34, 37]. These LCRs have radii of about 150 km and may reach depths of 800 m [25].

1.3 Main Data Sets and Methods

1.3.1 Surface Oil Extent

During the DWH response, the NOAA Office of Response and Restoration's Emergency Response Division provided daily forecasts of the movement of surface oil, predicting movement over 24, 48 and 72 h intervals [17]. In previous incidents, the primary dataset used to initialize oil distributions for modelling purposes was derived from overflight observations, which would ideally delineate the oil slick boundary and provide detailed descriptions of the distribution and percent coverage of differential oil thickness. However, even with multiple overflights per day being conducted from several locations along the Gulf Coast, the areal magnitude of this oil spill made it difficult for visual overflight observations to provide a comprehensive and complete picture of the oil distribution.

Two primary data types were used to monitor oil at the ocean surface from space: (a) surface roughness from microwave radiation; and (b) Visible and Near Infrared (VNIR) data. By the second week of the incident, the experimental Marine Pollution Surveillance Reports (MPSRs) provided by NOAA National Environmental Satellite, Data, and Information Service (NESDIS) were an integral dataset used in the model initialization. These analyses [32] provided an outer boundary for the extent of the surface oil in a time frame that allowed use by the command posts to direct operations, including overflights. The MPSRs delineated the extent of surface oil using satellite imagery from both active and passive sensors and from other supplementary information such as overflights and in situ observations. During the incident, the MPSRs were rapidly made available, providing information about the surface oil location after each satellite pass. The MPSRs were used in this study in combination with surface current fields to examine potential links between the GOM surface dynamics and the surface oil extent (Fig. 1.2).

Synthetic Aperture Radar (SAR) sensors have been the traditional approach used for assessing surface roughness for oil spill detection [2] since they are all-weather, day and night, active sensors that emit microwave pulses and measure the backscatter radiation reflected by the sea surface, which is a function of the sea surface roughness. The constellation of space-borne SAR sensors (onboard satellites such as

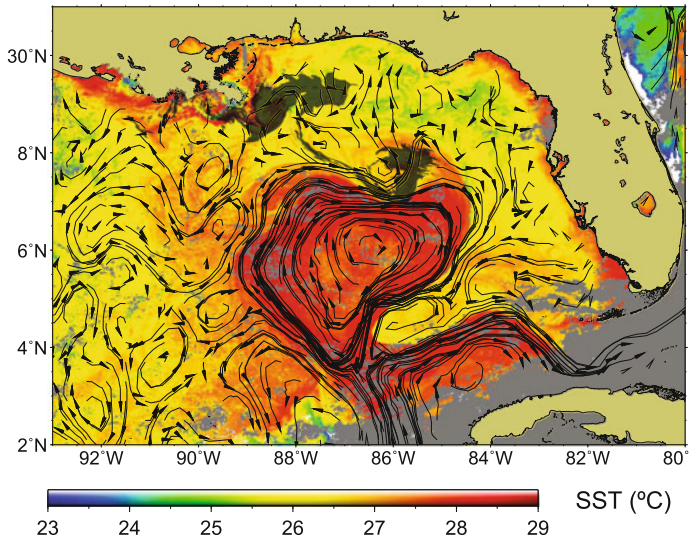

Fig. 1.2 Sea surface temperature (SST) composite for May 20, 2010. The detailed SST features can be used as a proxy for inferring surface circulation and to complement the altimetry derived surface current fields. The main features observed here are the anticyclonic Loop Current and the soon to be detached Loop Current ring, which have higher SST than their surrounding waters. The *arrows* correspond to a coincident geostrophic current velocity field computed using 11 days of satellite altimeter data centered on May 15. The surface oil extent, the two large linked areas shown in *dark green* and centered at 29°N and 27°N, corresponds to May 20–21; it is bounded to the south by the circulation of a Loop Current ring, and it retroflects to the north following the edge of a cyclonic eddy

Envisat, RadarSat 1&2, and TerraSAR-X) provided an almost daily coverage of the GOM region and were essential inputs for monitoring the extension and movement of the oil spill and, consequently, for creating the MPSRs.

On the other hand, VNIR and Infrared data are obtained from multiple passive sensors, such as the Advanced Very High Resolution Radiometer (AVHRR, on satellites within the Polar Orbiting Environmental Satellites constellation), the Moderate Resolution Imaging Spectroradiometer (MODIS on NASA Terra and Aqua satellites), MEdium Resolution Imaging Spectrometer (MERIS, on the Envisat satellite), the Advanced Spaceborne Thermal Emission and Reflection Radiometer (ASTER, on Terra), and the Multi-angle Imaging SpectroRadiometer (MISR, also on Terra) (Fig. 1.3). MODIS data were used primarily for broad-scale surface mapping, spill trajectory and ocean circulation model parameterization, and marine ecological impact analysis [16, 18, 22]. The thermal infrared bands of the ASTER instrument, MODIS and AVHRR were used to detect temperature differences, which in some cases could be caused by the difference between seawater temperature and the colder freshly emerging oil. The oil slick appeared in MODIS pseudo colour images differently depending on many different factors, including whether the oil was in

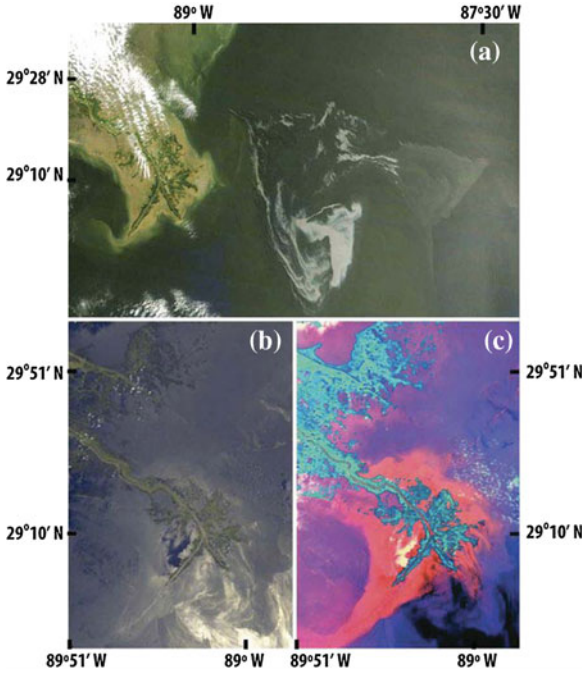

Fig. 1.3 **a** Oil slick as seen in a Terra MODIS visible-near IR image, distinguishable because of its a pale swirl in the darker seawater of the Gulf of Mexico just south of the Mississippi Delta on May 1, 2010; **b** MISR true colour image for May 17, 2010; **c** MISR multi-angle composite acquired on the same date that separates the oil spill (*black* and *dark blue*) from specular reflections

the sunglint pattern of the near-noon collections or outside (Fig. 1.3a). Oil at the sea surface can have a higher or lower reflectance than the surrounding seawater across the visible and near IR bands [8, 10]. As a result, these images were used to measure the surface area and edges of the spill and the direction of flow over time. The capabilities of MISR enhanced the difference in brightness by reducing sun glint, and the use of textural classifiers increased mapping accuracy by using single images. The MISR images (Fig. 1.3b, c) demonstrated how far the oil had dispersed on the sea surface around the Mississippi Delta. The MISR combines images taken at different angles into a single computerized colour image that distinguishes surface oil from seawater and silt. Oil is shown in black and dark blue colours, while silt from the Mississippi is shown as red, orange, and pink colours. Because oil has a different thermal inertia than seawater, multi-temporal thermal data from satellite sensors, such as MODIS or ASTER, were examined and used to further reduce the error in oil slick identification. Interpretations of these image types were verified by imagery derived from SAR images and from overflights.

The operational preparation of the MPSRs involved satellite imagery as well as ancillary data such as surface currents and winds. The different sources of radar and

VNIR imagery mentioned above were all used within an operational context during the DWH incident.

Due to the large area of the spill, view angle effects, and the limited size of the areas imaged by many of the satellites used, daily repeat satellite coverage of the entire spill was sometimes incomplete. To partly address the limitation of individual satellite passes, each daily estimate of the area time series used in this study corresponds to a three-day average. The variability in this time series may be due to several factors, including wind forcing, ocean dynamics, changes in the flow rate of oil from the well, recovery efforts (e.g. skimming efforts), oil washing ashore, and lack of measurements due to cloud coverage. A limitation of the MPSRs was the inability to differentiate a thin sheen from very thick oil. Also variations in the wind speed affect the interpretations of the satellite data. For example, high winds affect both the true and apparent extent of oil coverage. High surface wind speeds over the slick tended to decrease satellite-derived surface oil extent because wind and wave forcing caused oil droplets to become increasingly dispersed into the surface mixed layer and, consequently, become undetectable by satellite. Rough seas and deep convection caused oil to be difficult to view in satellite imagery. In addition, rough seas and high winds also enhanced natural dispersion, which resulted in apparent reduction of the surface oil extent. On the other hand, during calm wind periods, relatively thin oil sheens on the sea surface could be detected using satellite observations. Persistent (three days or longer) limitations in satellite coverage or optimal viewing conditions also affected the assessment of the extent of the detected surface oil, tending to create an underreporting of the amount of oil coverage. In addition, the satellite techniques presented here did not show onshore oil or, generally, oil in wetlands. Therefore, any oil that washed ashore or moved into the wetlands did not appear in the MPSRs and, thus, decreased the actual surface oil extent. At any rate, the detection of oil onshore and in wetlands falls outside the scope of this chapter.

The final MPSR analysis product was an outline of an ‘anomaly’ presumed to be oil. In fact, the surface oil varied substantially in type, thickness, concentration, and percent coverage. Identification and prediction of the location of thicker oil is of crucial importance to the response, as this oil may be recoverable via skimmers or targeted for in situ burning, and also poses the greatest threat to shorelines. Thinner and patchy relatively small oil slicks and lower concentrations of oil are also important in evaluating possible effects on the ecosystem. False-positives were also an issue, with transparent, presumably biological, sheens and patches of sargassum frequently erroneously identified as oil. Therefore, satellite analysis was critical to directing overflights, and overflight observations provided essential feedback for the validation of the satellite analysis. Ultimately, satellite and overflight data were used daily to initialize the surface oil distribution for modelling purposes by overlaying analyses from individual satellite passes and observations from multiple overflight tracks to create a time-dependent surface oil distribution.

The response to the DWH incident also demonstrated the benefits of combining SAR and VNIR, especially the latter under sunglint conditions, when oil slicks increase the specular reflectance of the sea surface, and the oil covered areas have more brightness than the regular oil-free ocean surface, making it easier to extract

information on the extent of the oil at the surface. A potential third approach using sea surface temperature (SST) observations was also explored during the monitoring efforts and showed good potential for analysis of changes in surface oil extent. No results using this type of analysis are presented in this chapter because they fall beyond the scope of the work carried out during the oil spill monitoring efforts. However, SST observations were also used to classify water masses with different and often unknown concentrations of oil as part of evaluating the possible pathways for dispersal.

1.3.2 Surface Currents

After the Seasat and Geosat satellites proved the concept that ocean currents could be monitored and studied from space using radar, a number of space-based altimeters have flown beginning in late 1992. Data obtained from an altimeter onboard a satellite, with the proper atmospheric corrections, represents the distance between the satellite and the sea surface, and indirectly serves to estimate the sea surface height anomaly (SSHA) along the altimeter groundtracks. The observations provided by altimeters are accurate estimates of the SSHA away (∼50 km) from coastal zones [3], and are referenced to a mean sea height, which may be generated from historical hydrographic observations and/or numerical models during a period of several years. This process smears out mesoscale ocean features smaller than approximately 100 km and those that move at speeds faster than a few kilometers per day.

During the DWH oil spill, fields of surface circulation were constructed using data from various sources, both in situ and remote. Results presented here focus on those fields obtained at the time of the oil spill using real-time satellite altimetry observations. However, this work presents results that use delayed-time altimetry observations, which generally become available with a several month delay. Two main data sets were used to derive the upper ocean circulation from satellite altimetry: (a) delayed-time altimetry-derived sea surface height (SSH) anomaly along-track data from the Jason-2 and Envisat satellite missions, whose groundtracks are separated by approximately 3 and 1 degrees in longitude, and are repeated approximately every 10 and 35 days, respectively; and (b) a synthetic mean dynamic topography or sea surface height [29]. Horizontal gradients of regularly gridded SSH fields derived from the alongtrack satellite altimetry data were used to estimate daily surface geostrophic currents following a well-established methodology [4]. The spatial gradients of these geostrophic currents were then used to determine the location of the fronts associated with the cyclonic and anticyclonic features, such as the LC, rings and eddies. Results regarding the separation of the LCR from the LC, based on these surface currents alone, may often differ from those obtained from satellite-derived SST estimates, as the boundaries of the mesoscale features observed from dynamic and temperature fields may not necessarily coincide. The fields of surface currents are used in this work to understand and assess how ocean dynamics delineate the outer boundary of the oil extent.

Fields of altimetry-derived surface currents and associated frontal regions were used operationally by the NOAA Office of Response and Restoration to monitor the upper ocean dynamics. The real-time fields produced during the oil spill event are located at www.aoml.noaa.gov/phod/dhos. Altimetry observations have the advantage that they are available year-round and are not affected by the near uniform SST values often observed over the GOM during the summer months. The altimetry fields also have the benefit of not being subject to cloud contamination. However, they cannot provide the fine spatial and high temporal resolution to resolve surface features obtained from satellite-derived fields of SST and ocean colour. Since altimetry fields are constructed using the alongtrack satellite data, which may not necessarily run along or across the region of LCR detachment, the exact date of detachment of a LCR as seen from altimetry observations is only approximate.

1.3.3 Surface Features from Sea Surface Temperature and Ocean Colour

Satellite observations of SST and ocean colour were used jointly to determine the size and location of smaller mesoscale features that satellite altimetry fields cannot observe or properly resolve. These smaller features were detected by adjusting the contrast of the images and outline in the image. Ocean colour data were particularly useful for mapping surface ocean circulation features during the summer months, when SSTs in the Gulf of Mexico (GOM) have relatively weak gradients compared with the winter months [24]. Ocean colour observations from MODIS, SeaWiFS (on SeaStar) and MERIS were routinely used to study regional dynamics. The gradients of ocean colour and derived surface chlorophyll concentration make these data particularly useful in the GOM.

Several passive satellite sensors were available to estimate SST by measuring thermal infrared (IR) and microwave radiation emitted by the ocean. During the DWH event, SST imagery collected using IR sensors, allowed researchers to make inferences about the distribution of surface features and frontal zones that could have been associated with different water masses in the GOM. The satellite sensors used in this study were the various AVHRR sensors, MODIS, and the European Advanced Along-Track Scanning Radiometer (AATSR, onboard Envisat). The 6 km resolution SST fields from the geostationary GOES-12 were also used to obtain coverage when clouds were present by virtue of its sub-hourly sampling. Of significance is that it is still not understood how oil present at the surface of the ocean affects the emissivity of the IR radiation, whether SST observations within oil-covered waters were accurate or not, or whether this signature changed with patchiness in the oil or weathering of the surface slicks. During the oil spill event, maps of SST (Fig. 1.2), ocean colour fields, ocean frontal zones and derived circulation were routinely prepared by ROFFSTM, NOAA, and other laboratories to monitor the upper ocean conditions. Some of these

fields can be found at www.aoml.noaa.gov/phod/dhos and http://www.roffs.com/research-environmental/deepwater-horizon-rig-oil-spill-monitoring.

1.4 Analysis and Discussion

1.4.1 Surface Oil Spill Extent

The extent of the surface oil was primarily estimated and analysed from blended satellite observations as explained in Sect. 1.3.1. The daily MPSRs were used to assess the daily extent of the surface oil and to link their temporal and spatial variability to the surface current fields (Fig. 1.4). The time series of the areal extent of the surface oil (Fig. 1.5b), as obtained from the MPSRs, had a mean value of approximately $20 \times 10^3\,km^2$ and exhibited large temporal variability. An evaluation of these reports indicates that the total cumulative area of oil detected over the open water during the 87 days of the oil spill between April and August 2010, was at least $130 \times 10^3\,km^2$ (Fig. 1.5c). The area covered by surface oil for more than 40 days was slightly smaller than $10 \times 10^3\,km^2$. The surface oil extent was at a maximum ($40 \times 10^3\,km^2$) between approximately May 14 and June 29, 2010, with one noticeable minimum value of less than $15 \times 10^3\,km^2$ around June 6, 2010.

Between April 22 and May 22, 2010, when the first maximum in surface area extent occurred, the surface oil extent increased at an average rate of $1.3 \times 10^3\,km^2$ per day. Areas larger than $40 \times 10^3\,km^2$ were observed during May 20–25, June 16–22, and June 24–27, 2010 (Fig. 1.5a). On the other hand, the areal extent of the surface oil decreased between June 27 and July 5 at a rate of $-4.4 \times 10^3\,km^2$ per day, a rate approximately three times faster than the increase rate during April 22–May 22, 2010. Significant progress had already been made by responders in dispersing, burning, or recovering the oil during this time period. The magnitude of the June 2–6, 2010 apparent decrease of approximately $-20 \times 10^3\,km^2$, was partly due to particularly limited satellite coverage during this time, although a true decrease in oil extent cannot be ruled out.

Wind fields used in the analysis of this work correspond to the 0.25° surface wind grid from NCEP Reanalysis-2 data [36]. The prevailing winds over the GOM during the oil spill were from the southeast and with an average speed of approximately 5 m/s, while winds from other directions were, in general, weaker, with average speeds around 2 m/s (Fig. 1.5a).

By the end of June, high winds, rough seas, and distant thunderstorm activity occurred as Hurricane Alex moved through the southwestern GOM, affecting conditions in the spill area, and causing satellite analysis to underreport the surface oil coverage during this relatively short time period. During the passage of the strong southeasterly winds associated with Hurricane Alex, the daily average wind speed at the oil spill site was approximately 7.4 ± 2.5 m/s, while outside this time period the daily average wind speed was approximately 4.1 ± 2.3 m/s (Fig. 1.5a). The

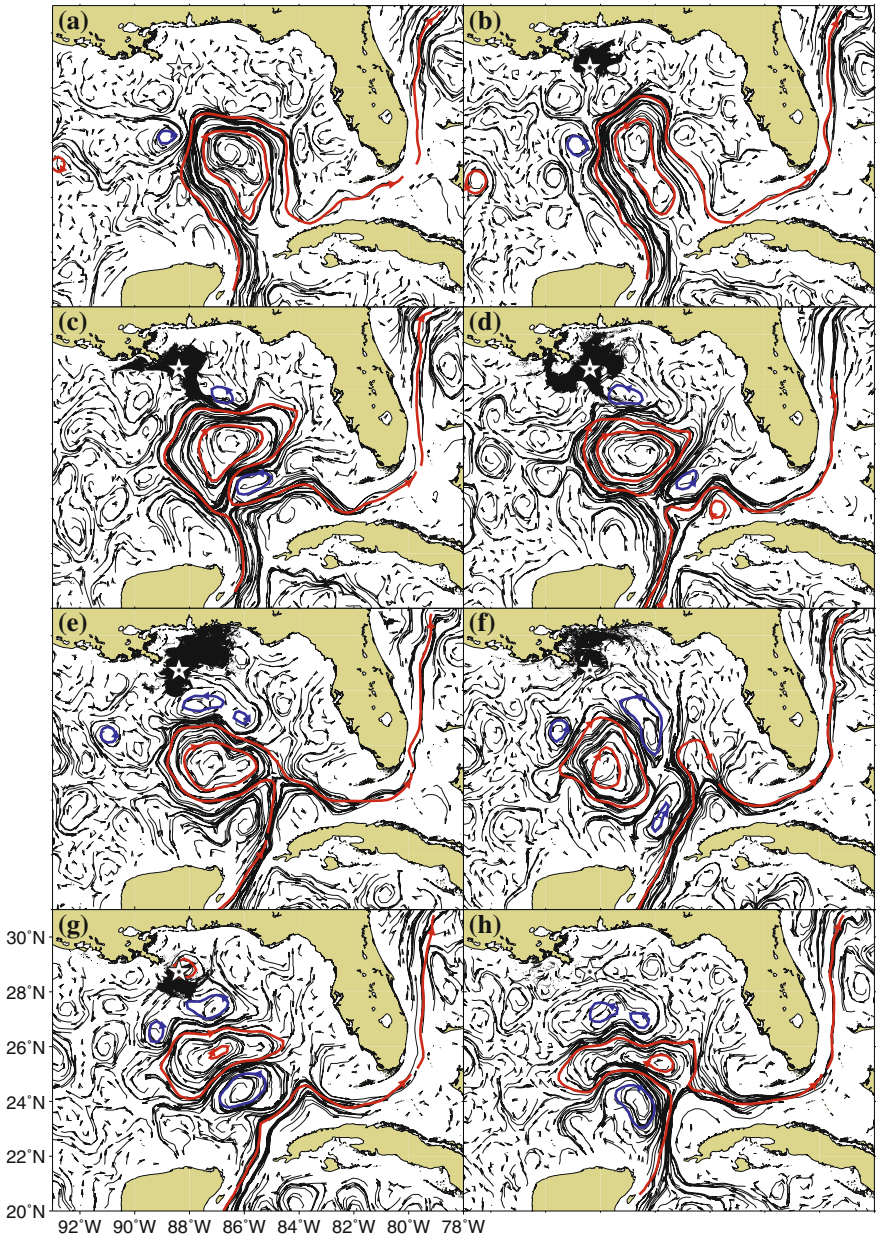

Fig. 1.4 Maps showing surface oil coverage (regions in *black*) for eight selected days in 2010 as obtained from five-day (centered on the referenced day) product superimposed on the altimetry-derived surface currents (*grey arrows*), showing selected sea height contours that are associated with the main mesoscale cyclonic and anticyclonic features (*blue* and *red lines*, respectively). The *star* placed at 88.36°W, 28.73°N, shows the location of the Deepwater Horizon oil spill site. **a** APR 15. **b** MAY 01. **c** MAY 15. **d** JUN 01. **e** JUN 15. **f** JUL 01. **g** JUL 15. **h** AUG 01

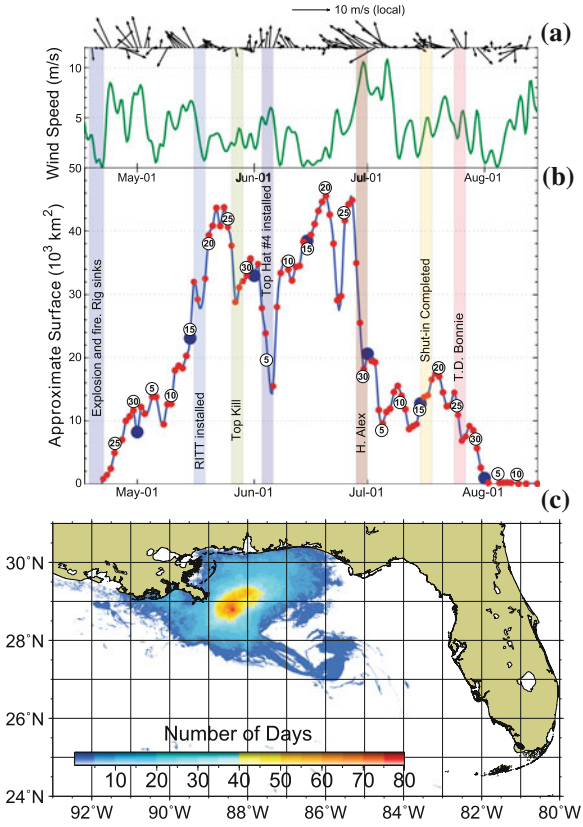

Fig. 1.5 **a** Time series of the wind direction and intensity. **b** Time series of the daily area (in 10^3 km^2) covered by surface oil as obtained from the Marine Pollution Surveillance Reports (MPSRs). A three-day running test on the presence of oil was applied to minimize the impact of partial satellite coverage. *Red circles* denote the estimated values, while the *blue line* shows the results of a cubic spline fit to these values. The numbers in the *white circles* indicate the day of the month. The *blue circles* indicate the dates in which maps of surface currents and surface oil spill extent are shown in Fig. 1.4. **c** Cumulative oil area during April–August, 2010. Colours indicate the number of days the oil slick was present in the daily MPSRs

predominant winds during Alex had the potential to cause the oil to move and concentrate in more westerly locations, enhance dispersion, or simply drive oil ashore predominantly along the barrier islands of the Mississippi Sound. The areal extent of the oil immediately after the passage of Hurricane Alex exhibited a reduction of approximately 28×10^3 km^2, a value of more than half the pre-hurricane surface oil extent (Figs. 1.5b and 1.6). Winds from Tropical Depression Bonnie on July 24–25, 2010, contributed partly to this temporary apparent decrease in surface oil extent.

The limits of the main surface oil area extended south to approximately 27°N 86°W during May 16–28, 2010, and east to approximately 85°W 28°N during May

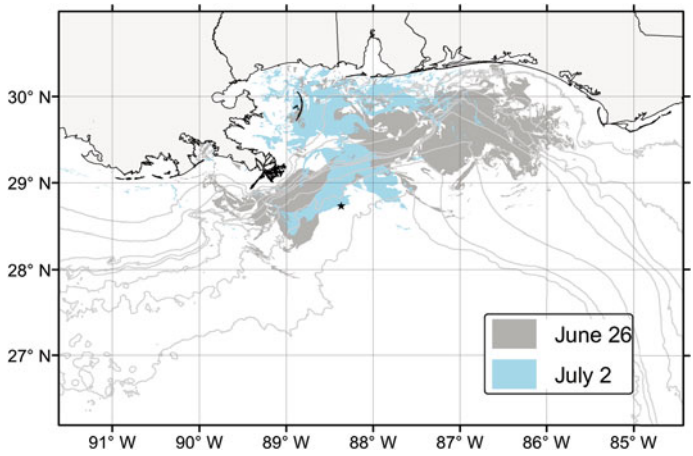

Fig. 1.6 Map showing two areas of extent of the surface oil obtained from the NOAA National Environmental Data and Information Services experimental Marine Pollution Surveillance Reports (MPSR) products. These maps correspond to pre- (June 26, 2010, in *dark gray*) and post- (July 2, 2010, *light blue*) Hurricane Alex. Average surface SE winds of 7.4 m/s during this time period contributed to the reduction of the surface oil extent. *Gray lines* indicate bathymetry contours of 25, 50, 100, 200, 500, 1000, and 2000 m

19–23, 2010. These locations only reflect the extent of surface oil identified in more than one report and as a single continuous area. In addition, smaller areas of potential surface oil slick were reported in the MPSRs. However, large uncertainties existed in their identification and location, and their confirmation therefore relied on visual inspection by overflights. These areas, which extended as far south and east as 24.1°N and 83.0°W, were generally not sampled, and very few of them were confirmed by overflights. Additionally, a relatively very small amount of this oil could have originated in natural seeps or other anthropogenic sources. Observations indicated that these areas consisted of transparent sheens, which may have been very thin oil (∼40 nm) or may have been biological in origin (natural sheening of sargassum). For example, a slick detected approximately 160 km southwest of Tampa, Florida, was confirmed as a transparent sheen by a C130 overflight conducted on June 2, 2010. No further visual analysis or sampling was carried out at later dates in this region. In addition, there were several short-lived slicks detected around the LCR that reached south of 27°N between 85°W and 87°W at the end of May and beginning of June. However, they were not confirmed by overflights or by in situ observations. These could have been formed due to ephemeral surface convergence as sequential image analysis suggested that it was possible for DWH oil to have reached this area. However, compared with the other areas, especially those with recoverable oil, these areas contribute to less than 5 % of the total surface oil spill area.

In addition to surface currents, the surface oil extent depended on other factors, such as the rate of oil flowing from the well, which on average was estimated to range between 50,000 and 70,000 barrels per day [19]. A suite of recovery efforts was

done (http://energy.gov/downloads/key-events-timeline) including the Riser Insertion Tube Tool (RITT) to recover oil from the riser to a surface ship; the pumping of heavy drilling fluids into the blowout preventer to restrict the flow of oil before sealing it permanently with cement (referred to as "top kill"); and the installation of a piece of equipment over the flowing well after the riser was removed to capture hydrocarbons so that they could be collected at the sea surface (referred as to top hat #4). The time line of these efforts with relation to the oil spill extent at the surface is included in Fig. 1.5.

1.4.2 Surface Ocean Circulation

Throughout the response it was critical to provide an early warning of possible threats to remote regions from surface oil entrained in the northern extension of the LC. The importance of identifying periods of time with northern extensions of the LC or LCR is that they had the potential to create direct pathways between the northern GOM and the LC and surrounding Gulf of Mexico including the West Florida Shelf and Florida Keys. In addition, surface mesoscale dynamics also exhibited a close relationship between the extent and shape of the surface oil during much of the DWH event. The complex surface circulation in the GOM, characterized by the LC and the presence of cyclonic and anticyclonic eddies (Figs. 1.1, 1.2 and 1.4) was assessed by the joint analysis of numerical model outputs and satellite observations. Hydrographic data and numerical models were used to assess the connectivity of the LC with the LCR below the surface [30, 31].

The front or core of the LC and rings were identified in terms of the highest geostrophic velocity values, which correspond to the highest horizontal gradient in SSH which for the LC is approximately 0.005 m/km. Values of SSH associated with these maximum gradients ranged from 0.020–0.050 m for anticyclonic features and from 0.00–0.020 m for cyclonic features. The altimetry-derived fields of geostrophic velocity were complemented by a limited number of available in situ observations from hydrographic cruises that were specifically geared towards understanding the connectivity between the LC and the LCR at depth [30]. Results regarding the separation of a LCR from the LC, based on surface currents alone, may also differ from those obtained from SST estimates, as the mesoscale features derived from dynamic and temperature fields may not necessarily coincide.

On April 15, 2010, before the oil spill occurred, the LC presented its northern limit at approximately 27°N with some of its circulation contained in an anticyclonic motion centred at 25.5°N inside the LC (Fig. 1.4a). At this time the LC northern boundary was translating to the north at ~40 km/week. When the oil spill occurred on April 20, 2010, the northern limit of the LC was located at around 27.5°N, approximately 190 km from the spill site. The LC reached its northernmost excursion of approximately 28°N during the first half of May, at approximately 150 Km from the oil spill site. Therefore, according to data analysed in this work, this is the closest distance between the LC/LCR system with the oil spill site. Around mid May, the

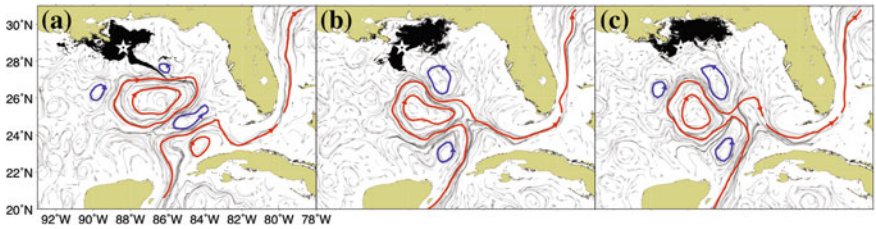

Fig. 1.7 Maps showing the areal extent of surface oil (regions in *black*) for three different dates (May 20, June 20, and June 27, 2010), as obtained from the 5-day (centred on the referenced day) experimental Marine Pollution Surveillance Reports (MPSR) product. These areas are superimposed on the altimetry-derived surface currents (*grey arrows*), showing selected sea height contours that are associated with the main mesoscale cyclonic and anticyclonic features (*blue* and *red lines*, respectively). The star placed at 88.36°W 28.73°N, shows the location of the Deepwater Horizon oil spill site. **a** MAY 20. **b** JUN 20. **c** JUN 27

surface oil began to spread and attained its first maximum of areal extent (Fig. 1.7b), approximately reaching its southernmost location at 27°N (Fig. 1.4c). At this time, the southern boundary of the main surface oil area, located at approximately 27°N, followed the shape of the northern edge of the large LCR and extended south and east of the small cyclonic eddy centred at approximately 86.5°W 27.5°N as revealed by satellite-derived surface currents (Fig. 1.4c) and pathways of water particles using numerical modelling (Fig. 1.1). However, these southern extensions of the surface oil extent did not necessarily correspond to the maximum oil extensions, except for mid May. These results highlight the close link between surface ocean dynamics and the surface oil extent.

The pathways and boundaries of the LC and LCRs were also partly defined by Lagrangian Coherent Structures (LCSs) patterns formed by passive tracers, e.g. [5], which control transport and mixing. These features are revealed using, for example, synoptic fields of sea surface temperature and ocean colour, or can be extracted from current velocity fields using Lagrangian techniques. For example, LCSs can help to explain the shape of the surface oil extent for May 20, 2010 (Fig. 1.1; [27]), which is one of the dates when a maximum of surface oil extent occurred (Figs. 1.4c and 1.5b). At the time of the oil spill, the dynamical conditions of the LC exhibited a marked northern excursion with the potential of GOM waters to get closer to the West Florida Shelf. Numerical experiments carried out in which water particles were released at the surface near the oil spill site indicate that none of the synthetic water particles made their way onto the shelf (Fig. 1.1). This is consistent with the presence of an unbroken barrier that partially inhibits transport across the shelf. In addition, numerical model experiments revealed that almost no particles ($<0.1\,\%$) reached the coastal waters near the Florida Keys (Fig. 1.1). The lack of agreement sometimes found between this type of study and simulated oil distributions may be partly attributed to neglecting the non-conservative behaviour of oil in the simulations.

After reaching its northernmost location in mid-May, the LC began shedding a LCR, aided in part by its interaction with the cyclonic eddy centred near 85°W 25°N

(Fig. 1.4d). On June 2, 2010, surface oil was observed 160 km SW of Tampa, Florida. The LCSs corresponding to this day indicated that the transport barrier was broken and closer to the shoreline on the West Florida Shelf (Fig. 1.1), which partly justified the presence of oil in this area. The LCR was shed and remained unattached from the LC at the surface until approximately June 14, 2010. Surface drifter trajectories confirmed that there was no surface connectivity between the LCR and the LC. During one hydrographic cruise, four surface drifters were deployed at approximately 84°W 26°N, outside the LC and LCR system, where tar balls had been observed. Their trajectories crossed the region between the LC and LCR at 84.5°W 24.5°N on June 13, 2010, (Fig. 1.8), providing an indication that these two features were probably not connected, and that there was no direct connectivity between the LCR and the LC, at least at the surface. However, by June 15, 2010, the LCR had reattached to the LC, as observed by altimetry (Fig. 1.4e) and SST observations. Consequently, from June 13–28, 2010, there was a direct path of waters from the anticyclonic ring into the LC.

Satellite-tracked surface drifting buoys trajectories (Fig. 1.8) were used to assess the upper ocean circulation in the area of the spill, the shedding of the LCR from the LC, the circulation of the LCR, and the cyclonic circulation located to the northeast of the LCR (Fig. 1.1) that was partly responsible for advecting surface oil to the southeast during May and June (Figs. 1.4c, d and 1.7a). On June 28, the warm anticyclonic LCR started to detach for a second time (Fig. 1.4f). This LCR remained detached

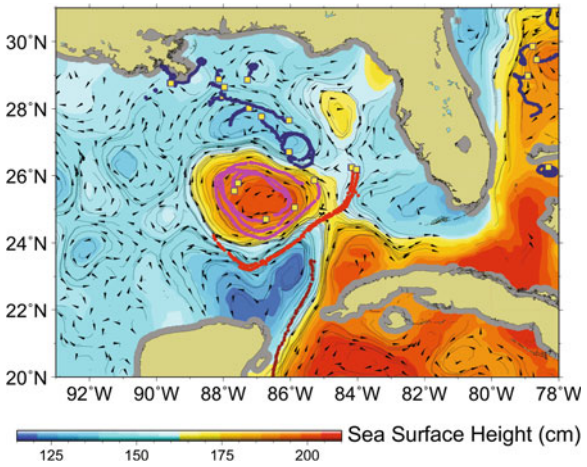

Fig. 1.8 Surface trajectories (coloured lines) of satellite-tracked drifting buoys ("drifters") between June 8–16. *Red lines* correspond to four drifters deployed during the Walton Smith research cruise [30] that served to assess the connectivity between the Loop Current and the Loop Current ring. *Purple lines* correspond to drifters that were used to monitor the circulation in the interior of the Loop Current eddy. *Black lines* correspond to drifters that served to monitor the ocean circulation to the northeast of the Loop Current ring. The background colours correspond to the altimetry-derived sea surface height while the *arrows* represent current vectors computed from the sea height field for June 13, 2010

until approximately August 1, 2010, when it reattached to the LC for a second time. Ultimately, only a small amount of surface oil was reported to have entered the northern LC/LCR system. Altimetry-derived observations show that this LCR, sometimes referred to as Eddy Franklin according to a naming protocol followed by some operational forecasters, eventually translated to the west and became undetectable early in 2011.

The scale of the DWH event required the use of satellite data to evaluate the impact of large oil spills on coastal and marine ecosystems. Satellite observations provided an important tool to conduct pre- and post-event evaluations of ecosystem processes. Current efforts are also focusing now on the investigation of the potential impact of oil on photosynthesis of plant species in the intertidal zone and of phytoplankton in offshore areas.

1.5 Conclusions

Hydrographic and satellite observations together with numerical model outputs played a key role in support of monitoring efforts during the DWH oil spill. The combined suite of observations and model outputs analysis can continually provide information about key parameters, such as ocean currents, frontal regions, water masses, and oil spill extent at the surface. This chapter presented important results on how the combined use of all available data and analysis were employed to monitor the surface oil areal extent and surface ocean currents in support of the restoration and recovery efforts, which were originally carried out under operational constraints involving short timelines and data resource availability.

Experimental Marine Pollution Surveillance (EMPS) reports, which provided an outer boundary of the extent of the surface oil, were used in this study to investigate the variability of the extent of surface oil using satellite imagery from both active and passive sensors and from supplementary information, such as overflights and in situ observations which were key for the assessment of numerical models. Results obtained from these reports show that the maximum surface area extent of the oil spill at the surface was approximately $47 \times 10^3\,km^2$, while the combined affected surface area was at least $130 \times 10^3\,km^2$. The oil spill surface extent exhibited large variability. The largest increase of surface oil occurred between April 22 and May 22, 2010, at an average rate of $1.3 \times 10^3\,km^2$ per day. On the other hand, the largest decrease in the extent of surface oil started on June 26, 2010, at an average rate of $4.4 \times 10^3\,km^2$ per day. The largest surface extensions ($>40 \times 10^3\,km^2$) occurred during several periods between late May and the end of June. The southernmost extension of the surface oil spill extent reached approximately 85°W 27°N during the beginning of June. Although smaller potential surface oil slicks were also identified to the south by MPSRs, only a few of them were observed from in situ and overflight observations, partly due to limited resources to evaluate them.

Real-time surface current fields derived from satellite altimetry were used to monitor conditions during the oil spill. In this work, delayed-time altimetry observations

were used to provide useful representations of the current fields. These observations, combined with the other satellite measurements and data from drifting buoys, provided a comprehensive view of the surface circulation dynamics. At the time of the oil spill, the core of the LC exhibited a northern extension (approximately 28°N), around 150 km from the oil spill site. At that time, this condition was hypothesized to have the potential of connecting waters, and probably oil particles, from the oil spill neighbouring areas into the central and southeastern GOM regions and beyond. Results obtained here indicate that surface currents, from the Loop Current, a Loop Current ring, and a cyclonic eddy, appeared to have controlled the southern and eastern extent of the surface oil during May and June. On the other hand, intense southeast winds associated with Hurricane Alex caused a reduction of the surface oil extent at the end of June and beginning of July, as oil was driven onshore and mixed underwater.

Results shown here represent a fraction of the combined DWH monitoring efforts and they clearly exemplify the key role that satellite observations and numerical model outputs play to monitor and analyse parameters critical for environmental studies at scales where in situ observations are not adequate or possible. For example, mesoscale features linked to the areal extent of surface oil confirm the important value of real-time eddy permitting satellite altimetry, along with SAR, IR and visible ocean colour data. This combination of active and passive satellite observations shows the utility of joint satellite data analysis for surface oil extent monitoring and studies. Although satellite observations serve to monitor surface parameters, in situ hydrographic observations and numerical modelling efforts are needed to obtain a subsurface assessment of the ocean conditions.

Results presented here also show the importance of extreme weather events in the oil spill areal extent, indicating that atmospheric ocean couple models may be necessary to properly monitor oil spacial extent.

Acknowledgments Funding for GG, JT, DS, and AMF was provided by NOAA. MJO was supported by NSF grant CMG0825547 and by a grant from BP/The Gulf of Mexico Research Initiative. JFM was partly funded by NASA grant NNX08AL60G, by a grant from BP/The Gulf of Mexico Research Initiative. We would also like to acknowledge the work of Mr. Gregory Gawlikowski (Roffer's Ocean Fishing Forecasting Service, Inc.) on mapping the distribution of oil and ocean frontal analyses, and to Dr. Francis Bringas for his support on numerical computations and distribution of fields of ocean currents through the NOAA/AOML web site. MAR was funded by Roffer's Ocean Fishing Forecasting Service, Inc., NASA Grant NNX08AL06G and University of Miami Cooperative Institute for Marine and Atmospheric Studies Grants NA10OAR432143 and R1100291, Florida Institute of Oceanography - University of South Florida grant 4710-1101-04. University of Miami CSTARS provided the SAR data. Altimetry sea height data are from AVISO. The information in this document reflects the views of the authors, and does not necessarily reflect the official positions or policies of the National Oceanic and Atmospheric Administration or the United States Department of Commerce.

References

1. Adcroft, A., Hallberg, R., Dunne, J.P., Samuels, B.L., Galt, J.A., Barker, C.H., Payton, D.: Simulations of underwater plumes of dissolved oil in the Gulf of Mexico. Geophys. Res. Lett. **37**, L18605 (2010). doi:10.1029/2010GL044689
2. Alpers, W., Espedal, H.A.: In: Jackson, Apel, (eds.) Synthetic Aperture Radar Marine Users Manual. NOAA NESDIS, pp. 262–276 (2004)
3. Emery, W.J., Strub, T., Leben, R., Foreman, M., McWilliams, J.C., Han, G., Ueno, H.: Satellite altimeter applications off the Coasts of North America. In: Vignudelli, S., Kostianoy, A., Cipollini, P., Benveniste, J. (eds.) Coastal Altimetry, pp. 417–451. Springer, New York (2011)
4. Goni, G.J., Johns, W.E.: A census of North Brazil current rings observed from TOPEX/POSEIDON altimetry: 1992–1998. Geophys. Res. Lett. **28**(1), 1–4 (2001)
5. Haller, G., Yuan, G.: Lagrangian coherent structures and mixing in two-dimensional turbulence. Physica D **147**, 352–370 (2000)
6. Hetland, D., Hsueh, Y., Leben, R., Niiler, P.: A loop current-induced jet along the edge of the West Florida Shelf. Geophys. Res. Lett. **26**, 2239–2242 (1999)
7. Hu, C., Nelson, J.R., Johns, E., Chen, Z., Weisberg, R.H., Muller-Karger, F.E.: Mississippi river water in the Florida Straits and in the Gulf Stream off Georgia in Summer 2004. Geophys. Res. Lett. **32**, L14606 (2005). doi:10.1029/2005GL022942
8. Hu, C., Li, X., Pichel, W.G., Muller-Karger, F.E.: Detection of natural oil slicks in the NW Gulf of Mexico using MODIS imagery. Geophys. Res. Lett. **36**, L01604 (2009). doi:10.1029/2008GL036119
9. Hulburt, H.E., Thompson, J.D.: A numerical study of loop current intrusions and eddy shedding. J. Phys. Oceangr. **10**, 1611–1651 (1980)
10. Klemas, V.: Tracking oil slicks and predicting their trajectories using remote sensors and models: case studies of the Sea Princess and Deepwater Horizon oil spills. J. Coast. Res. **25**, 789–797 (2010)
11. Lentini, C., Goni, G.J., Olson, D.: Investigation of Brazil Current rings in the confluence region. J. Geophys. Res. **111** (2000). doi:10.1029/2005JC002988
12. Lindo-Atichati, D., Bringas, F., Goni, G.: Loop Current Excursions and ring detachments during 1993–2009. Int. J. Remote Sens. **34**, 5042–5053 (2013)
13. Liu, Y., Weisberg, R.H.: Seasonal variability on the West Florida Shelf. Prog. Oceangr. **104**, 80–98 (2012). doi:10.1016/j.pocean.2012.06.001
14. Liu, Y., Weisberg, R.H., Hu, C., Kovach, C., Zheng, L.: Trajectory forecast as a rapid response to the deepwater horizon oil spill. In: Liu, Y., et al. (eds.) Monitoring and Modelling the Deepwater Horizon Oil Spill: A Record-Breaking Enterprise. Geophysical Monograph Series, vol. 195, pp. 153–165. AGU, Washington (2011). doi:10.1029/2011GM001121
15. Lugo-Fernandez, A.: Is the loop current a chaotic oscillator? J. Phys. Oceangr. **37**, 1455–1469 (2007)
16. Lubchenco, J., McNutt, M.K., Dreyfus, G., Murawski, S.A., Kennedy, D.M., Anastas, P.T., Chu, S., Hunter, T.: Science in support of Deepwater Horizon response. Proc. Natl. Acad. Sci. USA **109**, 20212–20221 (2012). doi:10.1073/pnas.1204729109
17. Macfadyen, A., Watabayashi, G.Y., Barker, C.H., Beegle-Krause, C.J.: Tactical modelling of surface oil transport during the Deepwater Horizon spill response. In: Liu, Y., Macfadyen, A., Ji, Z.-G., Weisberg, R.H. (eds.) Monitoring and Modelling the Deepwater Horizon Oil Spill: A Record-Breaking Enterprise. American Geophysical Union, Washington (2011). doi:10.1029/2011GM001128
18. Mariano, A., Kourafalou, V., Kang, H., Halliwell, G.R., Srinivasan, A., Ryan, E., Roffer, M.A.: On the modelling of the 2010 Gulf of Mexico Oil Spill. J. Dyn. Atmos. Oceans **52**, 322–340 (2011)
19. McNutt, M.K., Camilli, R., Crone, T., Guthrie, G., Hsieh, P., Ryerson, T.B., Savas, O., Shaffer, F.: Review of flow rate estimates of the Deepwater Horizon oil spill. Proc. Natl. Acad. Sci. USA **109**, 20260–20267 (2011). doi:10.1073/pnas.1112139108

20. Maul, G.A., Vukovich, F.M.: The relationship between variations in the Gulf of Mexico Loop Current and Straits of Florida volume transport. J. Phys. Oceanogr. **23**, 785–796 (1993)
21. Molinari, R.L., Mayer, D.A.: Current meter observations on the continental slope at two sites in the eastern Gulf of Mexico. J. Phys. Oceanogr. **12**, 1480–1492 (1982)
22. Muhling, B.A., Roffer, M.A., Lamkin, J.T., Ingram Jr, G.W., Upton, M.A., Gawlikowski, G., Muller-Karger, F.E., Habtes, S., Richards, W.J.: Overlap between Atlantic bluefin tuna spawning grounds and observed Deepwater Horizon surface oil in the northern Gulf of Mexico. Mar. Pollut. Bull. **64**, 679–687 (2012)
23. Muller-Karger, F.E., Walsh, J.J., Evans, R.H., Meyers, M.B.: On the seasonal phytoplankton concentration and sea surface temperature cycles of the Gulf of Mexico as determined by satellites. J. Geophys. Res. **96**, 12645–12665 (1991)
24. Muller-Karger, F.E.: The Spring 1998 NEGOM cold water event: remote sensing evidence for upwelling and for eastward advection of Mississippi water (or: How an Errant LC Anticyclone took the NEGOM for a spin). Gulf Mexico Sci. **1**, 55–67 (2000)
25. Oey, L.-Y., Ezer, T., Lee, H.C.: Loop Current, rings and related circulation in the Gulf of Mexico: a review of numerical models and future challenges. In: Sturges, W., Lugo-Fernandez, A. (eds.) Circulation in the Gulf of Mexico: Observations and Models, pp. 31–56. American Geophysical Union, Washington (2005)
26. Olascoaga, M.J.: Isolation on the West Florida Shelf with implications for red tides and pollutant dispersal in the Gulf of Mexico. Nonlinear Process. Geophys. **17**, 685–696 (2010)
27. Olascoaga, M.J., Haller, G.: Forecasting sudden changes in environmental pollution patterns. Proc. Natl. Acad. Sci. USA **109**, 4738–4743 (2012)
28. Olascoaga, M.J., Rypina, I.I., Brown, M.G., Beron-Vera, F.J., Kocak, H., Brand, L.E., Halliwell, G.R., Shay, L.K.: Persistent transport barrier on the West Florida Shelf. Geophys. Res. Lett. **33**, L22603 (2006). doi:10.1029/2006GL027800
29. Rio, M.H., Guinehut, S., Larnicol, G.: New CNES-CLS09 global mean dynamic topography computed from the combination of GRACE data, altimetry, and in situ measurements. J. Geophys. Res. **116**, C07018 (2011). doi:10.1029/2010JC006505
30. Smith, R. H., Johns, E. M., Goni, G. J., Trinanes, J., Lumpkin, R., Wood, A. M., Kelble, C. R., Cummings, S. R., Lamkin, J. T., Privoznik, S.: Oceanographic conditions in the Gulf of Mexico in July 2010, during the Deepwater Horizon oil spill. Cont. Shelf Res. **77**, 118–131 (2014). doi:10.1016/j.csr.2013.12.009
31. Shay, L.K., Jaimes, B., Brewster, J.K., Meyers, P., McCaskill, E.C., Uhlhorn, E., Marks, F., Halliwell Jr., G.R., Smedstad, O.M., Hogan, P.: Airborne ocean surveys of the loop current complex from NOAA WP-3D in support of the Deepwater Horizon Oil Spill. In: Liu, Y., et al. (eds.) Monitoring and Modelling the Deepwater Horizon Oil Spill: A Record-Breaking Enterprise. Geophysical Monograph Series, vol. 195, pp. 131–151. AGU, Washington (2011). doi:10.1029/2011GM001101
32. Streett, D.D.: NOAA'S satellite monitoring of marine oil. In: Liu, Y., Macfadyen, A., Ji, Z.-G., Weisberg, R.H. (eds.) Monitoring and Modelling the Deepwater Horizon Oil Spill: A Record-Breaking Enterprise. American Geophysical Union, Washington (2011). doi:10.1029/2011GM001104
33. Sturges, W., Leben, R.: Frequency of ring separations from the loop current in the Gulf of Mexico: a revised estimate. J. Phys. Oceanogr. **30**, 1814–1819 (2000)
34. Vukovich, F.M.: Climatology of ocean features in the Gulf of Mexico using satellite remote sensing data. J. Phys. Oceanogr. **37**, 689–707 (2007)
35. Yang, H., Weisberg, R.H., Niiler, P.P., Sturges, W., Johnson, W.: Lagrangian circulation and forbidden zone on the West Florida Shelf. Cont. Shelf Res. **19**, 1221–1245 (1999)
36. Zhang, H.-M., Bates, J.J., Reynolds, R.W.: Assessment of composite global sampling: sea surface wind speed. Geophys. Res. Lett. **33** (2006). doi:10.1029/2006GL027086
37. Zavala-Hidalgo, J., Morey, S.L., O'Brien, J.J., Zamudio, L.: On the loop current eddy shedding variability. Atmosfera **19**, 41–48 (2006)

Chapter 2
A Strategy for Bioremediation of Marine Shorelines by Using Several Nutrient Release Points

David Parra-Guevara and Yuri N. Skiba

Abstract In this chapter, a strategy for the bioremediation of marine shorelines polluted with oil is presented. Several discharge points are chosen in a limited region in order to release a nutrient and reach critical concentration of this substance in the oil-polluted shorelines. The strategy is optimal in the sense that the location of the discharge points and the release rates are planned so as to minimize the amount of the nutrient introduced into the aquatic system. To accomplish this task, a variational problem is solved to find the location of the discharge point in each oil-polluted zone, and to determine a basic (preliminary) shape of its release rate. After that, a quadratic programming problem is solved to specify the strength of these release rates in order to reach the critical concentration in all the polluted zones during the same time interval. An initial-boundary value 3D advection-diffusion problem and its adjoint problems are considered in a limited area to model, estimate and control the dispersion of the nutrient. It is shown that the advection-diffusion problem is well posed, and its solution satisfies the mass balance equation. In each oil-polluted zone, the mean concentration of nutrient is determined by means of an integral formula in which the adjoint model solution serves as the weight function showing the relative contribution of each source. Critical values of these mean concentrations are used as the constraints for the variational problem as well as for the quadratic programming problem. The ability of new method is demonstrated by numerical experiments on the remediation in oil-polluted channel using three control zones.

D. Parra-Guevara (✉) · Y.N. Skiba
Centro de Ciencias de la Atmósfera, Universidad Nacional Autónoma de México,
Circuito Exterior, Ciudad Universitaria, C.P 04510 Mexico, D.F., Mexico
e-mail: pdavid@atmosfera.unam.mx

Y.N. Skiba
e-mail: skiba@unam.mx

M. Ehrhardt (ed.), *Mathematical Modelling and Numerical Simulation of Oil Pollution Problems*, The Reacting Atmosphere 2, DOI 10.1007/978-3-319-16459-5_2

2.1 Introduction

Crude oil is one of the most important organic pollutants in marine environments. It has been estimated that worldwide approximately 1.3×10^6 tons of petroleum impact marine waters and estuaries annually [27]. Massive releases from pipelines, wells and tankers receive the most public attention, but in fact these account for only a relatively small proportion of the total petroleum entering the environment. Almost 50 % comes from natural seeps, and less than 9 % emanates from catastrophic releases. Consumption and urban run-off is responsible for almost 40 % of the input [27]. Independently of the source of pollution, a substantial number of smaller releases of petroleum occur regularly in coastal waters [14], as a result, oil stranded in shorelines has become a common problem which needs attention.

It is well known that oil is comprised of many different toxic compounds which endanger the marine environment involved in a spill, however there are many natural, native microorganisms which are not only capable, but thrive on the decomposition of these toxic compounds. This process of using microorganisms for such cleanup efforts in shorelines is known as bioremediation, and it has proven to be a successful method for the cleanup of marine areas affected by oil spills [7]. There are two different types of bioremediation used for oil spill cleanup: bioaugmentation and biostimulation. Bioaugmentation is the addition of microorganisms capable of degrading the toxic hydrocarbons, in order to achieve a reduction of the pollutants. Biostimulation is the addition of nutrients needed by indigenous hydrocarbon degrading microorganisms in order to achieve maximum degradation of toxic compounds present in the oil. The degradation of hydrocarbons (biodegradation) begins by the conversion of the alkane chain or polycyclic aromatic hydrocarbon (PAH) into alcohol. Oxidation then converts the compound to an aldehyde and then into an acid and eventually into water, carbon dioxide, and biomass. In the case of the PAH, fission occurs which ultimately leads to mineralization [47]. More than 170 genera of microorganisms have been identified in the environment which are able to degrade hydrocarbons, due to such diversity and different conditions at the spill site, hydrocarbons do not all biodegrade at similar rates, and not all hydrocarbons are degradable, but estimates for the biodegradability of different crude oils range from 70 to 97 %. What remain are principally the asphaltenes and resin compounds, which are essentially biologically inert [38].

Although biodegradation is a particularly important mechanism for removing the non-volatile components of oil from the environment, this is a relatively slow natural process and may require months to years for microorganisms to degrade a significant fraction of an oil stranded in shorelines, within the sediments of marine and/or freshwater environments [52]. The simplest way of stimulating biodegradation, and the only one that has achieved experimental verification in the field, is to carefully add nitrogen and phosphorus nutrients. This was first used on a large scale in Alaska, following the 1989 spill from the Exxon Valdez [4, 36, 37]. Two fertilizers were used in the large-scale applications: an oleophilic liquid product designed to adhere to oil, named Inipol EAP22 [19]; and a slow-release granular agricultural product

called Customblen [38]. The bioremediation was very successful, as shown in a joint monitoring program conducted by Exxon, the USEPA and the Alaska Department of Environmental Conservation [36]. Furthermore, this was achieved with no detectable adverse environmental impact [4, 36, 37]. Since then, bioremediation has been used on a limited site as part up of the cleanup of the Sea Empress spill [46], and has been demonstrated on experimental spills in marine or brackish environments on the Delaware Bay [48], a Texas wetland [26], a fine-sand beach in England [45], mangroves in Australia [40], and an Arctic shoreline in Spitsbergen [35].

Due to these successes, it is desirable to include bioremediation in responses to future spills where oil strands on rocky or inaccessible shorelines. In this situation currents can be used to carry the nutrients to the polluted zones instead of release it directly on the site. For such case, an important factor in achieving successful biostimulation, is obtaining an ideal (critical) concentration of nutrients needed for maximum growth of the organisms, and keeping this concentration as long as possible. This can become a difficult task taking into account that appropriate point for releasing the nutrients is unknown, and also because of physical influences, such as differences in densities, wave movements, and tidal influences. Tracer studies are often used to examine how the motion of the water and nutrients are influenced under different situations [2, 3].

In this chapter, a strategy is proposed for the remediation of oil-polluted marine environments which uses the fluid dynamic in a limited water region D to distribute a nutrient (nitrogen or phosphorus) and stimulate biodegradation in a few oil-polluted zones Ω_i of D, $1 \leq i \leq N$. For example, some recreation or aquaculture areas can be chosen as such zones. By the strategy, the nutrient released at points $r_1, r_2, \ldots, r_N$ of domain D with discharge rates $Q_1(t), Q_2(t), \ldots, Q_N(t)$ spreads by currents and turbulent diffusion and reaches all the contaminated zones. Moreover, a critical mean concentration of nutrient c_i (higher than the natural concentration) should be achieved and maintained in each oil-polluted zone Ω_i within a certain time to properly stimulate the growth of the oil degrading microorganisms [2]. This time interval is denoted below as $[T - \tau, T]$. It should be noted that an adequate set of release rates $\{Q_i(t)\}_{i=1}^N$ does not always exist, that is at times, this strategy fails. In particular, this can happen when the release points $\{r_i\}_{i=1}^N$ are improperly chosen with respect to the flow and the location of zones Ω_i, or when the time T is not large enough to let the nutrient to reach all the zones. In order to prevent such situations the problem is solved in two stages. In the first stage, each zone Ω_i is considered separately from other and contains just one source. A variational problem is posed and solved in order to find both the optimal location of release point r_i in the zone and the optimal release rate $Q_i(t)$ to reach the concentration c_i in Ω_i, $1 \leq i \leq N$. We prove that this problem has unique solution. In the second stage, we consider the process of dispersion of nutrient in all zones together. Due to advection by currents, the nutrient released in one zone can reach other polluted zones. Therefore we need to specify (modulate) the strength of all release rates $Q_i(t)$ in order to fulfil the critical mean concentrations c_i in all the polluted zones during the time interval $[T - \tau, T]$. To this end, we introduce a positive coefficient γ_i to modulate each release rate

$Q_i(t)$, such factors are chosen as the solution of a quadratic programming problem. Also, we prove the existence and uniqueness of this optimization problem. Note that a strategy is called optimal if it solves the problem and, at the same time, minimizes the total mass introduced into the aquatic system to mitigate the impact of nutrients on the marine environment and to reduce the remediation cost. Thus, by introducing the least amount of nutrients, the optimal control not only cleans the zones, but also protects the whole ecosystem.

The new strategy considers a few discharge points located so that each oil-polluted zone contains just one discharge point. It generalizes the previous strategy where the only source was used to distribute nutrient in all oil-contaminated areas. Analytical and numerical results for the case of unique source were obtained by considering variational formulations [31], quadratic programming problems [32] and linear programming problems [33].

Taking into account all the above remarks, the variational problem of the optimal two-stage remediation strategy is posed as follows:

$$\text{minimize} \quad m(Q_1, \ldots, Q_N) = \frac{1}{2} \sum_{i=1}^{N} \int_0^T Q_i^2(t)\, dt \tag{2.1}$$

$$\text{subject to:} \quad c_i - \alpha_i \leq J_i(\phi) = \frac{1}{\tau\, |\Omega_i|} \int_{T-\tau}^{T} \int_{\Omega_i} \phi(r,t)\, dr dt \leq c_i + \beta_i,\ 1 \leq i \leq N \tag{2.2}$$

$$0 \leq Q_i(t),\ 0 \leq t \leq T,\ \ 1 \leq i \leq N, \tag{2.3}$$

where m is the functional that represents the total mass of nutrient released into the aquatic system within a time interval $[0, T]$ and $\phi = \phi(r, t)$ is the concentration of this substance at point r in D at the time $t > 0$. Such concentration will be determined with a dispersion model described in Sect. 2.2. Besides, the functional $J_i(\phi)$ is the mean concentration of nutrient in the ith zone Ω_i within time interval $[T - \tau, T]$ $(1 \leq i \leq N)$. Hereafter, we refer to this functional as the *direct estimation* of nutrient concentration. Without loss of generality, all the zones Ω_i considered in this chapter are nonintersecting. The constraints in Eq. (2.2) are imposed to maintain the concentration $J_i(\phi)$ in a vicinity of the critical concentration c_i required for optimal biodegradation $(1 \leq i \leq N)$. Thus, $c_i - \alpha_i$ is the minimum concentration of nutrient in the oil-polluted zone Ω_i acceptable for efficient stimulation of the biodegradation process, while $c_i + \beta_i$ is the maximum allowable concentration of nutrient in the oil-polluted zone Ω_i established for the protection of aquatic system. Note that the introduction of small positive parameters α_i and β_i increases the number of feasible solutions of problem (2.1)–(2.3), and therefore this problem is less restrictive than that described by Parra-Guevara and Skiba [29, 31]. Finally, we note that the problem (2.1)–(2.3) can also be used to determine the optimal release parameters in a fairly common case, when the repeated application of nutrients is required

in the oil-contaminated areas due to the slow degradation of the oil in the marine environment. Sufficient conditions for such a methodology are given in Sect. 2.3.

2.2 Dispersion Model

The concentration of nutrient $\phi(r,t)$ in a bounded domain $D \subset \mathbb{R}^3$ and time interval $[0, T]$ is estimated by the following dispersion model

$$\frac{\partial \phi}{\partial t} + \mathbf{U} \cdot \nabla \phi - \nabla \cdot \mu \nabla \phi + \sigma \phi + \nabla \cdot \phi_s = \sum_{i=1}^{N} Q_i(t)\delta(r - r_i) \tag{2.4}$$

$$\phi_s = -v_s \phi \mathbf{k}\,, \quad \text{in } D \tag{2.5}$$

$$\mu \frac{\partial \phi}{\partial n} = \phi_s \cdot \mathbf{n} - \zeta \phi \mathbf{k} \cdot \mathbf{n} \text{ on } S_T \tag{2.6}$$

$$\mu \frac{\partial \phi}{\partial n} = 0 \text{ on } S^+ \tag{2.7}$$

$$\mu \frac{\partial \phi}{\partial n} - U_n \phi = 0 \text{ on } S^- \tag{2.8}$$

$$\mu \frac{\partial \phi}{\partial n} = 0 \text{ on } S_B \tag{2.9}$$

$$\phi(r,0) = \phi^0(r) \text{ in } D \tag{2.10}$$

$$\nabla \cdot \mathbf{U} = 0 \text{ in } D. \tag{2.11}$$

Here (2.4) is the advection-diffusion equation, $\mathbf{U}(r,t)$ is the known current velocity that satisfies the incompressibility condition (2.11), $\mu(r,t)$ is the turbulent diffusion coefficient, $\sigma(r,t)$ is the chemical transformation coefficient characterizing the decay rate of nutrient in water. Note that the first-order (linear) kinetics $\sigma\phi$ describing the process of chemical transformation is a reasonable approximation for such nutrients in water as the nitrogen and phosphorus. The term $\nabla \cdot \phi_s$ in (2.4), describes the change of concentration of nutrient per unit time because of sedimentation with constant velocity $v_s > 0$, and $\delta(r - r_i)$ is the Dirac delta centred at the discharge point r_i. Equation (2.6) is the boundary condition on the free surface S_T of domain D, where $\zeta(r,t)$ is the coefficient characterizing the process of evaporation of nutrient, and (2.9) represents the boundary condition on the bottom S_B of domain D. Equations (2.7) and (2.8) are the corresponding conditions on the lateral boundary of D, besides, S^+ is the rigid or outflow part of the boundary where $U_n = \mathbf{U} \cdot \mathbf{n} \geq 0$, and S^- is its inflow part where $U_n < 0$ (Fig. 2.1). Finally, Eq. (2.10) represents the initial distribution of the nutrient at $t = 0$. In all equations, $\mathbf{n}$ is the unit outward normal

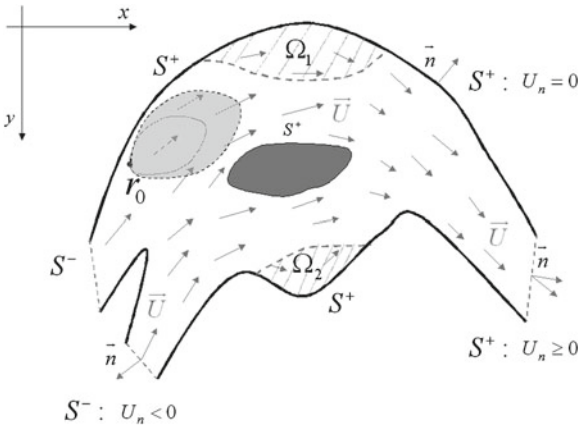

Fig. 2.1 View of domain D from above

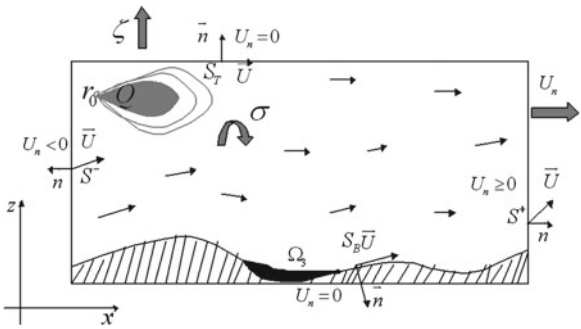

Fig. 2.2 Cross-sectional area of domain D

vector to the boundary $\partial D = S_T \cup S^+ \cup S^- \cup S_B$ of domain D, $\partial/\partial n$ is the derivative in the normal direction, and $\mathbf{k} = (0, 0, 1)^t$ is the unit vector directed upward in the Cartesian coordinate system (Fig. 2.2). We observe that

$$\mathbf{k} \cdot \mathbf{n} = 0 \text{ on } S^+ \cup S^- \text{ and } \mathbf{U} \cdot \mathbf{n} = 0 \text{ on } S_T \cup S_B. \tag{2.12}$$

Also note that the boundary conditions (2.6)–(2.9) are general (i.e., not only for horizontal free and bottom surfaces S_T and S_B), and hence, the dispersion model can take into account free surface wave motion and marine topography.

First of all we show that the solution of dispersion model (2.4)–(2.11) satisfies the mass balance equation. Indeed, integrating Eq. (2.4) over domain D we get

$$\frac{\partial}{\partial t}\int_D \phi\, dr + \int_D \mathbf{U} \cdot \nabla\phi\, dr - \int_D \nabla \cdot \mu \nabla\phi\, dr + \int_D \sigma\phi dr + \int_D \nabla \cdot \phi_s\, dr$$
$$= \sum_{i=1}^{N} \int_D Q_i(t)\delta(r - r_i)\, dr.$$

Applying the divergence theorem [18], it is possible to rewrite some integrals as

$$\int_D \mathbf{U} \cdot \nabla\phi \, dr = \int_D \nabla \cdot (\mathbf{U}\phi) \, dr = \int_{\partial D} \mathbf{U} \cdot \mathbf{n}\phi \, dS,$$

$$\int_D \nabla \cdot \mu \nabla\phi dr = \int_{\partial D} \mu \nabla\phi \cdot \mathbf{n} \, dS = \int_{\partial D} \mu \frac{\partial \phi}{\partial n} \, dS,$$

$$\int_D \nabla \cdot \phi_s \, dr = \int_{\partial D} \phi_s \cdot \mathbf{n} \, dS.$$

Finally, dividing each integral over boundary ∂D into the four integrals over S_T, S^+, S^- and S_B, and applying Eqs. (2.6)–(2.9) and observation (2.12), we obtain the mass balance equation:

$$\frac{\partial}{\partial t} \int_D \phi \, dr = \sum_{i=1}^{N} Q_i(t) - \int_D \sigma\phi \, dr - \int_{S^+} U_n \phi \, dS - \int_{S_T} \zeta\phi \mathbf{k} \cdot \mathbf{n} \, dS + \int_{S_B} v_s \phi \mathbf{k} \cdot \mathbf{n} \, dS. \tag{2.13}$$

Since $\mathbf{k} \cdot \mathbf{n} > 0$ at S_T and $\mathbf{k} \cdot \mathbf{n} < 0$ at S_B, the total mass of the nutrient increases due to the discharge processes ($Q_i(t) > 0$), and decreases because of the chemical transformations ($\sigma > 0$), advective outflow through S^+ ($U_n > 0$), superficial evaporation ($\zeta > 0$) and sedimentation ($v_s > 0$).

We now show that the dispersion problem (2.4)–(2.11) is well posed. Indeed, the model operator is:

$$A\phi = \mathbf{U} \cdot \nabla\phi - \nabla \cdot \mu \nabla\phi + \sigma\phi + \nabla \cdot \phi_s. \tag{2.14}$$

Defining the inner product in $L_2(D)$ as $(A\phi, \phi) = \int_D \phi A\phi dr$ we obtain the expression

$$(A\phi, \phi) = \int_D \phi \mathbf{U} \cdot \nabla\phi \, dr + \int_D \sigma\phi^2 \, dr - \int_D \phi \nabla \cdot \mu \nabla\phi \, dr + \int_D \phi \nabla \cdot \phi_s \, dr.$$

The divergence theorem allows modifying some integrals in the last equation:

$$\int_D \phi \mathbf{U} \cdot \nabla\phi \, dr = \frac{1}{2} \int_{\partial D} \phi^2 \mathbf{U} \cdot \mathbf{n} \, dS,$$

$$\int\limits_D \phi\nabla\cdot(\mu\nabla\phi)\,dr = \int\limits_{\partial D} \phi\mu\frac{\partial\phi}{\partial n}\,dS - \int\limits_D \mu\,|\nabla\phi|^2\,dr,$$

$$\int\limits_D \phi\nabla\cdot\phi_s\,dr = \frac{1}{2}\int\limits_{\partial D}\phi\phi_s\cdot\mathbf{n}\,dS.$$

Finally, dividing each integral over ∂D into the four integrals over S_T, S^+, S^- and S_B, and applying the conditions (2.6)–(2.9) and (2.12), we get

$$(A\phi,\phi) = \int\limits_D \sigma\phi^2\,dr + \int\limits_D \mu\,|\nabla\phi|^2\,dr + \int\limits_{S_T}\zeta\phi^2\mathbf{k}\cdot\mathbf{n}\,dS + \frac{1}{2}\left\{\int\limits_{S^+} U_n\phi^2\,dS - \int\limits_{S^-} U_n\phi^2\,dS + \int\limits_{S_T} v_s\phi^2\mathbf{k}\cdot\mathbf{n}\,dS - \int\limits_{S_B} v_s\phi^2\mathbf{k}\cdot\mathbf{n}\,dS\right\} \tag{2.15}$$

Since $U_n < 0$ in S^-, $\mathbf{k}\cdot\mathbf{n} > 0$ at S_T and $\mathbf{k}\cdot\mathbf{n} < 0$ at S_B, Eq. (2.15) can be rewritten as

$$(A\phi,\phi) = \int\limits_D \sigma\phi^2 dr + \int\limits_D \mu\,|\nabla\phi|^2\,dr + \int\limits_{S_T}\zeta\phi^2\mathbf{k}\cdot\mathbf{n}\,dS + \frac{1}{2}\left\{\int\limits_{S^+\cup S^-} |U_n|\,\phi^2 dS + \int\limits_{S_T\cup S_B} v_s\phi^2\,|\mathbf{k}\cdot\mathbf{n}|\,dS\right\}.$$

Thus, operator A is positive semidefinite: $(A\phi,\phi)\geq 0$.

Taking the inner product of every term of Eq. (2.4) with ϕ we obtain

$$\left(\frac{\partial\phi}{\partial t},\phi\right) = (f,\phi) - (A\phi,\phi), \qquad f(r,t) = \sum_{i=1}^{N} Q_i(t)\delta(r-r_i).$$

Using the condition $(A\phi,\phi)\geq 0$ and the Schwarz inequality [17], the last equation implies the inequality

$$\left(\phi,\frac{\partial\phi}{\partial t}\right) \leq \|\phi\|\,\|f\|, \qquad \|\phi\| = \sqrt{(\phi,\phi)}.$$

Further,

$$\left(\phi,\frac{\partial\phi}{\partial t}\right) = \frac{1}{2}\frac{\partial}{\partial t}\|\phi\|^2 = \|\phi\|\,\frac{\partial}{\partial t}\|\phi\|$$

and hence,

$$\frac{\partial}{\partial t}\|\phi\| \leq \|f\|.$$

Finally, the integration over time interval $(0, T)$ leads to

$$\|\phi\| \leq T \max_{0\leq t\leq T} \|f(r,t)\| + \left\|\phi^0(r)\right\|. \tag{2.16}$$

Since the dispersion model (2.4)–(2.11) is linear with respect to ϕ, estimation (2.16) assures that the solution of problem (2.4)–(2.11) is unique and continuously depends on the initial conditions and forcing. Also, using the method described by Skiba and Parra-Guevara [43], it is possible to prove the existence of generalized solution of problem (2.4)–(2.11), that is the model (2.4)–(2.11) is well posed in the sense of Hadamard [13]. Also note that the positive semidefiniteness of operator A allows us to split the operator A in coordinate directions, and with the help of numerical schemes by Marchuk [22] and Crank-Nicolson [8] construct unconditionally stable and efficient numerical algorithm of second approximation order in space and time for the solution of problem (2.4)–(2.11) [41].

2.3 Adjoint Functions and the Duality Principle

It is rather difficult to analyse and solve the variational problem (2.1)–(2.3) because the constraints in (2.2) are related with the solutions Q_i of the control problem implicitly through the solution ϕ of the dispersion model (2.4)–(2.11). In order to establish an explicit dependence of the constraints on the control functions Q_i, we now introduce one more model which is adjoint to the dispersion model (2.4)–(2.11). It means that the operator A^* is adjoint to the operator A of the model (2.4)–(2.11) in the sense of the Lagrange identity

$$(A\phi, g) = (\phi, A^* g),$$

where $(\cdot, \cdot)$ denotes the inner product in the Hilbert space $L_2(D)$ [22]. Solutions of this adjoint model will be used to establish a duality principle for the mean concentration of the released nutrient in the marine environment. Let us construct the operator A^*. The inner product $(A\phi, g)$ is

$$(A\phi, g) = \int_D g\mathbf{U}\cdot\nabla\phi\, dr + \int_D \sigma g\phi\, dr - \int_D g\nabla\cdot\mu\nabla\phi\, dr + \int_D g\nabla\cdot\phi_s\, dr.$$

The integrals in the last expression can be rewritten with the divergence theorem as follows

$$\int_D g\mathbf{U}\cdot\nabla\phi\, dr = \int_{\partial D} g\phi\mathbf{U}\cdot\mathbf{n}\, dS - \int_D \phi\mathbf{U}\cdot\nabla g\, dr,$$

$$\int_D g\nabla\cdot\mu\nabla\phi\,dr = \int_{\partial D} g\mu\frac{\partial\phi}{\partial n}\,dS - \int_{\partial D}\phi\mu\frac{\partial g}{\partial n}\,dS + \int_D \phi\nabla\cdot\mu\nabla g\,dr,$$

$$\int_D g\nabla\cdot\phi_s\,dr = \int_{\partial D} g\phi_s\cdot\mathbf{n}\,dS - \int_D \phi\nabla\cdot\mathbf{g}_s\,dr,$$

where $\mathbf{g}_s = -v_s g\mathbf{k}$. Then

$$(A\phi, g) = \int_D \phi(-\mathbf{U}\cdot\nabla g - \nabla\cdot\mu\nabla g + \sigma g - \nabla\cdot\mathbf{g}_s)\,dr + \int_{\partial D} g\phi\mathbf{U}\cdot\mathbf{n}\,dS + \int_{\partial D}\phi\mu\frac{\partial g}{\partial n}\,dS - \int_{\partial D} g\mu\frac{\partial\phi}{\partial n}\,dS + \int_{\partial D} g\phi_s\cdot\mathbf{n}\,dS.$$

Dividing the integrals over boundary ∂D into four integrals over S_T, S^+, S^- and S_B, and using conditions (2.6)–(2.9) and (2.12), we obtain that

$$(A\phi, g) = \int_D \phi(-\mathbf{U}\cdot\nabla g - \nabla\cdot\mu\nabla g + \sigma g - \nabla\cdot\mathbf{g}_s)\,dr$$

provided that the function g satisfies the boundary conditions (2.20)–(2.23) (see below). Thus, the Lagrange identity is fulfilled if

$$A^* g = -\mathbf{U}\cdot\nabla g - \nabla\cdot\mu\nabla g + \sigma g - \nabla\cdot\mathbf{g}_s.$$

On the other hand, multiplying Eq. (2.4) by g and integrating the result over the space-time domain $D\times(0,T)$, we get

$$\int_0^T\int_D g\frac{\partial\phi}{\partial t}\,drdt + \int_0^T\int_D gA\phi\,drdt = \int_0^T\int_D g\left\{\sum_{i=1}^N Q_i(t)\delta(r-r_i)\right\}drdt.$$

Integration by parts of the first integral, together with conditions (2.10) and $g(r,T)=0$, leads to

$$\int_0^T\int_D g\frac{\partial\phi}{\partial t}\,drdt = -\int_D g(r,0)\phi^0(r)\,dr - \int_0^T\int_D \phi\frac{\partial g}{\partial t}\,drdt$$

Applying now Eq. (2.4), the Lagrange identity and the well-known property of the Dirac delta one can obtain

$$\int_0^T \int_D \phi \left\{ -\frac{\partial g}{\partial t} + A^* g \right\} dr dt = \sum_{i=1}^{N} \int_0^T Q_i(t) g(r_i, t)\, dt + \int_D g(r, 0) \phi^0(r)\, dr. \quad (2.17)$$

In order to take advantage of Eq. (2.17), which explicitly relates the discharge rates of nutrient $Q_i(t)$ with the concentration of nutrient $\phi(r, t)$ through the adjoint function g, we consider the following adjoint dispersion model:

$$-\frac{\partial g}{\partial t} - \mathbf{U} \cdot \nabla g - \nabla \cdot \mu \nabla g + \sigma g - \nabla \cdot \mathbf{g}_s = p(r, t), \quad (2.18)$$

$$\mathbf{g}_s = -v_s g \mathbf{k} \text{ in } D, \quad (2.19)$$

$$\mu \frac{\partial g}{\partial n} + \zeta g \mathbf{k} \cdot \mathbf{n} = 0 \text{ on } S_T, \quad (2.20)$$

$$\mu \frac{\partial g}{\partial n} + U_n g = 0 \text{ on } S^+, \quad (2.21)$$

$$\mu \frac{\partial g}{\partial n} = 0 \text{ on } S^-, \quad (2.22)$$

$$\mu \frac{\partial g}{\partial n} = -\mathbf{g}_s \cdot \mathbf{n} \text{ on } S_B, \quad (2.23)$$

$$g(r, T) = 0 \text{ in } D. \quad (2.24)$$

Note that the boundary conditions (2.20)–(2.23) and final condition (2.24) imposed on the solution are those that guarantee the fulfilment of the Lagrange identity. Furthermore, one can see that the first, the second and the fifth terms of Eqs. (2.4) and (2.18) have opposite signs. Thus, the comparison of the equations and boundary conditions of the models (2.4)–(2.12) and (2.18)–(2.24) leads to the important result: if the adjoint model (2.18)–(2.24) is solved backward in time (from $t = T$ to $t = 0$) then it also has a unique solution, which continuously depends on the forcing $p(r, t)$. This result can be immediately shown by the transformation of variable $t' = T - t$, cf. [43].

Moreover, the forcing $p(r, t)$ of Eq. (2.18) can be defined so that the mean concentration of nutrient

$$J_i(\phi) = \frac{1}{\tau\, |\Omega_i|} \int_{T-\tau}^{T} \int_{\Omega_i} \phi(r, t)\, dr dt$$

in an oil-polluted zone $\Omega_i \subset D$ will be explicitly related with all the discharge rates $Q_j(t)$, $j = 1, \ldots, N$, and initial concentration of nutrient $\phi^0(r)$ through the adjoint

solution g. Indeed, let us take

$$p(r,t) = \begin{cases} \frac{1}{\tau|\Omega_i|}, & r \in \Omega_i \text{ and } t \in (T-\tau, T) \\ 0, & \text{otherwise} \end{cases}$$

where $|\Omega_i|$ denotes the volume of oil-polluted zone, and τ is the time required for the nutrient to reach its critical concentration in the zone. Then the use of this formula in (2.18) leads to

$$J_i(\phi) = \sum_{j=1}^{N} \int_0^T g_i(r_j, t) Q_j(t)\, dt + \int_D g_i(r, 0)\phi^0(r)\, dr, \tag{2.25}$$

also known as the duality principle. Provided that $\phi^0(r) = 0$ for the first discharge of nutrient, the last formula is reduced to

$$J_i(\phi) = \sum_{j=1}^{N} \int_0^T g_i(r_j, t) Q_j(t)\, dt. \tag{2.26}$$

The use of (2.26) in (2.2) for each zone Ω_i $(i = 1, \ldots, N)$, transforms the variational problem (2.1)–(2.3) to a more convenient form for the analysis:

$$\text{minimize} \quad m(Q_1, \ldots, Q_N) = \frac{1}{2} \sum_{j=1}^{N} \int_0^T Q_j^2(t)\, dt \tag{2.27}$$

$$\text{subject to:} \quad c_i - \alpha_i \le \sum_{j=1}^{N} \int_0^T g_i(r_j, t) Q_j(t) dt \le c_i + \beta_i, \quad 1 \le i \le N \tag{2.28}$$

$$0 \le Q_j(t), \qquad 0 \le t \le T, \qquad 1 \le j \le N. \tag{2.29}$$

Note that problem (2.27)–(2.29) uses N adjoint functions $g_i(r, t)$, which, when restricted to the discharge points r_j, $j = 1, \ldots, N$, generate N^2 temporal influence functions $g_i(r_j, t)$. Each function $g_i(r_j, t)$ compresses dynamical information necessary to estimate how a signal emitted at point r_j impacts the zone Ω_i. As a consequence, the duality principle (2.26) quantifies the total effect on zone Ω_i due to the signals emitted at points r_j, $j = 1, \ldots, N$.

However, if a repeated discharge of nutrient is needed for degrading oil-residuals, then the nonzero initial concentration of the nutrient must be taken into account (see (2.25)). It should be noted that, due to microbial intake of nutrient in the oil-polluted

zones and the water outflow from region D, the concentration of nutrient decreases in region D towards its natural value. Therefore, the following conditions for the mean concentration of nutrient must be fulfilled since the moment $t_0 > T$:

$$\frac{1}{|\Omega_i|}\int_{\Omega_i} \phi(r,t)\,dr < c_i + \beta_i \qquad i = 1,\ldots,N \quad t \geq t_0 \tag{2.30}$$

The moment t_0 can be determined through monitoring the mean concentration of nutrient in region D or by using the solution ϕ forecasted by the model (2.4)–(2.11) with the forcing $Q_j(t)$ equal to zero for $t > T$ and $j = 1,\ldots,N$. Once conditions (2.30) are fulfilled, the initial concentration for modelling the next application of nutrient is chosen as

$$\varphi^0(r) = \phi(r,t_0) \tag{2.31}$$

and the next time interval for such modelling is $[t_0, t_0 + T]$. Due to the conditions (2.30), the contribution of the new initial condition $\varphi^0(r)$ to the mean concentrations of nutrient during time interval $[t_0 + T - \tau, t_0 + T]$ is less than the upper bounds $c_i + \beta_i$ in Ω_i, $(i = 1,\ldots,N)$. Note that without such conditions the feasibility space for problem (2.1)–(2.3) is empty and there is no solution to the control problem.

Thus, if the conditions (2.30) are fulfilled then one can take $t_0 = 0$ and consider the problem (2.27)–(2.29) again for modelling the second discharge of nutrient with the following positive parameters:

$$c_i^{'} = c_i - \int_D g_i(r,0)\varphi^0(r)\,dr, \qquad i = 1,\ldots,N. \tag{2.32}$$

Note that the adjoint functions in (2.32) must be calculated in time interval $[t_0, t_0 + T]$. Also we assume, without loss of generality, that negative values, if they appear on the left side of the constraints (2.28), are replaced by zero. With these remarks, the variational problem (2.27)–(2.29) represents a general remediation strategy which can be applied repeatedly.

It is important to note that all the adjoint solutions $g_i(r_j,t)$ which figure in constraints (2.28) are independent of the discharge rates $Q_j(t)$. This non-negative solutions are determined by the dynamical processes in region D and serve in constraints (2.28) as the weight functions characterizing the effect of the discharge of nutrient at a point r_j on the mean concentration of nutrient in a zone Ω_i (see Figs. 2.3, 2.4 and 2.5). In other words, the adjoint solutions are the influence functions (or information functions) in the control theory. That is why the adjoint problem solutions are widely used in the sensitivity study of various models, and in particular, in the atmosphere and ocean model, weather forecast and climate theory [21, 23], data assimilation problems [24], problems of identification of unknown pollution sources, like nuclear accidents [28, 34, 39, 50], simulation of oil pollution [9, 42] and optimal control in pollution problems [1, 15, 16, 20, 22, 30, 33, 49].

2.4 Peculiarities of Dual Estimates and Sensitivity Formulas

We now discuss the main features of the dual estimate (2.25), or its simplification (2.26), and show the usefulness of the adjoint estimates in the study of sensitivity of mean concentration $J_i(\phi)$ to variations in the discharge rates and positions of the sources as well as in the initial distribution $\phi^0(r)$ of nutrient.

In environmental monitoring, the adjoint estimate (2.25) is a good complement to the direct mean concentration estimate $J_i(\phi)$. One can use either direct or adjoint estimates depending on the specific situation. Assume, for example, that the mean concentration $J_i(\phi)$ of a nutrient is monitored in N ecologically important zones Ω_i of domain D ($i = 1, \ldots, N$). If the number of zones N is large enough then it is better to solve problem (2.4)–(2.11) and use direct estimate of $J_i(\phi)$ in each zone. On the other hand, if number N is rather small then it is more effective and economical to solve adjoint problem (2.18)–(2.24) and use adjoint estimate (2.25). Unlike the direct mean concentration estimate of nutrient, the adjoint estimate (2.25) permits to explicitly evaluate the contribution of each source to value $J_i(\phi)$.

In the case of invariable emission rates ($Q_j(t) = Q_j$), evaluation (2.26) becomes even simpler:

$$J_i(\phi) = \sum_{j=1}^{N} Q_j w_{ij}, \tag{2.33}$$

where

$$w_{ij} = \int_0^T g_i(r_j, t)\, dt. \tag{2.34}$$

Each weight w_{ij} depends only on the adjoint solution and characterizes the contribution of the source with emission rate Q_j to the mean concentration $J_i(\phi)$ in Ω_i.

What is then the basic difference between the direct and adjoint estimates of the mean concentration of nutrient $J_i(\phi)$? The direct estimate, relating to the solution $\phi(r, t)$ of problem (2.4)–(2.11), is independent of a concrete zone Ω, but depends on the discharge rates Q_j and position r_j of sources, and also on the initial distribution of nutrient $\phi^0(r)$ in D. For this reason such a estimate is preferable if one needs to know the concentration of a substance in many zones of D, or in each point of $D \times (0, T)$. However, in the model sensitivity study, this approach requires much computing time, because the solution $\phi(r, t)$ of problem (2.4)–(2.11) must be recalculated whenever new values of the parameters Q_j, r_j or $\phi^0(r)$ are used. Unlike it, the solutions of adjoint problem $g_i(r_j, t)$ depend on Ω_i zone, but are independent of Q_j, r_j or $\phi^0(r)$. In the adjoint evaluation (2.25), $g_i(r_j, t)$ serves as the weight function characterizing the model response to these three parameters. Since the problem is linear, Eq. (2.25) leads to the main sensitivity formula

$$\delta J_i(\phi) = \sum_{j=1}^{N} \int_0^T g_i(r_j, t)\delta Q_j(t)\, dt + \int_D g_i(r, 0)\delta\phi^0(r)\, dr \tag{2.35}$$

that relates a variation $\delta J_i(\phi)$ in the mean concentration of nutrients in Ω_i with variations δQ_j and $\delta\phi^0$ in the emission rates Q_j and initial distribution of nutrient ϕ^0. It makes the estimates (2.25) and (2.35) rather efficient and computationally economical, because the solutions $g_i(r_j, t)$, once found, can be re-used in these formulas for different values of Q_j, r_j or $\phi^0(r)$.

The effect of changing the position of sources from r_j to $r_j^{'}$, $j = 1, \ldots, N$, is estimated by the formula

$$\delta J_i(\phi) = \sum_{j=1}^{N} \int_0^T \left\{ g_i(r_j^{'}, t) - g_i(r_j, t) \right\} Q_j(t)\, dt. \tag{2.36}$$

Finally, we give without proof a general sensitivity formula

$$\begin{aligned} \delta J_i(\phi) = & \sum_{j=1}^{N} \int_0^T g_i(r_j, t)\delta Q_j(t)\, dt + \int_D g_i(r, 0)\delta\phi^0(r)\, dr \\ & - \int_0^T \int_{S_T} g_i(r, t)\phi(r, t)\delta\zeta(r, t)\, dSdt - \int_0^T \int_D g_i(r, t)B(r, t)\, drdt, \end{aligned} \tag{2.37}$$

where

$$B(r, t) = \delta\mathbf{U} \cdot \nabla\phi - \nabla \cdot \delta\mu\nabla\phi + \delta\sigma\phi + \delta v_s \frac{\partial\phi}{\partial z},$$

cf. [43], taking into account arbitrary variations $\delta Q_j(t)$ and $\delta\phi^0(r)$, and small variations $\delta\mathbf{U}, \delta\sigma, \delta\mu, \delta v_s$ and $\delta\zeta$ in the domain D. Unlike the previous formulas, estimate (2.37) is more complicated, because it uses solutions of both problems (2.4)–(2.11) and (2.18)–(2.24) and linearised equations for perturbations.

2.5 Main and Adjoint Numerical Schemes of the Dispersion Problem

In this section, balanced and absolutely stable second-order finite diference schemes based on the application of the splitting method by Marchuk [22] and Crank-Nicolson schemes [8] are developed to solve numerically the dispersion model (2.4)–(2.11) and its adjoint formulation (2.18)–(2.24). Since they were described in detail in Skiba [41], we give here only basic results.

Using the continuity Eq. (2.11), the operator A of Eq. (2.4) can be written as $A = A_1 + A_2 + A_3$, where

$$
\begin{aligned}
A_1\phi &= \frac{1}{2}\frac{\partial}{\partial x}(u\phi) + \frac{1}{2}u\frac{\partial \phi}{\partial x} - \frac{\partial}{\partial x}\mu\frac{\partial \phi}{\partial x} + \frac{1}{3}\sigma\phi \\
A_2\phi &= \frac{1}{2}\frac{\partial}{\partial y}(v\phi) + \frac{1}{2}v\frac{\partial \phi}{\partial y} - \frac{\partial}{\partial y}\mu\frac{\partial \phi}{\partial y} + \frac{1}{3}\sigma\phi \\
A_3\phi &= \frac{1}{2}\frac{\partial}{\partial z}(\widetilde{w}\phi) + \frac{1}{2}\widetilde{w}\frac{\partial \phi}{\partial z} - \frac{\partial}{\partial z}\mu\frac{\partial \phi}{\partial z} + \frac{1}{3}\sigma\phi
\end{aligned}
\tag{2.38}
$$

and $\widetilde{w} = w - v_s$.

We now show that each one-dimensional split operator A_i $(i = 1, 2, 3)$ is positive semidefinite (or positive definite if $\sigma > 0$), cf. [41]. For simplicity, consider only the case when domain D is a cube $[0, X] \times [0, Y] \times [0, Z]$. Then

$$
\int_0^X \phi A_1\phi dx = \frac{1}{3}\int_0^X \sigma\phi^2 dx + \int_0^X \mu\left(\frac{\partial \phi}{\partial x}\right)^2 dx + \left[\frac{1}{2}\phi^2 u - \mu\phi\frac{\partial \phi}{\partial x}\right]_0^X.
$$

Assume that $u(0) > 0$ and $u(X) > 0$. Then the boundary point $x = 0$ belongs to S^-, while point $x = X$ belongs to S^+. Applying condition (2.8) at $x = 0$ and condition (2.7) at $x = X$, we get

$$
\left[\frac{1}{2}\phi^2 u - \mu\phi\frac{\partial \phi}{\partial x}\right]_0^X = \frac{1}{2}[\phi^2(X)u(X) + \phi^2(0)u(0)] \geq 0.
$$

Since $\sigma > 0$ and $\mu > 0$, we conclude that

$$
(A_1\phi, \phi)_{L_2(D)} = \int_0^Z \int_0^Y \int_0^X \phi A_1\phi \, dxdydz \geq 0.
$$

In the same way one can show that A_2 and A_3 are also positive semidefinite operators. It should be noted that this proof is also true for any region D which represents a union of finite number of cubes.

On the other hand, the operator of the adjoint problem (2.18)–(2.24) and (2.11) is the adjoint of A, and can be written as the sum $A^* = A_1^* + A_2^* + A_3^*$ where

$$
\begin{aligned}
A_1^* g &= -\frac{1}{2}\frac{\partial}{\partial x}(ug) - \frac{1}{2}u\frac{\partial g}{\partial x} - \frac{\partial}{\partial x}\mu\frac{\partial g}{\partial x} + \frac{1}{3}\sigma\phi \\
A_2^* g &= -\frac{1}{2}\frac{\partial}{\partial y}(vg) - \frac{1}{2}v\frac{\partial g}{\partial y} - \frac{\partial}{\partial y}\mu\frac{\partial g}{\partial y} + \frac{1}{3}\sigma\phi \\
A_3^* g &= -\frac{1}{2}\frac{\partial}{\partial z}(\widetilde{w}g) - \frac{1}{2}\widetilde{w}\frac{\partial g}{\partial z} - \frac{\partial}{\partial z}\mu\frac{\partial g}{\partial z} + \frac{1}{3}\sigma\phi.
\end{aligned}
\tag{2.39}
$$

Suppose for simplicity that $\mu = \mu(z)$, and define the net functions on different grids:

$$\phi_{ijk} = \phi(x_i, y_j, z_k),\ u_{ijk} = u(x_{i-1/2}, y_j, z_k),\ v_{ijk} = v(x_i, y_{j-1/2}, z_k)$$

$$w_{ijk} = w(x_i, y_j, z_{k-1/2}),\ \mu_k = \mu(z_k),\ v_{ijk} = v(x_i, y_j, z_{k-1/2})$$

The second-order discrete approximation of the operators A_i and continuity Eq. (2.11) have the following form (invariable indices i, j, k are omitted)

$$\left(A_1^h\phi\right)_{ijk} = \frac{u_{i+1}\phi_{i+1} - u_i\phi_{i-1}}{2\Delta x} - \frac{\mu_k\left[\phi_{i+1} - 2\phi_i + \phi_{i-1}\right]}{(\Delta x)^2} + \frac{\sigma\phi_i}{3} \tag{2.40}$$

$$\left(A_2^h\phi\right)_{ijk} = \frac{v_{j+1}\phi_{j+1} - v_j\phi_{j-1}}{2\Delta y} - \frac{\mu_k\left[\phi_{j+1} - 2\phi_j + \phi_{j-1}\right]}{(\Delta y)^2} + \frac{\sigma\phi_j}{3} \tag{2.41}$$

$$\left(A_3^h\phi\right)_{ijk} = \frac{\widetilde{w}_{k+1}\phi_{k+1} - \widetilde{w}_k\phi_{k-1}}{2\Delta z} - \frac{\mu_{k+1}(\phi_{k+1} - \phi_k) - \mu_k(\phi_k - \phi_{k-1})}{(\Delta z)^2} + \frac{\sigma\phi_k}{3} \tag{2.42}$$

$$\frac{(u_{i+1} - u_i)}{\Delta x} + \frac{(v_{j+1} - v_j)}{\Delta y} + \frac{(w_{k+1} - w_k)}{\Delta z} = 0 \tag{2.43}$$

We immediately obtain the form of adjoint operators $(A_i^h)^*$ if we substitute u, v, $\widetilde{w}$, and ϕ in (2.40)–(2.43) by $-u$, $-v$, $-\widetilde{w}$, and g, respectively. To show how the boundary conditions are discretised, we give only one example (see [41] for more details). Let u_{ijk} be a positive value of the u-component of the velocity at the left boundary point $M = (x_{1/2}, y_j, z_k)$ of the grid domain. Then, $U_n = -u_{1jk} < 0$, i.e., the point M belongs to S^-, and conditions (2.8) and (2.22) are approximated as

$$\mu_k\frac{(\phi_{0jk} - \phi_{1jk})}{\Delta x} - u_{1jk}\frac{(\phi_{0jk} - \phi_{1jk})}{2} = 0, \qquad g_{0jk} = g_{1jk} \tag{2.44}$$

Thus, for any i ($i = 1, 2, 3$), the discrete operators A_i^h and $\left(A_i^h\right)^*$ are positive semidefinite, and they are skew-symmetric if $\mu = \sigma = 0$ and S is the coast line ($U_n = 0$ everywhere at S).

The problems (2.4)–(2.11) and (2.18)–(2.24) are solved in time with the symmetrized double-cycle componentwise splitting method by Marchuk [23, 41], i.e., within each double time step interval $(t_n - \Delta t, t_n + \Delta t)$ the main and adjoint numerical schemes have the form

$$\Phi\left[n - \frac{3-i}{3}\right] - \Phi\left[n - \frac{4-i}{3}\right] = -\frac{\tau}{2}A_i^h\left(\Phi\left[n - \frac{3-i}{3}\right] + \Phi\left[n - \frac{4-i}{3}\right]\right)\ (i = 1, 2)$$

$$\Phi\left[n+\frac{1}{3}\right]-\Phi\left[n-\frac{1}{3}\right]=-\tau A_3^h\left(\Phi\left[n+\frac{1}{3}\right]+\Phi\left[n-\frac{1}{3}\right]\right)+2\tau q[n] \tag{2.45}$$

$$\Phi\left[n+\frac{4-i}{3}\right]-\Phi\left[n+\frac{3-i}{3}\right]=-\frac{\tau}{2}A_i^h\left(\Phi\left[n+\frac{4-i}{3}\right]+\Phi\left[n+\frac{3-i}{3}\right]\right)\ (i=2,1)$$

and

$$G\left[n+\frac{3-i}{3}\right]-G\left[n+\frac{4-i}{3}\right]=-\frac{\tau}{2}(A_i^h)^*\left(G\left[n+\frac{3-i}{3}\right]+G\left[n+\frac{4-i}{3}\right]\right)\ (i=1,2)$$

$$G\left[n-\frac{1}{3}\right]-G\left[n+\frac{1}{3}\right]=-\tau(A_3^h)^*\left(G\left[n-\frac{1}{3}\right]+G\left[n+\frac{1}{3}\right]\right)+2\tau p[n] \tag{2.46}$$

$$G\left[n-\frac{4-i}{3}\right]-G\left[n-\frac{3-i}{3}\right]=-\frac{\tau}{2}(A_i^h)^*\left(G\left[n-\frac{4-i}{3}\right]+G\left[n-\frac{3-i}{3}\right]\right)\ (i=2,1),$$

where Φ and G are the vectors representing the grid values of solutions ϕ and g at fractional time steps, and q and p are the vectors representing the grid values of functions Q and P at moment t_n, respectively [41]. The discretization in time of each one-dimensional split problem is performed with the Crank-Nicolson scheme, and the resulting discrete problem is efficiently solved by the Thomas' factorization method for the tridiagonal matrices [24]. The unconditional stability of the numerical schemes (2.45) and (2.46) directly follows from the inequalities

$$\|\Phi[n+1]\|\le\|\Phi[n-1]\|+2\tau\,\|q[n]\| \tag{2.47}$$

and

$$\|G[n-1]\|\le\|G[n+1]\|+2\tau\,\|p[n]\|\,, \tag{2.48}$$

where $\|\cdot\|$ is the Euclidean vector norm [41]. The use of Lagrange identity leads to the equation

$$G^*[n+1]\Phi[n+1]+\tau p^*[n]\left(\Phi\left[n+\frac{1}{3}\right]+\Phi\left[n-\frac{1}{3}\right]\right)=\tau\left(G^*\left[n+\frac{1}{3}\right]-G^*\left[n-\frac{1}{3}\right]\right)q\,[n]+G^*[n-1]\Phi[n-1] \tag{2.49}$$

in each subinterval $[t_n - \Delta t, t_n + \Delta t]$. The sum of such relations over all subintervals in $[0, T]$ (i.e., over all n) and the use of conditions (2.10) and (2.24) leads to a discrete version of adjoint estimate (2.26).

2.6 Theoretical Results: Existence, Uniqueness and Formulation of Discharge Parameters

2.6.1 *First Stage: Discharge Points and Basic Form of Discharge Rates of Nutrient*

In order to find the optimal discharge points r_i in D, and the basic shape of discharge rates $Q_i(t)$ at these points, we consider here the variational problem (2.27)–(2.29) for $N = 1$ and $\alpha_1 = \beta_1 = 0$. That is we consider in the first stage of the strategy just a local problem of remediation in which the critical concentration c_1 is reached exactly. Thus, taking into account the corresponding adjoint function $g_1(r, t)$ for the oil-polluted zone Ω_1, the variational problem becomes

$$\text{minimize} \quad m(Q) = \frac{1}{2}\int_0^T Q^2(t)\,dt \tag{2.50}$$

$$\text{subject to:} \quad \int_0^T g_1(r_1, t)\,Q(t)\,dt = c_1 \tag{2.51}$$

$$Q(t) \geq 0, \qquad 0 \leq t \leq T \tag{2.52}$$

where, for simplicity, we have omitted the subindex in the release rate, that is $Q(t) = Q_1(t)$. At first, the site $r_1 \in D$ is considered as any point such that

$$P(r_1) = \int_0^T g_1(r_1, t)\,dt > 0. \tag{2.53}$$

The set of points where condition (2.53) holds is called support of function P [11]. Note that condition (2.53) is necessary to satisfy constraint (2.51) and that such condition is fulfilled for any point r_1 in the polluted zone Ω_1. Moreover, condition (2.53) is also satisfied for points that are outside Ω_1 but fairly close to this area; such points are adjacent to Ω_1 and are located on the streamlines coming into the zone. The size of such set of points depends on how large is the parameter T and the velocity of the flow $\|\mathbf{U}\|_2$ in a neighbourhood of the zone Ω_1.

2.6.1.1 Existence and Uniqueness

In this section the existence and uniqueness of solution to variational problem (2.50)–(2.52) is proved. To this end, we remind some properties of the Hilbert space $H = L_2(0, T)$ together with a strong result of approximation theory (a minimum distance theorem).

Theorem 2.1 ([5]) *A non-empty closed convex set in a uniformly convex Banach space possesses a unique point closest to a given point.*

Lemma 2.1 ([5]) *The space $H = L_2(0, T)$ is a uniformly convex Banach space.*

We point out that the meaning of condition (2.50) is the minimization of the norm (distance) in the space H. It is for this reason Theorem 2.1 is useful in proving the existence and uniqueness. We now consider the specific set and point in space H for which Theorem 2.1 is applied.

Definition 2.1 The feasible space F for variation problem (2.50)–(2.53) is given as follows

$$F = \left\{ Q \in H;\ Q(t) \geq 0,\ 0 \leq t \leq T,\ \text{ and } \int_0^T Q(t) g_1(r_1, t) dt = c_1 \right\} \quad (2.54)$$

Lemma 2.2 *The feasible space F is a non-empty set in space H.*

Proof Because the adjoint solution $g_1(r_1, t)$ is a non-negative square-integrable function, we have that

$$Q^*(t) = \frac{c_1 g_1(r_1, t)}{\int_0^T g_1^2(r_1, t)\, dt} \quad (2.55)$$

is a function in H that fulfils constraints (2.51) and (2.52). Therefore, $Q^*(t)$ belongs to the feasible space F. The lemma is proved.

The meaning and usefulness of function $Q^*(t)$ defined by (2.55) is established in the next section.

Lemma 2.3 *The feasible space F is a convex set in H.*

Proof In fact, let $Q_1,\ Q_2 \in F$ and $\lambda \in (0, 1)$. Then, evidently, $\lambda Q_1 + (1 - \lambda) Q_2 \geq 0,\ 0 \leq t \leq T$. Besides,

$$\int_0^T (\lambda Q_1 + (1 - \lambda) Q_2) g_1(r_1, t)\, dt = \lambda c_1 + (1 - \lambda) c_1 = c_1$$

and hence, F is a convex set in H. The lemma is proved.

Lemma 2.4 *The feasible space F is a closed set in H.*

Proof To show this we must prove that $F = \overline{F}$ [10]. Let Q_0 be an element of $\overline{F}$. Then there is a sequence $\{Q_k\}_{k=1}^{\infty}$ in F such that

$$\|Q_k - Q_0\| \to 0 \ \text{ as } \ k \to \infty$$

Assume that $Q_0(t) < 0$ in some interval $I \subset (0, T)$ of positive measure $|I| > 0$. Then

$$\|Q_k - Q_0\|^2 = \int_0^T (Q_k - Q_0)^2 \, dt \geq \int_I (Q_k - Q_0)^2 \, dt \geq \int_I Q_0^2 \, dt = l > 0$$

The last inequality contradicts the convergence of sequence $\{Q_k\}_{k=1}^{\infty}$ in H, and hence, Q_0 is a non-negative function in $(0, T)$.

On the other hand, applying the Schwarz inequality we get

$$\left| c_1 - \int_0^T Q_0 g_1(r_1, t) dt \right| = \left| \int_0^T (Q_k - Q_0)\, g_1(r_1, t) dt \right|$$
$$\leq \|Q_k - Q_0\| \, \|g_1(r_1, t)\| \to 0 \ \text{ as } \ k \to \infty$$

and therefore $\int_0^T Q_0 g_1(r_1, t)\, dt = c_1$, that is $Q_0 \in F$. The lemma is proved.

Note that the zero function $q(t) \equiv 0$, $0 \leq t \leq T$, does not belong to the feasible set F. Indeed, the constraint (2.51) is not satisfied for such function because $c_1 > 0$. This remark allows us to establish the most important result of this section.

Theorem 2.2 *The variational problem* (2.50)–(2.52) *has non-trivial unique solution in the space* H.

Proof By Lemma 2.1, the space H is a uniformly convex Banach space. Besides, by Lemmas 2.1, 2.2 and 2.3, the feasibility space F is a non-empty closed convex set in H. Therefore, due to Theorem 2.1, there is a unique function $Q^* \in F$ that minimizes the distance between the set F and the point $q \equiv 0$. That is according to (2.50), function Q^* minimizes the objective functional $m(Q)$. Finally, we observe that $Q^* \neq 0$ because $q \notin F$, and hence, the unique solution of problem (2.50)–(2.52) is non-trivial. The theorem is proved.

It is shown in the next section that function Q^*, mentioned in Theorem 2.2, is precisely the function (2.55).

2.6.1.2 Optimal Discharge Parameters and the Adjoint Functions

The analytical expression for the optimal discharge rate Q^*, namely, the solution of variational problem (2.50)–(2.52), can be obtained by means of the method of

Lagrange multipliers [44]. Let

$$L(Q) = \frac{1}{2}\int_0^T Q^2(t)\,dt - \lambda\left\{\int_0^T g_1(r_1,t)Q(t)\,dt - c_1\right\} \tag{2.56}$$

be the Lagrange functional corresponding to problem (2.50)–(2.52), where λ is the respective Lagrange multiplier. The first variation of L in the sense of Gateaux [44] is calculated as

$$\delta L(Q;\delta Q) = \frac{\partial}{\partial\varepsilon}L(Q+\varepsilon\delta Q)_{\varepsilon=0} = \int_0^T \big\{Q(t) - \lambda g_1(r_1,t)\big\}\delta Q\,dt \tag{2.57}$$

where δQ is the variation of Q. A necessary condition for Q^* to be a minimum is $\delta L(Q^*;\delta Q) = 0$, for any δQ [44]. Therefore, from Eq. (2.57) we get

$$Q^*(t) = \lambda g_1(r_1,t), \tag{2.58}$$

where the Lagrange multiplier λ is determined by means of the constraint (2.51) in the way

$$\lambda = \frac{c_1}{\int_0^T g_1^2(r_1,t)\,dt}. \tag{2.59}$$

The final result is obtained by substituting Eq. (2.59) in (2.58).

Note that, due to Schwarz inequality [17],

$$0 < \int_0^T g_1(r_1,t)\,dt \le T^{\frac{1}{2}}\left\{\int_0^T g_1^2(r_1,t)\,dt\right\}^{\frac{1}{2}}$$

and therefore $\int_0^T g_1^2(r_1,t)dt > 0$, that is function Q^* is well-defined by the Eqs. (2.58) and (2.59). Besides, since $g_1(r_1,t) \ge 0$, we conclude that $Q^*(t) \ge 0$, $0 \le t \le T$.

We now show that Q^*, defined by (2.58) and (2.59), also satisfies the sufficient condition to be a minimum. Indeed, let $Q_0 = Q^* + \delta Q$ be a feasible discharge rate. From constraint (2.51) we have

$$\int_0^T g_1(r_1,t)\delta Q\,dt = 0, \tag{2.60}$$

where $\delta Q \neq 0$ is an arbitrary variation of Q^*. Then,

$$m(Q_0) - m(Q^*) = \int_0^T Q^*(t)\delta Q dt + \frac{1}{2}\int_0^T \delta^2 Q\,dt. \tag{2.61}$$

Due to Eq. (2.58) and condition (2.60), Eq. (2.61) can be written as

$$m(Q_0) - m(Q^*) = \lambda \int_0^T g_1(r_1, t)\delta Q \, dt + \frac{1}{2}\int_0^T \delta^2 Q \, dt = \frac{1}{2}\int_0^T \delta^2 Q \, dt > 0$$

where λ is given by (2.59). Thus, $m(Q_0) > m(Q^*)$, and hence, Q^* defined by (2.58) and (2.59) is the global minimum of variational problem (2.50)–(2.52). Note that Theorem 2.2 from the previous section ensures the uniqueness of this minimum.

On the other hand, the mass of nutrient introduced into the aquatic system by means of the discharge rate Q^* is assessed as

$$m(Q^*) = \frac{c_1^2}{2\int_0^T g_1^2(r_1, t)\, dt} \tag{2.62}$$

so that, in order to minimize the amount of mass, the integral

$$I(r_1) = \int_0^T g_1^2(r_1, t)\, dt \tag{2.63}$$

must take its maximum value. Thus, the optimal discharge point r_1^* is chosen so as to maximize the area under the function $g_1^2(r_1, t)$, $t \in (0, T)$. Note that $I(r_1)$ defined by (2.63) is a continuous non-linear function of three real variables $r_1 = (x, y, z)$, which has a global maximum in the closed set $\overline{\Omega_1}$. Indeed, according to the definition of the adjoint model forcing $p(r, t)$, the greatest values of the adjoint function are always achieved at the points of domain Ω_1.

Because all these results can successively be applied to each oil-polluted zone, we conclude that during the first stage of the remediation strategy, the method allows us to determine the discharge points r_i^*, one in each oil-polluted zone Ω_i, as well as to define with Eqs. (2.58) and (2.59) the corresponding basic discharge rates of nutrient:

$$Q_i^*(t) = \lambda_i g_i(r_i^*, t) = \frac{c_i}{\int_0^T g_i^2(r_i^*, t)dt} g_i(r_i^*, t), \qquad i = 1, \ldots, N. \tag{2.64}$$

Note that all the discharge parameters are calculated by using the adjoint model solutions.

2.6.2 Second Stage: Modulation of Basic Discharge Rates

In the second stage of the remediation strategy, we determine positive parameters $\gamma_1, \gamma_2 \ldots, \gamma_N$ such that the new discharge rates of nutrient

$$Q_i(t) = \gamma_i Q_i^*(t), \qquad 1 \le i \le N \tag{2.65}$$

would satisfy the (global) variational problem (2.27)–(2.29). These parameters modulate the intensity of the basic release rates to fulfil the requirements for the nutrient concentrations in all oil-contaminated zones Ω_i. Such correction on the basic discharge rates is needed because the nutrient discharged in one zone could reach the other zones during the time interval $(0, T)$ due to the processes of advection and diffusion.

Substituting Eq. (2.65) in the variational problem (2.27)–(2.29) we obtain a quadratic programming problem whose solution determines the optimal parameters γ_i^*, and hence, the optimal discharge rates at points r_i^*, $i = 1, \ldots, N$:

$$\text{minimize} \quad m(\gamma_1, \ldots, \gamma_N) = \frac{1}{2} \sum_{j=1}^{N} p_j^2 \gamma_j^2 \tag{2.66}$$

$$\text{subject to:} \quad c_i - \alpha_i \leq \sum_{j=1}^{N} a_{ij} \gamma_j \leq c_i + \beta_i, \qquad i = 1, \ldots, N \tag{2.67}$$

$$\gamma_j \geq 0, \qquad j = 1, \ldots, N \tag{2.68}$$

where $p_j^2 = \int_0^T [Q_j^*(t)]^2 \, dt$ and $a_{ij} = \int_0^T Q_j^*(t) g_i(r_j^*, t) \, dt$, $i, j = 1, \ldots, N$.

The solution of the quadratic programming problem (2.66)–(2.68) exists because the corresponding feasible space is a compact set in $\mathbb{R}^N$ and the objective function m is a continuous function of several real variables [17]. Besides, such a solution is unique because m is also a strictly convex function and the feasibility space is a convex set in $\mathbb{R}^N$ [5]. It is assumed here that the feasibility space is a non-empty set due to the introduction of suitable (large enough) parameters α_i and β_i .

The quadratic programming problem (2.66)–(2.68) can be solved using the *quadprog* routine of MATLAB as soon as the adjoint functions are determined. Regard to this routine, we point out that, when the only constraints of the problem are the upper and lower bounds of variables, i.e., no linear inequalities or equalities are specified, the default *quadprog* algorithm is the large-scale method. Moreover, if the problem has only linear equalities, i.e., no upper and lower bounds or linear inequalities are specified, the default quadprog algorithm is also the large-scale method. This method is a subspace trust-region method based on the interior-reflective Newton method described in Coleman and Li [6]. Each iteration involves the approximate solution of a large linear system using the preconditioned conjugate gradient method (PCG). Otherwise, medium-scale optimization is used, and *quadprog* uses an active set method, which is also a projection method, similar to that described in Gill et al. [12]. It finds an initial feasible solution by solving a linear programming problem [25, 51]. Due to the structure of quadratic programming problem (2.66)–(2.68), the second method of *quadprog* routine is applied in the examples.

2.7 Numerical Examples of Remediation in a Channel

In order to illustrate the method developed we now consider a two-dimensional example of remediation in a channel of one hundred and twenty metres long [0, 120] and ten metres wide [0, 10]. The channel contains three oil-polluted zones Ω_i ($N = 3$). The critical nutrient concentrations c_i (grm)$^{-3}$) in the zones vary from one experiment to another according to Table 2.1. The zones under consideration are: $\Omega_1 = [20, 30] \times [9, 10]$, $\Omega_2 = [40, 60] \times [9, 10]$ and $\Omega_3 = [96, 100] \times [0, 2]$. The parameters of the adjoint model (2.18)–(2.24) have been taken as follows: the velocity vector $\mathbf{U}$ is directed along the channel and is equal to 30 m h^{-1}, the diffusion coefficient μ is 6 m^2 h^{-1}, the coefficient of chemical decay σ is 1 h^{-1}, and $\zeta = v_s = 0$. The discharge of nutrient is performed from the optimal points during four hours, $(0, T) \equiv (0, 4)$, and the mean concentration is controlled within the last one-hour interval (3, 4), i.e., $\tau = 1\ h$.

For each oil polluted zone the adjoint model (2.18)–(2.24) was solved by means of the bidimensional version of the splitting-up method (2.45)–(2.46) which is described in Sect. 2.5. The parameters of discretization are the same in all the numerical experiments. The mesh size is the same in both directions, namely, $\Delta x = \Delta y = 0.4$, and the corresponding mesh size in the time direction is $\Delta t = 0.005$. The function I, given by Eq. (2.63), was built for each polluted zone through the respective adjoint solution. In each case, by the maximization of function I we determined the following optimal discharge points: $r_1^* = (20.2, 9.8)$, $r_2^* = (40.2, 9.8)$ and $r_3^* = (96.2, 0.2)$. For this grid (as well as for finer grids) we obtained that the optimal discharge site tends to be the point at the left-superior corner of the zones Ω_1 and Ω_2, and the left-inferior corner of zone Ω_3, as it must be in order to have the maximum impact of nutrient in each polluted zone.

The adjoint solutions $g_{ij} = g_i(r_j^*, t)$, for the ith polluted zone and the jth optimal discharge point, are plotted in Figs. 2.3, 2.4 and 2.5. According to Eq. (2.64), the basic discharge rate for each polluted zone Ω_i is a multiple of the adjoint function $g_{ii} = g_i(r_i^*, t)$. From the shape of these functions, given in Figs. 2.3, 2.4 and 2.5, one concludes that the basic discharge rates are equal to zero in the time interval [0, 2.25]. According to Eq. (2.25), this means that a basic discharge rate influences the nutrient concentration of a polluted zone only if the adjoint function of the zone is non-zero in the time interval [2.25, 4.0]. Figure 2.3 shows that g_{12} and g_{13} do not satisfy this condition, and therefore the discharge of nutrients at points r_2^* and r_3^* has no influence on its concentration in zone Ω_1, as it was to be expected due to the flow direction and the location of zones in the channel.

Table 2.1 Concentrations c_i (grm^{-3}) in the three polluted zones

Concentration\Experiment	1	2	3	4	5
c_1	0.8	1.0	0.5	1.2	0.6
c_2	0.8	0.8	1.0	0.5	1.2
c_3	0.8	0.5	1.5	1.2	0.6

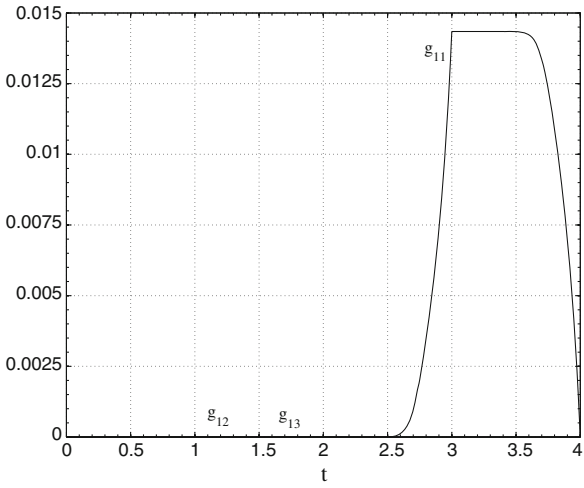

Fig. 2.3 Adjoint functions $g_{ij} = g_i(r_j^*, t)$ corresponding to zone Ω_1 $(i = 1)$ when they are restricted to the optimal discharge points r_j^* $(j = 1, 2, 3)$

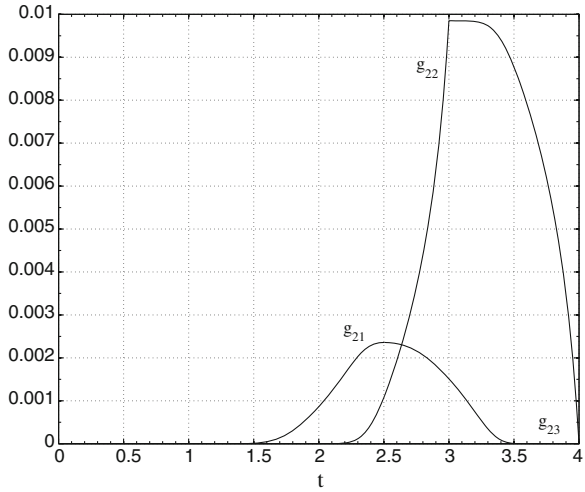

Fig. 2.4 Adjoint functions $g_{ij} = g_i(r_j^*, t)$ corresponding to zone Ω_2 $(i = 2)$ when they are restricted to the optimal discharge points r_j^* $(j = 1, 2, 3)$

A similar result follows from Fig. 2.5, since the adjoint functions g_{31} and g_{32} are almost zero in the time interval [2.25, 4.0], and therefore the discharge of nutrients at points r_1^* and r_2^* practically has no influence on its concentration in zone Ω_3. However, it follows from Fig. 2.4 that function g_{21} is positive in the time interval [2.25, 4.0], and hence, the discharge of nutrient at point r_1^* influences its concentration in zone Ω_2, as it was expected. Finally, the temporal behaviour of adjoint function g_{23} allows us to conclude that the discharge at point r_3^* does not affect the concentration of nutrient in Ω_2.

Thus, the polluted zones are not independent with respect to the dispersion process, since the release of nutrient in a particular zone can affect the concentration in

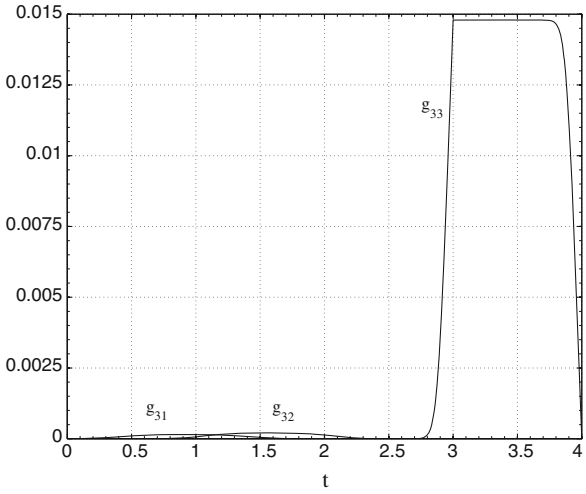

Fig. 2.5 Adjoint functions $g_{ij} = g_i(r_j^*, t)$ corresponding to zone Ω_3 ($i = 3$) when they are restricted to the optimal discharge points r_j^* ($j = 1, 2, 3$)

Table 2.2 Modulation parameters γ_i^* for the basic discharge rates

Parameter\Experiment	1	2	3	4	5
γ_1^*	1.0000	1.0000	1.0000	1.0000	1.0000
γ_2^*	0.9579	0.9473	0.9789	0.8989	0.9789
γ_3^*	1.0000	1.0000	1.0000	1.0000	1.0000

other zones. If it is the case, the application of second stage of the remediation strategy is necessary to correct the intensity of the basic discharge rates. To this end, the quadratic programming problem (2.66)–(2.68) was solved by using the adjoint functions $g_{ij} = g_i(r_j^*, t)$, the critical concentrations c_i given in Table 2.1 and the corresponding basic discharge rates. Table 2.2 summarizes the optimal modulation parameters γ_i^* obtained for each experiment.

For all the experiments, the slack variables of the quadratic programming problem (2.66)–(2.68) are taken equal to zero: $\alpha_i = \beta_i = 0$ ($i = 1, 2$ and 3), hence, each critical concentration c_i is reached in the respective oil polluted zone exactly. Table 2.2 shows that the only discharge rate which must be corrected is that located in zone Ω_2 ($\gamma_2^* < 1$ in the five experiments). This is a consequence of the impact that the discharge of nutrient at point r_1^* has on the zone Ω_2. The optimal discharge rates for experiments 1 and 4 are shown in Figs. 2.6 and 2.7, respectively. As compared with Fig. 2.6, the intensity of functions Q_1 and Q_3 in Fig. 2.7 has increased. This is the result of the raise in the critical concentrations from 0.8 to 1.2 (see Table 2.1. At the same time, the decrease in the intensity of function Q_2 in Fig. 2.7 compared to Fig. 2.6 is explained by the drop in the critical concentration of nutrient from 0.8 to 0.5 and also by the correction of Q_2 through the parameter γ_2^* (see Table 2.2).

It should be noted that in all the experiments, the slack variables are not necessary because the feasible space of problem (2.66)–(2.68) is nonempty when $\alpha_i = \beta_i = 0$

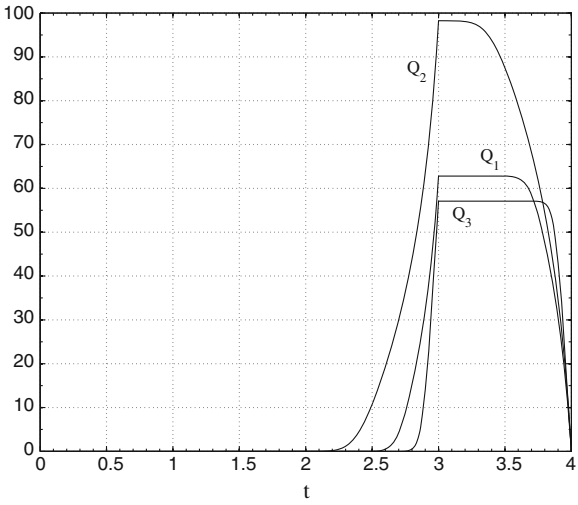

Fig. 2.6 Optimal discharge rates $Q_i(t) = \gamma_i^* Q_i^*(t)$, $i = 1, 2$ and 3, for Experiment 1

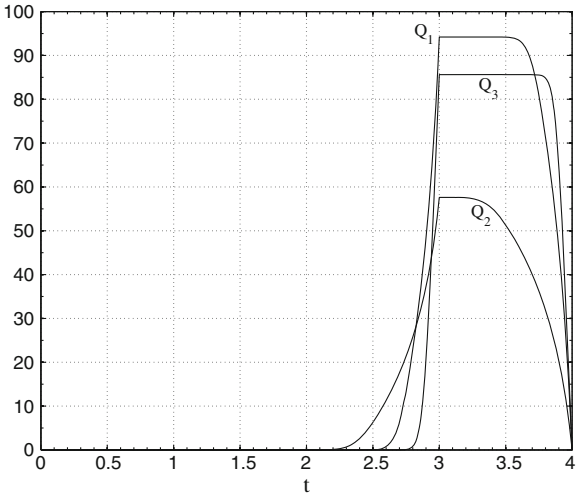

Fig. 2.7 Optimal discharge rates $Q_i(t) = \gamma_i^* Q_i^*(t)$, $i = 1, 2$ and 3, for Experiment 4

($i = 1, 2$ and 3), and therefore the existence of the optimal solution is assured. However, such variables are required for the general formulation of the strategy. For example, when the critical concentrations for the three polluted zones are $c_1 = 19.0$, $c_2 = 0.8$ and $c_3 = 0.8$ then the feasible space of problem (2.66)–(2.68) is empty. Indeed, in this case, the basic discharge rate at point r_1^* is so intensive that the concentration of nutrient in the zone Ω_2 cannot be maintained as low as 0.8. On the other side, if nonzero slack variables are introduced as $\alpha_1 = \beta_1 = 0.1$ and $\alpha_i = \beta_i = 0\,(i = 2, 3)$, then the feasible space of problem (2.66)–(2.68) is nonempty and we have the optimal solution: $\gamma_1^* = 0.9947$, $\gamma_2^* = 0.0048$ and $\gamma_3^* = 1.0000$. Figure 2.8 shows the optimal discharge rates obtained for the three polluted zones.

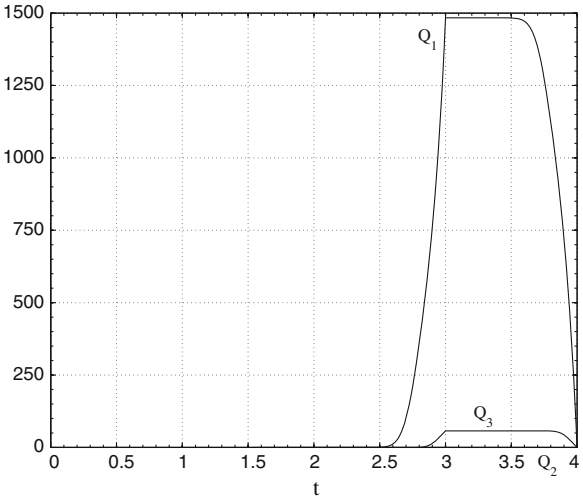

Fig. 2.8 Optimal discharge rates $Q_i(t) = \gamma_i^* Q_i^*(t)$, $i = 1, 2$ and 3, for the critical concentrations $c_1 = 19.0$, $c_2 = 0.8$ and $c_3 = 0.8$, and slack variables $\alpha_1 = \beta_1 = 0.1$ and $\alpha_i = \beta_i = 0$ $(i = 2, 3)$

Note that Q_2 is practically zero, and hence, the discharge rate Q_1 is responsible for the concentration reached in zone Ω_2.

2.8 Conclusions

The main objectives of the mathematical modelling in the environment protection are the identification of emission rates of sources and their positions, the prediction of concentrations of different substances (pollutants, cleanears, nutrients, etc.), the development of the methods which help to prevent dangerous pollution levels (control of emissions) and the search of new strategies for the remediation of polluted zones. In this chapter, we have presented a method for the cleanup of the oil-polluted marine environment through bioremediation. It is assumed that oil is stranded in some zones at the shoreline and the goal is to release a nutrient into aquatic system in order to increase the amount of indigenous microorganisms which degrade the pollutants in such zones. Thus, the specific objective is to determine the appropriate parameters of releasing the nutrient, namely, the discharge sites and the discharge rates, in order to reach critical (necessary) concentrations of the nutrient in the polluted zones. All the unknown parameters are chosen for minimizing the total mass of the released nutrient, with the aim to minimize the impact on the environment and the cost of remediation.

To this end, the problem is solved in two stages. In the first stage, each zone Ω_i is considered separately from other and contains just one source. In order to reach the critical concentration c_i in each polluted zone Ω_i $(1 \leq i \leq N)$, a variational problem is posed and solved with the aim to find both the optimal location of release point r_i

in the zone and the optimal release rate $Q_i(t)$, also named as basic or preliminary discharge rate. We prove that this problem has unique solution.

In the second stage, we consider the process of dispersion of nutrient in all zones together. Due to advection by currents, the nutrient released in one zone can reach other polluted zones. Therefore we must specify (modulate) the strength of all release rates $Q_i(t)$ in order to fulfil the critical mean concentrations c_i in all the polluted zones during the time interval $[T - \tau, T]$. To this end, we introduce positive coefficients γ_i to replace all release rates $Q_i(t)$ by $\gamma_i Q_i(t)$. These coefficients are chosen as the solution of a quadratic programming problem where the objective function for minimizing is the mass of nutrient introduced by the new discharge rates $\gamma_i Q_i(t)$. Also, we prove the existence and uniqueness of this optimization problem.

Both stages of this remediation strategy use the adjoint solutions to assess the mean concentration of nutrient in the oil-polluted zones. Such approach is quite useful. Indeed, in the first stage, the optimal release point for a specific oil-polluted zone is found by maximizing a continuous non-linear function of three real variables. The function is built with the adjoint problem solution corresponding to the selected zone. In addition, the respective basic discharge rate is determined as a multiple of the adjoint solution which is evaluated at the optimal discharge point. Of course, the basic discharge rate also depends on the critical concentration for the respective oil-polluted zone. And in the second stage, the adjoint solutions, evaluated at the optimal discharge points, are also used to pose the constraints for the quadratic programming problem.

Thus, this new remediation method is strongly based on the adjoint estimates. Nevertheless, it also uses the direct concentration estimates of nutrient in the polluted zones when various discharges of the nutrient are needed. Therefore, the two equivalent (direct and adjoint) estimates complement each other well in the assessment of nutrients and control of pollutants. The direct estimates, utilizing the solution of the advection-diffusion problem, enable making the comprehensive analysis of ecological situation in the whole area. On the other hand, the adjoint estimates use solutions of the adjoint problems and explicitly depend on the positions of sources, their discharge rates, and also on the initial distribution of nutrient in the region. Besides, the solutions of adjoint problem serve as influence (weight) functions, which show the impact of the location of discharge source and its intensity on the concentration of nutrient in each oil-polluted zone. Therefore, the adjoint estimates are effective and economical in the sensitivity study of the concentrations of nutrient to variations in the model parameters.

Owing to special boundary conditions, both the main and adjoint problems are well-posed according to Hadamard, that is the solution of each problem exists, is unique and stable to initial perturbations. These conditions are reduced to the well-known and natural boundary conditions in the non-diffusion limit (pure advection problem) and also in the case of a closed sea basin (when the boundary is the coast line).

Finite difference schemes for the solution of the main and adjoint transport problems are also given. The schemes are balanced, unconditionally stable, of second-order approximation, and are based on using the splitting method and Crank-Nicolson

scheme. In the absence of dissipation and sources, each scheme has two conservation laws. All one-dimensional discrete equations obtained at every fractional step of the splitting algorithm are efficiently solved by the Thomas factorization method for tridiagonal matrices.

Finally, we point out that the adjoint technique described in this chapter can also be used for the solution of such problems as the control of industrial emissions, the detection of the enterprises which violate the emission rates prescribed by a control, and the estimation of the intensity of a pollution source in the case when its position is known. For example, the last cases include a nuclear (or chemical) plant accident or nuclear bomb explosion (testing, terrorist attacks, and others). In all these situations, the source position is known or can easily be located (from a satellite or other monitoring equipment), and then our method gives a lower bound of the source intensity, which can be useful in the assessment of the scale of accident.

Acknowledgments This work was supported by the PAPIIT projects IN103313-2 and IN101815-3 (UNAM, México) and by the grants 14539 and 25170 of National System of Researches (CONACyT, México). The authors are grateful to Marco Antonio Rodríguez García for his help in preparing the final version of this manuscript in LaTeX.

References

1. Alvarez-Vázquez, L.J., García-Chan, N., Martínez, A., Vázquez-Méndez, M.E., Vilar, M.A.: Optimal control in wastewater management: a multi-objective study. Commun. Appl. Ind. Math. **1**(2), 62–77 (2010)
2. Boufadel, M.C., Suidan, M.T., Venosa, A.D.: Tracer studies in laboratory beach simulating tidal influences. J. Environ. Eng. **132**(6), 616–623 (2006)
3. Boufadel, M.C., Suidan, M.T., Venosa, A.D.: Tracer studies in a laboratory beach subjected to waves. J. Environ. Eng. **133**(7), 722–732 (2007)
4. Bragg, J.R., Prince, R.C., Harner, E.J., Atlas, R.M.: Effectiveness of bioremediation for the Exxon Valdez oil spill. Nature **368**, 413–418 (1994)
5. Cheney, E.W.: Introduction to Approximation Theory. Chelsea Publishing Company, New York (1966)
6. Coleman, T.F., Li, Y.: A reflective Newton method for minimizing a quadratic function subject to bounds on some of the variables. SIAM J. Optim. **6**(4), 1040–1058 (1996)
7. Coulon, F., McKew, B.A., Osborn, A.M., McGenity, T.J., Timmis, K.N.: Effects of temperature and biostimulation on oil-degrading microbial communities in temperate estuarine waters. Environ. Microbiol. **9**(1), 177–186 (2006)
8. Crank, J., Nicolson, P.: A practical method for numerical evaluation of solutions of partial differential equations of the heat conduction type. Proc. Camb. Philos. Soc. **43**, 50–67 (1947)
9. Dang, Q.A., Ehrhardt, M., Tran, G.L., Le, D.: Mathematical modeling and numerical algorithms for simulation of oil pollution. Environ. Model. Assess. **17**(3), 275–288 (2012)
10. Dieudonné, J.: Foundations of Modern Analysis. Academic Press, New York (1969)
11. Folland, G.B.: Real Analysis: Modern Techniques and Their Applications. Wiley, New York (1999)
12. Gill, P.E., Murray, W., Wright, M.H.: Practical Optimization. Academic Press, London (1981)
13. Hadamard, J.: Lectures on Cauchy's Problem in Linear Partial Differential Equations. Yale University Press, New Haven (1923)
14. Head, M., Swannell, R.P.J.: Bioremediation of petroleum hydrocarbon contaminants in marine habitats. Curr. Opin. Biotechnol. **10**(3), 234–239 (1999)

15. Hinze, M., Yan, N.N., Zhou, Z.J.: Variational discretization for optimal control governed by convection dominated diffusion equations. J. Comput. Math. **27**(2–3), 237–253 (2009)
16. Hongfei, F.: A characteristic finite element method for optimal control problems governed by convection-diffusion equations. J. Comput. Appl. Math. **235**(3), 825–836 (2010)
17. Kreyszig, E.: Introductory Functional Analysis with Applications. Wiley, New York (1989)
18. Kreyszig, E.: Advanced Engineering Mathematics. Wiley, New Jersey (2006)
19. Ladousse, A., Tramier, B.: Results of 12 years of research in spilled oil bioremediation: Inipol EAP22. In: Hildrew, J.C., Ludwigson, J. (eds.) Proceedings of the 1991 International Oil Spill Conference, vol. 1, pp. 577–582. American Petroleum Institute, Washington DC (1991)
20. Liu, F., Zhang, Y.H., Hu, F.: Adjoint method for assessment and reduction of chemical risk in open spaces. Environ. Model. Assess. **10**(4), 331–339 (2005)
21. Marchuk, G.I.: Numerical Solution of Problems of the Dynamics of Atmosphere and Ocean. Leningrad, Gidrometeoizdat (in Russian) (1974)
22. Marchuk, G.I.: Mathematical Models in Environmental Problems. Elsevier, New York (1986)
23. Marchuk, G.I., Skiba, Y.N.: Role of adjoint functions in studying the sensitivity of a model of the thermal interaction of the atmosphere and ocean to variations in input data. Izv., Atmos. Ocean. Phys. **26**, 335–342 (1990)
24. Marchuk, G.I.: Adjoint Equations and Analysis of Complex Systems. Kluwer, Dordrecht (1995)
25. Mehrotra, S.: On the implementation of a primal-dual interior point method. SIAM J. Optim. **2**, 575–601 (1992)
26. Mills, M.A., Bonner, J.S., Simon, M.A., McDonald, T.J., Autenrieth, R.L.: Bioremediation of a controlled oil release in a wetland. In: Proceedings of the 24th Arctic and Marine Oil Spill (AMOP) Program Technical Seminar, vol. 1, pp. 609–616. Environment Canada, Ottawa, Ontario, Canada (1997)
27. National Research Council: Oil in the Sea III: Inputs. Fates and Effects, National Academy of Sciences, Washington DC (2002)
28. Parra-Guevara, D., Skiba, Y.N., Reyes-Romero, A.: Existence and uniqueness of the regularized solution in the problem of recovery the non-steady emission rate of a point source: application of the adjoint method. In: Rodrigues, H.C., et al. (eds.) Proceedings of the International Conference on Engineering Optimization (ENGOPT 2014), Engineering Optimization IV, pp. 181–186. CRC Press/Balkema, The Netherlands (2015)
29. Parra-Guevara, D., Skiba, Y.N.: A variational model for the remediation of aquatic systems polluted by biofilms. Int. J. Appl. Math. **20**(7), 1005–1026 (2007)
30. Parra-Guevara, D., Skiba, Y.N., Pérez-Sesma, A.: A linear programming model for controlling air pollution. Int. J. Appl. Math. **23**(3), 549–569 (2010)
31. Parra-Guevara, D., Skiba, Y.N., Arellano, F.N.: Optimal assessment of discharge parameters for bioremediation of oil-polluted aquatic systems. Int. J. Appl. Math. **24**(5), 731–752 (2011)
32. Parra-Guevara, D., Skiba, Y.N.: An optimal strategy for bioremediation of aquatic systems polluted by oil. In: Daniels, J.A. (ed.) Advances in Environmental Research, vol. 15, pp. 165–205. Nova Science Publishers Inc, New York (2011)
33. Parra-Guevara, D., Skiba, Y.N.: A linear-programming-based strategy for bioremediation of oil-polluted marine environments. Environ. Model. Assess. **18**(2), 135–146 (2013)
34. Parra-Guevara, D., Skiba, Y.N.: Adjoint approach to estimate the non-steady emission rate of a point source. Int. J. Eng. Res. Appl. **3**(6), 763–776 (2013)
35. Prince, R.C., Bare, R.E., Garrett, R.M., Grossman, M.J., Haith, C.E., Keim, L.G., Lee, K., Holtom, G.J., Lambert, P., Sergy, G.A., Owens, E H., Guénette, C.C.: Bioremediation of a marine oil spill in the Arctic. In: Alleman, B.C., Leeson, A. (eds.) In Situ Bioremediation of Petroleum Hydrocarbon and Other Organic Compounds, pp. 227–232, Battle Press, Columbus (1999)
36. Prince, R.C., Clark, J.R., Lindstrom, J.E., Butler, E.L., Brown, E.J., Winter, G., Grossman, M.J., Parrish, R.R., Bare, R.E., Braddock, J.F., Steinhauer, W.G., Douglas, G.S., Kennedy, J.M., Barter, P.J., Bragg, J.R., Harner, E.J., Atlas, R.M.: Bioremediation of the Exxon Valdez oil spill: monitoring safety and efficacy. In: Hinchee, R.E., Alleman, B.C., Hoeppel, R.E., Miller, R.N. (eds.) Hydrocarbon Remediation, pp. 107–124. Lewis Publishers, Boca Raton (1994)

37. Prince, R.C., Bragg, J.R.: Shoreline bioremediation following the Exxon Valdez oil spill in Alaska. Bioremediation J. **1**, 97–104 (1997)
38. Prince, R.C., Lessard, R.R., Clark, J.R.: Bioremediation of marine oil spills. Oil Gas Sci. Technol. **58**(4), 463–468 (2003)
39. Pudykiewicz, J.: Application of adjoint tracer transport equations for evaluating source parameters. Atmos. Environ. **32**, 3039–3050 (1998)
40. Ramsay, M.A., Swannell, R.P.J., Shipton, W.A., Duke, N.C., Hill, R.T.: Effect of bioremediation on the microbial community in oiled mangrove sediments. Mar. Pollut. Bull. **41**, 413–419 (2000)
41. Skiba, Y.N.: Balanced and absolutely stable implicit schemes for the main and adjoint pollutant transport equations in limited area. Rev. Int. Contam. Ambient. **9**, 39–51 (1993)
42. Skiba, Y.N.: Dual oil concentration estimates in ecologically sensitive zones. Environ. Monit. Assess. **43**, 139–151 (1996)
43. Skiba, Y.N., Parra-Guevara, D.: Industrial pollution transport part I: formulation of the problem and air pollution estimates. Environ. Model. Assess. **5**, 169–175 (2000)
44. Smith, D.R.: Variational Methods in Optimization. Dover Publications, New York (1998)
45. Swannell, R.P.J., Mitchell, D., Jones, D.M., Petch, S., Head, I.M., Wilis, A., Lee, K., Lepo, J.E.: Bioremediation of oil-contaminated fine sediment. In: Marshall, S. (ed.) Proceedings of the 1999 International Oil Spill Conference, vol. 1, pp. 751–756. American Petroleum Institute, Washington DC (1999)
46. Swannell, R.P.J., Mitchell, D., Lethbridge, G., Jones, D., Heath, D., Hagley, M., Jones, M., Petch, S., Milne, R., Croxford, R., Lee, K.: A field demonstration of the efficacy of bioremediation to treat oiled shorelines following the Sea Empress incident. Environ. Technol. **20**, 863–873 (1999)
47. Venosa, A.D.: Oil spill bioremediation on coastal shorelines: a critique. In: Sikdar, S.K., Irvine, R.I. (eds.) Bioremediation: Principles and Practice, Vol. III. Bioremediation Technologies, pp. 259–301. Technomic, Lancaster (1998)
48. Venosa, A.D., Suidan, M.T., Wrenn, B.A., Strohmeier, K.L., Haines, J.R., Eberhart, B.L., King, D., Holder, E.: Bioremediation of an experimental oil spill on the shoreline of Delaware Bay. Environ. Sci. Technol. **30**, 1764–1775 (1996)
49. Yan, N.N., Zhou, Z.J.: A priori and a posteriori error analysis of edge stabilization Galerkin method for the optimal control problem governed by convection-dominated diffusion equation. J. Comput. Appl. Math. **223**(1), 198–217 (2009)
50. Yee, E.: Theory for reconstruction of an unknown number of contaminant sources using probabilistic inference. Bound.-Layer Meteorol. **127**(3), 359–394 (2008)
51. Zhang, Y.: Solving large-scale linear programs by interior-point methods under the MATLAB environment. Technical report TR96-01, Department of Mathematics and Statistics, University of Maryland (1995)
52. Zhu, X., Venosa, A.D., Suidan, M.T., Lee, K.: Guidelines for the Bioremediation of Marine Shorelines and Freshwater Wetlands. U.S. Environmental Protection Agency, Cincinnati (2001)

Chapter 3
Prediction of the Formation of Water-in-Oil Emulsions

Merv Fingas

Abstract The formation of water-in-oil emulsions, a major complication in oil spills, is described. Research has shown that asphaltenes are the prime stabilizers of water-in-oil emulsions and that resins are necessary to solvate the asphaltenes. It has also been shown that many factors play a role, including the amount of saturates and the oil viscosity. Two schemes are given to describe the formation of emulsions using the characteristics of starting oils including the resin and asphaltene contents and the viscosity. Essentially, water droplets injected into the oil by turbulence or wave action can be stabilized temporarily by the oil viscosity and on a longer-term basis by resins and then asphaltenes. Depending on the starting oil properties, four types of water-in-oil types are created: meso-stable and stable emulsions, entrained water-in-oil and unstable or those-that-do-not-form types. Each type is described and has unique properties. For most oils, loss of lighter components by evaporation is necessary before the oils will form a water-in-oil type. It was noted that variability in emulsion formation is, in part, due to the variation in types of compounds in the asphaltene and resins groups. Certain types of these compounds form more stable emulsions than others within the same asphaltene/resin groupings. A review of numerical modelling schemes for the formation of water-in-oil emulsions is given. A recent model is based on empirical data and the corresponding physical knowledge of emulsion formation. The density, viscosity, asphaltene and resin contents were correlated with a new stability index. A simplified screening approach is also described. Although of lesser accuracy, the approach is simple to implement.

3.1 Introduction

Water-in-oil emulsions sometimes form after oil products are spilled. These emulsions, often called chocolate mousse or "mousse" by oil spill workers, can make the cleanup of oil spills difficult [7]. When water-in-oil emulsions form, the physical properties of oil changes dramatically. As an example, stable emulsions contain from

M. Fingas (✉)
Spill Science, Edmonton, AB, Canada
e-mail: Fingasmerv@shaw.ca

M. Ehrhardt (ed.), *Mathematical Modelling and Numerical Simulation of Oil Pollution Problems*, The Reacting Atmosphere 2, DOI 10.1007/978-3-319-16459-5_3

60 to 80 % water, thus expanding the spilled material from 2 to 5 times the original volume. Most importantly, the viscosity of the oil typically changes from a few hundred to about 100,000 mPa s, an increase by a factor of 500–1000. A liquid product is changed into a heavy, semi-solid material. These thick emulsions are difficult to recover with ordinary spill recovery equipment.

3.2 Water-in-Oil Types

Fingas and Fieldhouse [3] found that four clearly-defined water-in-oil types are formed by crude oil when mixed energetically with water. This was shown by water resolution over time, by a number of rheological measurements, and by the water-in-oil products visual appearance, both on the day of formation and 1 week later. Some emulsions were observed for over a year, with the same results. The types are named stable water-in-oil emulsions, meso-stable water-in-oil emulsions, entrained water, and unstable water-in-oil types or those-that-did-not form. The differences among the four types are quite large and are based on at least two water content measurements and five rheological measurements. More than 400 oils or petroleum products were studied.

Stable emulsions are reddish-brown semi-solid substances with an average water content of about 70–80 % on the day of formation and about the same 1 week later, cf. [2]. Stable emulsions remain stable for at least 4 weeks under laboratory conditions. All of the stable emulsions studied, remained so for at least 1 year. The viscosity increase following formation averages 400 times the original viscosity and 1 week later averages 850 times the original viscosity. The average properties of the starting oil required to form a stable emulsion are: density −0.9 g/mL; viscosity −300 mPa s; resin content −9 %; asphaltene content −5 %; and asphaltene-to-resin ratio −0.6.

Meso-stable water-in-oil emulsions are reddish-brown viscous liquids with an average water content of 60–65 % on the first day of formation and less than 30 % 1 week later. Meso-stable emulsions generally break down within 1 week to a substance called rag with about 20 % water content. The viscosity increases over the initial viscosity on the day of formation averages a factor of 7 and 1 week later averages 5. The average properties of the starting oil required to form a meso-stable emulsion are: density −0.9 g/mL; viscosity −1300 mPa s; resin content −16 %; and asphaltene content −8 %; asphaltene-to-resin ratio −0.5. The greatest difference between the starting oils for stable and meso-stable emulsions are the ratio of viscosity increases (stable 400, first day and 850 in 1 week; meso-stable 7, first day and 5 in 1 week) and resin content (stable −9 %; meso-stable −16 %).

Entrained water-in-oil types are black viscous liquids with an average water content of 40–50 % on the first day of formation and less than 28 % 1 week later. The viscosity increase over the day of formation averages a multiple of two and 1 week later still averages two. The average properties of the starting oil required to form entrained water are: density −0.97 g/mL; viscosity −60,000 mPa s; resin content −18 %; asphaltene content −12 %; and asphaltene-to-resin ratio −0.75. The greatest

differences between the starting oils for entrained water-in-oil compared to stable and meso-stable emulsions are the viscosity of the starting oil (entrained starting oil averages 60,000 mPa s compared to 200 mPa s for stable emulsions and 1300 mPa s for meso-stable emulsions) and the ratio of viscosity increase (entrained = 2, first day and 2 in 1 week; stable 400, first day and 850 in 1 week; meso-stable 7, first day and 5 in 1 week). Entrained water-in-oil types appear to be applicable to viscous oils and petroleum products, but not extremely viscous products.

Unstable water-in-oil emulsion types or those oils that do not form any of the other three types are characterized by the fact that the oil does not hold significant amounts of water following mixing with water [2]. There is a much broader range of properties in the starting oil than for the other three water-in-oil states. For example, viscosities are very low or very high. Included in this group are light fuels such as diesel fuel and very heavy, viscous oil products such as heavy residual oils.

The differences between some of the basic properties of emulsions and water-in-oil types are shown in Fig. 3.1. Figure 3.1 uses umbrella or spider graphs to show the relationship of the ten average properties of each water-in-oil type compared to another water-in-oil type. Moving around the graph, the relative water content on the first day is plotted, then the water content after 1 week, then the starting oil density, then the starting oil viscosity, then the saturate, aromatic, resins and asphaltene contents. After this, the graph shows the asphaltene/resin (A/R) content, then the wax content. Each of these parameters are scaled on this graph from 1 to 10 based on the distribution from the lowest to highest relative value. As can be seen from these figures, there are significant differences between the various water-in-oil types.

The viscosity and water content differences among the four types of water content in oil are shown in Fig. 3.2. Figure 3.2a shows the water content change over 1 year. Stable emulsions, on average, begin at a high level (about 78 %) and lose little water over 1 year. Meso-stable emulsions, on the other hand, begin at about 65 % and lose most of this water within a few days. Entrained water-in-oil types pick up only about 40 % water and only slowly lose this over 1 year. Unstable water-in-oil types pick up only a few percent of water and this does not change much over 1 year. Figure 3.2b shows the apparent viscosity over 1 year. This graph shows that the apparent viscosity of stable emulsion increases over the period of 1 year and the others generally decline or only increase a small amount. Thus, after a few months, the stable emulsion will have the greatest viscosity.

3.3 Stability Indices

Fingas and Fieldhouse [3] carried out tests of several indices of stability, a single value that could provide good discrimination between water-in-oil types even on the first day. This was felt to be necessary as the water content alone was not entirely discriminating because some of the water loss occurs within hours or days, especially for meso-stable emulsions. A new stability index was found, and serves to describe the emulsion stability quite well.

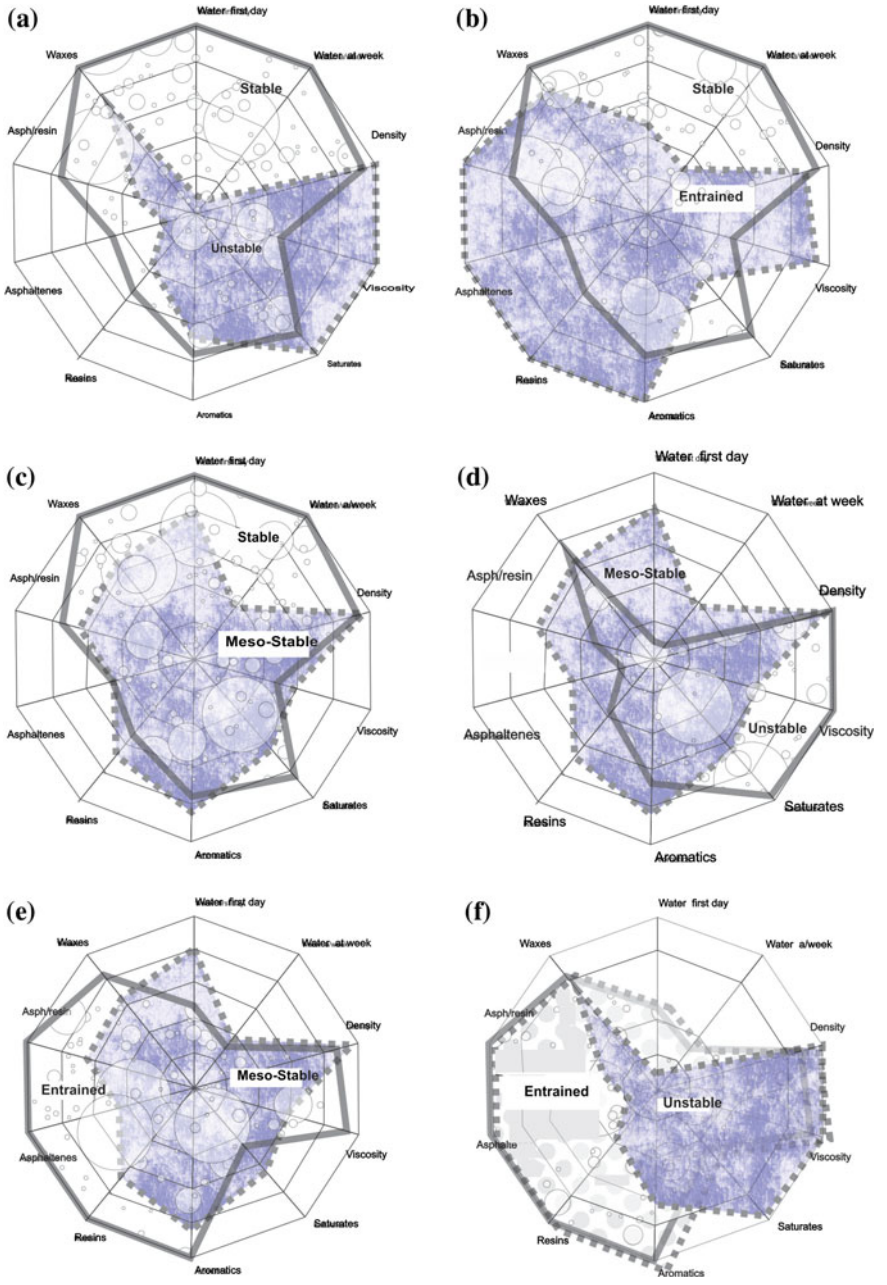
(a)
Water first day
Water a/week
Density
Viscosity
Saturates
Aromatics
Resins
Asphaltenes
Asph/resin
Waxes
Stable
Unstable
(b)
Water first day
Water a/week
Density
Viscosity
Saturates
Aromatics
Resins
Asphaltenes
Asph/resin
Waxes
Stable
Entrained
(c)
Water first day
Water a/week
Density
Viscosity
Saturates
Aromatics
Resins
Asphaltenes
Asph/resin
Waxes
Stable
Meso-Stable
(d)
Water first day
Water at week
Density
Viscosity
Saturates
Aromatics
Resins
Asphaltenes
Asph/resin
Waxes
Meso-Stable
Unstable
(e)
Water first day
Water a/week
Density
Viscosity
Saturates
Aromatics
Resins
Asphaltenes
Asph/resin
Waxes
Entrained
Meso-Stable
(f)
Water first day
Water a/week
Density
Viscosity
Saturates
Aromatics
Resins
Asphaltenes
Asph/resin
Waxes
Entrained
Unstable

Fig. 3.1

◀**Fig. 3.1** The relationships between oil properties and the four types of water-in-oil types. **a** The differences between stable emulsions (line around *shaded area*) and the unstable types or oils that do not form other types (line around *patterned area*). Note the lines indicate the typical boundaries and the areas are only shown to distinguish the lines. **b** The relationship between stable emulsions (line around shaded area) and the entrained type (line around *patterned area*). **c** The relationships between stable (line around *shaded area*) and meso-stable emulsions (line around *patterned area*). **d** Highlights the relationships between meso-stable emulsions (line around *patterned area*) and the unstable type or oils that do not form other types (line around *shaded area*). **e** The property differences between meso-stable emulsions (line around *patterned area*) and the entrained type (line around *shaded area*). Finally, **f** the relationship between the unstable (line around *patterned area*) and entrained types (line around *shaded area*)

The values of the stability index are shown in Table 3.1. This shows that the stability index can be simply calculated from rheological data and that it can be used, along with some basic property data such as density and viscosity, to classify the water-in-oil types.

3.4 Formation of Emulsions

3.4.1 The Role of Asphaltenes

Some researchers reported that asphaltenes were a major factor in water-in-oil emulsions more than 45 years ago [1]. The fundamental process is that water-in-oil emulsions are stabilized by the formation of high-strength visco-elastic asphaltene films around water droplets in oil [10]. Resins could also form emulsions, but resins do not form stable emulsions, and actually aid in asphaltene emulsion stability by acting as asphaltene solvents and by providing temporary stability during the time of the slow asphaltene migration. Overall, a wide spectrum of scientists has found that oil composition is the key factor in water-in-oil emulsion formation including the amounts and types of asphaltene, resin, and saturate contents.

Asphaltenes represent a very broad category of substances and several scientists reviewed concluded that the asphaltene content is the most important factor in the formation of emulsions [6]. Even in the absence of any other possibly-synergistic compounds such as resins, asphaltenes were found to be capable of forming rigid, elastic films which are the primary agents in stabilizing water-in-crude oil emulsions. The exact conformations by which asphaltenes organize at oil-water interfaces and the corresponding intermolecular interactions have not been elucidated. Other workers have noted that solid particles, such as clays, when present, can stabilize or enhance the stability of emulsions. This is true of emulsions formed by clay-containing bitumens. These clay-stabilized emulsions may have differences from the crude oil and petroleum product emulsions noted in this chapter.

Asphaltenes are a class of substances defined only by their precipitation from oil in pentane, hexane, or heptane. The specific structure of asphaltenes is unknown,

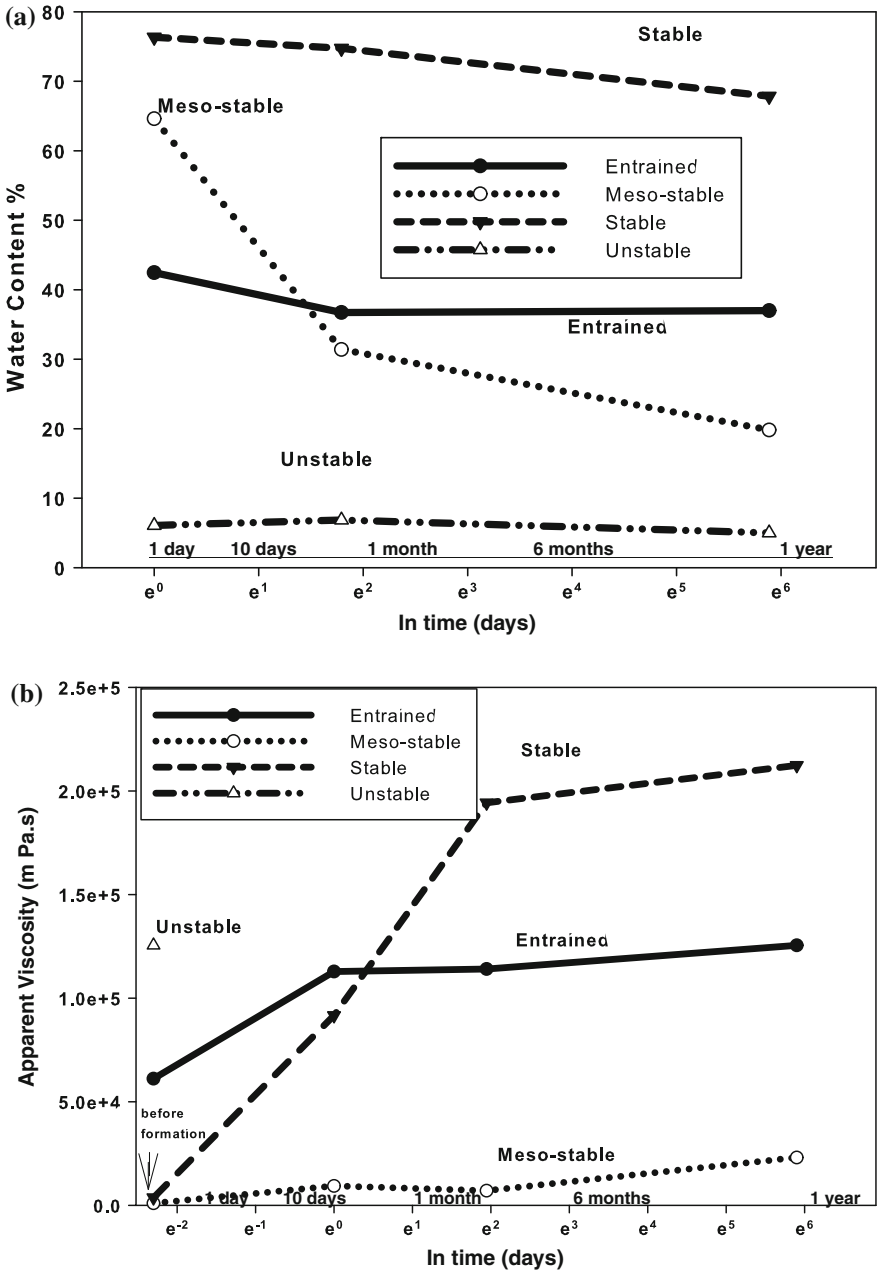

Fig. 3.2 Comparison of average properties of water-in-oil types over 1 year. **a** Comparison of water content, **b** comparison of apparent viscosity

Table 3.1 Stability values

Calculated stability		Starting oil properties	Water-in-oil type	Calculated average stability
Minimum	Maximum			
4	29		Stable	13
−10	5		Meso-stable	−2
−20	3	Density >0.94 viscosity >6000	Entrained	−7
−4	−18	Density <0.85 or >1.0 viscosity <100 or >800,000 Asphaltenes or resins <1 %	Unstable	−15

however the molecular weight averages about 750 Da or more and there is a planar aromatic structure surrounded by alkane groups, some with heteroatoms, S, N and O [5].

The absorption of asphaltenes at the water-oil interface proceeds for a long time and may still proceed after a year [3]. This implies that the absorption at the interface lowers the net energy of the system and thus is favoured thermodynamically. The bulk concentration of asphaltenes is important and drives the amount that is absorbed at the interface.

3.4.2 The Role of Resins and Other Components

Several researchers studied the role of resins in water-in-oil formation [4]. They noted that the main role appears to be solvation of the asphaltenes in the oil solution. Others have noted that resins and asphaltenes are somehow correlated in emulsion stability. Silset et al. [9] noted that many of the stability differences in emulsions can be explained by the interactions between asphaltenes and resins. The authors noted that asphaltenes are believed to be suspended as colloids in the oil with stabilization by resins. Each particle is believed to consist of one or more sheets of asphaltene monomers and absorbed resins to stabilize the suspension. Under certain conditions, the resins can desorb from the asphaltenes leading to increased asphaltene aggregation and precipitation of the larger asphaltene aggregates.

Some effect from naphthenic acids was also noted, cf. [4]. Waxes have not been found to stabilize oil water-in-oil emulsions.

3.4.3 Methods to Study Emulsions

The availability of methodologies to study emulsions is very important. In the past 15 years, dielectric methods and rheological methods and many other methods

have been used to study formation mechanisms and stability of emulsions [4]. Standard chemical techniques, including Nuclear Magnetic Resonance (NMR), chemical analysis techniques, Near-infrared spectroscopy (NIR), microscopy, interfacial pressure, and interfacial tension, are also being applied to emulsions. These techniques have largely confirmed findings noted in the dielectric and rheological mechanisms.

Most researchers studied the stability of emulsions by measuring the amount of water resolved with time [4]. This certainly is the baseline method. Some researchers also subjected the emulsions to centrifugation to assess stability.

3.4.4 The Overall Theory of Emulsion Formation

The data suggest that the water-in-oil types are stabilized by both asphaltenes and resins, but for greater stability, resin content should exceed the asphaltene content slightly [3]. However, excess resin content (A/R about >0.6) apparently destabilizes the emulsion. This does not consider the question of different types of asphaltenes or resins. A high asphaltene content (typically >10 %) increases the viscosity of the oil such that a stable emulsion will not form. Viscous oils will only uptake water as entrained water and will slowly lose much of this water over a period of about 1 week. Viscous oils (typically >1000 mPa s) will not form stable or meso-stable emulsions. Oils of low viscosity or without significant amounts of asphaltenes and resins will not form any water-in-oil type and will retain less than about 6 % water. Oils of very high viscosity (typically >20,000 mPa s) will also not form any of these water-in-oil types and thus are classified as unstable. This is probably due to the inability of water droplets to penetrate the oil mass.

The start of the process is the injection of water droplets into the oil mass. This would typically occur as the result of turbulence or wave action. This also could occur as the result of oil injection into water, such as from an underwater blowout. Once in the oil mass, the water droplets may coalesce and sink to the bottom unless these water droplets are somehow stabilized. Asphaltenes probably reside in the oil in the form of resin-solvated agglomerates. They are not likely to stabilize the water droplets immediately as the large asphaltene-resin agglomerates migrate too slowly. If, however, the oil has a viscosity between about 50–5000 mPa s, the water droplets will move slowly, allowing time for some chemical stabilization. It is thought that resins, weakly stabilize the water droplets initially. Resins are also polar compounds and can become associated with polar water. Once stabilized by resins, the large asphaltenes will move toward the water droplets and will form elastic films around the water droplets. The ratio of asphaltene to resins can affect this process. If the quantity of resins is too high, they will solvate the asphaltenes to the extent that their migration is affected and will also create a barrier between the asphaltenes and the water droplets. Thus in the case of too high resin content, destabilization will also occur. It is thought that this destabilization is the origin of meso-stable emulsions.

If the viscosity of the oil is too high, water droplets cannot penetrate the oil mass to a great extent and thus emulsions are not formed. At moderate oil viscosities, about

1000–10,000 mPa s, the water droplets may be retained by viscosity alone. This is felt to be the origin of the entrained water-in-oil type.

3.4.5 The Role of Weathering

Most crude oils and petroleum products require weathering (evaporation) before they will form emulsions [4]. Most typical crude oils require weathering to make the transition from the basic crude to a meso-stable or stable emulsion. Weathering is necessary to increase the viscosity and the asphaltene/resin content to the point where the next water-in-oil type is possible. It is also important to note that transitions cannot occur after a water-in-oil state is created. It should be noted that once a water-in-oil type is formed, it cannot make a transition to another type even if extensive weathering or mixing takes place. This is felt to be a result of the exacting conditions for each type. Further, asphaltenes appear to be tied up in the form of rag in broken meso-stable emulsions. This rag formation appears to prohibit the formation of other types of emulsions.

3.5 Modelling the Formation of Water-in-Oil Emulsions

3.5.1 Older Models

The emulsification processes described above were not apparent until about 20 years ago and have since been translated into modelling equations [4]. The different water-in-oil states dictate that one simple equation is not adequate to predict formation. Information on the kinetics of formation at sea and other modelling data was less abundant in the past. It is now known that emulsion formation is a result of surfactant-like action of the polar asphaltene and resin compounds. While these are similar compounds that both behave like surfactants when they are not in solution, asphaltenes form much more stable emulsions. Emulsions begin to form when the required chemical and viscosity conditions are met and when there is sufficient sea energy. Further, as pointed out above, three different water-in-oil types are formed, depending on the oil type and its composition. Some oils do not form any water-in-oil types and this fact is stated to be a fourth type.

In the distant past, the rate of emulsion formation was assumed to be first-order with time. This was approximated with a logarithmic curve. The physical assumption was that all oils uptake water on a first-order basis. This assumption resulted in large errors in spill models.

3.5.2 New Models

Several new models for the prediction of water-in-oil emulsions were recently developed by the present author [4]. These models used empirical data to predict the formation of emulsions using a continuous function and employing the physical and chemical properties of oil. The emulsification properties of more oils were measured and the properties of some of the oils in the existing oil set have been re-measured. This enables the models to be recalculated with sound data on over 400 discreet oil samples.

The basis of these models is the result of the knowledge demonstrated above—namely that models are stabilized by asphaltenes, with the participation of resins. Findings of this group and other groups show that the entire SARA (Saturates, Aromatic, Resins, and Asphaltene) distribution effects the formation of emulsions as the prime stabilizers, asphaltenes and secondarily resins, are only available for emulsion formation when the concentration of the saturates and aromatics are at a certain level and when the density and viscosity are correct.

The approaches to model development were implemented and are detailed in the literature [4]. One approach was to curve fit the physical and content data to a stability index. Then this stability factor was used in turn to predict a class (stable, meso-stable, entrained or unstable). The empirical data including oil content data, viscosity, density and the resulting water-in-oil type stability were used to develop mathematical correlation. The value for each parameter was correlated in a series of models using `DataFit` (Oakdale Engineering) [8]. A two-step process is necessary as DataFit is not able to calculate the specific mathematical function with more than 2 variables, due to the large number of possibilities. Thus, the functions (e.g., linear, square, log) were calculated using a two-way regression (`TableCurve`, [11]) and these functions were in turn used in developing a predictor model for emulsification.

The steps to produce the first models are summarized in earlier papers [4]. First the parameters available were correlated one at a time with a stability index as the target of the correlation. This new approach used a multi-regression program directly, using various multi-functional transformations of the input oil property data. This allowed the regression software to assign portions of the functions necessary to achieve the highest correlation factor.

A transformation is needed to adjust the data to a singular increasing or decreasing function. Regression methods will not respond correctly to a function that varies both directly and inversely with the target parameter. Most parameters have an optimal value with respect to class, that is the values have a peak function with respect to stability or class. Arithmetic converts values in front of the peak to values behind the peak, thus yielding a simple declining function. The optimal value of this manipulation is found by using a peak function. This peak function fit is available from TableCurve software.

The arithmetic to perform the transformation is: (1) if the initial value is less than the peak value, then the adjusted value is the peak value less the initial value; (2) and if the initial value is more than the peak value, the adjusted value is the initial value

Table 3.2 Model 1: values used to correct oil property input parameters

Parameter	Form	Correction value
Density	Exponential	2.5
Viscosity	Natural logarithm	5.8
Saturates	Standard %	45
Resins	Standard %	10
Asphaltenes	Standard %	4
Asphaltene/Resin ratio	Standard	0.6

less the peak value. The values found for the transformations are listed in Table 3.2. It should be noted that the exponential of density was used and the natural log of the viscosity. Previous modelling work had shown that these mathematical changes are necessary to achieve higher correlations, cf. [4].

Having the transformed values, the new model proceeds by fitting a multiple linear equation to the data. The choice of functions was achieved by correlating the stability function directly with the data and taking the best of the functions (e.g. square, log, etc.) into the regression process. The functionalities of square, logarithmic or exponential curves are achieved by correlating the straight value of the input properties plus their expanded values, taken here as the cube of the starting parameter as well as the square of the exponential of the starting value; and their companded values, the natural log (ln) and the logarithm (base 10) of the parameter divided by the square of the value. Each parameter is correlated with the stability index in five sets of mathematical statements. This is similar to the standard Gaussian expansion regression technique. In this method the regression is expanded to functionalities above and below linear until the entire entity is optimized. For example a linear function would be included, then a square and then a square root and so on until tests of the complete regression show that there are no more gains in increased expansions. Using this technique, six input parameters: exponential of density, ln of viscosity, saturate content, resin content, asphaltene content and the asphaltene/resin ratio (A/R) were found to be optimal. Thus with 4 transformation and the original values of these input parameters, there are 6 times 5 or 30 input combinations.

Using Datafit, a multiple regression software, a maximum of 20 of these could be taken at a time to test the goodness-of-fit. Values that yield Prob(t) factors of greater than 0.9 were dropped until all remaining factors could be calculated at once. The Prob(t) is the probability that input can be dropped without affecting the regression or goodness-of-fit. Over twenty regressions were carried out until the resulting model was optimal. The r2, the regression coefficient, was 0.75, which is quite high considering the many potential sources of error, etc. The statistics on the new model are shown in Table 3.3, along with the parameters to create the model. Table 3.3 shows that the 14 remaining parameters all contribute to the accuracy of the final result and that none of them can be cut without affecting the outcome of the model. The procedures for using model I are given below and summarized in Table 3.4.

Table 3.3 Regression results for model I

Variable	Value	Standard error	t-ratio	Prob(t)	Input variable	Math applied
a	0.0126	0.09	0.14	0.88694	Saturates	
b	−1.49	0.48	−3.11	0.00239	Resins	
c	−12.6	12.34	−1.02	0.30914	A/R	
d	−0.073	0.02	−3.97	0.00013	ln viscosity	Cubed
e	0.00193	0.00	2.08	0.0402	Resins	Cubed
f	0.00016	0.00	0.22	0.82677	Asphaltenes	Cubed
g	−4.23	14.21	−0.30	0.76648	A/R	Cubed
h	−0.59	0.77	−0.77	0.44215	ln viscosity	ln
i	1.59	1.03	1.55	0.12359	Resins	ln
j	4.03	2.53	1.59	0.11479	A/R	ln
k	3.73E-26	0.00	1.28	0.20272	ln viscosity	Exp squared
l	1.21	7.02	0.17	0.8639	A/R	Exp squared
m	0.022	0.01	1.59	0.11463	Exp density	log/square x
n	0.11	0.13	0.83	0.40933	A/R	log/square x
o	17.8	8.60	2.07	0.04066	Contant	

Table 3.4 Summary of calculations for model I

Basic inputs	Symbol	Units
Density	D	g/mL
Viscosity	V	mPa s
Saturate content	S	%
Resin content	R	%
Asphaltene content	A	%
First step—transformation	Description	
Density	expD	Take exponential of density
Viscosity	lnV	Take natural logarithm of viscosity
Asphaltene/Resin ratio	A/R	Divide asphaltene content by resin content
Second step—rationalization (converts units to simple declining or increasing functions)		
Density	Dst	if(expD<2.5, 2.5lnV, expD2.5)*
Viscosity	Vst	if(lnV<5.8, 5.8lnV, LnV5.8)
Saturate content	Sst	if(S<45, 45S, S45)
Resin content	Rst	if(R<10, 10R, R10)
Asphaltene content	Ast	if(A<4, 4A, A4)
Asphaltene/Resin ratio	A/Rst	if(A/R<0.6, 0.6A/R, A/R0.6)

(continued)

Table 3.4 (continued)

Third step—parsing zeros from SARA numbers**		
Resin content	Rst	Replace zero's at rationalization stage with '20.1'
Asphaltene content	Ast	Replace zero's at rationalization stage with '20.1'
Asphaltene/Resin ratio	A/Rst	Replace zero's at rationalization stage with '0.01'
Fourth step—calculate Gaussian expansion steps		
Viscosity cubed	Vst^3	Cube the rationalized viscosity
Resin content cubed	Rst^3	Cube the rationalized resin content
Asphaltene content cubed	Ast^3	Cube the rationalized asphaltene content
Asphaltene/Resin ratio cubed	A/Rst^3	Cube the rationalized asphaltene content
Natural log of viscosity	lnVst	Natural logarithm of rationalized viscosity
Natural log of resin content	lnRst	Natural logarithm of rationalized viscosity
Natural log of asphaltene/resin ratio	lnA/Rst	Natural logarithm of rationalized asphaltene/resin ratio
Exponential of viscosity squared	Exp^2 Vst	(Exp(Vst)*Exp(Vst)
Exponential of A/Rst ratio square	Exp^2 A/Rst	(Exp(A/Rst)*Exp(A/Rst)
Log over square of density	$LogDst^2$	$(Log(Exp(Dst))/(Dst^2)$
Log over square of A/R ratio	$LogA/Rst^2$	$(Log(Exp(A/Rst))/(A/Rst^2)$

* This is an Excel-like statement, in this case reads: if the exponential of density is less than 2.5, the standardized density becomes 2.5 less the exponential of density, if not the standardized density is the exponential of density less 2.5

** Zeros must be purged from numbers as they cause problems in division and with logarithmic expressions

3.5.3 Model I

The first step is to transform the input data so that it forms a continuous declining or increasing function. It should be noted that the greater than can also be read as greater or equal to.

Density: Take the exponential of the density. If the exponential of density is less than 2.5, then the density parameter is 2.5 less the density and if it is greater than 2.5, it becomes the density less 2.5. The value used in the equation is this transformed value. (3.1)

Viscosity: Take the natural logarithm (ln) of the viscosity. If the natural log of the viscosity is less than 5.8, then the viscosity parameter is 5.8 less the viscosity natural log and if it is greater than 5.8, it becomes the natural log of viscosity less 5.8. The value used in the equation is this transformed value. (3.2)

Saturate Content: If the saturate content is less than 45, then the saturate content parameter is 45 less the saturate content and if it is greater than 45, it becomes the saturate content less 45. The value used in the equation is this transformed value. (3.3)

Resin Content: If the resin content is less than 10, then the resin content parameter is 10 less the resin content and if it is greater than 10, it becomes the resin content less 10. The value used in the equation is this transformed value. If the value of the resins is zero, then set this value to 20. (3.4)

Asphaltene Content: If the asphaltene content is less than 4, then the asphaltene content parameter is 4 less the asphaltene content and if it is greater than 4, it becomes the asphaltene content less 4. The value used in the equation is this transformed value. If the value of the asphaltene content is zero, then set the value to 20. (3.5)

A/R or Asphaltene/Resin Ratio: The A/R is taken as the direct value of the asphaltene content in percent (untransformed) divided by the resin content in percent (again untransformed). If A/R is less than 0.6, then the A/R parameter is 0.6 less the A/R and if it is greater than 0.6, it becomes the A/R less 0.6.
The value used in the equation is this transformed value. (3.6)

The class of the resulting emulsion is then calculated as follows:

$$\begin{aligned}\text{Stability} = {} & 17.8 + 0.013 \cdot Sst - 1.49 \cdot Rst - 12.6 \cdot A/Rst - 0.073 \cdot Vst3 \\ & + 0.0019 \cdot Rst3 + 0.00016 \cdot Ast3 - 4.23 \cdot A/Rst3 - 0.59 \cdot ln(Vst) \\ & + 1.59 \cdot ln(Rst) + 4.028 \cdot ln(A/Rst) + 3.72X10 - 26 \cdot Exp(Vst)2 \\ & + 1.207 \cdot Exp(A/Rst)2 + 0.022 \cdot (LogDst/Dst2) \\ & + 0.11 \cdot (LogA/Rst/A/Rst2)\end{aligned} \tag{3.7}$$

where:

Stability is the stability of the resulting water-in-oil type,
Sst is the transformed saturate content as calculated in Eq. (3.3), abbreviated A here,
Rst is the transformed resin content as calculated in Eq. (3.4), abbreviated B,
A/Rst is the transformed asphaltene/resin ratio as calculated in (3.6), abbreviated C,
Vst3 is the cube of the transformed ln viscosity as calculated in (3.2), abbreviated D,
Rst3 is the cube of the transformed resin content as calculated in Eq. (3.4), abbreviated E,

Ast3 is the cube of the transformed asphaltene content as calculated in Eq. (3.5), abbreviated F,
A/Rst3 is the cube of the transformed A/R ratio as calculated in Eq. (3.6), abbreviated G,
lnVst is the natural logarithm (ln) of the transformed viscosity as calculated in Eq. (3.2), abbreviated H,
lnRst is the natural logarithm (ln) of the transformed resin content as calculated in Eq. (3.4), abbreviated I,
lnA/Rst is the natural logarithm (ln) of transformed asphaltene/resin ratio as calculated in (3.6), abbreviated J,
Exp(Vst)2 is the exponential of the transformed viscosity and squared—Vst as calculated in Eq. (3.2), abbreviated K,
Exp(A/Rst)2 is the exponential of the A/R ratio—squared—as calculated in Eq. (3.6), abbreviated L,
LogDst/Dst2 is the logarithm (base 10) of the exponential of the density—divided by the square of the transformed density—the transformed density as calculated in Eq. (3.1), abbreviated M,
LogA/Rst/A/Rst2 is the logarithm (base 10) of the exponential of the A/R ratio—divided by the square of the A/R ratio—the transformed A/R ratio as calculated in Eq. (3.6), abbreviated N.

A simplified version of the equation is then:

$$\begin{aligned}\text{Stability} = {} & 17.8 + 0.013A - 1.49B - 12.6C - 0.073D + 0.0019E \\ & + 0.00016F - 4.23G - 0.59H + 1.59I + 4.028J + 3.72X10 \\ & - 26K + 1.207L + 0.022M + 0.11N\end{aligned} \tag{3.8}$$

where the parameters A–N are defined as above.

The stability of the resulting product is calculated using the rheological measurements of the water-in-oil product formed. The basic uncorrected Stability or cross product is:

$$Xpr = \frac{\text{Complex Modulus}}{\text{Starting Oil Viscosity}} \times \frac{\text{Elastic Modulus}}{\text{Starting Oil Viscosity}} \tag{3.9}$$

The corrected stability is:

$$\text{Stability} = \ln((Xpr/10{,}000) \cdot (Xpr/10{,}000)) \tag{3.10}$$

where the Xpr is the value from Eq. (3.9).

The values of stability which are assigned to each class are given in Table 3.1. The viscosity of the resulting product can be taken as the average of the types at a given time as shown in Table 3.5.

Table 3.5 Viscosity increases from starting oil and typical water content

	Viscosity increase on		
	First day	Week	Year
Entrained	1.9	1.9	2.1
Meso-stable	7.2	11	32
Stable	405	1054	991
Unstable	0.99	1.0	1.0
	Typical water content		
	First day	Week	Year
Entrained	44.5	27.5	6
Meso-stable	64.3	30	6
Stable	81	78	70
Unstable	6.1	6	5

3.5.4 Model II

The differences between the equations shown above and those for model II include:

1. The Gaussian expansion is simplified to one term expansion and one term compression.
2. Three terms are not rationalized in the same manner as above, this includes density, viscosity and asphaltene/resin ratio. These are felt to be already continuous functions and thus can be used as such.
3. The input values are also used directly as well as the Gaussian expansion.

The first step to procedure 2 is to transform the input data so that it forms a continuous declining or increasing function. It should be noted that the greater than can also be read as greater or equal to.

Density: not transformed—just take the exponential, abbreviated Den,

Viscosity: not transformed—just take the natural log, abbreviated Visc,

Saturate Content: If the saturate content is less than 45, then the saturate content parameter is 45 less the saturate content and if it is greater than 45, it becomes the saturate content less 45. The value used in the equation is this transformed value. (3.11)

Resin Content: If the resin content is less than 10, then the resin content parameter is 10 less the resin content and if it is greater than 10, it becomes the resin content less 10. The value used in the equation is this transformed value. If the value of the resins is zero, then set this value to 20. (3.12)

Asphaltene Content: If the asphaltene content is less than 4, then the asphaltene content parameter is 4 less the asphaltene content and if it is greater than 4, it becomes the asphaltene content less 4. The value used in the equation is this transformed value. If the value of the asphaltene content is zero, then set the value to 20. (3.13)

A/R or Asphaltene/Resin Ratio: not transformed For procedure 2, the class of the resulting emulsion is then calculated as follows:

$$\begin{aligned}\text{Stability} = {} & 5667 - 9520 \cdot Den - 3.99 \cdot Visc + 0.138 \cdot Sst + 2.16 \cdot Rst \\ & - 0.395 \cdot Ast + 17.9 \cdot A/R + 224 \cdot exp(den) + 2.88e - 10 \cdot exp(Rst) \\ & - 4.35 \cdot exp(A/R) + 16823 \cdot ln(Den) + 10.5 \cdot ln(Visc) \\ & - .671 \cdot ln(Sst) + 0.147 \cdot ln(Rst) + 0.107 \cdot ln(Ast) + 1.62 \cdot ln(A/R)\end{aligned} \tag{3.14}$$

where:

Stability is the stability of the resulting water-in-oil type,
Den is the untransformed exponential of the density, abbreviated A here,
Visc is the untransformed natural logarithm (ln) of the viscosity, abbreviated B here,
Sst is the transformed saturate content as calculated in Eq. (3.11), abbreviated C here,
Rst is the transformed resin content as calculated in Eq. (3.12), abbreviated D,
Ast is the transformed asphaltene content as calculated in Eq. (3.13), abbreviated E,
A/R is the (untransformed) asphaltene/resin ratio, abbreviated F,
Exponential den is the exponential of the exponential of density, abbreviated G,
Exponential Rst is the exponential of the transformed resins, calculated in Eq. (3.12) abbreviated,
Exponential of A/R, abbreviated I,
Ln (natural logarithm) of the exponential of density, abbreviated J,
Ln (natural logarithm) of the natural logarithm of viscosity, abbreviated K,
Ln (natural logarithm) of the transformed saturates as calculated in Eq. (3.11), abbreviated L,
Ln (natural logarithm) of the transformed resins as calculated in Eq. (3.12), abbreviated M,
Ln (natural logarithm) of the transformed asphaltenes as calculated in Eq. (3.13), abbreviated N,
Ln (natural logarithm) of the (untransformed) (A/R) ratio, abbreviated O.

A simplified version of the equation is then:

Table 3.6 Regression results for the emulsification model II

Variable	Value	Standard error	t-ratio	Prob(t)	Input variable	Math applied
a	−9520	7200	−1.32	0.189	Density	Exp
b	−3.99	1.789	−2.23	0.028	Viscosity	ln
c	0.138	0.128	1.07	0.285	Saturates	Adjusted
d	0.216	0.224	0.966	0.336	Resins	Adjusted
e	−0.395	0.269	−1.47	0.145	Asphaltenes	Adjusted
f	17.9	13	1.37	0.172	A/R	
g	224	158	1.42	0.159	Exp density	Exp
h	2.883E-10	0.000	0.323	0.747	Exp resins	Exp
i	−4.35	3.64	−1.20	0.235	A/R	Exp
j	16830	13200	1.28	0.205	Exp density	Ln
k	10.5	12.1	0.867	0.388	Ln viscosity	Ln
l	−0.671	1.100	−0.610	0.543	Saturates_t	Ln
m	0.147	0.706	0.208	0.835	Resins_t	Ln
n	0.107	0.889	0.120	0.905	Asphaltenes_t	Ln
o	1.622	2.95	0.549	0.584	A/R	Ln
p	5667	4006	1.42	0.160	Contant	

't' subscript indicates adjusted value

$$\begin{aligned}\text{Stability} = {} & 5667 - 9520A - 3.99B + 0.138Ct + 2.16D - 0.395E \\ & + 17.9F + 224G + 2.88E - 10H - 4.35I + 16823J \\ & + 10.5K - 0.671L + 0.147M + 0.107N + 1.62O\end{aligned} \tag{3.15}$$

where the parameters A to O are defined as above.

As with model I, the values of stability which are assigned to each class are given in Table 3.1. The viscosities and water contents of the resulting products can be taken as the average of the types at a given time as shown in Table 3.5. The regression table for Model II is given in Table 3.6. The calculations for Model II are summarized in Table 3.7.

3.5.5 Model III—A Simplified Predictor

Previous equations have focussed on using a wide variety of data including physical properties and SARA data with which to predict the type of water-in-oil formed. Often such data are not available for oils and at most, density and viscosity are available. This model or method focuses on using only density and viscosity to predict water-in-oil type. This type of simplification is possible because certain types of water in oil emulsions have unique density/viscosity relationships.

Table 3.7 Summary of calculations for model II

Basic inputs	Symbol	Units
Density	D	g/mL
Viscosity	V	mPa s
Saturate content	S	%
Resin content	R	%
Asphaltene content	A	%
First step–transformation	Description	
Density	expD	Take exponential of density
Viscosity	lnV	Take natural logarithm of viscosity
Asphaltene/Resin ratio	A/R	Divide asphaltene content by resin content
Second step—rationalization (converts units to simple declining or increasing functions)		
Saturate content	Sst	if(S<45, 45S, S45)
Resin content	Rst	if(R<10, 10R, R10)
Asphaltene content	Ast	if(A<4, 4A, A4)
Third step—parsing zeros from SARA numbers*		
Resin content	Rst	Replace zero's at rationalization stage with '20.1'
Asphaltene content	Ast	Replace zero's at rationalization stage with '20.1'
Fourth step—calculate Gaussian expansion steps		
Exponential of density	exp(Den)	Exponential of the exponential of density
Exponential of resin content	exp(Rst)	Exponential of rationalized resin content
Exponential of A/R ratio	exp(A/R)	Exponential of A/R ratio
Natural logarithm of density	ln(Den)	Natural logarithm (ln) of the exponential of density
Natural logarithm of viscosity	ln(Visc)	Natural logarithm (ln) of the natural logarithm of viscosity
Natural logarithm of saturates	ln(Sst)	Natural logarithm (ln) of the rationalized saturate content
Natural logarithm of resins	ln(Rst)	Natural logarithm (ln) of the rationalized resin content
Natural logarithm of asphaltenes	ln(Ast)	Natural logarithm (ln) of the rationalized asphaltene content
Natural logarithm of A/R ratio	ln(A/R)	Natural logarithm (ln) of the A/R ratio

* Zeros must be purged from numbers as they cause problems in division and with logarithmic expressions

Entrained water-in-oil types show a unique character, that is they show a starting oil density of greater than 0.96 g/mL, but less than 1.0 g/mL. Further, the starting oils have a viscosity greater than 2300 mPa s and less than 200,000 mPa s. An example of the screening process is shown in Table 3.8. The screening (shown as screen entrained) is applied to all the oils and they are marked as sent if they meet this

requirement and are entrained and if not are marked as other. Those items in error are shown as a coloured entry. In doing the screening for entrained types, it is noted that only three oils were characterized incorrectly using the entrained screening for a total error of 1.5 %. This is an acceptable error rate.

Other items to note about Table 3.8 are that the oils are grouped by the water-in-oil types and that the summary of certain properties is given under each type as minimum, maximum and average. This aids in assessing the cut off points. The assessment rules are given in a column of the table as well. The basic data on each starting oil is given as well.

A second obvious cut-off screen is applied to those low-viscosity oils that do not form a water-in-oil type. Such oils as gasoline, diesel fuel, very light crudes, will never form a water-in-oil type. As shown in Table 3.8, this screening results in a low error rate of only 3.2 %.

The third screening can be applied to those oils that have a very high viscosity and do not form any type of water-in-oil type. This type is easily screened using only the criteria of viscosity, that of viscosity >200,000 mPa S. This results in a very high accuracy rate and a very low error rate, but there are few candidates for this type of oil. The third screening leaves the meso-stable and stable types. Several attempts to separate these included:

- regression of density and viscosity with the stability index,
- separate regressions of density and viscosity with the stability index,
- simple screening by either density and viscosity,
- Principle Components Analysis,
- graphical procedures, and
- relationship to other parameters.

None of these resulted in a successful screening out of the meso-stable and stable water-in-oil types. The difficulty of separating these two types has been noted in the past [4]. It is noted, however, that the stable types have somewhat more scatter than the meso-stable types. This can be used to provide a separation between the two. The best separation was obtained using the scatter in the prediction of viscosity from density. This is a fit of the equation:

$$\ln \text{visc} = 270 - 235.3 \cdot \exp \text{density} + 51.7 \cdot (\exp \text{density})^2 \tag{3.16}$$

Then taking the fact that the stables are more highly divergent then, the oil will form a stable emulsion if the deviation from Eq. (3.1) is greater than 7.5 %, and meso-stable emulsion otherwise. This results in an error of about 31 % as shown in Table 3.8. The screening is summarized in Table 3.9.

While not excellent, this screening technique does provide a means of separating the stable and meso-stable types using only density and viscosity as inputs.

Table 3.8 Example of model III screening

Oil	Oil Evaporation	Stability	Density	Viscosity	Resins	Asphaltenes	Rules	Entrained	DNF	DNF-heavy	Meso/Stable
	%	visual	(@15C)	mPa·s	%	%					
Belridge heavy	0	Entrained	0.9746	12,610	30	3	Density >0.966	Ent			
Beta	0	Entrained	0.9738	13,380	31	7	Density <1.000	Ent			
Bunker C (1987)	0	Entrained	0.9830	45,030	15	7	Viscosity >2300	Ent			
Bunker C (anchorage)	0	Entrained	0.9891	8706	17	11	Viscosity <200,000	Ent			
California API 11.0	0	Entrained	0.9882	34,000		16		Ent			
California API 15.0	0	Entrained	0.9770	6400	23	22		Ent			
Cold Lake Bitumen	0	Entrained	10.166	82,5000	13	17		Other	Other	Heavy uns	
Heavy fuel oil 6303	0	Entrained	0.9888	22,800	16	13		Ent			
Arabian light [2002]	0	Meso	0.8641	13	6	4	Variation of 7.5% from Regression Equation	Other	Light DNF		Stable
Carpenteria	10.31	Meso	0.9299	755	19	11		Other	Other	Other	Stable
Carpenteria	14.87	Meso	0.9482	3426	22	11		Other	Other	Other	Stable
Dos Cuadras	11.17	Meso	0.9270	187	20	7		Other	Other	Other	Meso

(continued)

Table 3.8 (continued)

Oil	Oil Evaporation	Stability	Density	Viscosity	Resins	Asphaltenes	Rules	Entrained	DNF	DNF-heavy	Meso/Stable
Dos Cuadras	20.3	Meso	0.9359	741	19	9		Other	Other	Other	Meso
Fuel oil #5 (2000)	0	Stable	0.9883	1410	8	8		Other	Other	Other	Stable
Fuel oil #5 (2000)	7.25	Stable	10.032	4530	8	13		Other	Other	Other	Stable
Garden banks 426	37.72	Stable	0.8993	136	10	3		Other	Other	Other	Stable
Hondo	0	Stable	0.9356	735	24	12		Other	Other	Other	Stable
Hondo	16.67	Stable	0.9674	9583	29	12		Other	Other	Other	Meso
Mississippi canyon 72	26.15	Stable	0.9095	195	11	3		Ent	Other	Other	Stable
Mississippi canyon 807	16.44	Stable	0.9375	491	13	7		Other	Other	Other	Meso
Mississippi canyon 807	25.51	Stable	0.9582	3454	18	8		Other	Other	Other	Meso
Neptune spar (viosca knoll 826)	ε22.62	Stable	0.8986	187	8	2		Other	Other	Other	Stable
Platform gail (sockeye)	0	Stable	0.9297	406	21	12		Other	Other	Other	Meso

Table 3.8 (continued)

Oil	Oil Evaporation	Stability	Density	Viscosity	Resins	Asphalteness	Rules	Entrained	DNF	DNF-heavy	Meso/Stable
Platform gail (sockeye)	7.34	Stable	0.9489	1450	21	13		Other	Other	Other	Meso
Platform gail (sockeye)	13.33	Stable	0.9645	7092	25	15		Ent	Other	Other	Meso
Point arguello comingled	0	Stable	0.9248	533	23	16		Other	Other	Other	Stable
Point arguello comingled	9.05	Stable	0.9528	4988	19	17		Other	Other	Other	Stable
Point arguello heavy	0	Stable	0.9447	3250	17	19		Other	Other	Other	Stable
Point arguello light	0	Stable	0.8739	22	9	7		Other	Light DNF		
Point arguello light	10.19	Stable	0.8979	76	9	8	Density <9.6	Other	Other	Other	Stable
Aviation gasoline 100LL	0	Unstable	0.7143	1				Other	Light DNF		

(continued)

Table 3.8 (continued)

Oil	Oil Evaporation	Stability	Density	Viscosity	Resins	Asphalteness	Rules	Entrained	DNF	DNF-heavy	Meso/Stable
Scotian light	0	Unstable	0.7655	1	1	0	Viscosity <50	Other	Light DNF		
Thevenard island	0	Unstable	0.7855	1	2	0	Asphalt <l	Other	Light DNF		
Barrow Island	0	Unstable	0.8410	2	4	0		Other	Light DNF		
Diesel (anchorage)	0	Unstable	0.8300	2	1	0		Other	Light DNF		
Jet Al	0	Unstable	0.8159	2	0	0		Other	Light DNF		
Jet Al	12.03	Unstable	0.8193	2	0	0		Other	Light DNF		
Jet Al	23.21	Unstable	0.8216	2	1	0		Other	Light DNF		
Jet Al	37.14	Unstable	0.8244	2	0	0		Other	Light DNF		
Jet Fuel (Anchorage)	0	Unstable	0.8111	2	0	0		Other	Light DNF		
IFO - 300	5.33	Unstable	0.9996	22,0000	30	17	Density >0.84	Other	Other	Heavy uns	
Hondo	32.29	Unstable	0.9881	44,9700	32	13	Viscosity >200,000	Other	Other	Heavy uns	

Table 3.9 Screening criteria

Water-in-oil type	Starting oil properties				Error % in test set
	Minimum density	Maximum density	Minimum viscosity	Maximum viscosity	
Entrained	0.966	1	2300	200,000	1
Did not form—light		0.966		50	3.2
Did not form—heavy			200,000		0.5
Mesostable	Use exp density/ln viscosity equation to predict				31.3
	ln viscosity	$\mathbf{ln\ visc = 270 - 235.3 \cdot exp\ density + 511.7 \cdot (exp\ density)^2}$			
	If deviation of ln viscosity $< 7.5\,\%$ then it is 'mesostable'				31.3
Stable	If deviation of ln viscosity $> 7.5\,\%$ then it is 'stable'				As above

3.6 Development of an Emulsion Kinetics Estimator

The kinetics of emulsion formation have been studied and data are available to compute the time to formation, see [4]. This study has shown the times to formation for stable emulsions is particular rapid and that of entrainment is also rapid—both in a matter of minutes. The past study yielded data in terms of relative formation time and energy (rpm) of the mixing apparatus. Further studies were performed in a larger test tank.

3.7 Model Certainty

A comparison of the models is presented in Table 3.10. This shows that Model II provides the greatest accuracy and that the difficulty particularly lies with predicting stable and meso-stable types. Several observations can be made about modelling water-in-oil type formation:

(a) Unstable types or those oil that do not form any of the other three types, generally consist of three widely separate classes of oils or fuels, very light oils such as the fuels which have little or no resins or asphaltenes; those very heavy oils which are so viscous that they will not uptake water; and those oils that have the incorrect ratio or amounts of resins or asphaltenes. It is difficult to mathematically incorporate all three of these variances into one grouping.
(b) Some of the oils may be able to form different water-in-oil types, but emulsion inhibitors or asphaltene suspenders have been added to the products. These types of oils make prediction very difficult and

Table 3.10 Comparison of models

Point	Model I	Model II	Model III	Total numbers of data points
R^2 correlation coefficient	0.46	0.69		
Number of parameters	14	15	5 screens	
Number of Gaussian sets	4	2		
Errors on stable emulsions	40 %	5 %	54 %	42
Errors on mesostable emulsions	63 %	26 %	53 %	43
Errors on entrained type	10 %	5 %	9 %	41
Errors on all types	35 %	12 %	43 %	126
Advantages	Low coefficients	Accurate, simpler math	Very simple	
Disadvantages	Lower accuracy	High coefficients	Lower accuracy	

(c) There are many different asphaltenes some of which make much more stable emulsions than others. Recent work has shown that there are hundreds of asphaltene sub-components varying very much in composition and molecular size. Thus the percent of asphaltenes (or resins) certainly does not tell the whole story about the emulsion-stabilizers.

3.8 Conclusions

Water-in-oil emulsions are formed as a result of asphaltene and resin surfactant characteristics in oil of moderate viscosity (50–2000 mPa s). Four types of water-in-oil products are formed: stable and meso-stable emulsions, entrained water in oil and unstable (or those that do not form any of the other three types). Each of these types has unique characteristics and are thought to be non-convertible to other types once formed.

The knowledge that water-in-oil types exist and that a new scheme to classify their stability enables the development of new and much more accurate emulsion formation models. The density, viscosity, asphaltene and resin contents are used to develop a regression equation to stability, which in turn predicts either an unstable or entrained water-in-oil state or a meso-stable or stable emulsion. The new models can

provide accurate prediction of class about 90 % of the time. A major inaccuracy lies with the unstable types and these because of the fact that there are three distinct types of oils or fuels in this class, each very different, and because of the possible presence of emulsion breakers or asphaltene suspenders in the oils. The greatest difficulty however is separating meso-stable and stable types.

References

1. Berridge, S.A., Dean, R.A., Fallows, R.G., Fish, A.: The properties of persistent oils at sea. J. Inst. Pet. **54**, 300–309 (1968)
2. Fingas, M., Fieldhouse, B.: Studies on water-in-oil products from crude oils and petroleum products. Mar. Pollut. Bull. **64**, 272–283 (2011)
3. Fingas, M., Fieldhouse, B.: Studies on crude oil and petroleum product emulsions: water resolution and rheology. Colloid. Surf. A **333**, 67–81 (2009)
4. Fingas, M.: Models for water-in-oil emulsion formation (Chapter 10). Oil Spill Science and Technology, pp. 243–273. Elsevier, New York (2011)
5. Groenzin, H., Mullins, O.C.: Asphaltene molecular size and weight by time-resolved fluorescence depolarization. In: Mullins, O.C., Sheu, E.Y., Hammami, A., Marshall, A.G. (eds.) Asphaltenes, Heavy Oils and Petroleomics, pp. 17–40. Springer, New York (2007)
6. Gu, G., Xu, Z., Nandakumar, K., Masliyah, J.H.: Influence of water-soluble and water-insoluble natural surface active components on the stability of water-in-toluene-diluted bitumen emulsion. Fuel **81**, 1859–1869 (2002)
7. NAS, Oil in the Sea III, Inputs, Fates and Effects, National Research Council, National Academies Press, Washington (2003)
8. Oakdale Engineering: DataFit. http://www.oakdaleengr.com/datafit.htm
9. Silset, A., Hannisdal, A. Hemmingsen, P., Sjöblom, J.: Emulsions of heavy crude oils. II. Viscous responses and their influence on emulsion stability measurements. J. Disp. Sci. Technol. 1432–1445 (2010)
10. Sjöblom, J., Hemmingsen, P.V., Kallevik, H.: The role of asphaltenes in stabilizing water-in-crude oil emulsions. In: Mullins, O.C., Sheu, E.Y. Hammami, A., Marshall, A.G.: (eds) Asphaltenes, Heavy Oils and Petroleomics, pp. 549–608. Springer, New York (2007)
11. Systat Software Inc.: TableCurve 2D. http://www.sigmaplot.com/products/tablecurve2d/

Chapter 4
Equilibrium Theory of Bidensity Particle-Laden Flows on an Incline

Sungyon Lee, Jeffrey Wong and Andrea L. Bertozzi

Abstract The behaviour of inhomogeneous suspensions in a viscous oil is relevant in the context of oil spill and other oil-related disasters which may lead to the unwanted mixture of sand grains and oil. This warrants the fundamental study of the dynamics of solid particles in a thin film of viscous fluid. Specifically, sheared concentrated suspensions in a viscous fluid are subject to a diffusive mechanism called shear-induced migration that consists of "drift diffusion" and "self or tracer diffusion". Drift diffusion causes particles to move from high to low concentrations, while tracer diffusion dictates mixing between particles of the same size. The latter mechanism becomes important in polydisperse slurries. In this chapter, we incorporate the effects of shear-induced migration and sedimentation to develop a model for the gravity-driven thin film of bidensity suspensions. We use this mathematical model to validate recent experimental results.

4.1 Introduction

Particle-laden flows are ubiquitous in nature and in industrial applications; however, the nonlinear coupling between particles and fluid motion presents challenges in the development of mathematical models. In the case of monodisperse slurries, there have been advances both in experiments and modelling based on diffusive flux phenomenology [12] and, more recently, suspension balance approach [17]. In particular, [12] developed a diffusive model to justify the behaviour of sheared monodisperse

S. Lee (✉)
Departmant of Mechanical Engineering, Texas A&M,
College Station, TX 77843, USA
e-mail: sungyon.lee@tamu.edu

J. Wong · A.L. Bertozzi
Department of Mathematics and Applied Mathematics Laboratory,
University of California, Los Angeles, CA 90095, USA
e-mail: jtwong@math.ucla.edu

A.L. Bertozzi
e-mail: bertozzi@math.ucla.edu

M. Ehrhardt (ed.), *Mathematical Modelling and Numerical Simulation of Oil Pollution Problems*, The Reacting Atmosphere 2, DOI 10.1007/978-3-319-16459-5_4

suspensions in a Couette device [6]. In the presence of shear, particles undergo a random walk that results in no net displacement. This source of diffusive flux is called "shear-induced self or tracer diffusion" [12, 13]. In the case of non-uniform concentrations in shear, particles tend to drift from regions of high to low particle concentrations due to particle collisions, which is referred to as "drift diffusion" [13]. While effective shear diffusivity consists of both drift diffusion and aforementioned tracer-diffusion, drift diffusion dominates in the case of concentrated monodisperse suspensions.

While both diffusive flux models and suspension balance models have been successful in capturing the particle migration behaviour under shear, they differ substantially in their derivation of particle flux. The diffusive flux phenomenology consists of semi-empirical laws that describe particle migration based on irreversible particle collisions and does not account for the non-Newtonian viscosity of the particle-fluid mixture. The suspension balance approach, on the other hand, relies on the non-Newtonian normal stresses induced by shear, which give rise to the particle migration. Therefore, viscously generated normal stresses are crucial in the suspension balance approach. In particular, the anistropic normal stresses have been shown to be important in predicting correct secondary flows in a pressure-driven tube flow [20]. Thus, the neglect of normal stress differences in the diffusive flux model is problematic especially in the non-dilute concentration limit, as Couturier and co-authors [3] experimentally demonstrated the significance of normal stress differences for the volume fraction greater than 0.17.

Despite the apparent limitations, the diffusive flux approach is "contained" within the suspension balance model and can yield the same set of equations in the unidirectional, fully-developed flows [17]. For instance, Timberlake and Morris [24] experimentally and theoretically studied the gravity-driven, free-surface flow containing neutrally buoyant particles. They observed the deformation of the free surface and particle migration, which sufficiently matched their mathematical model. Although their model was based on the suspension balance approach, the resultant equations for the flux of particles were essentially identical to those derived based on diffusive flux approach of [16]. More recently, [21] observed the accumulation and depletion of the particles on the advancing meniscus and found that, based on the suspension balance model, this depended on the balance between gravitational flux and shear-induced migration. This particular result corresponds exactly to the findings of [15] who identified different particle regimes at varying inclination angles and particle volume fractions based on the diffusive flux approach, further demonstrating the validity of the simpler diffusive flux model in primarily unidirectional flows.

Contrary to the monodisperse case, tracer diffusion becomes important in polydisperse suspensions. Reference [25] investigated the resuspension of heavy particles in a Couette device, with the addition of neutrally buoyant particles of the equal size. At a given shear rate, they found that an increasing concentration of neutrally buoyant particles caused the heavy particles to rise higher to mix with neutrally buoyant ones on the free surface. Based on diffusive flux phenomenology, Tripathi and Acrivos derived a continuum model to match the experimental observations and found that the tendency of particle species to mix is attributed to tracer diffusivity.

In the current work, we extend the equilibrium model of [15] to thin free surface flows of bidensity suspensions. This equilibrium theory is a crucial component of the dynamic problem, since the leading order dynamic equations have shock solutions whose structure is determined by the equilibrium profiles [14, 26]. This warrants a careful study of the equilibrium problem before proceeding to the dynamic case, analogous to the work of [16]. Distinct from the monodisperse case, tracer diffusivity is included in the bidensity model and compared to recent experimental results by [9]. This work provides an important theoretical framework for segregating particles of different densities, which has industrial applications.

This chapter is organized as follows. In Sect. 4.2, we introduce the governing equations for bidensity suspensions and develop the equilibrium model by applying lubrication approximations. In Sect. 4.3, we obtain the solution to the equilibrium model for varying parameters to validate previous experimental results. The chapter concludes with the summary of results and discussion of future directions in Sect. 4.4.

4.2 Problem Formulation

We consider the dynamics of a bidensity slurry flowing down an incline, in which the mixture consists of a viscous fluid with density ρ_l and viscosity μ_l and two species of negatively buoyant particles (See Fig. 4.1). The two particle types have uniform diameter d but variant densities, ρ_1 and ρ_2, such that $\rho_2 > \rho_1 > \rho_l$. The local volume fractions of each species are denoted as ϕ_1 and ϕ_2, respectively, while $\phi = \phi_1 + \phi_2$ is the total volume fraction. By assuming a sufficiently small particle size, the particle-fluid mixture is modelled as a continuum and is governed by the following momentum equations:

$$\rho\left(\partial_t \mathbf{u} + \mathbf{u}\cdot\nabla\mathbf{u}\right) = \nabla\cdot\left(-p\mathbf{I} + \mu(\nabla\mathbf{u} + \nabla\mathbf{u}^\top)\right) + \rho\mathbf{g}, \tag{4.1}$$

where $\mathbf{u}$ and p are the velocity vector and pressure, respectively, and $\mathbf{g}$ denotes the gravitational acceleration vector. As in [15, 16], the mixture density, ρ, is given by $\rho = \rho_1\phi_1 + \rho_2\phi_2 + \rho_l(1-\phi)$, while effective viscosity $\mu = \mu_l\,(1-\phi/\phi_\mathrm{m})^{-2}$, where ϕ_m is the maximum volume fraction. In addition to momentum, we have mass conservation of the mixture:

$$\partial_t\rho + \nabla\cdot(\rho\mathbf{u}) = 0. \tag{4.2}$$

The velocity satisfies the no-slip condition ($\mathbf{u} = 0$) on the bottom of the channel, while the stresses vanish both in normal and tangential directions on the free surface: $\mathbf{n}\cdot\left(-p\mathbf{I} + \mu(\nabla\mathbf{u} + \nabla\mathbf{u}^\top)\right) = 0$. The free surface also satisfies the kinematic boundary condition, $\mathbf{n}\cdot\mathbf{u} = 0$.

The conservation equation for particles is given by

$$\partial_t \phi + \mathbf{u} \cdot \nabla \phi + \nabla \cdot \mathbf{J} = 0, \tag{4.3}$$

which accounts for the advection of particles due to flow ($\mathbf{u} \cdot \nabla \phi$) and particle diffusion ($\nabla \cdot \mathbf{J}$), where $\mathbf{J}$ is the particle flux vector that is semi-empirically constructed [13, 19]. For particle-laden flows down an incline, effects of gravity and shear flow govern the particle dynamics inside the thin film, leading to *sedimentation* [4] and *shear-induced migration* [13, 19] of particles that opposes settling. The expressions for $\mathbf{J}$ that account for these competing effects have been derived and experimentally validated for the monodisperse case [2, 15, 16]. For a bidensity slurry in the same geometry, the same physical effects of gravity and shear are present, with added complexities due to the presence of two particle species. By combining previous works [7, 15, 16, 25] and recent experimental results [10], we construct a new particle flux vector $\mathbf{J}$ that accounts for the mixing and sedimentation of two particle species at varying rates.

Based on the formulation by [22, 25], the flux of the ith particle species due to sedimentation corresponds to

$$\mathbf{J}_{\mathrm{grav},i} = \frac{\mathbf{g} d^2 \phi_i}{18 \mu_l} \left[M_0 (\rho_i - \rho_l) + M_I \sum_{j=1}^{2} (\rho_j - \rho_l) \frac{\phi_j}{\phi} \right], \tag{4.4}$$

where $i = 1, 2$. The first term in Eq. (4.4) refers to the self-mobility of particles, $M_0 \sim 1 - \phi/\phi_\mathrm{m}$ [25]. The second contribution to sedimentation comes from interaction mobility, $M_I \sim f(\phi) - M_0$, where the hindrance function $f(\phi) = \mu_l (1 - \phi)/\mu(\phi)$ [13, 15, 16]. The total flux due to sedimentation, $\mathbf{J}_\mathrm{grav}$, is given by $\mathbf{J}_\mathrm{grav} = \mathbf{J}_{\mathrm{grav},1} + \mathbf{J}_{\mathrm{grav},2}$.

As well as settling due to gravity, particles are subject to shear flow inside the thin film and undergo two types of shear-induced diffusion processes [11, 13]. The first type—shear-induced "drift" diffusion—refers to the net drift of particles from the regions of high to low total particle concentration and also from high to low shear stress [12, 19]. In the thin free-surface flows, this diffusive mechanism causes particles to aggregate near the free surface where shear stress vanishes [2, 15, 16]. Since drift diffusion does not distinguish between particle types of equal size, we use the empirical model for particle flux, $\mathbf{J}_\mathrm{drift}$, as used in [2, 15, 16]:

$$\mathbf{J}_\mathrm{drift} = -\frac{d^2 \phi}{4} \left[K_c \nabla (\dot{\gamma} \phi) - K_v \frac{\phi \dot{\gamma}}{\mu(\phi)} \frac{d\mu}{d\phi} \nabla \phi \right], \tag{4.5}$$

where K_c and K_v are empirically determined constants, and $\dot{\gamma} = \frac{1}{4} \| \nabla \mathbf{u} + \nabla \mathbf{u}^\top \|$ is the shear rate. The corresponding flux for each species is $\mathbf{J}_{\mathrm{drift},i} = \mathbf{J}_\mathrm{drift} \phi_i / \phi$.

The second type of shear-induced diffusion is known as shear-induced "tracer"- (or self-) diffusion [1, 5, 7, 13, 23, 25]. Distinct from drift diffusion, it refers to the

random motion of particles in shear that occurs even in the absence of concentration gradient and leads to zero net drift of particles. While tracer diffusion does not affect ϕ, it governs how one particle species mixes with the other in bidensity suspensions, resulting in the flux of individual species:

$$\mathbf{J}_{\text{tracer},i} = -\frac{\dot{\gamma} d^2}{4} D_{\text{tr}}(\phi)\phi \nabla \left(\frac{\phi_i}{\phi}\right), \tag{4.6}$$

where $D_{\text{tr}}(\phi)$ is the tracer diffusivity and dictates the extent of mixing in our model. In the limit of dilute suspensions, [11, 13] proposed the empirical expression $D_{\text{tr}} = \phi^2/2$. For large concentrations, numerical simulations and experiments [23] suggest that the tracer diffusivity becomes constant beyond a value $\phi_{\text{tr}} \approx 0.4$. Therefore, we use the expression: $D_{\text{tr}}(\phi) = \frac{1}{2}\min\{\phi^2, \phi_{\text{tr}}^2\}$.

Combining Eqs. (4.4)–(4.6) yields the total flux of the ith species, $\mathbf{J}_i$,

$$\mathbf{J}_i = \mathbf{J}_{\text{grav},i} + \frac{\phi_i}{\phi}\mathbf{J}_{\text{drift}} + \mathbf{J}_{\text{tracer},i}, \tag{4.7}$$

and the total flux $\mathbf{J}$ of both species simply corresponds to $\mathbf{J} = \mathbf{J}_{\text{grav}} + \mathbf{J}_{\text{drift}}$. Notably, tracer diffusion drops out of the total particle flux (i.e. $\mathbf{J}_{\text{tracer},1} + \mathbf{J}_{\text{tracer},2} = 0$), justifying its neglect in modelling monodisperse slurries [2, 15, 16, 19]. In addition, Brownian diffusion is not included in particle fluxes by assuming a large Péclet number, or $\text{Pe} = \dot{\gamma} d^2/D \gg 1$, where D is the solvent diffusivity.

4.2.1 Thin Film Approximations and Equilibrium Theory

A thin film geometry [18] gives us the following dimensionless variables:

$$(\widehat{x}, \widehat{z}) = \frac{1}{H}(\delta x, z), \quad \widehat{\mathbf{u}} = \frac{1}{U_0}\left(u, \frac{w}{\delta}\right), \quad \widehat{\mathbf{J}} = \frac{H^2}{d^2 U_0}\left(\frac{J_x}{\delta}, J_z\right),$$
$$\widehat{p} = \frac{H}{\mu_l U_0} p, \quad \widehat{\mu} = \frac{\mu}{\mu_l}, \quad \widehat{\rho}_{s,i} = \frac{\rho_i - \rho_l}{\rho_l},$$

where H and L are the characteristic film thickness and axial length scale, respectively, and $U_0 = H^2 g \sin\alpha/\nu_l$. Hats denoting the dimensionless quantities will be subsequently dropped for brevity. In the thin film limit of $\delta \equiv H/L \ll 1$, the momentum equation in the axial direction reduces to

$$\sigma' = -(1 + \rho_{s,1}\phi_1 + \rho_{s,2}\phi_2), \tag{4.8}$$

where $\sigma = \mu(\phi)\partial u/\partial z$ is the dimensionless shear stress, and the prime denotes the derivative with respect to z. In addition, we assume $\delta \ll (d/H)^2 \ll 1$, which

reduces Eq. (4.3) to $J_z' = 0$ at leading order. This scaling indicates that particles must rapidly equilibrate in the the z-direction [16]. Integrating $J_z' = 0$ with respect to z and applying $J_z(z = 0) = 0$ yields $J_z = 0$, or

$$0 = \phi\sigma' + \sigma\phi'\left[1 + c_1\frac{\phi}{\phi_\mathrm{m} - \phi}\right] + c_0(1-\phi)\left[\rho_{s,1}X + \rho_{s,2}(1-X)\right], \tag{4.9}$$

where $X \equiv \phi_1/\phi$, while $c_0 \equiv 2\cot\alpha/(9K_c)$ and $c_1 \equiv 2(K_v - K_c)/K_c$ are constants. As expected, Eq. (4.9) exactly matches the monodisperse model of [15, 16], when X is set to 0 (i.e. $\phi_1 = 0$) or 1 (i.e. $\phi_2 = 0$). For equilibrium inside the thin film, we also require zero net flux of each particle species in the z-direction, $J_{z,i} = 0$, and set $J_{z,1}\phi_2 - J_{z,2}\phi_1 = 0$, which leads to

$$X' = c_2\frac{X(1-X)}{\sigma D_\mathrm{tr}}\left(\frac{\phi_\mathrm{m}}{\phi_\mathrm{m} - \phi}\right), \tag{4.10}$$

where $c_2 = 2(\rho_{s,2} - \rho_{s,1})\cot\alpha/9$.

The Eqs. (4.8)–(4.10) form a system of ODEs for the unknowns: ϕ, X and σ. Following [16], we define the scaled height $s = z/h$, where h is the dimensionless film thickness, so that $\widetilde{\phi}(s) = \phi(hs)$, $\widetilde{X}(s) = X(hs)$, and $\widetilde{\sigma}(s) = \sigma(hs)/h$; tildes are subsequently dropped from the text. In addition, the average particle concentration ϕ_0 and proportion of lighter particles X_0 correspond to:

$$\phi_0 = \int_0^1 \phi(s)\mathrm{d}s, \qquad X_0 = \frac{1}{\phi_0}\int_0^1 X(s)\phi(s)\mathrm{d}s. \tag{4.11}$$

For given ϕ_0 and X_0 with $0 \le \phi_0 < \phi_\mathrm{m}$, the system has a unique solution for $s \in [0, 1]$. Solutions in Sect. 4.3 are computed via shooting in MATLAB, with an inclination angle fixed at $\alpha = 30°$ unless otherwise noted.

4.3 Results

We begin by briefly reviewing the monodisperse theory described by [15]. For the monodisperse system which consists of (4.9) and (4.8) with $X = 0$ or 1, there is a critical particle concentration ϕ_c such that $\phi(s)$ is monotone increasing (i.e. $\phi' > 0$) when $\phi_0 > \phi_c$ and monotone decreasing (i.e. $\phi' < 0$) when $\phi_0 < \phi_c$. The constant solution $\phi = \phi_c$ separating the two regimes is an unstable equilibrium. This bifurcation is illustrated in Fig. 4.2. In [15], the two regimes are referred to as 'ridged' and 'settled', respectively. Physically, ridged solutions describe aggregation of particles at the fluid surface, while a settled solution describes particles settling to the substrate, which leaves a clear fluid layer above. As there are two particle species to consider here, we denote as $\phi_{c,i}$ the critical concentration for the ith species in the

corresponding monodisperse problem ($X = 1$ for $i = 1$ and $X = 0$ for $i = 2$) and note that $\phi_{c,1} < \phi_{c,2}$ since the second particle is heavier. For $\alpha = 30°$, these values are $\phi_{c,1} = 0.459$ and $\phi_{c,2} = 0.521$ based on [15].

For the bidisperse system, we begin by discussing the structure of $X(s)$ and the mixing behaviour between particle species. As s increases from 0 to 1, $X(s)$ consists of an interval with $X \approx 0$, followed by a transition region centred at $s = s_{\text{tr}}$, such that $X(s_{\text{tr}}) = 1/2$, and finally an interval with $X \approx 1$. The ODE (4.10) can be approximated near s_{tr} as

$$X' \approx C^{-1} X(1 - X), \tag{4.12}$$

which has an explicit solution, $X(s) = 1 - \left(1 + \exp\left(\frac{s_{\text{tr}} - s}{C}\right)\right)^{-1}$. Here C is the constant given by evaluating all other variables at $s = s_{\text{tr}}$:

$$C = \frac{9 \tan\alpha}{2(\rho_{s,2} - \rho_{s,1})} D_{\text{tr}}(\phi(s_{\text{tr}}))\sigma(s_{\text{tr}}) \left(1 - \frac{\phi(s_{\text{tr}})}{\phi_{\text{m}}}\right).$$

In order to quantify the amount of mixing between two particle species, we define the width of the mixing layer, w, to be the interval for which $0.05 < X < 0.95$. Based on the solution to (4.12), we find that $w \approx 5.9C$, valid for $w \ll 1$. Since the value of C primarily depends on $\tan\alpha$, it can be shown that the mixing layer width, w, scales with $\tan\alpha$ (Fig. 4.3, right), and is approximately linear where the solution profiles are insensitive to changes in angle. This suggests that there will be little mixing for small inclination angles. Experimentally, [10] observed the bidensity slurry at low inclination angles to stratify into three layers of heavy particles, light particles, and clear fluid. This results in three distinct fronts flowing down the plane (Fig. 4.1, bottom right). At higher inclination angles they observed a 'ridged' regime with more mixing of particles, consistent with our theoretical predictions (Fig. 4.1, top right).

In order to investigate the bifurcation behaviour of bidensity slurries, we now consider the total concentration $\phi(s)$ and the individual concentrations, $\phi_1(s)$ and $\phi_2(s)$. Analogous to the monodisperse system, we call a solution 'settled' if neither species of particles are present up to the surface (i.e. $\phi = 0$ for some $s \in [0, 1]$), and 'ridged' if particles (of either kind) aggregate at the surface ($\phi \to \phi_{\text{m}}$ as $s \to 1$). Like the monodisperse case, the settled regime (S) corresponds to the case where ϕ is monotone decreasing. Monotonicity of solutions is important for analysis of the dynamic problem, which motivates a careful description of the equilibrium profiles in [26]. For the bidisperse system, ϕ is not necessarily monotonic in the ridged regime, but the individual concentrations ϕ_1 and ϕ_2 undergo similar transitions from decreasing to increasing as in the monodisperse case. Within the ridged regime, there exist critical concentrations ϕ_A, ϕ_B and ϕ_C as functions of X_0, such that the profiles for ϕ, ϕ_1, and ϕ_2 change from decreasing to mixed signs to increasing. This further partitions the ridged regime into three distinct sub-regions (R_A, R_B, and R_C), as summarized in Fig. 4.4. We now discuss each region in greater detail.

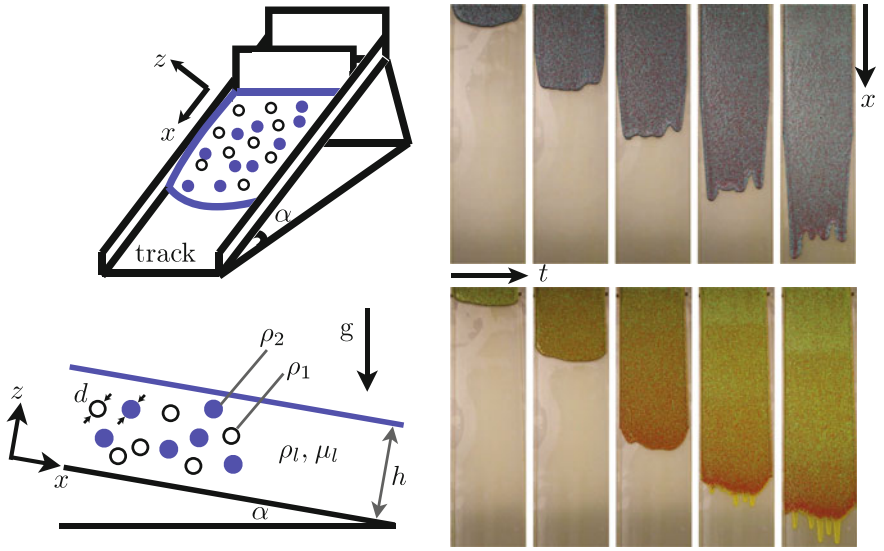

Fig. 4.1 (*top left*) Schematic of the experimental apparatus; (*bottom left*) The thin film of fluid of ρ_l and μ_l that contains two particle species of equal diameter d and variant densities, such that $\rho_2 > \rho_1 > \rho_l$. Two sets of experimental results are shown on the right. In the *bottom right panel*, as time evolves (images from *left* to *right*), clear fingers form on the flow front, indicating that both particle species have settled to the channel walls with a clear fluid layer on top that moves ahead. On the other hand, the particles appear to remain aggregated and well-mixed on the front in the 'ridged' regime, as shown in the *top right panel*

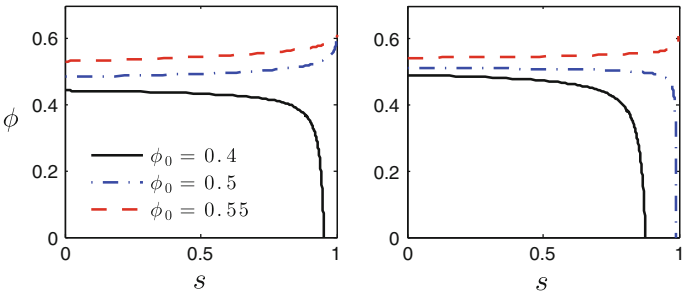

Fig. 4.2 Transition from settled to ridged solutions in ϕ for the monodisperse system, for $X = 1$ (*left*) and $X = 0$ (*right*). The critical concentrations are $\phi_{c,1} = 0.459$ and $\phi_{c,2} = 0.521$

Settled ($0 < \phi_0 < \phi_A$): In the settled regime, the heavy particles settle to the substrate, with a layer of the lighter particles above, and then a clear fluid layer up to the free surface. The upper bound for the settled region, ϕ_A decreases from $\phi_{c,2}$ to $\phi_{c,1}$ as X_0 increases from 0 to 1. If $\phi_0 < \phi_{c,1}$, then the ODE system guarantees that ϕ is monotonically decreasing regardless of X_0.

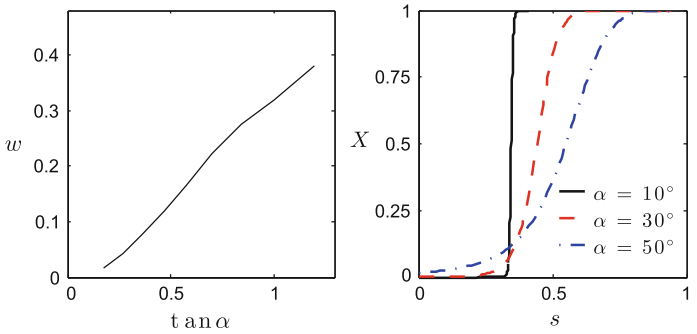

Fig. 4.3 Dependence of the width w of the mixing region (where $0.05 < X < 0.95$) on $\tan\alpha$; the relationship, shown on the *left*, is approximately linear. The *right panel* shows the X profiles for $\alpha = 10, 30, 50°$

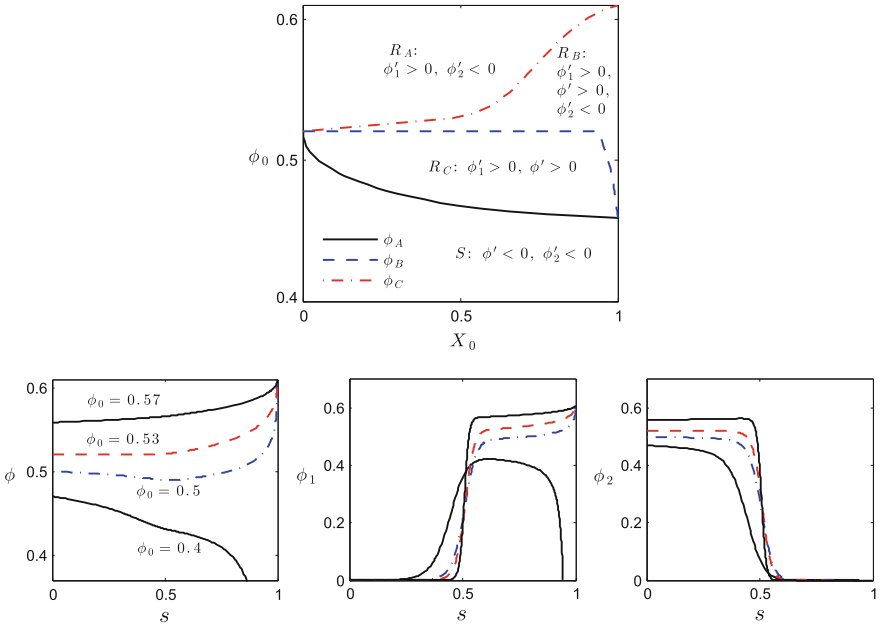

Fig. 4.4 The *left panel* shows a phase diagram of solution regimes determined by total and relative concentrations (X_0, ϕ_0), separated by transition curves ϕ_A, ϕ_B and ϕ_C. Profiles in each region are shown below, for total concentration ϕ (*left*) and for the individual concentrations ϕ_1, ϕ_2

Ridged A ($\phi_A < \phi_0 < \phi_B$): When $\phi_{c,1} < \phi_0 < \phi_{c,2}$, the monodisperse theory suggests that the lighter species ϕ_1 is more likely to aggregate on the free surface ($\phi_1 \to \phi_m$ as $s \to 1$) due to shear-induced migration while ϕ_2 favours settling. Therefore, in this regime, ϕ_1 is monotonically increasing (i.e. $\phi_1' > 0$) with the lighter particles mostly confined to a top region $[s_{tr}, 1]$. The heavier particles settle

so that $\phi_2' < 0$, with negligible but non-zero concentration beyond s_{tr}. Focusing on the top layer $[s_{\text{tr}}, 1]$ where $X \approx 1$, we view this as a perturbed version of the monodisperse bifurcation. As ϕ_0 is increased across ϕ_A, the average concentration of lighter particles in $[s_{\text{tr}}, 1]$ becomes large enough to produce a ridged solution.

Ridged B ($\phi_B < \phi_0 < \phi_C$): If $\phi_0 > \phi_{c,2}$, then ϕ is always monotone increasing ($\phi' < 0$), which defines this second ridged regime, R_B. The heavier particles still settle to the substrate as in the R_A case, so that $\phi_2' < 0$. Note that, in the absence of tracer diffusivity (no mixing layer), $\phi_B = \phi_{c,2}$, unless $X = 1$ exactly, leading to $\phi_B = \phi_{c,1}$. This (discontinuous) ϕ_B closely approximates the actual curve in Fig. 4.4, which curves due to the mixing of particle layers but retains the same endpoints. There are two situations for $\phi_0 < \phi_{c,2}$ in which tracer diffusion can produce a ridged solution. First, if ϕ_0 is very close to $\phi_{c,2}$, then even a small concentration of lighter particles can perturb the otherwise settled solution in the heavier layer so that $\phi' > 0$. Second, if X_0 is close to 1 and $\phi_0 > \phi_{c,1}$, then there is no well-defined settled layer of heavier particles, so the ridged behaviour of the lighter layer ensures that $\phi' > 0$.

Ridged C ($\phi_C < \phi_0 < \phi_{\text{m}}$): For sufficiently large ϕ_0, the average concentration of ϕ_2 near $s = 0$ (where $X \approx 0$) is large enough to produce an initially increasing solution in ϕ_2. Thus, distinct from R_A and R_B, the heavier particles tend to migrate away from the substrate in this last ridged regime. However, the lighter particles displace the heavier particles near the free surface so that $\phi_2 \to 0$. Hence ϕ_2 is still not monotone increasing—it eventually decreases sharply to nearly zero around s_{tr}.

4.4 Conclusions

The same pattern of transitions is also observed for fixed ϕ_0 with varying X_0 and α, both experimentally and theoretically. As with increasing ϕ_0, an increase in α has the effect of altering the balance of fluxes to favour shear-induced migration, in this case by reducing the normal component of gravity [15]. The previous discussion applies to the (X_0, α) plane as well, and, in particular, there is a critical $\alpha_A(X_0)$, analogous to $\phi_A(X_0)$, separating settled and ridged solutions. The predicted bifurcation is shown in Fig. 4.5 along with experimental results [10] identifying settled or ridged behaviour. Experiments to date have not measured the particle concentrations inside the thin film and thus do not distinguish between different theoretically predicted types of ridged behaviour. Overall, the current theory captures the bifurcation curve obtained experimentally, although the critical angles predicted by the model are greater than what is measured in the experiment by about five degrees. This discrepancy can be attributed primarily to the value of the empirical parameter K_c. While we based the value of K_c on [15, 16], the types of beads used in [10] differ slightly in size and texture from the previous experiments and warrant further experiments to better estimate K_c.

In this chapter, we derive a diffusive model of bidensity suspensions flowing down an incline and use it to describe the normal equilibrium of the suspensions inside the thin film. The mixture consists of the viscous fluid of density, ρ_l, and two negatively

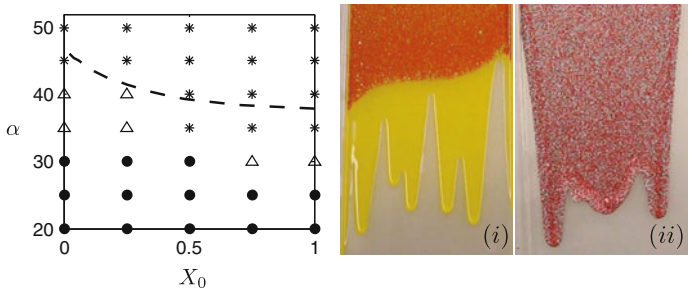

Fig. 4.5 (*Left*) Bifurcation $\alpha_A(X_0)$ (*dashed line*) between settled and ridged regimes for fixed $\phi_0 = 0.4$ with varying α and X_0. The symbols indicate experimental results identified as ridged (*star*) or settled (*circle*). The *triangles* mark results for which the particles did not equilibrate in the duration of the experiment. (*Right*) Photographs of the experiment in the settled and ridged regimes are shown on the *right* for experimental parameters, (i) $\alpha = 20°$, $X_0 = 0.5$ and (ii) $\alpha = 50°$, $X_0 = 0.5$

buoyant particle species of the equal diameter, d, and variant densities, such that $\rho_2 > \rho_1 > \rho_l$. In the monodisperse case of the same geometry, heavy particles in the viscous fluid were shown to either settle rapidly to the channel walls ('settled' regime) or collect on the free surface ('ridged'), depending on the channel inclination angle and the total volume fraction. This bifurcation behaviour was explained by [2, 15, 16] by balancing particle fluxes due to sedimentation and drift diffusion. The analogous bifurcation behaviour was observed in bidensity suspensions experimentally by [10] and is explained by our current equilibrium model.

Notably, additional complexities arise due to the presence of a second particle species. For instance, the ridged regime in the bidensity suspensions now consists of three sub-regimes (R_A, R_B, and R_C) that display different profiles of ϕ_1 and ϕ_2, depending on the relative particle volume fraction, X_0. It would be interesting to explore the sub-regimes in future experiments, which would require new experimental techniques to measure the volume concentration of different particle species through the layer. In addition, the mixing behaviour between particle species is investigated by incorporating tracer diffusion in our model. This mixing effect is shown to depend on the inclination angle, such that lower angles lead to less mixing. This behaviour has been observed experimentally in [10] where they found the bidensity mixture to stratify into separate layers forming three distinct fronts at smaller inclination angles. Therefore, our equilibrium model and experimental observations suggest that particle segregation is more pronounced in the 'settled' regime, while particles remain well-mixed in the 'ridged' regime.

Particle segregation is fundamentally important in oil refinement, waste-water treatment, and mineral processing via a spiral separator. However, these applications lack quantitative models that are important for predictive design. Recently, [8, 9] demonstrated that the equilibrium model for monodisperse slurries on an incline is valid in spiral geometries to leading order and derived a simple steady state model. We believe the present model could lead to a valid equilibrium theory for more

general polydisperse slurry segregation models in helical domains. Furthermore, such equilibrium models are the building blocks for the development of implicit flux functions for dynamic transport models [14, 16, 26]. The current bidensity theory may lead to new dynamic models that could predict multilayer stratified flows as observed in [10].

Acknowledgments This work is supported by NSF grants DMS-1312543 and DMS-1048840 and UC Lab Fees Research Grant 09-LR-04-116741-BERA.

References

1. Breedveld, V., van den Ende, D., Tripathi, A., Acrivos, A.: The measurement of the shear-induced particle and fluid tracer diffusivities in concentrated suspensions by a novel method. J. Fluid Mech. **375**, 297–318 (1998)
2. Cook, B.P.: Theory for particle settling and shear-induced migration in thin-film liquid flow. Phys. Rev. E **78**, 045303 (2008)
3. Couturier, É., Boyer, F., Pouliquen, O., Guazzelli, É.: Suspensions in a tilted trough: second normal stress difference. J. Fluid Mech. **686**, 26–39 (2011)
4. Davis, R.H., Acrivos, A.: Sedimentation of noncolloidal particles at low Reynolds numbers. Annu. Rev. Fluid Mech. **17**, 91 (1985)
5. Eckstein, E.C., Bailey, D., Shapiro, A.H.: Self-diffusion of particles in shear flow of a suspension. J. Fluid Mech. **79**, 191–208 (1977)
6. Gadala-Maria, F., Acrivos, A.: Shear induced structure in a concentrated suspension of solid spheres. J. Rheol. **24**(6), 799–814 (1980)
7. Krishnan, G.P., Beimfohr, S., Leighton, D.T.: Shear-induced radial segregation in bidisperse suspensions. J. Fluid Mech. **321**, 371–393 (1996)
8. Lee, S., Stokes, Y.M., Bertozzi, A.L.: A model for particle laden flow in a spiral concentrator. In: 23rd International Congress of Theoretical and Applied Mechanics (ICTAM) Procedia IUTAM (2012)
9. Lee, S., Stokes, Y.M., Bertozzi, A.L.: Behavior of a particle-laden flow in a spiral channel. Phys. Fluids **26**, 043302 (2014)
10. Lee, S., Mavromoustaki, A., Urdaneta, G., Huang, K., Bertozzi, A.L.: Experimental investigation of bidensity slurries on an incline. Granul. Matter **16**(2), 269–274 (2014)
11. Leighton, D., Acrivos, A.: Viscous resuspension. Chem. Eng. Sci. **41**, 1377–1384 (1986)
12. Leighton, D., Acrivos, A.: Shear-induced migration of particles in concentrated suspensions. J. Fluid Mech. **181**, 415 (1987)
13. Leighton, D., Acrivos, A.: Measurement of shear-induced self-diffusion in concentrated suspensions of spheres. J. Fluid Mech. **177**, 109–131 (1987)
14. Mavromoustaki, A., Bertozzi, A.L.: Hyperbolic systems of conservation laws in gravity-driven, particle-laden thin-film flows. J. Eng. Math. **88**, 29–48 (2014)
15. Murisic, N., Ho, J., Hu, V., Latterman, P., Koch, T., Lin, K., Mata, M., Bertozzi, A.L.: Particle-laden viscous thin-film flows on an incline: experiments compared with an equilibrium theory based on shear-induced migration and particle settling. Physica D **240**, 1661–1673 (2011)
16. Murisic, N., Pausader, B., Peschka, D., Bertozzi, A.L.: Dynamics of particle settling and resuspension in viscous liquid films. J. Fluid Mech. **717**, 203–231 (2013)
17. Nott, P.R., Brady, J.F.: Pressure-driven flow of suspensions: simulation and theory. J. Fluid Mech. **275**, 157–199 (1994)
18. Oron, A., Davis, S.H., Bankoff, S.G.: Long-scale evolution of thin liquid films. Rev. Mod. Phys. **69**, 931 (1997)

19. Phillips, R.J., Armstrong, R.C., Brown, R.A., Graham, A.L., Abbott, J.R.: A constitutive equation for concentrated suspensions that accounts for shear-induced particle migration. Phys. Fluids **4**, 30–40 (1992)
20. Ramachandran, A., Leighton, D.T.: Viscous resuspension in a tube: the impact of secondary flows resulting from second normal stress differences. Phys. Fluids **19**(5), 053301 (2007)
21. Ramachandran, A., Leighton, D.T.: The effect of gravity on the meniscus accumulation phenomenon in a tube. J. Rheol. **51**, 1073–1098 (2007)
22. Revay, J.M., Higdon, J.J.L.: Numerical simulation of polydisperse sedimentation: equal-sized spheres. J. Fluid Mech. **243**, 15–32 (1992)
23. Sierou, A., Brady, J.F.: Shear-induced self-diffusion in non-colloidal suspensions. J. Fluid Mech. **506**, 285–314 (2004)
24. Timberlake, B.D., Morris, J.F.: Particle migration and free-surface topography in inclined plane flow of a suspension. J. Fluid Mech. **538**, 309–341 (2005)
25. Tripathi, A., Acrivos, A.: Viscous resuspension in a bidensity suspension. Int. J. Multiph. Flow **25**(1), 1–14 (1999)
26. Wang, L., Bertozzi, A.L.: Shock solutions for high concentration particle-laden thin films. SIAM J. Appl. Math. **74**, 322–344 (2014)

Chapter 5
Operational Oil Spill Modelling: From Science to Engineering Applications in the Presence of Uncertainty

Ben R. Hodges, Alejandro Orfila, Juan M. Sayol and Xianlong Hou

Abstract Quantifying uncertainties in real-time operational oil spill forecasts remains an outstanding problem, but one that should be solvable with present science and technology. Uncertainties arise from the salient characteristics of oil spill models, hydrodynamic models, and wind forecast systems, which are affected by choices of modelling parameters. Presented and discussed are: (1) a systems-level approach for producing a range of oil spill forecasts, (2) a methodology for integrating probability estimates within oil spill models, and (3) a multi-model system for updating forecasts. These technologies provide the next steps for the efficient operational modelling required for real-time mitigation and crisis management for oil spills at sea.

5.1 Introduction

Modelling of oil spills on the water's surface has reached an important milestone. We believe the next major advance for improving operational oil spill forecasts is by addressing the accumulation of uncertainty in the wind, wave, and current models. In this chapter, we propose modelling approaches for real-time evaluation of uncertainty in oil spill trajectory models and explore the underlying sources and analyses methods for uncertainty. Our objective is to stimulate development of quantitative model

B.R. Hodges (✉) · X. Hou
Department of Civil, Architectural, and Environmental Engineering,
University of Texas at Austin, Austin, USA
e-mail: hodges@utexas.edu

X.Hou
e-mail: xianlonghou@gmail.com

A. Orfila · J.M. Sayol
Marine Technology and Operational Oceanography Department,
Mediterranean Institute for Advanced Studies (CSIC-UIB), Mallorca, Spain
e-mail: aorfila@imedea.uib-csic.es

J.M. Sayol
e-mail: jsayol@imedea.uib-csic.es

M. Ehrhardt (ed.), *Mathematical Modelling and Numerical Simulation of Oil Pollution Problems*, The Reacting Atmosphere 2, DOI 10.1007/978-3-319-16459-5_5

evaluation methods that can be readily used to improve management and response of oil spills. Herein we develop two major options in advancing oil spill modelling with uncertainty: in Sect. 5.6 a systems-level approach is proposed for evaluating real-time uncertainty at each level of modelling, and in Sect. 5.9 a probability-based approach for oil spill modelling that could be used either as part of a systems-level approach or on its own if the uncertainty in wind, wave, and hydrodynamics can be *a priori* quantified.

Operational modelling of marine oil spill trajectories serves two key purposes: (i) forecast the likely spill path for immediate mitigation and capture operations [16, 23], e.g. deployment of booms, skimmer boats, and dispersants; and (ii) hindcast the likely impacted coastal shorelines, bays, and estuaries that might be affected by escaping oil and hence require further monitoring (e.g. [26]). We are focused on issues associated with operational modelling for the first purpose, where time constraints require immediate application of available models that can be quickly run immediately after a spill is reported.

Predictive oil spill models are inextricably linked to predictive numerical models of atmospheric and oceanic dynamics [14]. In many places, operational numerical models can provide the short-term (usually around the next 72–96 h) forecasts for ocean currents, wave conditions, and wind fields as input to oil spill fate and transport models. These operational models integrate the conservation laws for mass and momentum forward in time to provide physics-based (in contrast to statistics-based) predictions of ocean and atmosphere dynamics. Due to the nonlinear nature of the governing equations, there is a continuous need for acquisition of real-time ocean data to validate, update, and adjust the model to better match reality. The complex dynamics and limited predictability of coastal oceans has motivated development of Coastal Observing Systems (COS), which are being implemented in many regions (e.g. [30, 40, 44, 51]). COS typically monitor physical, chemical and biological ocean properties by combining remote monitoring (HF-Radar, satellite imagery) and in situ devices (floats, drifters, gliders, moorings, etc.). This process, from the acquisition of real data to the dissemination of ocean currents for diagnostic or prognostic purposes, requires the combined efforts of basic and applied research in several engineering fields as well as computer sciences, along with coordination and support from government mission agencies. The goals for all such systems are essentially the same: fast, accurate and user-friendly tools with visual interfaces capable of providing the information needed for making timely and well-founded decisions regarding coastal protection, security and implementation of rapid, effective contingency plans [7, 11].

Oil spills in coastal waters require rapid deployment of mitigation personnel and equipment to the right places at the right time to maximize recovery and minimize environmental damage. For spills sufficiently far offshore in good weather, distance equates to time and emergency managers have the (relative) luxury of tracking actual spill motion via aircraft, boats, and satellite. However, as weather turns foul or a spill occurs close to shore (where response time is short), models provide a key source of information for equipment deployment decisions. The value of model-produced data for emergency managers depends on its timeliness and the reliability of the predictions—both *actual* and *perceived*. Unfortunately, there is little guidance

available for practical evaluation of how well (or poorly) any particular model will predict spill transport or how cumulative effects of uncertainty should be evaluated. This hole in our knowledge is the motivating focus of our work.

This chapter presents an overview of a generic oil spill forecast system (Sect. 5.2), followed by a discussion of salient characteristics of oil spill models (Sect. 5.3), sources of uncertainty (Sect. 5.4), model parameters affecting uncertainty (Sect. 5.5), a proposed systems-level approach for producing a range of oil spill forecasts (Sect. 5.6), a multi-model system for updating forecasts (Sect. 5.7), discussion of uncertainty evaluation methods (Sect. 5.8), and methods for integrating probability estimates within oil spill models (Sect. 5.9).

5.2 Oil Spill Forecast Systems

Predicting the fate and transport of an oil spill requires a system of models, including forecast models for wind, water currents, waves, oil advection/dispersion, and the weathering processes that alter oil properties [24]. A monolithic model that predicts all driving/response processes is simply impractical to build and maintain, so operational models generally use forecast models for wind, waves, and currents originally designed for other purposes. An efficient operational system requires automated linking of models (i.e. output from one model is input to another), along with integration of real-world observational data (e.g. [27, 47]). For rapid use in emergency operations, an oil spill forecast system also benefits from a user interface displaying the model predictions as a geo-referenced visualization that can be readily interpreted by oil spill response personnel. These components can be generally structured as in Fig. 5.1 with three different computational modules, (i) geophysical forcing, (ii) oil transport and chemistry, and (iii) visualization; which are linked to COS data and known (or estimated) information about the oil spill source [46]. Note that the spill forecast system illustrated in Fig. 5.1 has a unidirectional flow of data: there are no feedbacks from the oil spill model to the geophysical forcing models. However, we know that surface oil can affect wave development and the transfer of wind energy into the water, which in turn affects local surface currents and near-surface turbulence. Given the uncertainties in present modelling systems, it is likely that such feedback effects are of minor consequence, but this remains an area where (to our knowledge) there have been no clear quantitative evaluations of these phenomena or applications within operational models.

5.2.1 Oil Spill Data

An oil spill model requires data for the spill location, event time, spilled volume, oil type, fraction of oil at the water surface, and information on the ocean conditions that can affect the near-field behaviour. Most oil spill transport models are designed to

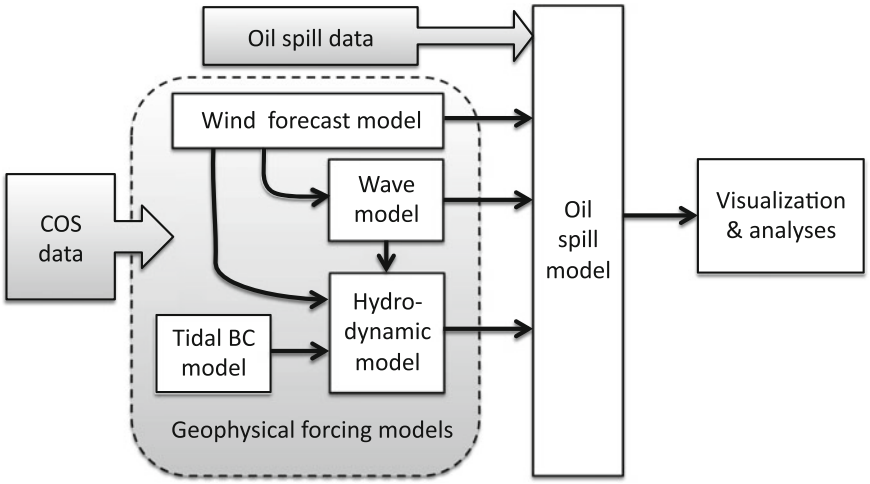

Fig. 5.1 General structure of an oil spill forecast system. Geophysical models typically require data from a coastal observation system (COS). River inflow forecasts can be considered part of typical COS data. Individual components are discussed in text

advect and disperse oil at (or near) the water surface at relatively coarse grid scales, so the near-field spill behaviour must be either modelled separately (particularly for deep-water spills, [31, 56]) or estimated based on previous experience with similar spills.

5.2.2 Geophysical Forcing Models

Developing an integrated geophysical forecast system is a non-trivial effort. Ideally, such a system should be in place and continuously running so that nowcast and forecast winds, waves, tides, river inflows, and currents are always available. Such a modelling system should be integrated with COS data so that each successive forecast uses the latest available observations and the latest forecast data. Where predictive numerical models have not been developed and tested, it is possible to use COS measurements and climatology data to build a forecast model based on statistics [2]; however, until such models are more comprehensively tested, they are best used in response planning and management rather than for an actual event response.

5.2.3 Oil Spill Models

An oil spill model represents the physical and chemical processes governing advection, dispersion, and weathering of the spill. Oil advection is driven by water currents, wind, and waves [45]. The dispersion of the oil depends on wave conditions,

turbulence in the ocean surface layer, and advective processes smaller than the grid scale of the hydrodynamic model. Chemical processes lead to degradation and transformation of the spill (e.g. spreading, emulsification, dissolution, evaporation [57]), which can reduce the surface oil volume and change the oil response to physical forcing. For example, emulsified oil "tarballs" take on the density of the surrounding water and will sink below the water surface if advected into a region of warmer (less dense) water. Near-surface submerged tarballs can be affected by currents diverging from the surface currents, resulting in different transport paths.

5.2.4 Visualization and Analyses

The output from an oil spill model is the time evolution of the expected location, composition, and extent of spilled oil. Ideally, an integrated operational system would include visualization of a probability envelope for the future spill positions, much as is done in the hurricane/typhoon forecasting community. However, present oil spill visualizations are generally based on producing either a snapshot map of representative oil spill particle trajectories (i.e. a "spaghetti" diagram), or a movie of an evolving point cloud of particles. As Geographical Information Systems (GIS) become more powerful and usable over mobile platforms (e.g. smart phones, tablets), oil spill visualization systems should employ GIS standard formats for output data to allow web-based access for emergency response personnel. Standardization within a GIS also allows spill trajectories to be linked to existing Environmental Sensitivity Indexes that classify sensitive coastal areas by their degree of exposure and vulnerability [20].

5.3 Oil Spill Models

Oil spill models typically represent the spill as a collection of mass-less particles moving passively with the water and without any particle-particle interaction. These Lagrangian particles are advected based on modelled fields of the wind, waves, and currents in a deterministic fashion: as the simplest example, given a position vector of a single particle at time step n as $\mathbf{x}^n$, the position at succeeding time step $n+1$ is given by

$$\mathbf{x}^{n+1} = \mathbf{x}^n + \Delta t \, (\mathbf{U}_{\text{wind}} + \mathbf{U}_{\text{wave}} + \mathbf{U}_{\text{current}}) \tag{5.1}$$

where Δt is the particle transport time step and the $\mathbf{U}$ vectors are the modelled effects of wind, waves and currents on the particle. Note these are not the wind, wave, and current velocities themselves, but their modelled net effects with the underlying assumption of linear superposition. More complex algorithms are often used in place of the simple explicit Euler scheme above, e.g. the Runge-Kutta 4th-order (RK4) [6]. The $\mathbf{U}$ fields are typically based on coarse spatial and temporal scales relative to the

finer-scale motions that physically spread oil across wider areas, so some form of dispersion (or diffusion) sub-model is required or the particle cloud will remain unrealistically compacted. For models including chemical evolution, the oil weathering can affect the spill's interactions with wind, waves, currents, and dispersion, which further change the spill response over time.

Oil spill models are available with several degrees of complexity for both physics and chemistry. The simplest physics represent only movement of surface particles driven by the 2-dimensional (2D) water surface velocity, wind drag, and waves. Such models typically use statistics-based dispersion parameterizations (e.g. white noise, Markov chains). More advanced physics models include 3D currents and transport [53], along with more physics-based dispersion models (e.g. mechanical spreading, particle breakup [43], Langmuir circulations [50]). Although 3D models should theoretically be preferred, representing the vertical distribution of oil in the near-surface water column remains a challenge: the vertical grid resolution in most hydrodynamic models is relatively coarse and we lack the comprehensive data on vertical oil dispersion under wave-breaking conditions that are necessary for coarse-grid model parameterization. Indeed, it remains an open question as to whether 3D models are necessary for operational modelling or if forecast uncertainties will dominate the 3D effects. Oil spill models with simpler physics are suitable where confidence in the underlying geophysical forcing models is low, e.g. where a coarse hydrodynamic model grid makes impossible to resolve the important velocity strain-rates required by a physics-based dispersion model.

The simplest oil spill chemistry model is no model at all, which is appropriate where uncertainty in the geophysical forcing dominates the results over short time periods (for which weathering is less important). More advanced models include effects of the type of oil along with processes such as dissolution, emulsification and/or evaporation [12]. It should be noted that 3D transport and chemical evolution for a deepwater blowout remains a scientific challenge due to the complex physics of an oil/gas plume and transformations of the gas phase during ascent [13].

5.4 Sources of Uncertainty

From a science point of view, we seek to understand and minimize sources of error and uncertainty in any modelling system. However, for emergency management we need rapid answers to some practical questions: *How good is this prediction and can we rely on it for deploying response equipment?* Before trying to quantify uncertainty, it is useful to review the fundamental sources.

The major contributors to uncertainty in any modelling system fall into four categories:

(i) structure of the model,
(ii) empirical parameters,
(iii) initial conditions,
(iv) boundary conditions.

5.4.1 Structural Uncertainty

Choices made in governing equations (e.g. use of hydrostatic instead of non-hydrostatic equations for a hydrodynamic model) and choices made in developing a discrete version of the equations (e.g. grid scale, time step, numerical solution method) contribute to an underlying structural uncertainty, which imposes limitations on how well the model can represent the actual physics. This structural uncertainty exists for both geophysical and oil spill models.

5.4.2 Empirical Parameter Uncertainty

Any oil spill modelling system has dozens, if not hundreds, of parameters; e.g. coefficients for sub-models of turbulence, wind/wave drag, and oil spreading. Parameters are typically selected based on combinations of laboratory studies, prior field studies, theory, and modelling experience. Unfortunately, one can never be sure of having the exactly "correct" set of parameters—even if we simply define "correct" as the set of parameters for a given model structure that provides a prediction within some desired accuracy. To add further complexity, parameters are often used to compensate for model structural errors and thus cannot always be taken from experiments or theory without considering the model formulation. For example the turbulent eddy diffusion coefficient in a hydrodynamic model is typically a function of the local shear stress; at different grid scales the resolved shear will have different values and hence needs different eddy diffusion coefficients to match real-world physics. Furthermore, if the hydrodynamic eddy diffusion coefficient is overestimated then a corresponding underestimate of oil spill diffusion might be necessary for a highly-accurate prediction. We generally do not know whether a particular parameter is over- or underestimated, so it is impossible to specifically set compensating parameters; as a result, there are multiple layers of interaction between parameter uncertainties.

5.4.3 Initial Condition Uncertainty

The output from an oil spill forecast system is subject to initial condition (IC) uncertainty for both the oil spill event and the geophysical forcing models. The IC uncertainty for the oil spill includes the initial volume [55] and the near-field forces that give shape to the initial slick. In some cases the chemical composition of the oil might also be uncertain at the time of the spill [37]. In contrast to this irreducible oil spill IC uncertainty, the geophysical forcing IC uncertainty can be readily addressed by having geophysical models that are continuously (or periodically) running. When a hydrodynamic model is started at some time $t = 0$, the initial velocity field over the entire model domain is typically zero because we do not have sufficient data for anything more complex. There is some *spin-up* time that it takes a model to

"forget" that it started with the wrong velocities [21]. Hydrodynamic spin-up time can vary from days to several weeks, depending on the scales of the system. Testing for spin-up time is relatively straightforward by starting the model from successively older time points. When starting at an older time does not change the prediction for today, the model results are effectively independent of the starting conditions and the geophysical IC uncertainty is essentially zero. The key point is that operational oil spill models *must* start from a hydrodynamic model that is already running and past its spin-up time; for any significant domain, a hydrodynamic model cannot be expected to reach spin-up in time for an accurate forecast if the model is only started after a spill is reported.

5.4.4 Boundary Condition Uncertainty

Boundary condition (BC) uncertainty also includes both oil spill and geophysical forcing components. At the oil spill itself, any ongoing leakage and its subgrid (near-field) oil distributions are typically uncertain. Where the oil hits a land boundary, the processes by which the oil adheres or remobilizes are poorly understood, again resulting in highly uncertain BC. In geophysical modelling, the 3D currents and water surface elevations at the computational domain's edges are never known exactly, but modelers have developed sophisticated methods to reduce the effects of these uncertainties (e.g. [59]). Nevertheless, it is necessary that the hydrodynamic model's artificial boundaries should be as far as possible from the location of an oil spill to minimize BC effects.

Wind plays a major role in BC uncertainty. The spatial and temporal fluctuations of the wind field are never precisely known (even in hindcast), and the modelling of wind-driven waves, turbulence, and currents is strongly affected by empirical parameter choices and model structures. Added to these effects is the inherent uncertainty in the overall wind forecast speed and direction. It can be argued that the BC uncertainty associated with how energy from the wind affects waves, currents, and the oil spill is the dominant form of uncertainty for any spill [15].

In a more general sense, the uncertainties above can be divided into "epistemic" and "aleatoric" classes [32]. For our purposes, the former can be thought of as uncertainty developed in modelling system through lack of either adequate models or data (i.e. things we either know or should know); whereas the latter can be thought of as uncertainty associated with the chaotic behavior of highly nonlinear systems, which is deterministically unknowable (i.e. things we can only "know" stochastically) [38]. This classification concept can be used to focus model development efforts on reducing epistemic uncertainties, whereas system operational efforts can be focused on evaluating effects of irreducible aleatoric uncertainties. For example, part of the uncertainty in near-surface ocean currents in a coarse-grid hydrodynamic model is epistemic uncertainty, which can be reduced by using finer grid—a choice made during model development. In contrast, the effects of aleatoric uncertainty associated with forecast wind conditions can only be evaluated for a particular event (e.g. by

Monte-Carlo simulation using a range of possible forecasts), but cannot be precisely known a priori. However as a practical matter, once a modelling system has been put into operation—that is, the science has been executed to minimize epistemic uncertainty as much as practical for available resources—then any uncertainty in the system, whether aleatoric or epistemic, is essentially irreducible. Thus, we need practical methods for evaluating uncertainty during both model building (to focus our efforts in uncertainty reduction) and model operation (to understand effects of remaining uncertainty).

5.5 Model Design and Parameters Affecting Uncertainty

The generic forecast system of Fig. 5.1 includes models with a wide variety of parameters and settings that affect uncertainty. Many parameters are specific to particular model designs; but the following provides an overview of some of the more common parameters.

5.5.1 Oil Spill Model Time Step

The time step used for the Lagrangian integration of oil spill movement is a control on the relationships between space, time, and the partitioning of transport between advection and a stochastic model of diffusion. Coastal ocean studies have typically used 30 minute time steps consistent with their spatial resolution and water velocities, e.g. [22, 39]. For higher-resolution models close to shore, smaller time steps are typically necessary for velocity fields that are more highly variable in time and space.

5.5.2 Numerical Scheme

Oil spill transport models can be coded with different options for transport. The simplest Lagrangian models are 1st-order forward Euler transport, which use time n velocity contributions at a particle position to compute the particle displacement, as in Eq. (5.1) above. However, such simple models are recognized as having limited accuracy [5]. The Runge-Kutta 4th-order (RK4) is a popular high-order method as it takes into account the changing velocity field over a particle path. Although the RK4 itself is computationally efficient, its overall performance depends on the speed of the interpolation scheme from the hydrodynamic model grid to an arbitrary particle location. For an unstructured (triangular or generalized polyhedron) hydrodynamic grid, this interpolation can be computationally expensive.

5.5.3 Wind Forcing

The direct force of the wind on an oil spill is arguably negligible; however, few operational hydrodynamic models are designed with the fine-resolution vertical grid scales and algorithms that can accurately reproduce the surface and near-surface water velocities. Thus, the hydrodynamic model surface water velocity field is *not* the velocity field that an oil spill will actually see. Because the surface and near-surface velocities are strongly affected by the local speed and direction of the wind, oil spill models typically include a "wind drag" parameter that provides a correction to the hydrodynamically-modelled water surface velocities for particle transport.

5.5.4 Wave Forcing

The transport cause by waves is typically added through a Stokes drift term that requires empirical parameterization. Selection of the parameter depends on the type of wave model.

5.5.5 Diffusivity

Diffusivity parameterization controls the overall spread of particles produced by an oil spill model; i.e. this is not *diffusion* of oil molecules into solution with water, but the *dispersion* or spreading of the oil on or near the water surface. This diffusivity is not generally a direct representation of the dispersion physics acting on an oil slick, but instead a stochastic parameterization of turbulence and the unresolved spatial structure of the modelled water velocities. Thus, the appropriate oil spill diffusivity is difficult to directly link to physically-based eddy diffusion coefficients (e.g. [34]) or turbulence models used in hydrodynamic simulations. Diffusivity for an oil spill is often modelled as parameterized white noise.

5.5.6 Hydrodynamic Model Grid

Grid spacing affects the spatial and temporal velocity gradients that can be represented in the hydrodynamic model. Most models are limited by a CFL condition such that $u\Delta t/\Delta x < C_{limit}$, where u is the water velocity, Δt is the model time step, Δx is the local model grid scale in the same direction as u, and C_{limit} is the CFL limit that is typically $O(1)$, with the exact value depending on the numerical algorithm. Thus, the model grid spacing also controls the model time step. For coarser model grids, both spatial and temporal gradients will be less accurate than with finer

grids [9], so the wind forcing and diffusivity parameters will need to be different (typically higher). In particular, for large-scale oceanographic models the effects of submesocale instabilities are poorly modelled and must be parameterized [17].

The challenge facing any oil spill forecast system is that the parameterization of these different aspects are interdependent. Obtaining a "best" value of any given parameter is impossible without considering the system modelled, the types of models applied, and choices in the model setup (e.g. grid spacing). From the standpoint of uncertainty evaluation, determining the best value is less important than estimating a range of reasonable parameters for a given system. In Sect. 5.8 we discuss some of the ways that hindcast modelling and drifter data can be used to improve our understanding of these parameters.

5.6 Systems for Real-Time Forecast Uncertainty

Emergency responders need estimates of spill forecast accuracy and likely outcomes, such as when and where a spill might make landfall. Ideally, forecasts should contain a range of results, such as the earliest time landfall is expected or the widest range of beaches that could be affected. A single model forecast cannot provide the necessary range of data for effectively deploying emergency response equipment. Obtaining systematic estimates of real-time forecast uncertainty requires an operational system that evaluates the key uncertainty sources outlined in Sect. 5.4, above. Some uncertainties can be minimized in model construction, but the remaining uncertainties need to be evaluated and reported to emergency managers with visualization tools that are easy to use and understand. Although some progress has been made (e.g. [18, 39, 41], presently there are no operational systems that can evaluate the accumulation of uncertainty from the wind forecast through hydrodynamic, wave, and oil spill modelling. Fortunately, the tools and technology to build such a system are now available.

Perhaps the simplest way to evaluate forecast uncertainty is a brute-force multimodel approach that takes the real-time forecast system of Fig. 5.1 and creates multiple model instances in a hierarchical series of solutions (Figs. 5.2 and 5.3). A multimodel operational system provides a range of forecast oil spills that can be used to develop probability maps instead of a prediction cloud. Some number, N_{wind}, of wind forecasts are created based on a primary wind forecast and likely perturbations. For each wind forecast a set of independent hydrodynamic models is run. These models use some N_{wave} different wave model coefficients and some N_{hydro} different hydrodynamic model conditions (e.g. different wind drag coefficients, tidal forecasts, or turbulence parameters). For each hydrodynamic model, a set of independent oil spill models is run with N_{IC} different oil spill initial conditions and N_{oil} different oil model parameters. This system requires a set of $N_{wind}N_{wave}N_{hydro}$ hydrodynamic models and a total of $N_{wind}N_{wave}N_{hydro}N_{IC}N_{oil}$ oil spill models.

Three perturbations at each system level could be used to represent the expected parameters along with high and low sets that bound the expected values. Note that

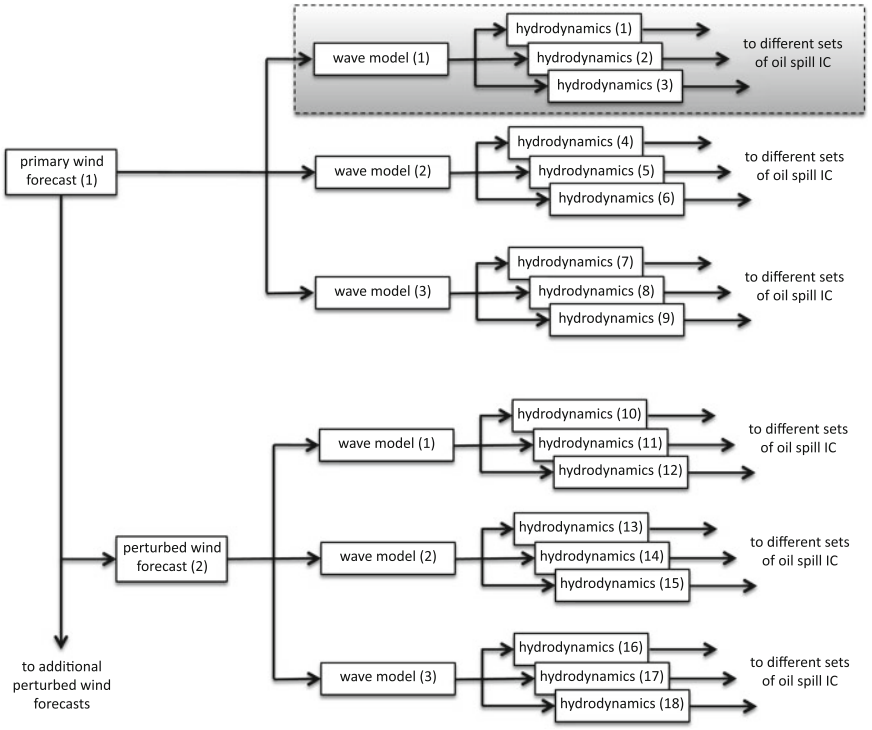

Fig. 5.2 Top-level structure for multi-model operational forecast system. Multiple wind forecasts are used to drive sets of hydrodynamic models using different wave model parameters and different hydrodynamic parameters. Highlighted section is expanded in Fig. 5.3

full Monte-Carlo methods (random selection of the parameters and conditions over a statistically valid set at each model level) would produce an impractically-large set of simulations. Selection of high and low conditions/parameters requires thorough understanding of uncertainty contributions, which can be readily handled by hindcast analyses during development of an operational system (Sect. 5.8). A system with three condition sets at each level (i.e. Figs. 5.2 and 5.3) would require 27 hydrodynamic model runs and 243 oil spill model runs, which could be accomplished with modest investment in a set of standard workstation computers. A relatively small number of perturbations in each step of the modelling provides a wide range of model results for statistical processing.

Implementing an operational system with this large number of simulations might appear to be computationally impractical. However, the continuing advance of low-cost multiprocessor workstations and GPU computing changes the question from "can we do this?" to "given our budget, how big can N_x be for each component?" Compared to hydrodynamic models, oil spill models run very quickly and take relatively little memory, so running a large number of such models is eminently practical.

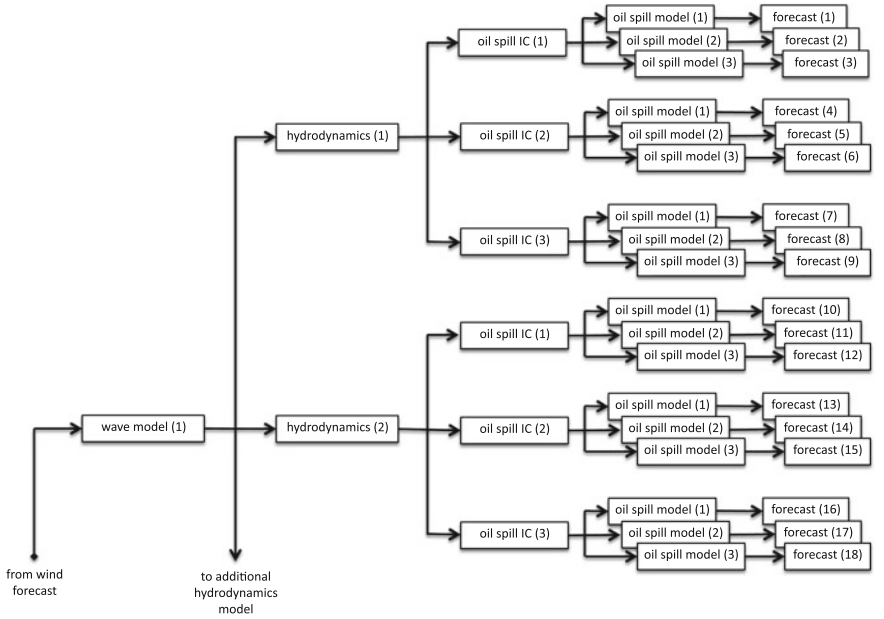

Fig. 5.3 Second-level structure for multi-model forecast system. Each hydrodynamic model drives multiple oil spill models with different IC and different oil spill model parameters, providing multiple forecasts that can be used for probability map visualizations. This figure is expanded detail of highlighted portion of Fig. 5.2

Hydrodynamic models present a greater challenge, but can be implemented using separate logical processors of a single workstation for separate models (where N_{hydro} is small) or with multiple networked workstations (where N_{hydro} is large). The number of hydrodynamic models can be reduced if the uncertainty contributions in the wave model and hydrodynamic model parameters can be minimized; indeed, if these can be neglected the only uncertainty driving hydrodynamics will be wind forecast, so that $N_{hydro} = N_{wave} = 1$, and the number of hydrodynamic models is simply N_{wind} and the total number of oil spill models is $N_{wind}N_{IC}N_{oil}$. A key point is that multiple hydrodynamic models are only needed after a spill has occurred; that is only a single hydrodynamic model is necessary to minimize *initial condition uncertainty* of spin-up (Sect. 5.4). Thus, if new forecast data is available every 3 h and a 72 h forecast is desired, computational power must be continuously available to run a single hydrodynamic simulation at least 24× faster than real time. Additional computational resources are only needed when a spill occurs and the full multi-model forecast system is invoked.

The proposed operational forecast system described above is effectively *static*; that is, it provides the data for a single animation of a probability field for an oil spill location based on data available at the initiation of the modelling. However, during an emergency there will be new COS data and updated wind forecasts available

on a regular basis, which requires a *dynamic* modelling system; i.e. the operational system should automatically obtain new data/forecasts, integrate the new data into the models, and re-run all the models to produce a new set of forecasts and visualizations. Techniques for handling these issues are discussed in Sect. 5.7, below. To make such a system practical, computational power needs to be made available such that an entire multi-model forecast sequence, from wind to hydrodynamics to oil spill model, can be completed before the next COS data and wind forecasts become available.

A further difficulty in providing operational forecasts is the fact that any Lagrangian particle simulation has a limited time-horizon for reliability. Because the Lagrangian particles are inherently integrative of error, their divergence from the real-world will increase with time. The most effective operational system will integrate data sources for estimating the real-world position of the oils spill (e.g. through satellite tracking, [54]) that can be used to periodically reset the oil spill particles to a new "known" position.

Clearly, creating and automating a multi-model operational system with forecast uncertainty presents a number of challenges, including (i) generation of perturbed wind forecasts, (ii) selecting parameter sets for wave, hydrodynamics, and oil spill models, (iii) selecting sets of reasonable initial conditions for the oil spill, (iv) analyzing and visualizing the combined forecast data, (v) automated updating of models as new data and forecasts are received, and (vi) creating a system that integrates models and data so that the user provides the location, estimated size, and oil type that is spilled and obtains an animation of the time-evolution of a probability map for the oil spill. To address some of these challenges, authors Sayol and Orfila have developed new techniques for probability simulations within oil spill models and probability mapping visualization (Sect. 5.9), while simultaneously authors Hou and Hodges have developed the HyosPy system of model integration (Sect. 5.7).

5.7 Multi-Model Integration and Updating Predictions

The *Hydrodynamic and oil spill Python* (HyosPy) code has been developed as a testbed for integrating hydrodynamics and oil spill models in a flexible manner [18, 19]. Presently, HyosPy is designed to integrate COS data, wind forecasts, and multiple hydrodynamic models linked to independent oil spill models, as illustrated in Fig. 5.4. The results are visualized in Google Earth/Maps applications. HyosPy uses the Python scripting language, which provides a flexible "wrapper" to integrate existing models, servers, connections to online data services, and visualization tools. The present version of HyosPy is being tested for coastal embayments of Texas (USA) with automatic tidal data downloads from the Texas Coastal Ocean Observation Network (TCOON) [49] and wind forecast data from a Texas A&M University server. The hydrodynamic model used is SELFE [42], which has been under review by the Texas Water Development Board (TWDB) and General Land Office (TGLO) as a replacement for the TxBlend model, which is presently the operational oil spill model used inside barrier islands along the Texas coastline [52]. The oil spill model

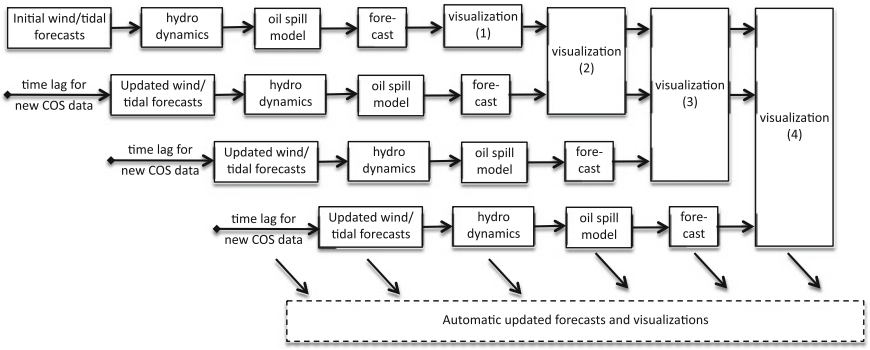

Fig. 5.4 HyosPy structure for automatic updating of forecasts and visualizations. Here each forecast wind/tidal condition drives a single hydrodynamics and oil spill model, with each model based on the latest available data and forecasts. Visualizations include both the latest forecasts and prior forecasts

for HyosPy is the NOAA PyGnome model, which is a new Linux/Python version of the GNOME operational oil spill model used by emergency response agencies across the USA [4, 33].

HyosPy was run as a real-time demonstration on Feb 4, 2014 using COS and forecast data downloaded from the internet as it became available and an imaginary oil spill near a beach in Corpus Christi Bay (Texas, USA). As shown in Figs. 5.5 and 5.6, HyosPy produced tracks 3 h apart, where each track is based on combination of the latest available hindcast and forecast data with new instances of both the hydrodynamic model and the oil spill model. The oil spill diffusivity coefficient in these models is low, so the Lagrangian particle stay close together in each track, which provides clearer visualization of how the model operates.

Key innovations of HyosPy are (i) automated re-running of the hydrodynamic model as new data becomes available, and (ii) using successive forecasts in the visualization to provide insight into how the model predictions are changing as new data is added. Because HyosPy is a wrapper around models rather than a model itself, it can be readily modified to include multiple perturbed forecasts, hydrodynamic models, and oil spill models along each of the linear paths of Fig. 5.4; that is, we can implement Figs. 5.2 and 5.3 by creating multiple model instances within the existing system. As an operational approach, HyosPy could be set up with a single continuously-running hydrodynamic model using the latest wind/tidal forecast data. When a spill occurs, additional computer resources can be added to allow multiple hydrodynamics models and oil spill models to be run using perturbed forecast data. Recent tests have shown that HyosPy can be operated as a web service with a continuously-running hydrodynamic model [18, 19]. For a real (or imaginary) oil spill, the user enters the oil spill location, time, oil type, and quantity into boxes on a web site and HyosPy produces, then automatically updates, a series of predicted spill tracks. HyosPy handles the data manipulation, reformatting, and initiation calls between models without user guidance, which makes the complex multi-model processing entirely invisible.

Fig. 5.5 HyposPy visualization of forecast tracks for an imaginary oil spill in Corpus Christi Bay (Texas, USA). *Upper frame* is the initial forecast track available within minutes of the spill. The *middle frame* is the forecast tracks available at 0900 using new wind forecast data. Note the 0000–0600 forecasts are almost indistinguishable in their prediction of the 48 h position. *Lower frame* shows predictions in the afternoon initially move away from and then back toward the beach. Continued in Fig. 5.6. Visualization using Google Earth with additional annotations (in *yellow*) for clarity

Fig. 5.6 HyposPy visualization of forecast tracks, continued from Fig. 5.5. Forecast tracks in the second day (0000–1200) are moving consistently closer to the beach. Visualization using Google Earth

HyosPy development was motivated by a need for integrative tools that are extensible and flexible so that new models and new data sources can be readily implemented. HyosPy is formulated with two module levels: high-level modules controls the overall logic and the Application Program Interface (API), whereas lower-level modules process specific tasks, e.g. converting data from particular hydrodynamics model to a common NetCDF format for oil spill models. Adding new models or data is straightforward as the input/output for each module is designed without downward/upward restrictions. Using the Google Maps/Earth visualization tools provide portability, with results displayable over the web on any Java-enabled browser for all supported terminal platforms (e.g., laptop, tablet, and smart phone) and operating systems (Windows, Mac OSX, Linux, and Android) [18].

5.8 Evaluation of Uncertainty

Evaluating uncertainty with hindcast models and field-deployed drifter experiments [35] can provide insight into setting up both the "best" parameters and upper and lower bounds for a multi-model operational system (e.g. as in Sect. 5.6). For an oil spill model, a typical IC uncertainty is in the oil spill shape. Typical BC problems include the appropriate effect of wind drag on the oil and effective diffusivity of the oil. Quantification methodologies for these issues are discussed and demonstrated below. These methodologies were designed to provide rapid multiple oil spill

model predictions, which can be used to develop probability contours for emergency responders [39]. The present discussion is for a 2D oil spill confined to the water surface, however there are no theoretical impediments for extension to 3D.

5.8.1 Geometric Uncertainty

A critical decision in the design of any operational oil spill forecast system is in the choice of the model grids—both for the hydrodynamic model and the oil spill model. For the hydrodynamic model, geometrical uncertainty is affected by interaction of the numerical algorithm accuracy, the hydrodynamic model time step, and the grid cell spacing. Further complexity is added by the choice of unstructured, curvilinear, or Cartesian grids. The advantages and disadvantages of different grid methods for hydrodynamics are subjects of ongoing debate; however, from the oil spill modelling perspective the important issue is that finer model grids provide a more accurate resolution of the spatio-temporal evolution of the surface currents, and hence reduce the uncertainty in oil spill modelling associated with hydrodynamics. Unfortunately, decreasing the grid length scale by 50 % in each horizontal direction requires an increase of the number of horizontal grid cells of 4× and a reduction in the model time step by 50 %, which leads to an 8× increase in computational requirements for only a factor of two improvement in grid resolution. Thus, operational models are a compromise between what is desirable and what is achievable with the computational resources at hand. As discussed in Sect. 5.6, for a practical system the hydrodynamic model should be able to produce a set of velocities fields for the desired forecast interval (e.g. 72 h) in substantially less than the time between new updated forecasts. This need inherently limits the practical grid resolution of the hydrodynamic model.

As further issue in geometrical uncertainty, Lagrangian particle transport oil spill models are faster (and easier to code) for structured model grids (either Cartesian or curvilinear) because Lagrangian particle models generally operate with each particle defined by vector position $\mathbf{s} = a\hat{i} + b\hat{j} + c\hat{k}$ in a 3D space (or 2D for surface models). To move a particles through space/time, the velocity at the particle's present location must be interpolated from the velocity field on the hydrodynamic model grid. If a structured hydrodynamic grid is used, identifying the neighbour velocities is trivial; however, for an unstructured grid the identification problem can be computationally expensive. Nevertheless, unstructured hydrodynamic models are desirable for many coastal oceans and embayments. One approach to simplifying the interface between a Lagrangian particle and unstructured hydrodynamic grid is to "rasterize" the velocity fields; i.e. interpolate the velocities to a structured grid before computing the Lagrangian particle motion. This adds a second layer of interpolation (hydrodynamics to raster, raster to Lagrangian particle) and hence another source of uncertainty.

Geometrical uncertainty cannot be easily evaluated during run-time of an operational forecast system. Instead, the effects of geometrical uncertainty should be analyzed during development of the system through model-model comparisons and

drifter analyses using hindcasts. For model-model comparisons, a hydrodynamic model can be run with the smallest practical grid and time step over a number of hindcast periods to provide a set of reference cases. These reference cases can be considered the best possible simulations for the available model. Statistical analyses can be used to evaluate the difference between the reference cases and simulations at the coarser grid scales and larger time steps that are practical for an operational system. There remains an open question as to the best approach to incorporate such data into an effective parameterization of uncertainty. The most obvious possibility is to use the local velocity variance to scale a random perturbation in the velocities used for the oil spill Lagrangian transport.

5.8.2 Wind Drag Coefficient

Modelled surface oil spills are directly affected by wind; that is they will move with velocity vectors slightly different than the modelled water currents at the surface. In hydrodynamics, the wind causes shear stress at the surface that creates 3D turbulence and transfers momentum down from the surface into the wind-mixed layer. Hydrodynamic models focus on getting the net downward transfer of energy and momentum, and the modelled "surface" velocity actually represents the spatially-averaged velocity in the surface grid cell whose thickness is typically $O(1) - O(10)$ m, depending on the model scale. In contrast, the wind effect on surface oil (or a floating object) does not have a significant downward transfer of momentum and must be directly included in the floating oil particle transport computation. The effect of wind drag on the oil velocity ($\mathbf{U}_{\text{wind}}$) is typically represented using a drag coefficient (γ) and the wind velocity ($\mathbf{V}_{\text{wind}}$) such that $\mathbf{U}_{\text{wind}} = \gamma \mathbf{V}_{\text{wind}}$. Because the drag is generally small, γ is often reported as a percentage of the wind speed. Using winds measured at 10 m above the water surface, γ in the range $[0,\ 3.5\,\%]$ have been recommended [3, 29]. More recently, [22] argued for γ values up to 6.0 %.

The sensitivity of an oil spill model to the selection of γ can be evaluated by model-model hindcast comparisons and the "best" γ for a particular combination of hydrodynamic and oil spill models can be selected by comparison to drifter experiments. As an example, a surface drifter was deployed during a cruise around the Balearic Sea in October, 2012. An operational ROMS model is available for the same time period. Using the oil spill model of [39], an initially circular spill is transported as shown in Fig. 5.7.

The sensitivity of the results to the γ can be evaluated by running hindcast simulation similar to Fig. 5.7 for a range of values. Figure 5.8 shows the Root Mean Square Error (RMSE) of the cloud of particles relative to the drifter position at the end of 72 h for simulations with $0 \leq \gamma \leq 4\,\%$.

$$\text{RMSE} = \sqrt{\frac{1}{N_p}\sum_{n=1}^{N_p} d_n^2},$$

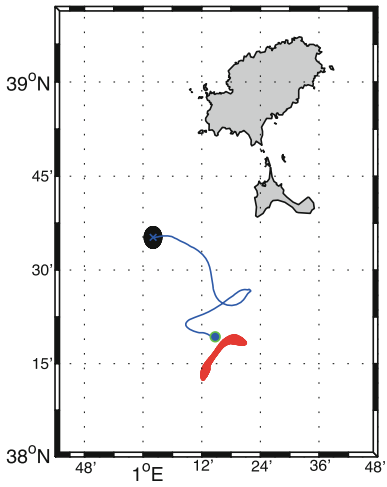

Fig. 5.7 Simulation of an initially circular oil spill advected for 72 h with modelled ocean currents and a $\gamma = 0.5\,\%$ of wind velocity (provided by the atmospheric numerical model at 10 m above the sea level). *Black* is initial spill location and the *red* is final distribution. *Blue line* is the real drifter trajectory for the same period

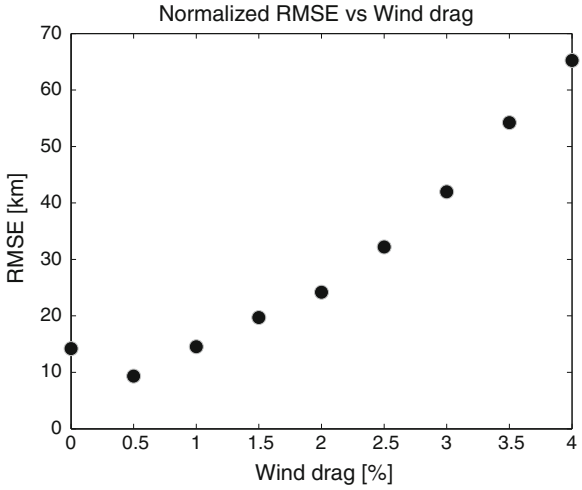

Fig. 5.8 RMSE (units in km) obtained for several wind drag values computed for the same initial cloud and period of study in relation to a real drifter

where N_p is the number of particles deployed, and d_n is the spherical distance (the arc-length over the Earth surface) between the virtual particle n and the real drifter after 72 h, defined as the haversine formula:

$$d_n = \mathrm{R_T}\alpha = \mathrm{R_T}\, 2 \arcsin\left(\sqrt{\sin^2\left(\frac{\Delta_\phi}{2}\right) + \cos(\phi_n)\cos(\phi_d)\sin^2\left(\frac{\Delta_\lambda}{2}\right)}\right),$$

where $\mathrm{R_T}$ is the average Earth radius (6371 km) and α is an angle; for a particle and a drifter with positions $(\lambda_n,\ \phi_n)$ and $(\lambda_d,\ \phi_d)$, the Δ terms are $\Delta_\phi = \phi_d - \phi_n$ and $\Delta_\lambda = \lambda_d - \lambda_n$.

For the modelled conditions, it is clear that $\gamma = 0.5\,\%$ should be preferred, and that both decreasing or increasing the drag will increase the error. Note that the γ derived herein is merely illustrative for the particular model and conditions, and should not be taken as a recommended value for other models or conditions.

The "best" drag coefficient for an oil spill model is a subject of ongoing research, and arguably depends on interactions between the modelled hydrodynamics and the oil spill. That is, our operational goal is to predict the probable movement of an oil spill, and the best γ is the one that compensates for the difference between the modelled transport of near-surface currents ($\mathbf{U}_{\text{current}}$) and the real transport. If the hydrodynamic model poorly predicts the near-surface current effects, then the best γ will be different than what would be used with a hydrodynamic model that has better predictions. Thus γ will inherently be uncertain and a multi-model operational system (Sect. 5.6) should include oil spill models with at least three γ values (low, high, best) to cover a range of possible results. In particular, using a $\gamma = 0$ as a lower bound provides the expected transport for subsurface oil, and can be useful for oil spill models that are otherwise confined to modelling 2D surface transport (e.g. GNOME, [58]).

5.8.3 Diffusivity

The physical diffusion of oil into water is a very slow process, and is generally not represented in an oil spill model. Indeed, by definition the Lagrangian particles used in oil spill models are unitary and cannot diffuse. Instead, the "diffusivity" (or dispersion) model for Lagrangian particles is designed to represent the transport processes and turbulence effects that are not resolved in either the hydrodynamic model or the oil spill model itself [10]. A stochastic approach to diffusivity is to modify Eq. (5.1) to include a diffusion term for each particle as

$$\mathbf{x}^{n+1} = \mathbf{x}^n + \Delta t\,(\mathbf{U}_{\text{wind}} + \mathbf{U}_{\text{wave}} + \mathbf{U}_{\text{current}}) + \delta\mathbf{x}_{\text{diff}} \tag{5.2}$$

where $\delta\mathbf{x}_{\text{diff}}$ represents a vector random walk added to the deterministic particle motion from the $\mathbf{U}$ terms. A diffusion rate (D) resulting in a normal distribution over time Δt will have a variance $\sigma^2 = 2D\Delta t$, such that the standard deviation (σ) is an expected length scale for diffusive transport [8]. A random walk distance vector can be modelled using the ratio of the variance of the diffusivity to the variance of a random number generator, e.g. [25, 36], as:

$$\delta\mathbf{x}_{\text{diff}} = \mathbf{R}\sqrt{\frac{2D\,\Delta t}{\sigma^2}} \tag{5.3}$$

where $\mathbf{R}$ is a uniform random number vector in the range $[-1, 1]$ with a vanishing mean and a variance of $\sigma^2 = 1/3$. Note that Δt here is the time step of the oil spill model, which is not necessarily the same as the time step of the hydrodynamic model.

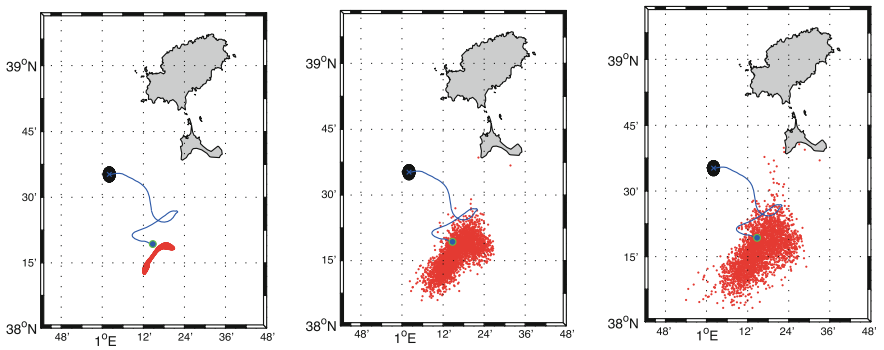

Fig. 5.9 Simulation of a circular oil spill advected for 72 h with $\gamma = 0.5\,\%$ with no diffusivity (*left*), with $D = 10\,\mathrm{m}^2/\mathrm{s}$ (*center*) and with $D = 100\,\mathrm{m}^2/\mathrm{s}$. *Black circle* indicates the initial location of particles whereas the *red dots* the final distribution. The drifter trajectory is depicted with the *blue line* where the *blue cross* is the starting position and the *blue circle* the final one

The effects of varying diffusivity can be illustrated as shown in Fig. 5.9. Determining the appropriate diffusion coefficient for an oil spill model is a challenge as it depends directly on how well the hydrodynamic model captures the structure of velocity field, which may vary in both time and space. If we assume spatial variability in diffusion is a primary concern, the approach of [39] allows development of a spatial map of estimated diffusivity based on multi-year simulations of particle transport.

5.8.4 Oil Spill Shape

Although aerial or satellite imagery can sometimes be used to obtain a visual approximation of an oil spill's initial shape, there will generally be some uncertainty in the shape and/or extent of coverage for the early stages of spill. There is an open question as to how uncertainties in the initial shape and size of an oil spill affect the forecast. Unfortunately, the overall effect of the initial shape is also likely influenced by the selected diffusivity, with higher diffusivities being less affected by the initial shape. A simple test for the influence of the shape and diffusivity can be carried out with representative initial shapes. If a and b are defined as the major and minor semi-axis of an initial elliptical distribution of oil particles, insight can be provided with study cases: (i) $a = b$ a circle, (ii) $a = 2b$ a prolate ellipse, and (iii) $a = b/2$ an oblate ellipse. For each shape, a set of diffusivities over the range 0–100 m^2/s has been run using the same simulation setup as in Fig. 5.9. The RSME results are provided in Table 5.1, with typical particle clouds after 72 h of simulation shown in Fig. 5.10. These results indicate that the model tested is relatively insensitive to the initial shape, and a circular spill is a reasonable initial condition when more detailed data is not available.

Table 5.1 Root Mean Square Error (in km) for circular and elliptical initial distributions of oil spill particles for simulations similar to Fig. 5.10

RMSE (km)	$D = 0\,\mathrm{m}^2/\mathrm{s}$	$D = 1\,\mathrm{m}^2/\mathrm{s}$	$D = 10\,\mathrm{m}^2/\mathrm{s}$	$D = 100\,\mathrm{m}^2/\mathrm{s}$
$a = b$	7.44	7.57	8.25	12.7
$a = 2b$	6.89	7.03	8.04	12.48
$a = b/2$	8.09	8.15	8.71	13.07

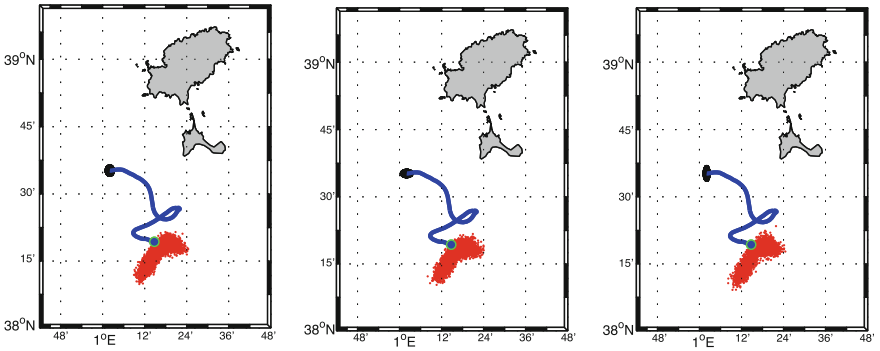

Fig. 5.10 Trajectories of virtual particles deployed inside a circle (*left*), ellipse oriented N–S (*middle*) and ellipse oriented W–E (*right*). Simulations are performed for 72 h with $\gamma = 0.5\,\%$ and with $D = 10\,\mathrm{m}^2/\mathrm{s}$. *Black cloud* indicates the initial location of particles and the *red dots* the final distribution. The drifter trajectory is depicted with the *blue line*

5.9 Integrating Probability Within an Oil Spill Model

A disadvantage of the multi-model approach (Sect. 5.6) is the need for systemic, real-time uncertainty modelling through all models of the forecasting system. This problem might be reduced by making use of a computationally inexpensive oil spill model to rapidly create real-time simulation ensembles that can be visualized as probability maps. In the simplest incarnation, such an approach is complementary to the multi-model system, i.e. simply replacing the multiple oil spill models and initial condition perturbations in Fig. 5.3 with a single ensemble model. However, there is also the potential for an alternative approach that entirely replaces the multi-model system. Our principal concern is in the range of possible future positions of the oil spill and the probabilities associated with this range. If the uncertainties in wind, wave, and hydrodynamic models (driving forces) can be quantified in terms of their effects on stochastic diffusivity (particle response) [29], then the multi-model system could be replaced with single instances of best estimate wind, wave, and hydrodynamic models accompanied by an ensemble uncertainty approach. This approach requires all the uncertainties in the wind, wave, and currents to be re-parameterized in terms of diffusivity. Methodologies and metrics for translating the chain of uncertainties from driving force models to particle models remain relatively unexplored, but are likely

to require extensive hindcast analyses that are customized to the driving models and the regional/local conditions [39].

An ensemble approach requires setting perturbation values for the parameters and initial conditions for the oil spill model. These can be set as part of a Monte Carlo approach over the expected range. Lagrangian particle from all simulations are then combined into a single data set that can be analyzed for any particular time point using the following steps:

(i) Define a bounding box covering all the particles at a given forecast time.
(ii) Subdivide the bounding box in a grid.
(iii) Compute the probability density based on particle counts in the grid cells.
(iv) Accumulate probability starting from high values and working downwards so that the integrated probability over the area is 100 %.
(v) Construct and visualize probability contours.

A demonstration of the probability approach is illustrated in Fig. 5.11. The grid size within the bounding box is chosen to ensure statistically significant grid cells over majority of the forecast spill area, which will depend on the number of simulated particles and their effective diffusion. The probability density can be computed by any number of kernels, (e.g. [28, Chap. 9]), but a simple Gaussian kernel is arguably appropriate for an oil spill [1, 39]. Accumulating probability contours from high to low values allows development of probability distributions with multiple local maxima and disconnected contours. The probability approach, whether adopted within a multi-model forecast system or simply within the oil spill model itself, provides the end user with a better understanding of the results of an oil spill simulation than does the traditional point cloud or particle tracks.

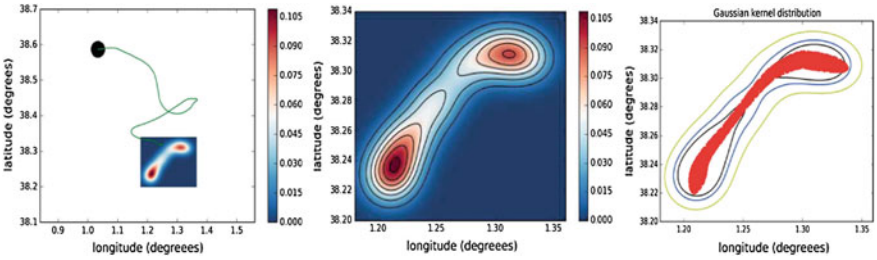

Fig. 5.11 The simulation from Fig. 5.7 using a probability approach for the particle distribution instead of the particle cloud. Colour in *left* and *centre panels* represents probability of finding a Lagrangian particle in each subgrid cell of the bounding box. *Right panel* compares the particle cloud (*red*) to 50, 70 and 90 % contours of accumulated probability

5.10 Conclusions

This chapter has presented a discussion of the major challenges and opportunities involved in creating oil spill forecasting systems that account for uncertainty. Forecast uncertainty is added with each modelling step and parameterization, from the initial wind forecast to the oil spill diffusivity. There is a need for emergency responders to have a real-time understanding of the uncertainty of the forecast for today's spill, which might not be well predicted by hindcast studies at different times or locations. A systematic approach to including uncertainty at all levels in real-time forecasts has been proposed (Sect. 5.6), but there are significant engineering challenges to putting these ideas into operation at any particular location. Probably the most daunting challenge for many operational agencies will be bureaucratic rather than scientific or engineering: for a viable multi-model uncertainty forecast system, a research team needs direct access to an operational coastal hydrodynamic model to run multiple simulations with different wind forecasts. However, if the uncertainty associated with wind, wave, and hydrodynamic forecasts can be parameterized into a range of diffusivities for an oil spill model, then an approximation of the multi-model uncertainty can be directly integrated into an ensemble approach to the oil spill modelling (Sect. 5.9). The key point is that uncertainty in wind forecasts and the surface water's response to the wind are the critical drivers of uncertainty [27, 48], and therefore must be included in any uncertainty evaluation system—either directly through a multi-model approach, or indirectly through hindcast analyses and parameterization of particle diffusivity for a forecast oil spill model.

Acknowledgments The work of X. Hou and B.R. Hodges is based upon work supported by the Research and Development program of the Texas General Land Office Oil Spill Prevention and Response Division under Grant No. 13-439-000-7898 and in part by a grant from BP/The Gulf of Mexico Research Initiative. A. Orfila and J.M. Sayol would like to thank the support from MICINN through Project CGL2011-22964. J.M. Sayol is supported by the PhD CSIC-JAE program cofunded by the European Social Fund (ESF) and CSIC.

References

1. Abascal, A.J., Castanedo, S., Medina, R., Losada, I.J., Alvarez-Fanjul, E.: Application of HF radar currents to oil spill modelling radar. Mar. Pollut. Bull. **58**, 238–248 (2009)
2. Abascal, A.J., Castanedo, S., Medina, R., Liste, M.: Analysis of reliability of a statistical oil spill response model. Mar. Pollut. Bull. **60**, 2099–2110 (2010)
3. ASCE.: State-of-the-art review of modelling transport and fate oil spills, ASCE committee on modelling oil spills water resources engineering division. J. Hydraul. Eng. **122**, 594–609 (1996)
4. Beegle-Krause, C.J.: GNOME: NOAA's next-generation spill trajectory model. In: Oceans'99 MTS/IEEE Proceedings Conference Committee, vol. 3, pp. 1262–1266 (1999)
5. Bennett, J.R., Clites, A.H.: Accuracy of trajectory calculation in a finite-difference circulation model. J. Comput. Phys. **68**, 272–282 (1987)
6. Berry, A., Dabrowski, T., Lyons, K.: The oil spill model OILTRANS and its application to the Celtic Sea. Mar. Pollut. Bull. **64**, 2489–2501 (1990)

7. Castanedo, S., Juanes, J.A., Medina, R., Puente, A., Fernandez, F., Olabarrieta, M., Pombo, C.: Oil spill vulnerability assessment integrating physical, biological and socio-economical aspects: application to the Cantabrian coast (Bay of Biscay, Spain). J. Environ. Manag. **91**, 149–159 (2009)
8. Csanady, G.T.: Turbulent diffusion in the environment. Geophysics and Astrophysics Monographs, vol. 3. Reidel, Boston (1973)
9. Davies, A.M., Kwong, S.C.M., Flather, R.A.: On determining the role of wind wave turbulence and grid resolution upon computed storm driven currents. Cont. Shelf Res. **20**, 1825–1888 (2000)
10. De Dominicis, M., Leuzzi, G., Monti, P., Pinardi, N., Poulain, P.-M.: Eddy diffusivity derived from drifter data for dispersion model applications. Ocean Dyn. **62**, 1381–1398 (2012)
11. De Dominicis, M., Pinardi, N., Zodiatis, G., Archetti, R.: MEDSLIK-II, a Lagrangian marine surface oil spill model for short-term forecasting—part 2: numerical simulations and validations. Geosci. Model Dev. **6**, 1871–1888 (2013)
12. De Dominicis, M., Pinardi, N., Zodiatis, G., Lardner, R.: MEDSLIK-II, a Lagrangian marine surface oil spill model for short-term forecasting-part 1: theory. Geosci. Model Dev. **6**, 1851–1869 (2013)
13. Farrington, J.W.: Oil pollution in the marine environment i: inputs, big spills, small spills, and dribbles. Environ.: Sci. Policy Sustain. Dev. **55**, 3–13 (2013). doi:10.1080/00139157.2013.843980
14. Galt, J.A.: Uncertainty analysis related to oil spill modelling. Spill Sci. Technol. Bull. **4**, 231–238 (1998)
15. Gilbert, T.: Maritime response operations requirements for metocean data and services. In: Conference and Workshop on Meteorological and Oceanographic Services for Marine Pollution Emergency Response Operations, Townsville, Australia, 13–17 July 1998
16. Hackett, B., Comerma, E., Daniel, P., Ichikawa, H.: Marine oil pollution prediction. Oceanography **22**(3), 168–175 (2009). doi:10.5670/oceanog.2009.75
17. Haza, A.C., Ozgokmen, T.M., Griffa, A., Garraffo, Z.D., Piterbarg, L.: Parameterization of particle transport at submesoscales in the Gulf Stream region using Lagrangian subgridscale models. Ocean Model. **42**, 31–49 (2012). doi:10.1016/j.ocemod.2011.11.005
18. Hou, X., Hodges, B.R.: Integrating Google Maps/Earth in an automated oil spill forecast system. Mar. Technol. Soc. J. **48**(4), 78–85 (2014)
19. Hou, X., Hodges, B.R., Negusse, S., Barker, C.: A multi-model Python wrapper for operational oil spill transport forecasts. Comput. Sci. Discov. (submitted) (2014)
20. Jensen, J.R., Ramsey III, E.W., Holmes, J.M., Michel, J.E., Savitsky, B., Davis, B.A.: Environmental Sensitivity Index (ESI) mapping for oil spills using remote sensing and geographic information system technology. Int. J. Geograph. Inf. Syst. **4**, 181–201 (1990)
21. Ji, Z.G.: Hydrodynamics and Water Quality: Modelling Rivers, Lakes, and Estuaries. Wiley, Hoboken (2008)
22. Kim, T.-H., Yang, C.-S., Oh, J.-H., Ouchi, K.: Analysis of the contribution of wind drift factor to oil slick movement under strong tidal condition: Hebei spirit oil spill case. PLoS ONE **9**(1), e87393 (2014)
23. Lardner, R., Zodiatis, G., Hayes, D., Pinardi, N.: Application of the MEDSLIK Oil Spill Model to the Lebanese Spill of July 2006. European Group of Experts on Satellite Monitoring of Sea Based Oil Pollution, European Communities (2006)
24. Lehr, W., Jones, R., Evans, M., Simecek-Beatty, D., Overstreet, R.: Revisions of the ADIOS oil spill model. Environ. Model. Softw. **17**, 191–199 (2002)
25. Marinone, S.G.: A numerical simulation of the two- and three-dimensional Lagrangian circulation in the northern Gulf of California. Estuar., Coast. Shelf Sci. **68**, 93–100 (2006)
26. Mariano, A.J., Kourafalou, V.H., Srinivasan, A., Halliwell, G.R., Ryan, E.H., Roffer, M.: On the modelling of the 2010 Gulf of Mexico Oil Spill. Dyn. Atmos. Ocean **52**, 322–340 (2011). doi:10.1016/j.dynatmoce.2011.06.001
27. Marta-Almeida, M., Ruiz-Villarreal, M., Pereira, J., Otero, P., Cirano, M., Zhang, X., Hetland, R.D.: Efficient tools for marine operational forecast and oil spill tracking. Mar. Pollut. Bull. **71**, 139–151 (2013). doi:10.1016/j.marpolbul.2013.03.022

28. Martinez, W., Martinez, A.: Computational Statistics Handbook. Chapman and Hall/CRC, Boca Raton (2002)
29. Minguez, R., Abascal, A.J., Castanedo, S., Medina, R.: Stochastic Lagrangian trajectory model for drifting objects in the ocean. Stoch. Environ. Res. Risk Assess. **26**(8), 1081–1093 (2012)
30. Nittis, K., Perivoliotis, L., Korres, G., Tziavos, C., Thanos, I.: Operational monitoring and forecasting for marine environmental applications in the Aegean Sea. Environ. Model. Softw. **21**, 243–257 (2006). doi:10.1016/j.envsoft.2004.04.023
31. North, E.W., Adams, E.E., Schlag, Z., Sherwood, C.R., He, R., Hyun, K.H., Socolofsky, S.A.: Simulating oil droplet dispersal from the deepwater horizon spill with a Lagrangian approach. In: Liu, Y., Macfadyen, A., Ji, Z.-G., Weisberg, R.H. (eds.) Monitoring and Modelling the Deepwater Horizon Oil Spill: A Record-Breaking Enterprise. Geophysical Monograph Series, vol. 195, pp. 217–226. American Geophysical Union, Washington (2011). doi:10.1029/2011GM001102
32. Oberkampf, W.L.: Uncertainty quantification using evidence theory. Validation and Uncertainty Quantification Department, Sandia National Laboratories, Albuquerque, New Mexico (2005). http://web.stanford.edu/group/cits/pdf/lectures/oberkampf.pdf
33. O'Connor, C., Barker, C., Beegle-Krause, C.J., Eclipse, L., Zelenke, B.: General NOAA Operational Modelling Environment (GNOME) Technical Documentation. U.S. Department of Commerce, NOAA Technical Memorandum NOS OR&R 40, 105 pp. (2012)
34. Okubo, A.: Oceanic diffusion diagrams. Deep Sea Res. **18**, 789–802 (1971)
35. Price, J.M., Reed, M., Howard, M.K., Johnson, W.R., Ji, Z.-G., Marshall, C.F., Guinasso Jr., N.L., Rainey, G.B.: Preliminary assessment of an oil-spill trajectory model using satellite-tracked, oil-spill-simulating drifters. Environ. Model. Softw. **21**, 258–270 (2006). doi:10.1016/j.envsoft.2004.04.025
36. Proehl, J.A., Lynch, D.R., McGillicuddy Jr., D.J., Ledwell, J.R.: Modelling turbulent dispersion on the North Flank of Georges Bank using Lagrangian particle methods. Cont. Shelf Res. **25**, 875–900 (2005)
37. Reddy, C.M., Arey, J.S., Seewald, J.S., Sylva, S.P., Lemkau, K.L., Nelson, R.K., Carmichael, C.A., McIntyre, C.P., Fenwick, J., Ventura, T., van Mooy, B.A.S., Camilli, R.: Composition and fate of gas and oil released to the water column during the Deepwater Horizon oil spill. Proc. Natl. Acad. Sci. **109**(50), 20229–20234 (2012). doi:10.1073/pnas.1101242108/-/DCSupplemental
38. Samson, S., Reneke, J.A., Wiecek, M.: A review of different perspectives on uncertainty and risk and an alternative modelling paradigm. Reliab. Eng. Syst. Saf. **94**, 558–567 (2009)
39. Sayol, J.M., Orfila, A., Simarro, G., Conti, D., Renault, L., Molcard, A.: A Lagrangian model for tracking surface spills and SaR operations in the Ocean. Environ. Model. Softw. **52**(2), 74–82 (2014)
40. Schoch, G.C., Chao, Y., Colas, F., Farrara, J., McCammon, M., Olsson, P., Singhal, G.: An ocean observing and prediction experiment in Prince William Sound Alaska. Bull. Am. Meteorol. Soc. **92**, 997–1007 (2011). doi:10.1175/2011BAMS3023.1
41. Sebastiao, P., Soares, C.G.: Uncertainty in predictions of oil spill trajectories in open sea. Ocean Eng. **34**, 576–584 (2007)
42. SELFE v3.1dc User Manual. http://www.stccmop.org/knowledge_transfer/software/selfe/v3manual (2014). Accessed 21 Dec 2014
43. Shaw, J.M.: A microscopic view of oil slick break-up and emulsion formation in breaking wave. Spill Sci. Technol. Bull. **8**(5/6), 491–501 (2003). doi:10.1016/S1353-2561(03)00061-6
44. Singhal, G., Panchang, V.G., Lillibridge, J.L.: Reliability assessment for operational wave forecasting system in Prince William Sound, Alaska. J. Waterw., Port, Coast., Ocean Eng. **136**, 337–349 (2010). doi:10.1061/(ASCE)WW.1943-5460.0000056
45. Sobey, R.J., Barker, C.H.: Wave-driven transport of surface oil. J. Coast. Res. **13**(2), 490–496 (1997)
46. Sotillo, M.G., Fanjul, E.A., Castanedo, S., Abascal, A.J., Menendez, J., Emelianov, M., Olivella, R., Garcia-Ladona, E., Ruiz-Villarreal, M., Conde, J., Gomez, M., Conde, P., Gutierrez, A.D., Medina, R.: Towards an operational system for oil spill forecast over Spanish waters: initial developments and implementation test. Mar. Pollut. Bull. **56**, 686–703 (2008)

47. Stanovoy, V.V., Eremina, T.R., Isaev, A.V., Neelov, I.A., Vankevich, R.E., Ryabchenko, V.A.: Modelling of oil spills in ice conditions in the Gulf of Finland on the basis of an operative forecasting system. Oceanology **52**(6), 754–759 (2012). doi:10.1134/S0001437012060136
48. Stringari, C.E., Marques, W.C., Eidt, R.T., Mello, L.F.: Modelling an oil spill along the Southern Brazilian Shelf: Forcing characterization and its influence on the oil fate. Int. J. Geosci. **4**, 397–407 (2013). doi:10.4236/ijg.2013.42038
49. Texas Coastal Observation Network. http://www.tcoon.org (2014). Accessed 21 Dec 2014
50. Thorpe, S.A.: Langmuir circulation and the dispersion of oil spills in shallow seas. Spill Sci. Technol. Bull. **6**(3/4), 213–223 (2000)
51. Tintore, J., et al.: SOCIB: The Balearic Islands coastal ocean observing and forecasting system responding to science, technology and society needs. Mar. Technol. Soc. J. **47**(1), 101–117 (2013)
52. Texas Water Development Board Oil Spill Prevention & Response. http://www.twdb.texas.gov/surfacewater/bays/oil_spill (2014). Accessed 21 Dec 2014
53. Wang, S.-D., Shen, Y.-M., Guo, Y.-K., Tang, J.: Three-dimensional numerical simulation for transport of oil spills in seas. Ocean Eng. **35**, 503–510 (2008). doi:10.1016/j.oceaneng.2007.12.001
54. Xu, Q., Li, X., Wei, Y., Tang, Z., Cheng, Y., Pichel, W.G.: Satellite observations and modelling of oil spill trajectories in the Bohai Sea. Mar. Pollut. Bull. **71**, 107–116 (2013)
55. Xu, H.-L., Chen, J.-N., Wang, S.-D., Liu, Y.: Oil spill forecast model based on uncertainty analysis: a CAD study of Dalian Oil Spill. Ocean Eng. **54**, 206–212 (2012). doi:10.1016/j.oceaneng.2012.07.019
56. Yapa, P.D., Dasanayaka, L.K., Bandara, U.C., Nakata, K.: A model to simulate the transport and fate of gas and hydrates released in deepwater. J. Hydraul. Res. **48**(5), 559–572 (2010). doi:10.1080/00221686.2010.507010
57. You, F., Leyffer, S.: Mixed-integer dynamic optimization for oil-spill response planning with integration of a dynamic oil weathering model. AIChE J. **57**(12), 3555–3564 (2011)
58. Zelenke, B., O'Connor, C., Barker, C., Beegle-Krause, C.J., Eclipse, L.: General NOAA Operational Modelling Environment (GNOME) Technical Documentation. U.S. Department of Commerce, NOAA Technical Memorandum NOS OR&R 40. Seattle, WA USA: Emergency Response Division, NOAA. 105 pp. (2012)
59. Zhang, Y.J., Baptista, A.M.: SELFE: A semi-implicit Eulerian-Lagrangian finite-element model for cross-scale ocean circulation. Ocean Model. **21**, 71–96 (2008)

Chapter 6
Application of a Numerical Statistical Model to Estimate Potential Oil Spill Risk

Weijun Guo and Tiaojian Xu

Abstract Both deterministic and probabilistic strategies are employed in numerical oil spill model to estimate potential oil spill risk. The deterministic model simulates transport and weathering processes by means of a particle tracking method. While a Monte Carlo stochastic simulation approach is run for multiple scenarios, spill size, oil type, and environmental conditions (meteorological and hydrological data) combinations, to characterize the consequences of spills for a specified potential spill location. The statistically-defined oil spill map does not demonstrate the probabilities of oil-slick presence for each grid area, but also provide the information of the shortest arrival time which is quite vital for oil contingency plan.

6.1 Introduction

Oil spills has been a worldwide problem and are regarded as one of the most critical forms of marine pollution, bringing high risks to the open and coastal seas. Oil spill risk analysis is an area of research that becomes more and more important, especially after the Deepwater Horizon oil platform accident [10], due to the ever-increasing demand for fossil fuels. The transport and fate of spilled oil in the marine environment is affected by several dynamics processes, such as: the mechanical spreading, advection, turbulent diffusion, natural dispersion, sedimentation, resurfacing, stranding, evaporation, emulsification, dissolution, photo-oxidation, and biodegradation. The Lagrangian tracking method has been widely used to predict the motion of numerous individual oil particles, meanwhile the weathering model consisting of algorithms

W. Guo (✉)
College of Environmental Sciences and Engineering, Dalian Maritime University, Dalian 116026, China
e-mail: gwj5268@126.com

T. Xu
State Key Laboratory of Coastal and Offshore Engineering, Dalian University of Technology, Dalian 116024, China
e-mail: tjxu@dlut.edu.cn

M. Ehrhardt (ed.), *Mathematical Modelling and Numerical Simulation of Oil Pollution Problems*, The Reacting Atmosphere 2, DOI 10.1007/978-3-319-16459-5_6

to describe the mechanisms governing the fate of oil slick has also been developed [5, 11]. The principal aim of oil spill numerical model is for oil spill response strategy to reduce environmental and economic impacts when spills happen. A lot of deterministic models have evolved from two-dimensional trajectory-type models to three-dimensional models that include transport and fate processes [1, 13]. Forecasts of the oil trajectory and distribution are very useful to help make decisions to control and clean up spilled oil, but most oil spill models consider the oil-slick movement as a deterministic mechanism [2, 9]. When it comes to the problem of forecasting oil spill risk, the deterministic approach seems inadequate. Since the oil spill impacts vary according to a range of factors—from spill size, meteorological and hydrological conditions, and physicochemical properties of the oil, to the characteristics of the affected areas, statistical methods need to be employed to present a risk map of oil impacting. There is uncertainty on not only the amount and the position of oil that would be released but also the site and time dependent environmental conditions. Compared with the direct usage of hydrological and meteorological data in a deterministic model, adopting multiple scenarios run during a long period seems appropriate more to represent the feature of a specified domain. The progressive advancement of computer speed in the last decade makes the implementation of vast test simulation computations to investigate oil spill risk possible. The statistical model should evaluate not only the probability of a region to be influenced by spilled oil, but should also predict the time taken for the oil to reach the location.

What calls for special attention is that the degree of the vulnerability associated to oil spills for different regions varied obviously. For example, the marine protected areas are more sensitive for contaminants than harbour area. A quantitative methodology, by introducing the index accounting for both ecological and socioeconomic dimensions of vulnerability, to assess the spatial distribution and the degree of coastal vulnerability to oil spills was developed by [7].

6.2 The Basics of Oil Spill Modelling

6.2.1 Environmental Dynamical Factors

It benefits us little to have excellent results for spilled oil distribution if we are unable to accurately describe the surrounding conditions. Linkage to environmental dynamical model is of paramount importance for oil spill modelling since flow regimes are necessary for transport process. A high-resolution flow model is required to provide the complex hydrodynamics information of sea waters of the influence of atmospheric forcing, tide, surface wave, and river discharge.

Not only do the winds directly drift oil slick horizontally, they drive the breaking waves spilt the surface slick into droplets and then propel them into the water column, even as a crucial factor affecting evaporation process. The wind data can be obtained from field measurements for forecast/hindcast oil spills. Since the in-situ

meteorological data from the ocean is rare, it can be derived from spatial blending of high-resolution satellite data (for example, seawinds instrument on the QuikSCAT satellite– QSCAT) or numerical atmosphere models (for example, Fifth-Generation Pennsylvania State University/National Center for Atmospheric Research mesoscale model (known as MM5)). It is suggested that, in light winds, 3.5 % of the wind speed in the direction of the wind gives a good simulation of oil slick drift in offshore areas. The deflection angles vary between 0 and 25° to the right/left of the wind direction (northern/southern hemisphere) with a mean value of about 15° [1].

It is encouraging that a whole host of modern ocean circulation codes have enjoyed considerable success in simulating 3D ocean circulation, such as POM [3]; ROMS [14]; FVCOM [6]; ELCIRC [17] and SELFE [18]. Though their different numerical algorithms, the primitive equation are solved for describing the ocean motions induced by winds, tides and baroclinic effects. One main challenge to ocean circulation model is to resolve the complex geometry and bathymetry commonly found in coastal and estuary area in an accurate, efficient and robust way. An unstructured grid method used to discretize arbitrary geometries is a right key for this problem. It becomes particularly important for oil spill model for the grid can be densified in interested areas, which are near spill source points or highly sensitive to oil spill pollution.

Although surface wave makes water particles perform periodic back-and-forth excursions resulting in feeble net mass transport, they can modify ocean currents in many ways, wave radiation stresses, Stokes drift, forcing in form of dissipation of wave energy, and the surface/bottom drag coefficient. The progress in ocean wave forecasting during the last twenty years is outstanding. Nowadays we are able to estimate and forecast wave conditions, often with great accuracy, even with a detailed description of the event. Compared with phase-resolved type ocean wave model (e.g. Boussinesq equations and the mild slope equation), the phase-averaged model can provide the great advantage in terms of computational efficiency for the grid size is large enough to cover many wavelengths. The high-speed makes energy spectral model is widely adopted in a large area for predicting oil spill trajectory. At present, the third generation wave models (e.g. WAM, WAVEWATCH, SWAN) fully resolve the physical processes such as wind input, propagation and dissipation [4]. Through coupled with ocean circulation model, the spectral model is capable of resolving the flow change within wavelength and wave period in the computation [12].

6.2.2 Lagrangian Particle Method

To accurately describe the oil slick after breaking up into small fragments due to surface wave action and shear current, Lagrangian particle modelling of the transport process of clusters of leaking oil has been a common technique in oil spill numerical models for close to 20 years.

In this method, the particles will represent the mass of released oil which transported under the influence of the environmental forcing, turbulent diffusion and spreading processes. The Lagrangian particle-tracking trajectory algorithm is according to the simple formula

$$\frac{\mathrm{d}x_i}{\mathrm{d}t} = \mathbf{U}_a(x_i, t) + \mathbf{U}_d(x_i, t), \tag{6.1}$$

where x_i is the i particle position, $\mathbf{U}_a$ is the advective velocity from hydrodynamic model, and $\mathbf{U}_d$ is the random velocity fluctuations.

The advective velocity $\mathbf{U}_a$ of the oil particle is obtained by

$$\mathbf{U}_a = \mathbf{U}_{cr} + C_{wind} D_{wind} \mathbf{U}_{wind} + \mathbf{U}_{wave}, \tag{6.2}$$

where $\mathbf{U}_{cr}$ is the water current velocity interpolated from hydrodynamic model; $\mathbf{U}_{wind}$ is the wind velocity at 10 m above the water surface, C_{wind} is the wind drift factor. D_{wind} is the transformation matrix used to account the wind deflection angle, and this matrix is defined as follows:

$$D_{wind} = \begin{pmatrix} \cos B & \sin B \\ \sin B & \cos B \end{pmatrix}, \tag{6.3}$$

where $B = 25° \exp(-10^{-8}\mathbf{U}^3_{wind}/\nu g)$, ν is the kinematic viscosity of the seawater.

$\mathbf{U}_{wave}$ represents the wave Stokes drift calculated as

$$\mathbf{U}_{wave} = \frac{k\sigma H_s^2 \cosh(2kz_0)}{8\sinh^2(kh)}, \tag{6.4}$$

where k is the wave number, σ is the angular frequency, H_s is the significant wave weight, z_0 is the vertical position of oil particles measured upwards from the still water surface.

In addition to the determinate advective movements, oil droplets experience a random diffusion due to the turbulent fluctuations. The turbulent diffusive transport is calculated by a random walk procedure with a horizontal diffusion coefficient. Based on the previous study, the diffusive distance can be expressed by:

$$\Delta S = [R]_0^1 \sqrt{12 D_h \Delta t}, \tag{6.5}$$

where $[R]_0^1$ is the random number in the interval [0,1], D_h is the horizontal diffusion coefficient calculated from Smagorinsky formulation.

During the early stages of oil slick transformation, the mechanical spreading is a dominant process, which is treated as a diffusion process and is also simulated using the random walk method. The diffusion-like spreading coefficient is calculated from the following formulation:

$$D_{sp} = \frac{\pi K_s^2}{16}\left(\frac{\Delta g V_0^2}{\nu_w^{1/2}}\right)\frac{1}{\sqrt{t}}, \tag{6.6}$$

where V_0 is the volume of spilled oil, ν_w is water kinematic viscosity, ρ_w and ρ_o are the water and oil density, K_s is the empirical constant.

The process by which wind-driven breaking and non-breaking waves split the surface oil layer into droplets and then propel them into the water column is called natural dispersion. The rate of oil entrainment from slick to the water column can be scaled as [16]:

$$\lambda_{ow} = \frac{k_e \sigma \gamma H_s}{16 \alpha L_{ow}}, \tag{6.7}$$

where λ_{ow} is the entrainment rate, k_e is the coefficient evaluated from experiments, usually 0.3–0.5, γ is the dimensionless damping coefficient, α is coefficient concerning the mixing depth of the individual particles, L_{ow} is the vertical length-scale parameter.

Based on the laboratory data, the intrusion depth z_H that the oil droplet may penetrate is assumed as:

$$z_H = \left(1.5 + 0.35 \cdot [R]_0^1\right) H_s. \tag{6.8}$$

The horizontal diffusion coefficients are calculated from Smagorinsky formula, while the vertical is obtained from the level 2.5 turbulence model [3].

6.2.3 Weathering Processes

The fate of oil at sea is governed by the external environmental conditions as well as the several physicochemical properties of the oil. The change of physicochemical properties that spilled oil undergoes is collectively known as "weathering". The main weathering mechanisms which determine the fate of the oil slick are evaporation, emulsification, dissolution, oil-beaching, sedimentation, photo-oxidation, and biodegradation. Although the individual processes may act simultaneously, their behaviour importance varies with time. The last three ones will be predominant after the first week, but they are ignored for our short-term forecasting.

Evaporation, which usually accounts for about 30 % of spill oil mass loss, is a significant process changing oil mass and physical chemical properties during the first hours of an oil spill. The rate of evaporation is determined by the physicochemical properties of the oil as well as sea water temperatures, winds and other processes such as spreading and emulsification. The most frequently used equation to predict evaporation loss is proposed by [15]:

$$F_E = \frac{T_s}{BT_G} \ln\left[\frac{BT}{T}\frac{K_a t}{h}\exp\left(A - \frac{BT_0}{T}\right) + 1\right], \tag{6.9}$$

where F_E is the fraction evaporated; T_s is the sea temperature; T_0, T_G, A, and B are constants derived from distillation data; K_a is the mass transfer coefficient for evaporation; h is the slick thickness.

Emulsification is the process of the formation of water-in-oil emulsions changing the properties and characteristics of oil to a large degree. The rate of water incorporation increases as the water content in emulsion increases, so it is usually to character the emulsification degree. Most models that incorporate the phenomenon use an equation proposed by [8].

$$Y_w = K_b \left[1 - \exp\left(\frac{-2 \times 10^{-6}}{K_b} (1 + W)^2 t \right) \right], \tag{6.10}$$

where Y_w is the fractional water content; K_b is mousse viscosity constant.

Although it is considered that oil spilled on the sea surface will go much faster into evaporation than solution, the soluble oil components (in particular the aromatic compounds) can bring disaster to biologic life form a toxicological point of view. In this oil spill model, the mass of soluble is negligible compared to the dispersed oil droplet near the surface but of the same order of magnitude in the deeper water. The rate of dissolution is written as

$$D_t = K_d A_S D, \tag{6.11}$$

where D_t is the total dissolution rate of the oil slick; K_d is a dissolution mass transfer coefficient; A_S is the slick area; D is the oil solubility in water.

An oil slick may deposit or re-enter into the sea after reaching a shoreline. There are several factors affecting the result, including oil properties, shoreline types, onshore currents driven by wind stress and tidal currents. A model incorporating all these factors is almost impossible due to limited data available. So far, the simulation of the oil-shoreline interaction is primarily through empirical formulation because complex processes and limited available data. A parameter oil-holding capacity, which means how much oil will retain per unit area on a given type shoreline, is defined to quantify the interaction of oil with the shoreline. Once the shoreline oil-holding capacity is reached, oil will undergo longshore transport processes. Based on Humphreys study, the maximum beach capacity for oil can be expressed as

$$Q_{max} = L_s W_s D_s \eta_{eff}, \tag{6.12}$$

where Q_{max} is maximum capacity of a beach for oil; L_s, W_s and D_s are respectively length, width, and depth of sediments on the beach; and η_{eff} is effective porosity of the sediments on the beach (0.12–0.46).

6.3 Model Computational Frame

The main aim of the proposed model is to demonstrate the capability of a probabilistic method to predict the oil-impacted risk of around areas during a certain period.

For a typical trial, the model predicts the risk map of a certain location oil spill accidents adopting eight steps:

1. Forecasting the spill size, based on the historical data.
2. Selecting the oil properties of leaking oil (density, viscosity, surface tension, volatility, solubility, etc.).
3. Selecting the initial time when the spill happens, assuming spill accidents occur independently and uniformly in time.
4. Providing accurate information of temporal environmental conditions (currents, waves, and winds).
5. Simulating the processes of oil-slick transport and fate, recording relevant information (each grid be polluted or not, the shortest time for oil slick reaching each grid, the maximum of slick thickness on each grid during every scenario, etc.).
6. Running numerous times oil-spill events for statistical results.
7. Normalising different indicators into a homogeneous scale.
8. Synthesizes the environmental sensitivity indices for a risk map.

As mentioned above, the accurate information of environmental conditions is quite vital for oil spill model. The system provides the water flow dynamic information by employing the three-dimensional SELFE hydrodynamic model and SWAN wave generation and propagation model. SWAN supplies SELFE with arrays of significant wave height, wavelength, average wave periods, and wave direction, which are used to estimate the radiation stress terms in the momentum equations in SELFE, as well as the wave enhanced bottom friction and eddy viscosity. SELFE, in turn, sends to SWAN arrays of water depth, sea-surface elevation, and current velocity. Therefore, the coupled SELFE-SWAN allows the wave and current to interact with each other for improving accuracy.

The study sea area is divided into a number of unstructured grid cells, where all environmental data are based. The wind data are also interpolated on every grid cell. The deterministic oil spill model, based on Lagrangian oil spill transport module and weathering module, is run repeatedly under various possible environmental conditions including tidal current patterns, wind data and wave conditions. Then, a series of probability statistics analysis are performed to obtain oil spill influence data, such as the probability of water surface exposed to floating oil, mean oil slick thickness, and minimum oil slick arrival time. Combined with environmental sensitivity index, the final risk potential is acquired from these statistical data, called oil affecting parameter. The computational Frame is presented in Fig. 6.1.

Different sea waters polluted by the same volume oil pollutant may suffer from different degrees of impacts. To quantitatively assess the degree of vulnerability to oil spills, the environmental sensitivity indices (ESI), taking into account both ecosystem and human socioeconomic, are employed to evaluate the level of

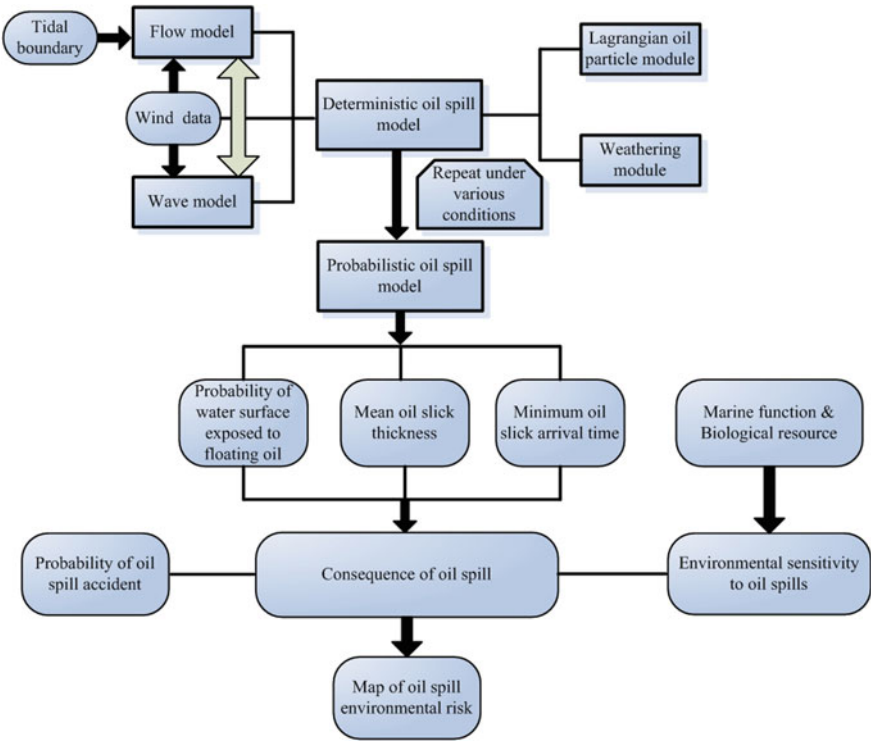

Fig. 6.1 Flowchart of computational frame

potential impacts. Referring to previous studies, we divide sea areas into five categories: marine conservation areas, fisheries, tourist areas, port and waterway areas and the general areas. The most sensitive ocean environment for oil spills is given an index of 1 (marine conservation area), the least sensitive, an index value of 0.1 (port and waterway area). The final composite index (R) of ocean vulnerability to oil spills formula is presented as follows:

$$R_j = \sum_{i=1}^{M} OP_i \cdot ESI_j, \tag{6.13}$$

where, *OP* are oil spill affecting parameters (i.e. the possibility of each grid being polluted, the shortest arrival time, and the thickness of the slick, etc.), *M* is the type number of oil spill affecting parameters.

6.4 Probabilistic Model Application

The Liaodong Bay is a semi-enclosed embayment located between the Liaodong Peninsula and Hebei Province. The bottom of bayhead is varied and is quite shallow, especially at the Liaohe Estuary where the water depth is generally less than 10 m. The basin geometry and shallow water cause the low water exchange ability and poor marine environmental capacity. A certain amount of marine reserves and leopard seal habitat are located in Liaodong Bay, meanwhile there are several oil terminal harbours distributed along the coastline (Fig. 6.2). Ocean transportation has been growing in recent years, and with it, the inherent risk towards the marine environment. Take a part for example, more than 3,000 tons crude oil has been inbound every year at the Port of Xianren Island. What is more, Panjin crude oil terminal, capable of receiving 300,000 deadweight tonnes (DWT) carriers, is being planned to construct. Assessment of oil spill risk for the ecology of the gulf needs to be addressed through scientific techniques to help manage the sensitive waters from accidental oil spills.

The SWAN with a time step of 60 min and SELFE with a time step of 5 min are both run over the 10-year period, from August 1, 1999 to July 31, 2008, based on the same computational grid containing 53,058 triangles and 32,296 nodes with the finest resolution near Panjin Port (Fig. 6.3). The spill location is set at the multi-channel intersection waters (121°57.55′E, 40°37.56′N), where oil pollution damage caused by collision between ships is most likely to occur. Due to no occurrence of oil

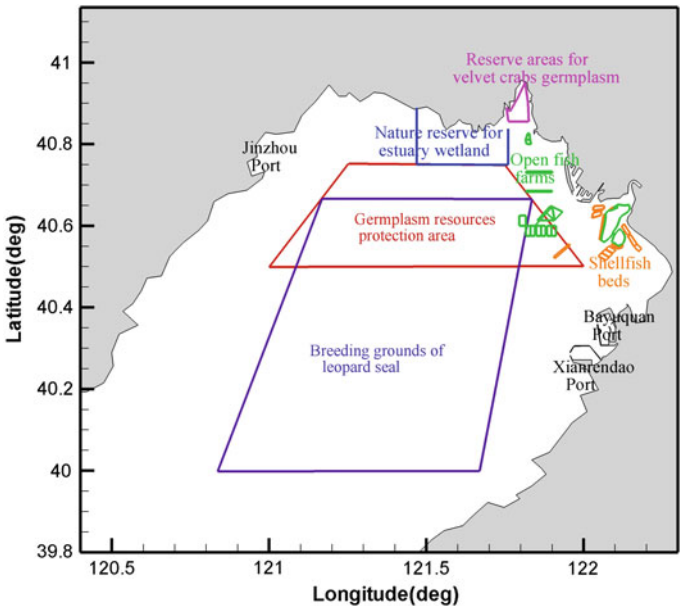

Fig. 6.2 Location map of Liaodong Bay

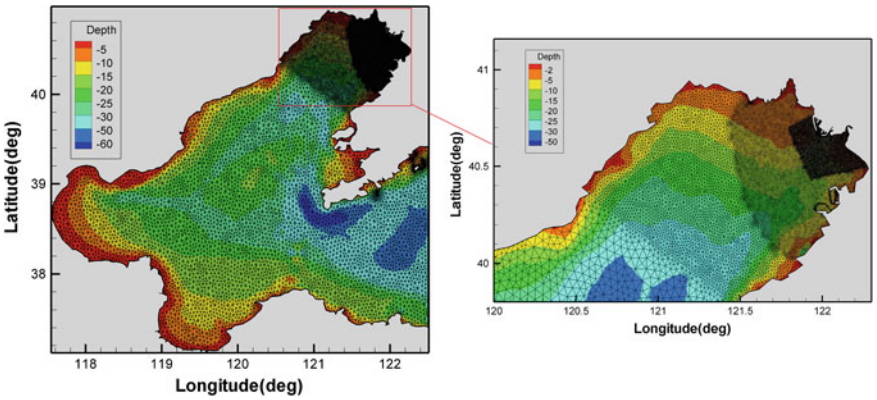

Fig. 6.3 The computational domain extends from Liaodong Bay to the Bohai Sea

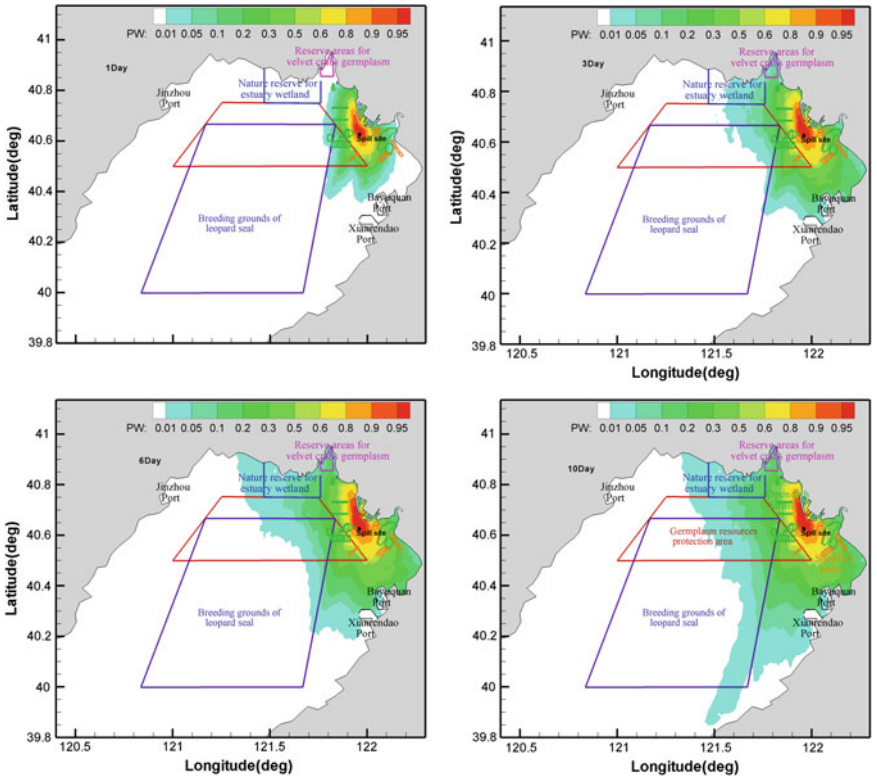

Fig. 6.4 Probability of sea surface to be polluted, 1, 3, 6 and 10 days after spill

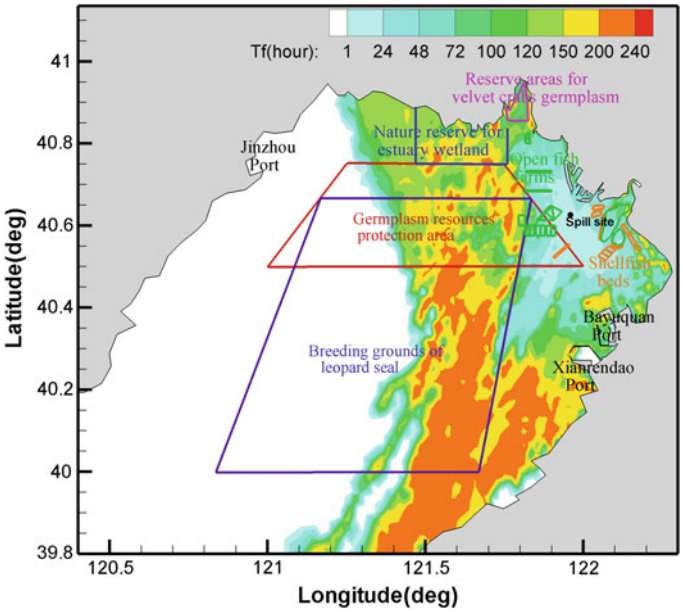

Fig. 6.5 Minimum arrival time to each cell

spill accidents for the newly planned port, the amount of released crude oil is set as 20,000 t by referring to the historical spill data of around identical one. The validity of the deterministic oil spill model has been proved available for the real oil spill event in Dalian New Port of China on 16 July, 2010 [9]. Trajectories of hypothetical spills are simulated stochastically for as long as 10 days over the 10-year simulation period. In theory, the more trials made, the more reliable results will be acquired. After 300 independent simulations of oil spill accident, it is found that oil reaching different locations varied less than 5 % if more than 200 runs have been made. So we are convinced that statistics from 300 times tests is adequate enough for risk analysis.

After 300 times simulation, Fig. 6.4 demonstrates the average probability distribution of spilled oil at various moments. The area likely to be affected (i.e. PW > 1 %) increases from 1,419 km^2 on the first day to 6,371 km^2 on the tenth day. Meanwhile, the area contaminated more than 50 % increases from 218.7 km^2 to 459.3 km^2, with the apparent slowdown in growth. This is because oil slick may travel back in the initial place under the effect of periodical tidal currents. Figure 6.5 shows the minimum arrival time affected by the oil slick for every cell, and Fig. 6.6 presents the distribution maximum oil slick thickness. The minimum arrival time to the nearby aquaculture areas is about 1 day, putting forward higher request to salvage. Its worth noting that part of germplasm resources protection area may be affected within 24 h. Once that occurs, it is a formidable task to protect the fragile reserve from oil spill. As for nature reserve for estuary wetland and breeding grounds of leopard seal, and reserve areas for velvet crabs germplasm, the minimum arrival time mostly exceeds

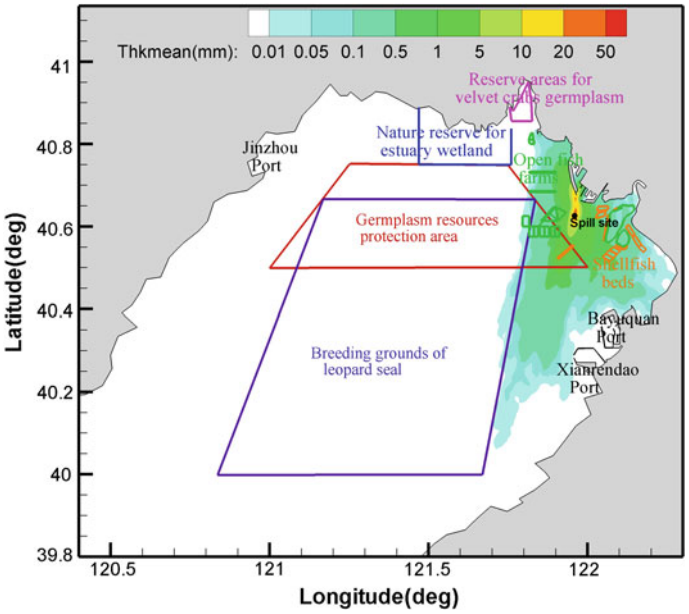

Fig. 6.6 The distribution average oil slick thickness

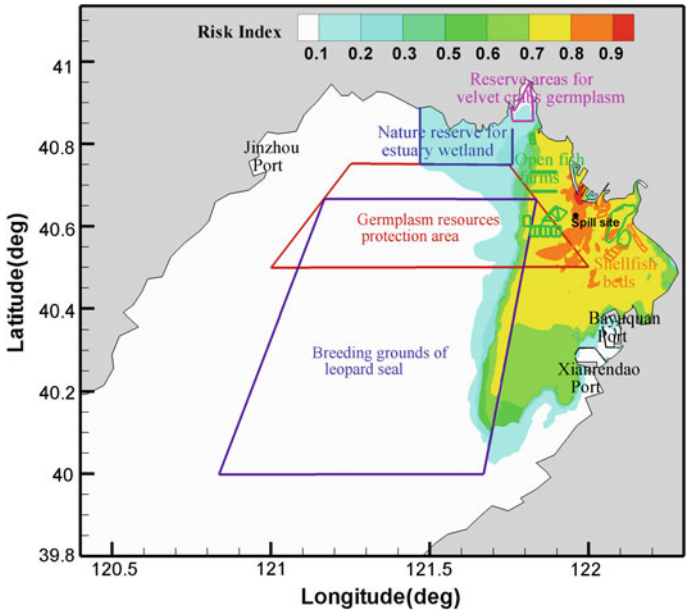

Fig. 6.7 Potential oil risk maps of Panjin Port

72 h, providing sufficient time for adopting protective measures. The sea surface covered by oil slick more than 10 mm distributes mainly around the spill site 10 km from north to south. The complex pattern extends along the local prevailing wind direction.

Synthesizing each kind of oil spill affecting parameters and the environmental sensitivity indices, the potential impact by oil spill of Panjin Port is obtained (Fig. 6.7). It is evident that the environmental resource locations closest to the spill site have the greatest risk. The potential risk of protected areas increased markedly, implying that their fragile vulnerability to spilled oil.

6.5 Conclusions

The ongoing development of international marine traffic brings serious oil spill risk to the water bodies adjacent to shipping zone. The regions of semi enclosed sea area are particularly sensitive with regards to environmental impact from oil spill. Run numerous times hypothetical spill accidents under varied realistic data fields of environmental conditions, the numerical statistical model has been developed to estimate the impact degree of the spills, including the probability of oil slick occurrence on water surface, mean average slick thickness on a given water surface, and minimum oil slick arrival time to a specified region. The sensitivity of different types of marine function zone taken into consideration, the comparative risk map is acquired which appears to be more effective for assessment of the ocean sensitivity around the potential hazard. An application is presented to generate the Panjin Port oil spill risk map by running the model. The results are quite vital for decision support providing regulating agencies with a guide for combating oil spills.

Nevertheless, further study is necessary for model improvements. This model is designed for use as a hazard-based assessment, so the possibility of oil spills occurring is not taken into consideration adequately in the analysis. In future work, the probability function of spill location and size based on both location sea state and human activities should be taken into account to reflect the nature of oil spill risk.

Acknowledgments The work described here would not have been possible without the efforts of my colleagues and students, including Li Zhang, Hui Liu, Yanni Hao, Yan Zou and Qi Guo. This work is sponsored by the Ministry of Transport of China under No. 2013 329 225 240, the Fundamental Research Funds for the Central Universities (2012QN059) and National Natural Science Foundation of China (No. 41206095, No. 51409037).

References

1. ASCE, Task Committee.: State-of-the-art review of modeling transport and fate of oil spills. J. Hydraul. Eng. **122**, 594–609 (1996)
2. Azevedo, A., Oliveira, A., Fortunato, A.B., Zhang, J., Baptista, A.M.: A cross-scale numerical modeling system for management support of oil spill accidents. Mar. Pollut. Bull. **80**, 132–147 (2014)

3. Blumberg, A.F., Mellor, G.L.: A description of a three-dimensional coastal ocean circulation model. In: Heaps, N. (ed.) Three-Dimensional Coastal Ocean Models, vol. 4, pp. 1–16. AGU, Washington (1987)
4. Booij, N., Ris, R.C., Holthuijsen, L.H.: A third generation wave model for coastal regions, part I: model description and validation. J. Geophys. Res. **104**(C4), 7649–7666 (1999)
5. Chao, X., Shankar, N.J., Wang, S.S.Y.: Development and application of oil spill model for Singapore coastal waters. J. Hydraul. Eng. **129**, 495–503 (2011)
6. Chen, C., Liu, H., Beardsley, R.C.: An unstructured grid, finite-volume three-dimensional, primitive equations ocean model: application to coastal ocean and estuaries. J. Atmos. Ocean. Technol. **20**, 159–186 (2003)
7. Frazão Santos, C., Carvalho, R., Andrade, F.: Quantitative assessment of the differential coastal vulnerability associated to oil spills. J. Coast. Conserv. **17**, 25–36 (2013)
8. Guo, W.J., Wang, Y.X.: A numerical oil spill model based on a hybrid method. Mar. Pollut. Bull. **58**, 726–734 (2009)
9. Guo, W., Hao, Y., Zhang, L., Xu, T., Ren, X., Cao, F., Wang, S.: Development and application of an oil spill model with wavecurrent interactions in coastal areas. Mar. Pollut. Bull. **84**, 212–224 (2014)
10. Mariano, A.J., Kourafalou, V.H., Srinivasan, A., Kang, H., Halliwell, G.R., Ryan, E.H., Rofferc, M.: On the modeling of the 2010 Gulf of Mexico oil spill. Dyn. Atmos. Oceans **52**, 322–340 (2011)
11. Marta-Almeida, M., Ruiz-Villarreal, M., Pereira, J., Otero, P., Cirano, M., Zhang, X., Hetland, R.D.: Efficient tools for marine operational forecast and oil spill tracking. Mar. Pollut. Bull. **71**, 139–151 (2013)
12. Mellor, G.L.: The depth-dependent current and wave interaction equations: a revision. J. Phys. Oceanogr. **38**, 2587–2596 (2008)
13. Reed, M., Johansen, Ø., Brandvik, P.J., Daling, P., Lewis, A., Fiocco, R., Mackay, D., Prentki, R.: Oil spill modeling towards the close of the 20th century: overview of the state of the art. Spill Sci. Technol. Bull. **5**, 3–16 (1999)
14. Shchepetkin, A.F., McWilliams, J.C.: The regional oceanic modeling system (ROMS): a split-explicit, free-surface, topography-following-coordinate oceanic model. Ocean Model. **9**, 347–404 (2005)
15. Stiver, W., Mackay, D.: Evaporation rate of spills of hydrocarbons and petroleum mixtures. Environ. Sci. Technol. **18**, 834–840 (1984)
16. Tkalich, P., Chan, E.S.: Vertical mixing of oil droplets by breaking waves. Mar. Pollut. Bull. **44**, 1219–1229 (2003)
17. Zhang, Y., Baptista, A.M., Myers, E.P.: A cross-scale model for 3D baroclinic circulation in estuary-plume-shelf systems: I. Formulation and skill assessment. Cont. Shelf Res. **24**, 2187–2214 (2004)
18. Zhang, Y., Baptista, A.M.: SELFE: a semi-implicit Eulerian-Lagrangian finite-element model for cross-scale ocean circulation. Ocean Model. **21**, 71–96 (2008)

Chapter 7
Structural Analysis of Oil-Spill Booms

Frédéric Muttin

Abstract Floating barriers, often named booms, are used to contain oil. They are a main device installed during pollution response and their efficient positioning is a critical question for both effective oil containment and structural material resistance. A 3D non-linear finite element model for static moored booms is forced by sea current hydrodynamic pressure. To improve the numerical convergence of the membrane equilibrium during the Newton-Raphson scheme we initialize the 3D solution by using a 2D non-linear cable model. The membrane stretched surface representing the boom permits to define the material stress and the boom subsea skirt angulation. Full-scale experiments are performed on the European Atlantic coast to measure boom mooring tension and boom skirt geometry. In this chapter, *in-situ* experimental method at coastal sea is given. Validation protocol of numerical results by experimental ones is described. Threshold values on boom tension, to avoid structural break, and skirt angle to evaluate the oil containment efficiency are discussed. Finally, methodological aspect to combat oil pollution by using contingency planning based on such numerical modelling of booming structure is addressed.

7.1 Introduction

Oil-spills at large medium or small scales are a main challenge for response preparedness. First challenge for intervention is to contain the oil on the sea surface so that the pollutant can be recovered. When oil containment fails, the risk is that the pollutant enters in contact with the shore giving a polluted material weight multiplied by a ratio generally known to be 10. This ratio was observed during Erika tanker crisis [16].

The purpose of this chapter is to study a mechanical device named boom which constitutes a floating barrier against oil drift. Such response material can be used to contain the oil when the sea current is small and under 0.35 m/s. When the current

F. Muttin (✉)
EIGSI, La Rochelle and Casablanca Engineering School, 26 Rue Vaux de Foletier, 17041 La Rochelle, France
e-mail: muttin@eigsi.fr

M. Ehrhardt (ed.), *Mathematical Modelling and Numerical Simulation of Oil Pollution Problems*, The Reacting Atmosphere 2, DOI 10.1007/978-3-319-16459-5_7

is higher and remains moderate, less than around 1 m/s, a boom can be moored to deviate the pollutant to a sheltered place. For higher current velocity, the strategy is to tow with one ship or more a boom to collect the oil as a sweeping process. The oil pollution concerned is the floating fraction. The others are the sinking, diluted and evaporated fractions [7].

A boom is composed of fabric materials, with a float and a subsea skirt, reinforced by longitudinal leach and a weighting chain at its bottom. Such device is efficient to contain oil because of the hydrodynamic of the floating oil above the sea water along its subsea part. The hydrodynamic efficiency is the scientific challenge mostly addressed [2, 6, 15, 17]. The leakage modes [3] are studied experimentally [2] and numerically [17]. Installed in the environment or in an harbour a boom is a coastal structure who can fails by swinging mooring or material breaking as a consequence of large stress in the fabric or strong tension in the mooring lines. The structural behaviour of booms is a scientific challenge weakly studied [11, 12].

The scientific question addressed here is to propose a numerical modelling of boom considered as a structural component. To that end a finite element method is used. The results of the model permit to construct a scientifically based response plan using boom instead of resorting to empirical approach. The numerical results are compared to an *in-situ* experiment to validate the model. An oil leakage criterion based on the boom subsea skirt vertical angulation permits to evaluate the operational performance of a boom plan in its environment during a given time.

Many boom references are proposed by the manufacturers. Nevertheless, we adopt the general usage of two main classes to distinguish the different products. The booms dedicated to high sea and relatively general environmental conditions are made of a pneumatic floating tube having a diameter around 0.5 m. The skirt height composed of a single fabric layer can be around 0.75 m. They can be named curtain or inflated boom. A such material is shown on the following Fig. 7.1.

The booms used in calm water or harbour with safe environmental conditions are smaller and lighter than curtains. They are composed of a sequel of juxtaposed vertical rigid bodies assembled between two vertical fabric layers. Their total height is around 0.7 m. They can be named barrier or rigid boom. The following Fig. 7.2 shows such boom reference.

The chapter is organised as follows. First, a 2D numerical model is described based on a non-linear elastic cable element. Secondly, a 3D membrane model permits to enrich the 2D solution by giving the geometry of the boom components and the internal stress in the constitutive materials. The third part is dedicated to the full-scale experiment carried out in the Elorn estuary, Brittany, France, with the material shown in Fig. 7.2.

Fig. 7.1 Curtain or inflated boom

Fig. 7.2 Barrier or rigid boom

7.2 Oil-Spill Booms as a Curvilinear Elastic 2D Domain

7.2.1 Context

Floating booms to combat oil pollution are analysed as a curvilinear domain c moving in the two-dimensions of the free surface of the sea water. The vertical motion depending of the buoyancy/gravity forces is not considered here. The horizontal behaviour depends only on the pressure of a water current. Supplementary waves and wind forces can be taken into account. The wind generates an aerodynamic pressure on the aerial part of the boom which remains low considering the wind gradient leading to a zero value of wind on the water surface.

7.2.2 The Theoretical Model

The curvilinear model for a floating boom section AB is based on its spatial position $\xi(s)$ having two coordinates x and y on the sea surface. The domain c is defined in term of the curvilinear coordinate s by

$$\xi(s) = (x, y)(s), \qquad s_A \leq s \leq s_B, \tag{7.1}$$

where s_A and s_B represent the boom end-points A and B. The domain is supposed static without time dependency.

The nonzero derivative of $\xi(s)$

$$T(s) = \frac{d}{ds}\xi(s) \tag{7.2}$$

defines the unit tangent vector to the boom. The unit normal vector $N(s)$ is defined by

$$\frac{d}{ds}T(s) = \frac{N(s)}{R(s)}, \tag{7.3}$$

where

$$R(s) = \frac{1}{\| \frac{d}{ds}T(s) \|} \tag{7.4}$$

denotes the radius of curvature.

The stress force along the boom is defined in term of s by

$$F_{int}(s) = t(s) \cdot T(s), \tag{7.5}$$

where $t(s)$ represents the tension of the domain.

The external force along the curvilinear domain is defined by the normal current pressure $p(s) \cdot N(s)$ and the tangential hydrodynamic friction $\tau(s) \cdot T(s)$

$$F_{ext}(s) = p(s) \cdot N(s) + \tau(s) \cdot T(s), \tag{7.6}$$

where $p(s)$ is the pressure and $\tau(s)$ is the tangential friction on the boom c.

Neglecting inertial force corresponding to very low acceleration of booms, the equilibrium equation of the curvilinear domain is

$$\frac{d}{ds} F_{int}(s) + F_{ext}(s) = 0, \qquad \forall s \in]s_A, s_B[. \tag{7.7}$$

This equation is strongly non-linear and depends on the elastic force $t(s)$ and on the boom position ξ.

The constraint on the boom section length L between A and B permits to pose the problem. Generally we use $s_A = 0$ and $s_B = L$.

We will consider mainly moored static booms. It is commonly accepted that the friction $\tau(s)$ of the flow along the boom is negligible. This is not the case for boom during towing as a flag-like structure (i.e. one end-point is free). In this case, the tangential friction outweighs the normal pressure.

Remark 7.1 The external force F_{ext} has an implicit dependence with the position of the unknown domain c. To simplify the fluid-structure interaction problem we use a predictor of the boom domain geometry. This predictor can be built for example by a catenary curve as barrier geometry.

Dirichlet boundary conditions are applied at the end-points of the curvilinear domain $\xi(s_A) = A$ and $\xi(s_B) = B$. They represent the mooring positions of a boom section AB. It should be noted that a boom plan can be made of several adjacent sections.

Remark 7.2 The oil pollutant behaviour is not included in the domain equilibrium because the oil density is near the water density and thus it does not affect the hydrodynamic pressure.

We do not consider sorbent boom which can have a non-linear stress/strain behaviour. A non-woven material can be non-elastic. Netting structures are not considered.

7.2.3 The Numerical Model

The finite element method is used to define a set c_{h_H} of rectilinear segments representing an approximation of the curvilinear domain c. The mesh horizontal resolution is denoted as h_H. Each two-node element represents a small elastic cable which remains straight during any kind of deformation. The tension $t(s)$ is considered constant along each cable and it depends on the initial and deformed lengths of the

element, the Young modulus and the cable straight section [13]. This section is a normal section of the floating barrier which is composed of three kinds of materials: the curtain fabric, the upper aerial leach and the subsea chain.

The approximation of the continuous equilibrium equation permits to define a discrete problem. The curvilinear derivative operator on the internal force $\frac{d}{ds}F_{int}(s)$ is transformed into a vectorial difference at each node between neighbouring element tensions. A weighted summation of the external force $F_{ext}(s)$ is made at each node over its two adjacent elements. The nodal displacement vector is denoted U. We use the same notations F_{int} and F_{ext} after the transformations from the continuous to the discrete formulations. They depend on the discrete problem unknown U, i.e., the equivalent internal force vector $F_{int}(U)$ and external force vector $F_{ext}(U)$. The non-linear discrete equation is written in term of the residual vector $R(U)$

$$R(U) = F_{int}(U) - F_{ext}(U) = 0. \tag{7.8}$$

The equation is solved using the Newton-Raphson method. The method uses the derivative $\frac{d}{dU}R(U)$. The derivative of the internal force vector is defined on each element by a stiffness matrix. The external force vector derivative is not taken into account here.

Remark 7.3 The current pressure $p(s)$ is defined by a classical hydrodynamic rule

$$p(s) = \frac{1}{2}\,\rho_w\, C\, v(s)^2, \tag{7.9}$$

where ρ_w is the water density, C the drag coefficient and $v(s)$ the current velocity.

The atmospheric wind action on the aerial part of the barrier can be defined by using a similar rule than those for the current pressure by considering the air density ρ_{air} and the wind velocity taken at the altitude of the float.

The waves generated by the wind act on the subsea part of the barrier. A wave pressure can be added to the current pressure by using an incident velocity v_w supplementary to the current velocity $v(s)$. The velocity v_w can be defined by using the square root of the significant wave height.

7.2.4 Operational Point of View of the Numerical Results

From the operational point of view the 2D model gives the boom tensions $t(A)$ and $t(B)$ at both end-points A and B of a boom section. The direction of the mooring tensions $T(A)$ and $T(B)$ are also given by the numerical model. The hydrodynamic current can vary in time depending on the tide stages. As a consequence boom tension and boom tangent direction can be time-dependent.

The oil effective containment is defined by a post-treatment based on the current velocity giving the oil normal velocity to the boom. The threshold normal velocity generally considered is 0.35 m/s

$$v(s) \cdot N(s) \leq 0.35\,\text{m/s} \qquad \forall s \tag{7.10}$$

for boom efficiency to contain oils.

The oil leakage can be based on the current velocity $v(s)$ the normal vector $N(s)$ to the boom and the oil properties. As a consequence the oil containment efficiency of the barrier can vary during time in term of the current velocity and the boom geometry. We use the Lee criteria [10] to define the oil leakage at any curvilinear coordinate of the domain. A Boolean value is defined by using the comparison of $v(s) \cdot N(s)$ with a threshold velocity depending of the oil density ρ_{oil}, the oil-water interfacial tension σ_{ow}, ρ_w and the boom draught.

The hydrodynamic friction (tangential viscous drag) has not been considered. This force can occur for example during the towing of a barrier. The friction is defined by using the tangent velocity $v(s) \cdot T(s)$ to the boom. The friction coefficient of the boundary layer of the fluid in the vicinity of the boom is not detailed here. The non-smooth geometry of a barrier (Fig. 7.2) and the smoother geometry of a curtain, suggest that the friction during towing is lower for curtain than for barrier, considering same boom draught and length.

Generally, the ratio between the boom section length L and the end-points distance belongs to [1.07, 1.10]. It permits to avoid boom over-tension. The model results can be used for a preliminary evaluation of the barrier length installed between the mooring points.

7.2.5 Others Notions

The boom model uses as input the velocity of the surface of the water domain. The velocity map of the coastal water is a time-dependent function which can be solution of an hydrodynamic model. Such data may depend on local ocean-atmosphere interaction and river-estuarine morphology of the coastal region studied.

The mooring lines connected to the boom end-points have not been studied here. The end-points are supposed fixed. The hypothesis made permits to reduce considerably the computation time, for example when the current direction reverses at high and low tides. The drawback of this hypothesis is the avoidance of the swinging radius prediction of the moored device.

This section presents a curvilinear numerical model for a floating boom in the horizontal plane of the water surface. The next section will describe a 3D membrane model including a vertical motion of the boom. The 2D result initializes the 3D fine grid solution with a similarity to the injection used in a multi-grid V-cycle [8].

7.3 Floating Booms as a 3D Elastic Membrane

7.3.1 Context

This section presents a 3D model representing an oil-spill boom by using an elastic surface. For a numerical convergence reason, this approach is described after the 2D curvilinear model described in Sect. 7.2. The convergence of the 3D non-linear problem solution is a tricky question. The convergence can be accelerated or obtained at least if the 3D domain equilibrium geometry possesses a valuable initial position. This one can be given by the extrapolation of the curvilinear domain result.

7.3.2 Non-Linear Elastic Membrane

A floating boom is supposed to be a domain ω composed of several parts. For curtains (Fig. 7.1) we define four parts having different geometries and roles. The float inflated by air is a cylinder; the skirt is a rectangle made of fabric material composed by one or two layers; the chain at the bottom of the skirt permits to weight the curtain and to concentrate the longitudinal tension is a rectangle made of steel material, the leach at the top the float permits to handle by hand the boom and to concentrate equally longitudinal tension is a rectangle made of fabric material. An eventual fifth part is another leach in the vicinity of the waterline.

For barriers which have a simplified design, the float and the skirt are gathered (Fig. 7.2). We define three parts. The float and the skirt are composed of rigid vertical bodies assembled between two fabric sheets are a rectangle made of a fabric material. Bottom chain and upper leach parts are defined in a same way than curtains.

During the displacement u of ω the domain can be deformed and the strain measure is given by the Green tensor $x(u)$ defined in term of the displacement differential du. The mechanical stress inside the membrane is defined by the Piola-Kirchhoff tensor of second kind $\sigma(u)$. Taking into account the high stiffness of the constitutive coated fabric we use an approximation by considering a linear behaviour law between strain and stress tensors. The material is supposed elastic having a high Young modulus.

The internal elastic energy $e(u)$ inside the elastic membrane is defined by

$$e(u) = \frac{1}{2} \int_{\omega} \mathrm{tr}(\sigma(u)x(u))\, d\omega, \tag{7.11}$$

where tr denotes the trace operator.

Moored in sea water to contain floating oil, the external loads on booms are the normal pressure of the float pneumatic inflation, the normal hydrodynamic pressure of the flow on its submarine part (skirt and subsea float part), the normal hydrostatic

pressure and the gravity force. The potential energy of the external actions is defined by the linear form l

$$l(v) = \int_{\omega} (p_N \cdot v) + (\rho_\omega g \cdot v)\, d\omega, \tag{7.12}$$

where p_N is the resultant normal pressure, ρ_ω is the membrane surface density and g is the gravity vector.

The non-linear equilibrium equation is given by

$$\text{Find } u \text{ admissible, such that } \quad \frac{d}{du}\, e(u) \cdot v = l(v) \quad \forall v \text{ admissible}, \tag{7.13}$$

where the displacement field u respects the boundary conditions at the end-parts and waterline of the boom domain.

Dirichlet boundary conditions are used at the two end-parts $\partial\omega_A$ and $\partial\omega_B$ of the boom domain boundary corresponding to the end-points A and B of the curvilinear domain c. The same kind of boundary condition is applied to the displacement along the vertical z of the membrane waterline $\partial\omega_c$ in the vicinity of c.

$$\begin{aligned} u &= 0 \quad \text{on} \quad \partial\omega_A \quad \text{and} \quad \partial\omega_B \\ u &= 0_z \quad \text{on} \quad \partial\omega_c \end{aligned} \tag{7.14}$$

As a consequence, the boom hydrostatic pressure is defined as the reaction force resulting from the Dirichlet boundary condition applied to $\partial\omega_c$.

A classical mooring device of a boom is composed of a transverse rigid beam linked to two mooring cables, a buoy, a mooring chain and a dead-mass on the sea floor. Such parts of a boom implementation are not detailed here. Adjacent barrier or curtain sections can be connected by using standardized self-rigid ending beams having a Z-shape. Boom inertial force can be neglected in the membrane equilibrium as has been the case in Sect. 7.2.2.

7.3.3 The Numerical Method

The Haug-Powell quadrilateral finite element is used to define the discrete problem [9]. This element is based on the four bilinear shapes functions

$$N_i(\xi_1, \xi_2) = \frac{1}{4}(1 \pm \xi_1)(1 \pm \xi_2), \qquad i = 1, 2, 3, 4 \tag{7.15}$$

As for the curvilinear domain approach (7.8) the 3D non-linear equations of the discrete equilibrium problem can be written

$$\text{Find } U \text{ admissible, such that } \quad F_{int}(U) = F_{ext}(U), \tag{7.16}$$

where U denotes the nodal displacements of the finite element mesh, F_{int} are the equivalent nodal forces representing the internal membrane stress and F_{ext} are the external loads resulting from the pressures and gravity forces.

The external forces are supposed to be given by $F_{ext,prox}$ defined over the initial geometry of the membrane mesh and remaining independent of the displacement U.

To achieve the convergence of the Newton-Raphson method we use a threshold on the maximal nodal displacement component to avoid unrealistic position updating. As mentioned in the context we must use an initialization of the membrane position given by the curvilinear domain solution to have a convergence of the Newton-Raphson method. The quadratic convergence is observed when U is in the solution vicinity.

The mesh size is defined by using two resolutions. The horizontal resolution h_H follows the curvilinear domain resolution. The vertical resolution h_V takes into account the different parts of the curtain or barrier, the upper leach, the float, the skirt and the bottom chain. The vertical resolution permits to define the skirt angulation θ along the curtain or barrier. Measure the skirt curvature necessitates three nodes at least on a same vertical boom section.

The number of iterations required for the Newton-Raphson method convergence depends on two precisions. The first one is the maximal out of balance between external and internal forces. The second one is the maximal nodal coordinate updating. The values commonly used using S.I. units are 1 N for the out of balance of nodal forces and 10^{-3} m for the nodal displacements.

7.3.4 Operational Usefulness of the Numerical Results

For oil-spill response using floating barrier, the 3D approach permits a complementary prediction of the pollutant containment with respect to the curvilinear model. The indicators focus principally on the skirt angulation and mooring tensions at both end-parts of the boom.

The skirt angulation is a curvilinear function θ given by the angle between the vertical and the skirt section considered as a segment defined with the bottom chain node and the upper finite element node at the vicinity of the sea surface. The geometry of the boom ω is numerically defined in term of the sea water current. Oil-spill model can use at the water surface the equilibrium geometry of the boom during time. Depending of the oil containment efficiency of the boom, the oil-spill model can use a boundary condition for the oil drifting velocity.

The mooring tension at a boom section end-part is defined by the summation of the nodal reaction forces corresponding to the Dirichlet boundary condition at this location. The eigenvalues of the stress tensor σ defined on the membrane at equilibrium give the principal stresses σ_{max} and σ_{min} on the tensile structure. Fabric, leach and bottom chain tensions are defined in term of the boom plan geometry for the given conditions. The 3D model gives results for an evaluation of contingency plan and boom design.

Safety coefficient can be introduced to choose the suitable mooring line or towing device attached to the boom. The safety coefficient to be applied for a numerical result on boom tension varies from 1.8 to 7. This large amplitude illustrates the difficulty to quantify the uncertainty in the forcing conditions during a maritime or coastal operation.

The reaction force along the vertical at a node belonging to $\partial\omega_c$ on the sea surface is interpreted as the local buoyancy force of the boom. Under normal boom usage, without the observation of swimming, surfing or splashing behaviours, the vertical reaction permits a model validation. The local reaction can be interpreted as the linear mass density of the boom. Depending of boom size and design the linear density varies from 4 to 12 kg/m. The numerical result on the vertical reaction can be interpreted in another way. The nodal reaction differs significantly from the boom linear density can be interpreted as a wrong implementation of the boom under the given conditions.

When the current velocity is higher than a threshold value of a barrier efficiency, a dynamic recovery of oil by using a towed barrier can be proposed. Based on the above static model a pseudo dynamic model for a towed barrier can be defined. Let us consider a towing along a line parallel to a uniform sea current and a boat moored at each boom end-parts. The sea water velocity along the barrier becomes the velocity V_b of the boat. At each time step, the equilibrium geometry is moved according to the updated towing boat position. The Dirichlet boundary conditions are applied to both updated end-parts of the barrier. The mooring line tensions can be used to limit the velocity V_b and thus to avoid structural damage. Velocities interpolation and composition as well as geometry updating, during more general towing circumstances with non-straight route, using two boats and under a non-uniform sea current are not detailed here.

7.3.5 Statement

The principal drawback of the 3D membrane model usage is the difficulty to ensure in any case the convergence of the Newton-Raphson method. Initialization with a 2D model result allows to increase the robustness of the approach. With the vertical component, a principal advantage of the 3D model is to give the skirt motion throughout boom section. As a consequence, a fluid flow study of the sea water and oil pollutant can be based on a realistic boom geometry.

7.4 Full-Scale Experiment of a Floating Boom in a Coastal Environment

7.4.1 Introduction

We present an experiment carried out during the beginning of November 2009 in the Elorn estuary located in the Brest Bay, Brittany, France. This experiment of a 210 m long curtain composed of three sections of 70 m has followed a previous experiment in May 2008 in the Harbour of La Rochelle with a 100 m long barrier. This first experiment has permitted to elaborate the experimental protocol and the logistic and maritime operations. Presently, we will describe essentially the Elorn experiment and we will refer to the first experiment when necessary.

7.4.2 Materials and Methods

Let us describe the natural site, the floating boom and the instruments used for measurements.

Elorn Site

The winter season is representative of a real oil-spill incident having higher probability to occur in winter for this Atlantic region. The nominal period for measurements is taken at the mid flooding tide during the afternoons of November 2–6, 2009. Time of low tide is 11h49 and high tide occurs at 17h47 during November 4. Tide heights are respectively 1.3 and 7.05 m at these times.

The Elorn site at the bottom of the Brest bay has been chosen for two reasons. The probability of a spill exists in that site with respect to the maritime traffic and overall activity. The sensitivity of the coast where the boom was installed is very high considering the presence of the pyrotechnic plan of the French Navy.

The site is a relatively protected area from ocean waves and swell. The existence of hills parallel to the estuary coasts can create a Venturi effect for wind coming from the South West direction.

More precisely, the site is located North East in the “Rade de Brest”, and belongs to the Elorn river estuary, in the vicinity of the maritime access and port named “Le passage” of the Relecq-Kerhuon city.

The boom position corresponds to a part of the National contingency plan “ORSEC Maritime” of the department “Finistère”. The Elorn estuarine site used for the experiment is shown on the following Fig. 7.3.

The estuary is oriented from South West to North East. The ocean flooding tide current (i.e., the tide goes up) comes from the South West. The Elorn river flows from the North East.

Fig. 7.3 Elorn estuarine site for experiment

Curtain

The boom plan is composed of 210 m long curtain and four mooring devices. The skirt height is 0.61 m (including chain) and the inflated float diameter is 0.45 m. The linear density of the boom is 8.6 kg/m. The tension limit of the chain is 15 and 14 T for the leach at the waterline. Each mooring device uses buoyancy coffer (volume 2 m^3), mooring chain (diameter 0.0035 m) and dead-mass (3 T). As a consequence of non-constant bathymetry and tide amplitude, the four mooring chain lengths are respectively 15 m, two times 20 and 25 m. The maximal tide amplitude of the site is 6.9 m. The tide level coefficient attains 93 during the experiment period.

The following Fig. 7.4 shows the Elorn site, the boom plan with its four theoretical mooring points, *A*, *B*, *C*, *D* and the buoy moored position *BM*.

The minimal water height is theoretically 4.5 m at point *D*. The mooring point positions are given in the following Table 7.1.

A lighting device is attached to the coffer at point *D* to orient above two fixed lights *FI–R* in the South East and North East of the site. It allows safe maritime traffic during night periods in the maritime channel located at the near East of point *D* and around the boom.

The maritime and terrestrial materials as well as the administrative and operational staffs necessary for the experiment implementation are not detailed here. The launching of the boom in the Elorn estuary is illustrated by the following Fig. 7.5 with a photo taken by a resident.

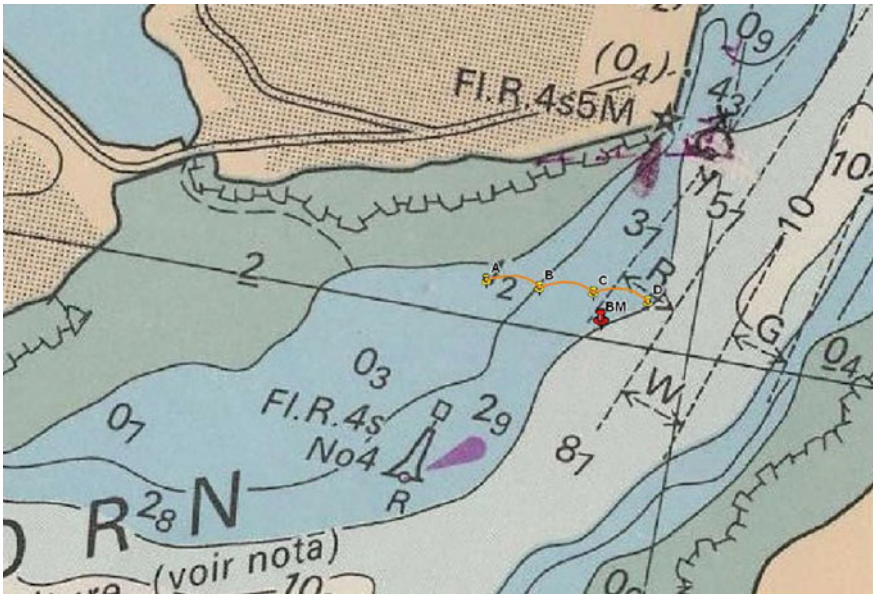

Fig. 7.4 Site of Elorn plan with mooring points and buoy positions

Table 7.1 Mooring point positions ordered from West to East

A	B	C	D
4°22, 286′ W	4°22, 235′ W	4°22, 183′ W	4°22, 130′ W
48°23, 964′ N	48°23, 965′ N	48°23, 968′ N	48°23, 968′ N

Instruments

The scientific material is composed of different sensors installed on three supports, the moored buoy, a small ship and the boom itself.

First, the sensors installed on the buoy are described. All of these sensors are connected to a data logger using the same registration period of 15 s.

- Acoustic directional current meter giving the current velocity vector at the buoy bottom.
- Directional anemometer giving the wind vector at the buoy head.
- Water column height under the buoy.
- Buoy position by using GPS.
- Buoy battery charge indicator by using the current voltage.

The buoy must be anchoraged at higher than 50 m with the boom to avoid a collision. The La Rochelle preliminary experiment has permitted to improve the battery capacity, to define a common sampling time step for the different sensors and to upgrade the reliability of the VHF transmission from the dynamometer.

Secondly, the sensors linked to the boom are described. At the buoyancy coffer connected to the boom at point *D* a dynamometer is installed on the mooring line

Fig. 7.5 Launching of the boom in the Elorn estuary

shackle. The measurement period is 15 s and the maximal measurable tension is 20 T. This sensor gives mooring tension data at point *D* via an antenna into a data logger mass storage strapped on the top platform of the buoyancy coffer. To measure the vertical skirt angulation, three lightweight sticks are attached to connections throughout curtain section *CD*. Using a photo of these sticks can give their respective angles by a simple post-treatment. The La Rochelle experiment permits the stick design improvement as well as its attachment on the curtain connection.

At last, we describe the sensors installed on a small boat running around the boom. An ADCP current meter uses four 600 kHz signal transducers. These ones built a set of three conic surfaces forming a 40° divergent. A valuable modulation of the acoustic signal has been defined during the La Rochelle preparatory experiment. Two current meters placed at a depth of 0.8 m are used to calibrate the ADCP sensor. It permits to measure the 3D sea current velocity components throughout the water column. The depth of the first cell is 0.39 m. The distance between two cells is 0.2 m. The depth of the last cell is 6.99 m. The sampling period is 5 s. The measurements are made for upstream and downstream flows in the vicinity of the boom. The water column height is equally measured.

To measure directly the boom geometry a man-hand GPS is applied by considering the positions of the curtain section connections. The boat running around the boom permits two measures (upstream and downstream runs) for each connection. Taking into account the variable environment of the boom, these two measurements must be as close as possible during time. Measurement of the barrier geometry with a

theodolite based on a laser ray and a mirror as boom reflector has not been retained after testing in the preliminary experiment of La Rochelle. Ground vibrations where the theodolite is installed, generated for example by truck traffic on a harbour quay, does not permit a precise measure.

7.4.3 Results

Let us describe the measurements obtained from the buoy, the pneumatic boat and the numerical and experimental analysis on the floating curtain.

Buoy

The water height under the buoy and the boom tension at the mooring point *D* during November 5, 2009 are represented on the following Fig. 7.6. The horizontal axis represents the time between 00h10 and 22h50.

On Fig. 7.6 we observe that during flooding tide the tension is very low (0.1 T). For ebbing tide (i.e., the tide goes down) the tension is higher (0.33 T). At high and low tides (ebb and flood times) the tension is nearly zero. The remaining question is how to explain the large difference observed on the tension in term of tide directions.

For the same period of time, we present on the following Fig. 7.7 the boom tension at point *D* and the sea current velocity at the buoy location.

We notice that a peak on boom tension corresponds to a peak on the current velocity. The current velocity is a driver on the boom tension. Nevertheless, it remains a large difference on this tension between the flooding and ebbing tides. The current velocity is not the solely reason explaining that effect.

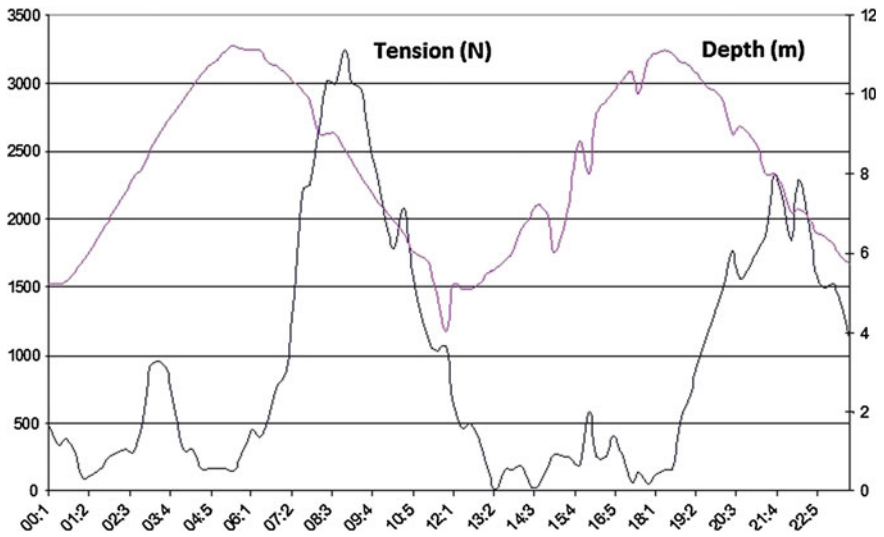

Fig. 7.6 Water height and boom tension during time

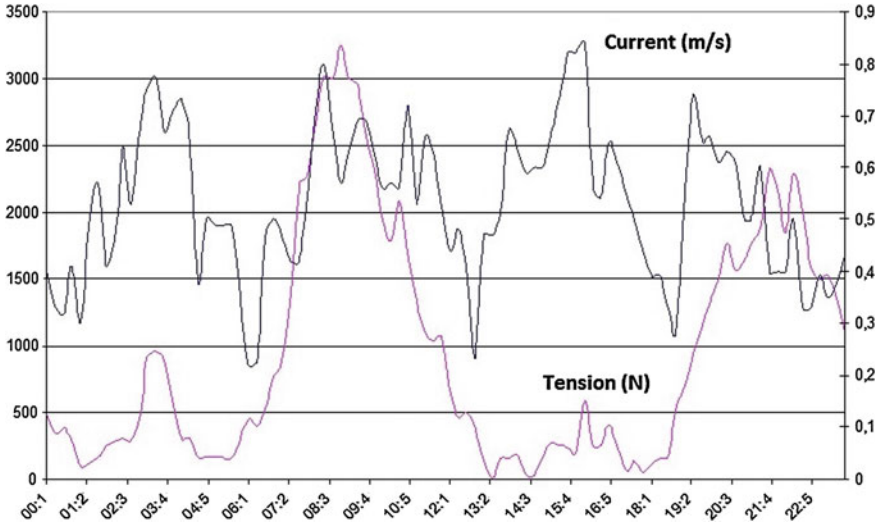

Fig. 7.7 Current velocity and boom tension during time

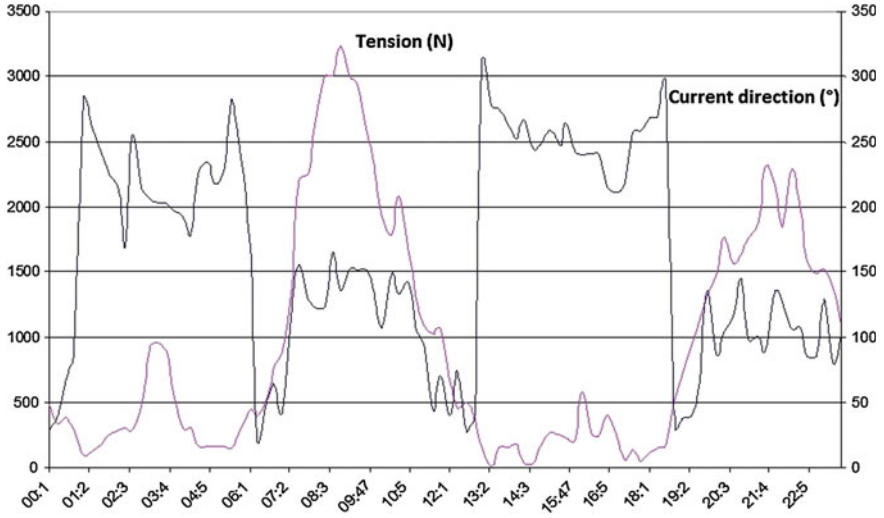

Fig. 7.8 Current direction and boom tension during time

The following Fig. 7.8 represents the boom tension at point *D* and the current direction at the buoy.

The difference of the boom tension between the two tide directions appears to be in relation with the sea current direction toward the boom direction. During flooding tide, the current and the boom directions are almost parallel. As a consequence, the current inducts very low stress in the curtain. At the contrary, during ebbing tide,

the current direction is more close to the normal direction of the curtain. This effect induces more stress in the curtain.

Pneumatic Boat

During favourable weather condition, the relative position of the small boat with the floating boom can be approximatively constant. The operational mode of the GPS position measure at a boom connection is shown on the following Fig. 7.9.

The sea situation allows a valuable number of 7 satellites for GPS tracking. The constant distance between the small boat and the boom permits to construct the boom geometry by using the boat positions. These boat and boom positions are shown on the following Fig. 7.10. The buoy position is indicated on Fig. 7.10. The coordinates system used is "Lambert I Nord". A 27 min period of time has been necessary December 4 for GPS measurements between 15h39 and 16h06.

A screenshot of the ADCP current profiler installed on the small boat permits to show the following Fig. 7.11. Figure 7.11 gives the vertical current profiles observed during different runs of the boat around the boom.

We observe two white zones near the sea surface and sea bottom. These disadvantages are sometimes encountered with the ADCP measure. We obtained white zones at mid-depth which indicated measure with lack of consistency. These ones can be interpreted by the presence of phytoplankton going suspended or a large temperature or salinity gradient between river flow and tide flow. Another possibility is the presence of sediment in suspension. We notice that this effect is only present for deep water.

Fig. 7.9 Boom geometry measurement with GPS

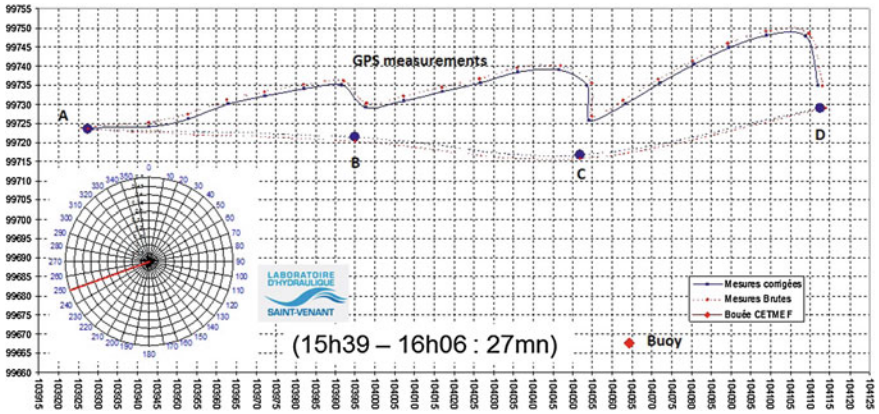

Fig. 7.10 GPS positions of the boom connections

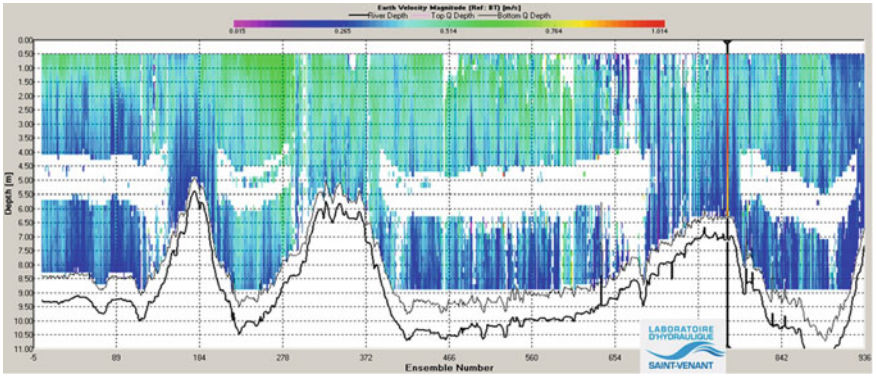

Fig. 7.11 Current profiles during three runs around the boom

Boom

The following Fig. 7.12 shows the third section *CD* of the Elorn boom plan during a flooding tide. On the Fig. 7.12 is indicated the threshold 10° giving the maximal skirt angulation, allowing oil containment without leakage under the boom by current entertainment. To measure the boom efficiency the lightweight sticks bolted to the section connections are compared with the threshold on Fig. 7.12 as indicated by an arrow. The skirt angle at a connection appears to be larger than the efficiency limit. It suggests that under these environmental conditions the boom operates outside its efficiency limit at this time.

Remark 7.4 We use the notation $\theta_{h_V}^{[0,-1]}$ for the vertical skirt angulation obtained numerically and to be compared with the measure using a stick on the boom. We suggest that this angle evaluation considers one fiber. We can define the ruban $r = c \times D$ where c is the one-dimensional boom domain and D the set of the vertical

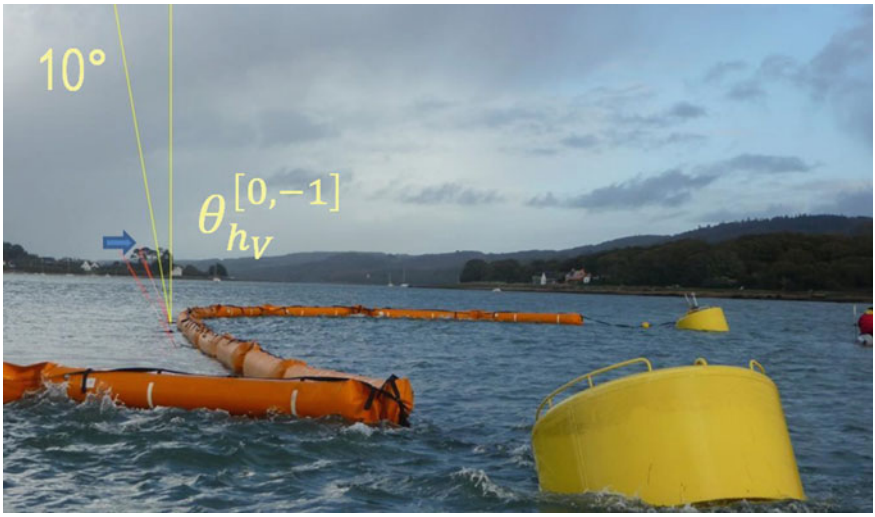

Fig. 7.12 One fiber D (vertical stick) and angle evaluation $\theta_{h_V}^{[0,-1]}$ in Elorn estuary, Brittany, November 2009

sticks or fibers along the boom height. The upper script $[0, -1]$ means that the boom part considered is defined between the sea surface and the skirt bottom chain. The down script h_V represents the resolution of the boom finite element mesh along the vertical.

The maximal eigenvalue of the stress tensor σ defined on the membrane stretched surface is shown on the following Fig. 7.13. The 3D solution computation time is 4 min 7 s on a PC. The solver convergence necessitates 75 iterations.

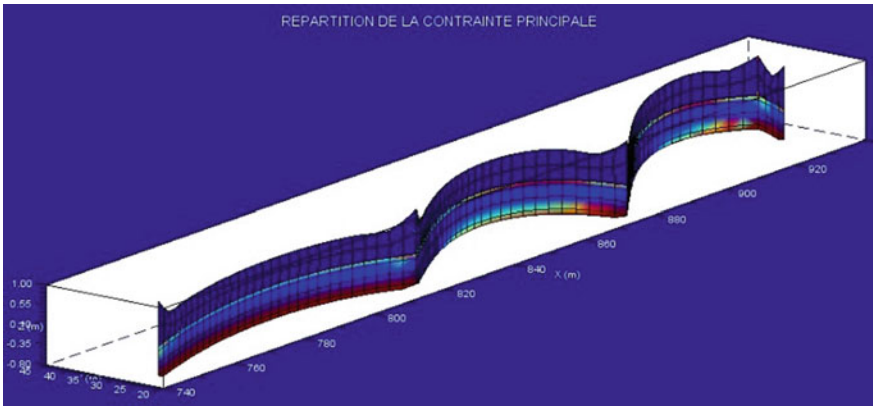

Fig. 7.13 Three sections of Elorn curtain and membrane stress map

The stress are concentrated on the skirt at its bottom chain and its upper leach. We notice that the third boom section *CD* on the upper right of the Fig. 7.13 takes the form of a buckling structure. It is a consequence of a reduced radius of curvature $R(s)$ of that section under a normal pneumatic pressure of the float.

The following Fig. 7.14 shows the comparison of the Elorn boom geometry between the GPS measurements at the top of the figure, a one-dimensional numeric approximation of the boom in the middle of the figure and the 3D numerical solution at the bottom of the figure.

To favour the comparison we have adjusted along the horizontal axis the end-points *A* and *D* for the three geometries. We observe again the buckling pattern of the section *CD* in the 3D solution at the down right side of the Fig. 7.14.

During November 4 between 15h22 and 15h26 the dynamometer indicates a maximal tension of 135 kg, a minimal tension of 86 kg and a mean tension of 107 kg. At the same time, the 3D solution indicates a tension of 206 kg at point *D* while the current meter at the buoy in the South East of point *D* indicates a maximal current of 0.7 knot at 254.5°, a minimal current of 0.5 knot at 218.9° and a mean current of 0.6 knot at 237.9°. The ADCP measure of the current indicates respectively as maximal, minimal and average values around the boom at that time: 0.6 knot at 264.7°, 0.4 knot at 227.0° and 0.5 knot at 243.4°. The anemometer at the buoy indicates a maximal wind velocity of 15.2 knots at 272.8°, a minimal velocity of 9.1 knots at 239.7° and a mean velocity of 11.7 knots at 255.7°. The ADCP current measure (November 4, 15h22:15h37 duration of 15 min) has been made after the GPS evaluation of the boom geometry.

The following Fig. 7.15 shows on the top the skirt angle of the 3D solution of the Elorn boom and on the bottom the third section *CD* of the experiment.

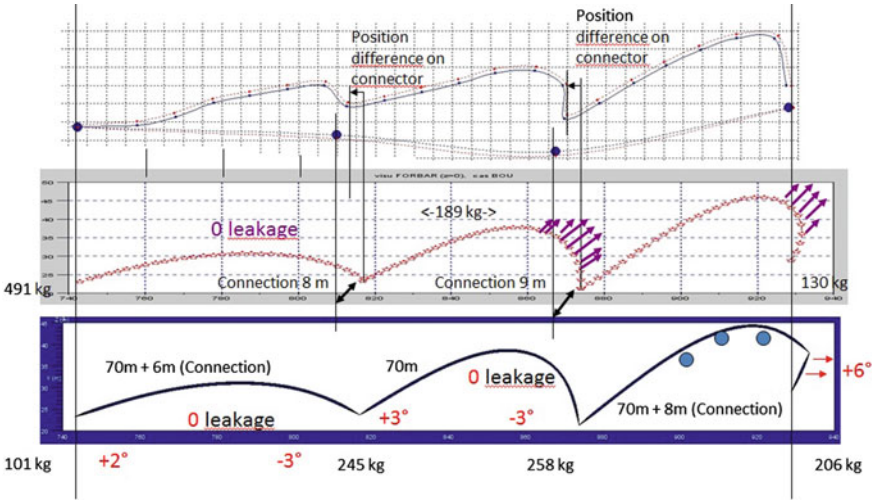

Fig. 7.14 Elorn curtain geometry using GPS, 2D and 3D models

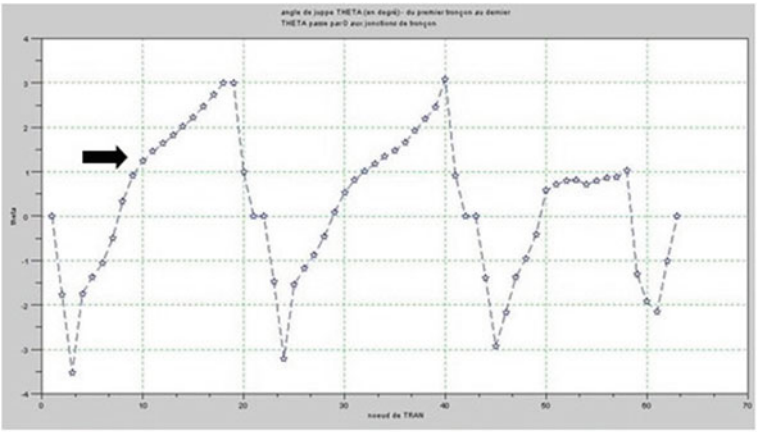

Fig. 7.15 Skirt angle, numerical and experimental, on three sections of the Elorn plan

The black arrow on the left of the Fig. 7.15 underlines a numerical result corresponding to the stick observed during the experiment shown by a white arrow on the right of the figure.

7.4.4 Interpretation

Toward the oil-spill response tactics, we begin by the interpretation of the boom tension in term of the current direction. The Elorn boom plan is oriented approximatively from West to East. During flooding tide the current at the buoy comes from the West and slightly South. For ebbing tide the current goes to the South East. During November 5, 2009, and flooding tide, the Elorn boom plan will have the deviation function for a pollution coming from the Bay of Brest. Under these conditions the boom is weakly stressed. For ebbing tide, the Elorn plan will have the containment function for an oil pollution coming upstream from the Elorn river. In that case the boom stress is high.

The boom geometry measured by GPS permits an interpretation in term of oil-spill preparedness, during a typical period of flooding tide. We consider an oil pollution drifting according to the tide current direction. At that time of November 4, 2009, the section *AB* tends to have a flag-like geometry. During a pollution deviation by the curtain, this section should contain a reduce volume of oil. The sections *BC* and *CD* take the J-form geometry. This favours a large oil accumulation in the vicinity of the section bottom. There is suggested a valuable position to install a skimmer or a sorbent material for oil recovery.

Several considerations must be underlined when using ADCP sensor in our situation. We enumerate several of them. We underline that the ADCP uses the magnetic north while the GPS uses the geographic north. The sensor gives the current profile when both the small boat and the sea bottom are immobile. When the ship moves, the sensor can give its velocity if this one is moderate. By time integration we can obtain the ship displacement. If the sea bottom is composed of tidal mud flat and has a small drifting velocity, from sea current entertainment, then we can observe that the small boat position drifts slightly.

The measured current profiles around the boom are homogeneous along the vertical. It is observed from the first cell at 0.5 m depth. It suggests homogeneity of the current in the first meters of the water depth. The elaboration of the Elorn estuary contingency plan depends principally on the temporal and horizontal current variations. The implementation of 3D oil-spill or hydrodynamic models must give such current velocity field with a vertical homogeneity along the Elorn plan.

The skirt angle evaluation uses light stick attached to boom section connection. We underline that this measurement delivers the angle of the connection which is a rigid beam having low flexibility. The instrument must be improve to measure the angle of the fabric part of the skirt which is a flexible tensile structure. A subsea photography system within low turbidity water may be envisaged to capture the angle and the vertical curvature of the boom skirt.

The stress map in the boom structure permits to define the suitable materials. The finite-element mesh of the boom float is based on a single cylinder. The float can buckle depending of the loadings on the structure. To avoid that effect, the boom sections are built with a sequel of elementary tubes having a reduced length. Each boom element used in the Elorn experiment has a length of 5 m. An improvement of

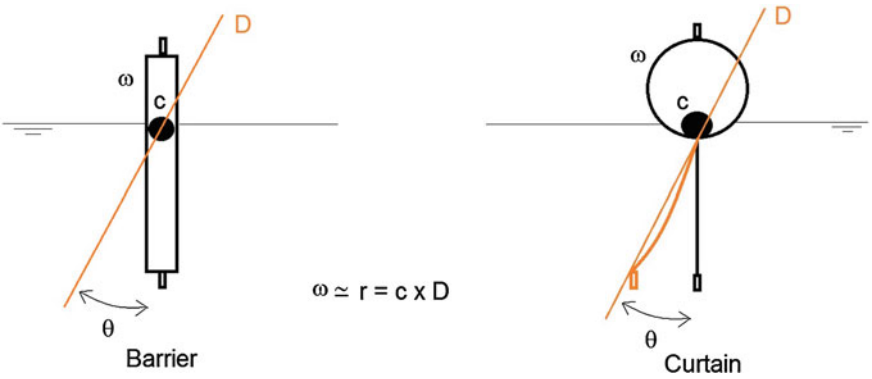

Fig. 7.16 Fiber *D* for barrier and curtain skirts

the boom mesh can be made by proposing a numerical stretching of the float nodes every 5 m.

The geometries of the Elorn boom given by GPS measure, 2D and 3D computations are in relatively good agreement. These geometries depend on the environmental conditions. Experimental and numerical approaches must be based on the same environmental data. The Elorn boom uses mooring lines connected to the buoyancy coffers. The boom mesh can be improved to take into account the mooring lengths.

Along the Elorn boom, the numerical evaluation of the skirt angle follows qualitatively the experimental evaluation of the skirt angle by sticks. A more precise comparison between numerical and experimental approaches can be made in an hydrodynamic channel at a reduced scale.

The above Fig. 7.16 illustrates the vertical injection between the curvilinear domain c and the boom surface ω for both barrier and curtain designs. The Fig. 7.16 presents the manifold of fibers D constructed by using the skirt angle θ. When $\theta = 0$ the bottom part of the ruban $r = c \times D$ corresponds to the non-deformed boom skirt. For other θ values the ruban approximates the deformed boom skirt.

The knowledge of the ruban r is a modelling and operational challenge for oil-spill contingency plan. The installation of a physical measure of one fiber on a barrier during La Rochelle preparatory experiment is shown on Fig. 7.2.

7.5 Conclusions

The main results are the reliability of the 2D cable model to represent a boom device during its mooring in the environment, and the ability of the 3D model results, initialized by using the previous 2D solution, to evaluate the oil containment efficiency and the structural safety. The principal advantage of the proposed approach is to show both numerical method and operational experiment on a same boom part of

a National contingency plan dedicated to oil-spills. More precisely, the numerical solution can be obtained in a relative short delay so that a high reactivity is possible between numerical computation and response planning. A weakness can be underlined concerning the computational time necessary to quantity the sea current map for a valuable boom geometry forecasting. To that end, pre-defined coastal current map can be measured experimentally or numerically to dispose of the necessary environmental hindcast for boom computation. Forecast coastal hydrodynamics can equally be proposed to faster operational action concerning boom relevance during a shortcoming time [1].

Such tensile membrane structure is constitutive of a complex and interdisciplinary problem. From the fluid and solid mechanics points of view, the present study is a structure-fluid interaction problem involving principally two liquids the sea water and the oil. For coastal engineering and civil engineering, the boom behaviour depends on sea current hydrodynamics and mooring or towing floating structure. Several others approaches can be cited such as the atmospheric and oceanic interaction on wind waves and current forcing, decision support systems using software and geographic information system. The overall approach is dedicated to emergency situation and disaster risk reduction of an oil-spill. The accessibility for wide and diversified audience of research results is a main issue to handle more complex situations and provide local stakeholders participation.

The future of the scientific and operational works can be the generalization of boom usages. In term of oil response protocol we can cite the static or dynamic oil recovery and the mostly probable new risks [4]. The environmental conditions can be more complex: current in tidal inlet [14], river or estuarine terminal and artificial lakes. From a numerical analysis point of view, progress can be made to be more sure that there is convergence of the non-linear membrane equation solution. Concerning a view in an operational mode of coastal hydrodynamics with boom structural analysis, the development of oil-spill model [5] can be made so that realistic boom boundary condition is integrated to the oil slick moving.

Acknowledgments The author acknowledges the support of the BAR3D research project co-funded by the French National Research Agency, ANR. The POLMAR center of CETMEF-CEREMA Brest and the "Laboratoire d'Hydraulique Saint-Venant" of EDF R and D Chatou are gratefully acknowledged. The author thanks the support of the ISDAMP+ project. The project is co-funded by the European Union "Humanitarian Aid and Civil Protection", DG-ECHO, and the Civil Protection Financial Instrument, grant agreement 638516/2012/ECHO/A5/SUB. The author acknowledges the support of the ARCOPOL-Platform project. The project is co-funded by the European Union, European Regional Development Fund, ERDF, Atlantic Area Transnational Programme "Investing in our Common Future", project number 2013-1/252. The author thanks Mr. T. Ternisien and Dr. R. Campbell for their valuable advices.

References

1. Castanedo, S., Medina, R., Losada, I.J., Vidal, C., Méndez, F.J., Osorio, A., Juanes, J.A., Puente, A.: The Prestige oil spill in Cantabria (Bay of Biscay). Part I: operational forecasting system for quick response, risk assessment, and protection of natural resources. J. Coast. Res. **22**(6), 1474–1489 (2006)
2. Castro, A., Iglesias, G., Carballo, R., Fraguela, J.A.: Floating boom performance under waves and currents. J. Hazard. Mater. **174**(1), 226–235 (2010)
3. CEDRE, Centre de Documentation de Recherche et d'Expérimentations sur les Pollutions Accidentelles des eaux: Les barrages flottants dans la lutte contre les pollutions en zone côtière. Etat de l'art sur les matériels commercialisés. Report CEDRE no R.95.14.C (1995)
4. Dismukes, D.E., Barnes, S.R., Upton, G.B.: Economic and policy issues in sustaining an adequate oil spill contingency fund in the aftermath of a catastrophe incident. Paper presented at the 37th AMOP Technical Seminar on Environmental Contamination and Response, Environment Canada, Canmore, Alberta, 3–5 June 2014
5. De Dominicis, M., Pinardi, N., Zodiatis, G., Lardner, R.: MEDSLIK-II, a Lagrangian marine surface oil spill model for short-term forecasting-part 1: theory. Geosci. Model Dev. **6**(6), 1851–1869 (2013). doi:10.5194/gmd-6-1851-2013
6. Fang, F., Johnston, A.J.: Oil containment by boom in waves and wind. I: numerical model. J. Waterw., Port, Coast., Ocean Eng. **127**(4), 222–227 (2001)
7. Fingas, M.F.: The Basics of Oil Spill Cleanup, 3rd edn. CRC Press, Boca Raton (2012)
8. Hackbusch, W.: Multi-Grid Methods and Applications. Springer Series in Computational Mathematics. Springer, Berlin (2003)
9. Haug E., Powell G.H.: Finite element analysis of non linear membrane structures. Paper presented at the IASS Pacific symposium, part II on tension structures and space frames. Conference proceedings paper no 23, Architectural Institute of Japan (1972)
10. Lee, C.M., Kang, K.H.: Prediction of oil boom performance in currents and waves. Spill Sci. Technol. Bull. **4**, 257–266 (1997)
11. Muttin, F.: Structural analysis of oil-spill containment booms in coastal and estuary waters. Appl. Ocean Res. **30**(2), 107–112 (2008)
12. Muttin, F.: Oil spill boom modelling, numerical approximation and contingency plan optimization. Pac. J. Optim. **5**(1), 111–126 (2009)
13. Muttin, F.: Umbilical deployment modeling for tethered UAV detecting oil pollution from ship. Appl. Ocean Res. **33**(4), 332–343 (2011)
14. Owens, E.H., Castle, R.W., Fitzgerald, D.M., Chapman Dubach, H.: Tidal inlet protection strategies (tips) field guide for shoreline protection. Paper presented at the International Oil Spill Conference Proceedings, vol. 2014(1), pp. 2112–2126 (2014)
15. Sayah, S., Boillat, J., Schleiss, A.: Behavior of a contractile floating reservoir for the confinement and recovery of oil slicks. J. Waterw., Port, Coast., Ocean Eng. **130**(5), 266–271 (2004)
16. Scherrer, P., Couvreur, J.-F.: Treatment of waste from the Erika Spill. Paper presented at the International Oil Spill Conference Proceedings, vol. 2001(1), pp. 745–749 (2001). doi:10.7901/2169-3358-2001-1-745
17. Violeau, D., Buvat, C., Abed-Meraim, K., De Nanteuil, E.: Numerical modelling of boom and oil spill with SPH. Coast. Eng. **54**(12), 895–913 (2007)